Characterization and Simulation of Warm Forming of 6xxx and 7xxx Series Aluminum Alloys

by

Jacqueline Noder

A thesis

presented to the University Of Waterloo

in fulfilment of the

thesis requirement for the degree of

Master of Applied Science

in

Mechanical and Mechatronics Engineering

Waterloo, Ontario, Canada, 2017

Author's Declaration

I hereby declare that I am the sole author of this thesis. This is a true copy of the thesis, including any required final revisions, as accepted by my examiners.

I understand that my thesis may be made electronically available to the public.

Abstract

This thesis investigates warm forming of 6000 and 7000 series aluminum alloys, namely AA6013 T6, AA7075 T6 and a developmental 7000 series alloy (designated AA70XX T76), including characterization and validation of the material constitutive and friction behaviour at elevated temperature. Experiments and supporting numerical models were developed of warm cup drawing, as well as definition of the thermal process window for a near-commercial structural rail part.

The hardening behavior of the AA70XX T76 was well-captured through a temperature- and rate-dependent modification of the Hockett-Sherby model [1] which was developed and calibrated as part of this work. This model was fit to constitutive data measured by DiCecco [2] and Rahmaan [3].

A steady-state coefficient of friction (COF) of 0.032 for the synthetic alcohol-based Fuchs (Forge Ease AL278), 0.007 for the Teflon film, 0.048 for the graphite-based OKS 536, and 0.047 for the LPS Dry Film PTFE Spray, was obtained in the Twist Compression Test (TCT) at a test temperature of 170°C. For uncoated tooling, the steady-state COF and observation of surface damage demonstrated early film breakdown for the LPS Dry Film PTFE Spray at 170°C whereas the OKS 536 experienced failure at the end of the 50 mm sliding distance at 200°C. Fuchs exhibited onset of scoring only at 230°C. Scoring was prevented by using the Fuchs lubricant in combination with CrWN PVD-coated tooling.

Circular cup draw operations were performed to assess the performance of the different lubricants under warm forming conditions. Punch force was identified as the most sensitive ranking parameter followed by visual inspection of surface condition, measurement of cup flange perimeter, and draw-in length. The obtained lubricant ranking in the draw experiments was in good accordance with the performance results from the TCT. The earing profile of drawn cups revealed strong in-plane anisotropy for AA70XX T76 versus moderate in-plane anisotropy for AA7075 T6 and AA6013 T6, respectively. Numerical models of the cup-draw operations were developed for AA70XX T76 considering the calibrated rate-dependent hardening model and temperature-dependent COF. A rather complex plasticity formulation was needed to capture the earing response of the AA70XX T76 alloy, using a non-associative Barlat YLD2000-2d [4] function for the plastic potential and a Hosford [5] yield function (as implemented within a user subroutine by Prof. Butcher [6]). While the earing profile

(number and shape of ears) was in good experimental agreement, some discrepancies in the peak force and surface strains were observed that were believed to be attributed to model simplifications.

The final aspect of this research involved the warm forming of a near-commercial structural rail component with the intention of defining a process window in terms of final part strength, surface quality, and thinning. Two process routes (isothermal forming in heated tooling and non-isothermal forming in room temperature tooling) were considered at various forming temperatures (177°C, 204°C, and 233°C). Micro hardness measurements identified peak-aged AA6013 as displaying low sensitivity (low tendency to overage) for the temperature histories considered. AA7075 T6 exhibited some strength loss (7.8%) when exposed to 177°C even for short heating times. The final part strength of the as-processed AA70XX T76 identified exposure at 204°C for 120 s as critical temperature before considerable hardness loss occurred. Due to the simple geometry of the formed rails, formability was not an issue, as was confirmed by very mild thinning in the formed part.

Acknowledgements

First and foremost I would like to express my gratitude to Prof. Worswick for giving me the great opportunity to work on this research project and to be part of his group. His enthusiasm, patience, and support towards his students is exceptional. I would also like to thank my co-supervisor Prof. Butcher – it was your encouragement and passion for solid mechanics that made me discover my interest in material modeling. Thank you to both of you for teaching me.

What would have been the work in the lab without the precious help of technicians and technologists: Eckhard Budziarek, Andy Barber, Tom Gawel, Karl Janzen, Neil Griffett, Jeff Wemp, and Richard Gordon. Thank you for all the trouble-shooting and discussions. Greatly appreciated is the support and work done by the machine shop which always tried to accommodate my rush orders.

I would also like to express my profound acknowledgment to the post-docs and PhD students in Prof. Worswick's research group, in particular Armin Abedini, who was always available for discussions and taught me a lot. It was a pleasure and honour to collaborate with you. Thank you Dr. Imbert for your advice and consultation in the lab. Your in-depth experience is greatly appreciated.

To Sante DiCecco and Mass Di Ciano, I am proud and grateful for being part of "Team Warm Forming". It would not have been so much fun without you two. Thank you for all the late-lab hours and support! I will miss our discussions about strain and over-aging ☺.

I would like to thank Dr. Bruce Williams, Mr. Jonathan McKinley and Mr. Lucian Blaga from CanmetMATERIALS, who performed the Argus strain measurements on the deep drawn cups.

The support of our sponsors, Honda R&D Americas Inc., Arconic Ground Transportation Group, and Prometek Research Centre, the Natural Sciences and Engineering Research Council (NSERC), the Canada Foundation for Innovation, and the Canada Research Chairs Secretariat, is profoundly appreciated. I would also like to express my gratitude to the German government funding organization, DAAD, for supporting me through my Graduate Scholarship.

Thank you to all the other grad students and research engineers, specifically Pedram Samadian, Amir Zhumgalov, Cameron O'Keeffe, Cale Peister, Kyu Bin Han, Taamjeed Rahmaan, and Ryan George. Thank you Chi-Hsiang Liao for the weekend shifts and your good musical taste in the lab.

Danke Eckhard, dass du meine Zeit in Kanada zu meinem zweiten Deutschland gemacht hast. Ich werde oft an die Zeit mit einem Lächeln zurückdenken.

Nivi, Arshee, Kritika, Maggi, Namrah and Rabeeah, I do not know what I would have done without you girls – thank you for going through these two years together!

Kein Weltmeer und Abenteuer ist groß genug um unsere Freundschaft zu trennen. Danke, dass du immer bei mir bist, Lisa.

"Trenne dich nie von deinen Illusionen und Träumen. Wenn sie verschwunden sind, wirst du weiter existieren, aber aufgehört haben, zu leben." by Mark Twain – Danke, Mama.

Für Mama

(For my mother)

Table of Contents

List of Figures

List of Tables

List of Abbreviations

AE	Acoustic Emission
AFR	Associative flow rule
bcc	body-centered cubic (crystal structure)
COF	Coefficient of friction
CVD	Chemical Vapor Deposition
DAQ	Data acquisition (system)
DBS	Draw-bead Simulator
DD	Diagonal direction
DIC	Digital Image Correlation
DLC	Diamond-like carbon (coating)
DSC	Differential Scanning Calorimetry
fcc	Face-centered cubic (crystal structure)
FE	Finite Element
FEM	Finite Element Method
GP	Guinier Preston (zones)
HSLA	high-strength low-alloy (steel)
htc	Heat transfer coefficient
ISO	Isothermal (forming)
LDH	Limiting Dome Height (test)
LDR	Limiting drawing ratio
ND	Normal direction
Non-AFR	Non-associative flow rule
NON-ISO	Non-isothermal (forming)
PVD	Physical Vapor Deposition
RD	Rolling direction
RRA	Retrogression and Re-Aging (treatment)
SAED	Selected Area Electron Diffraction
SEM	Scanning Electron Microscope

TCT	Twist Compression Test
TD	Transverse direction
Temp	Temperature
TTCT	Through-thickness Compression Test
umat	User-defined material sub-routine
VH	Vickers Hardness

List of Symbols

A_{ap}	Apparent contact area
A_{tr}	True contact area
A_{fr}	Free surface area
A, B, n, C, m	Material parameters in the Johnson-Cook model
$a_1, a_2, n_0, b_1, b_2, m_0, C_0, c$	Material parameters in the Extended-Nadai model
α_i	Anisotropy coefficients of the yield function
b	Burger's vector in the Bergström model
β_i	Anisotropy coefficients of the flow potential
ε_{pl}	Equivalent plastic strain
ε_0	Pre-strain
$\dot{\varepsilon}$	Strain rate
$\dot{\varepsilon}_{ref}$	Reference strain rate
$\varepsilon_1, \varepsilon_2, \varepsilon_3$	Principal strain
ε_{true}	True strain
ε_{eng}	Engineering strain
C_T, T_1	Calibration paramters in the Bergström model
F_{fric}	Frictional force
F_{draw}	Drawing force
F_{roller}	Pulling force with roller instead of draw-beads
F_{fixed}	Pulling force for fixed roll
F_{bead}	Pulling force in draw-beads
F_N	Normal load
G	Material shear modulus
k	Material shear strength
L', L''	Transformation tensors in the Barlat YLD2000 yield function
$d\lambda$	Plastic multiplier
L_s	Shear gage length
m_{shear}	Shear factor

m	Strain-rate sensitivity in the Bergström model
Ω_0	Low temperature high strain-rate limit of remobilization probability in the Bergström model
o, N	Calibration parameters in the Hockett-Sherby model
P	Interface pressure
p	Dislocation density in the Bergström model
Q_v	Activation energy for vacancy migration in the Bergström model
r_m	Mean TCT cup radius
R	Lankford strain parameter
S	Stress ratio (Ratio of stress along a particular material direction normalized by the corresponding stress along the rolling direction)
σ	Cauchy stress
$\sigma_1, \sigma_2, \sigma_3$	Principal stress
σ_{true}	True stress
σ_{eng}	Engineering stress
σ_{eff}	Effective stress
σ_{flow}	Flow stress
σ_{sat}	Saturation stress
σ_w	Stress due to work hardening in the Bergström model
σ_0	Strain and strain-rate independent stress in the Bergström model
T	Reaction torque
t	Thickness
T_m	Melting temperature
T_0	Reference temperature
τ	Frictional shear stress
Θ	Angle (e.g. with respect to the rolling direction)
Φ	Yield function
Ψ	Flow potential
U_0	Intrinsic immobilization rate in the Bergström model
dw_{pl}	Plastic work increment
w	Width

X', X''	Transformed stress tensors in the Barlat YLD2000 yield function
Y	Yield stress in uniaxial tension

1 Introduction

In working to meet governmental legislative requirements for automotive carbon dioxide emissions and fuel economy standards, the automobile industry is challenged to minimize fuel consumption while maintaining comfort and driving performance [7]. A weighted overview of design factors that contribute to harmful emissions is illustrated in Figure 1 that identifies the vehicle weight reduction as a most promising approach to reduce CO_2 emissions.

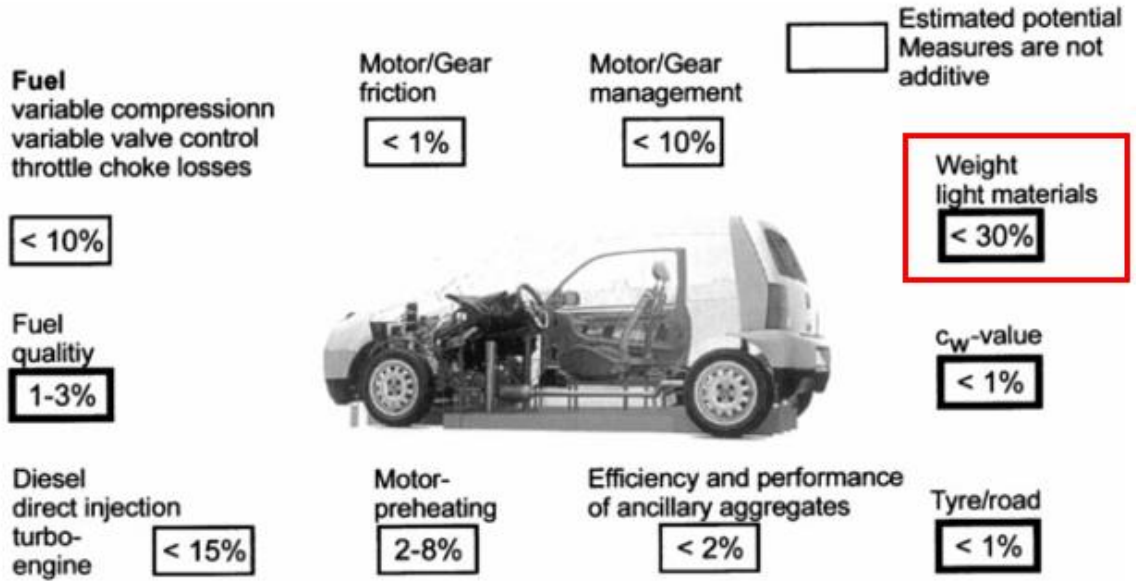

Figure 1: Factors influencing CO_2 emissions [8]

Lightweight materials such as magnesium, and particularly aluminum, have gained interest as potential vehicle structural materials to reduce weight due to their high strength-to-weight ratio, good corrosion resistance, and excellent thermal and electrical conductivity [7]. This trend is well-recorded in the steady increase in the fraction of aluminum alloys making up the vehicle curb weight, as shown in Figure 2. In 1970 the body-in-white almost exclusively consisted of steel and only 2% aluminum was used, this number has increased by a factor of five since then.

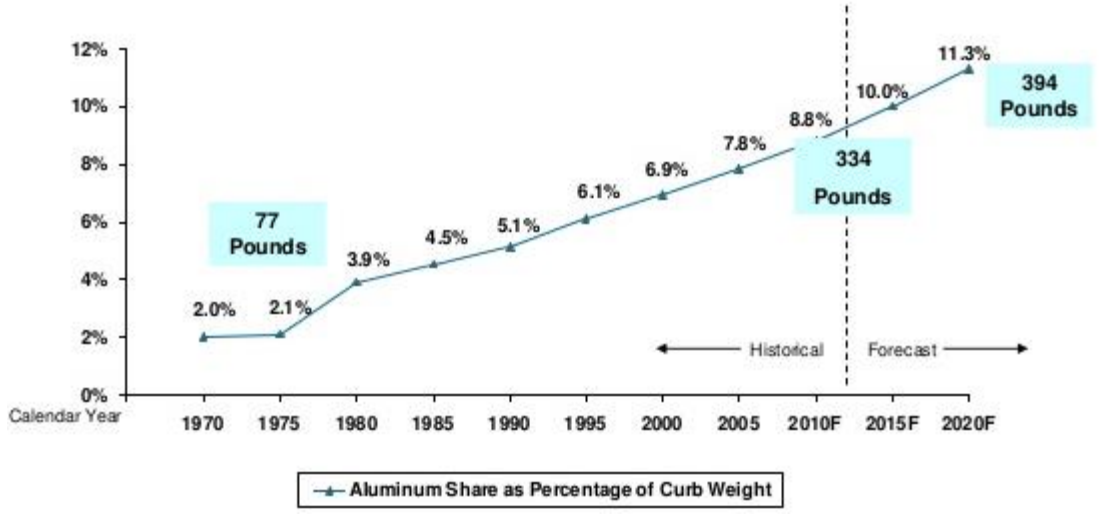

Figure 2: Development of aluminum share of car curb weight [Ducker Research Institute]

The Audi A8 model – known as the Audi Space Frame Concept Car – provides an excellent example of the incorporation of lightweight materials within automotive structures: its body-in-white consists of 92% aluminum and 8% high strength steel (see Figure 3) and demonstrates that the B-pillar is the only part that is still served by steel in view of its high strength requirements.

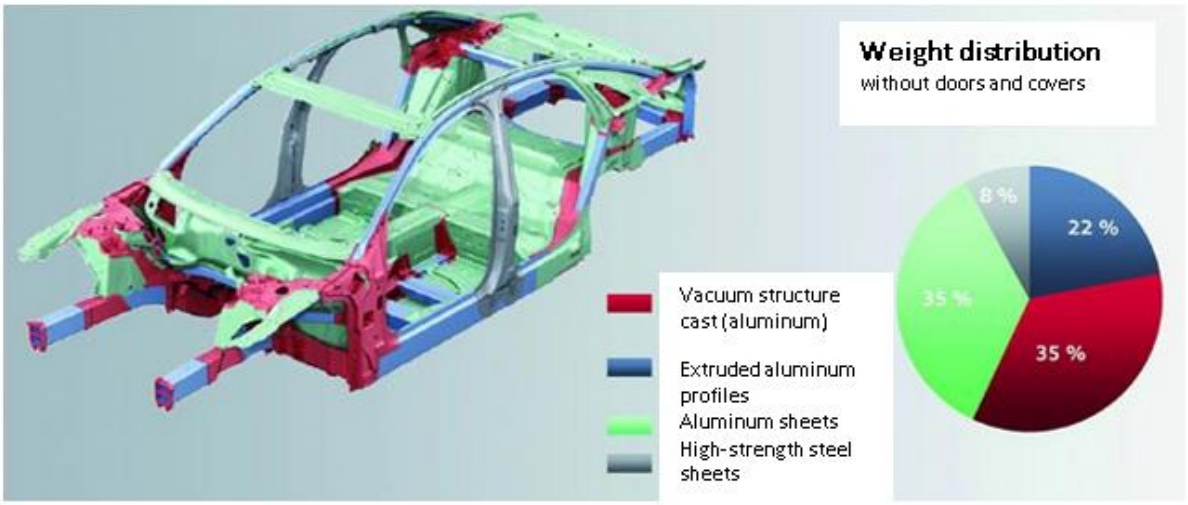

Figure 3: Material selection in the Audi Space Frame Concept Car - Audi A8 [9]

The potential savings of replacing steel components with aluminum are intriguing: 1 kg of aluminum instead of 2 kg steel could yield 10 kg less CO_2 emissions based on the average vehicle life cycle [10].

Currently, structural components such as the B-pillar, using medium-strength 5xxx or 6xxx series aluminum alloys, are not competitive with respect to current ultra-high strength hot stamped steel technology [11]. In contrast to, for example, the 5xxx work-hardened alloys, the 6xxx and 7xxx series aluminum alloys obtain their higher strength levels from precipitation processes that, at the same time, represent a risk of precipitation coarsening (over-aging) if exposed to high temperatures. 7xxx series aluminum alloys do offer higher strength levels (and a comparable strength-to-weight ratio to UHSS), however, these alloys have low formability and multi-step forming processes with intermediate heat treatments are required to overcome forming issues such as thermal distortion, excessive springback, or changes in the microstructure. These additional operations along with the relatively higher cost of 7xxx alloys contribute to both a lengthy and costly process [12]. One option to overcome the limited formability of high strength aluminum alloys is warm forming, however, heat exposure must be limited to prevent changes to the microstructure that would result in a drop in the final part strength and would also affect the corrosion performance.

Forming limit curves represent the critical major to minor strain ratios for which necking is observed under different loading conditions and serve to compare the formability of a material. A material which can sustain higher major to minor strain ratios before necking exhibits better formability. Aluminum alloys can be characterized as having limited formability at room temperature that, however, can be improved at elevated temperatures [7] as demonstrated by Kumar [13] in Figure 4 for AA5754-H22 compared to IF steel.

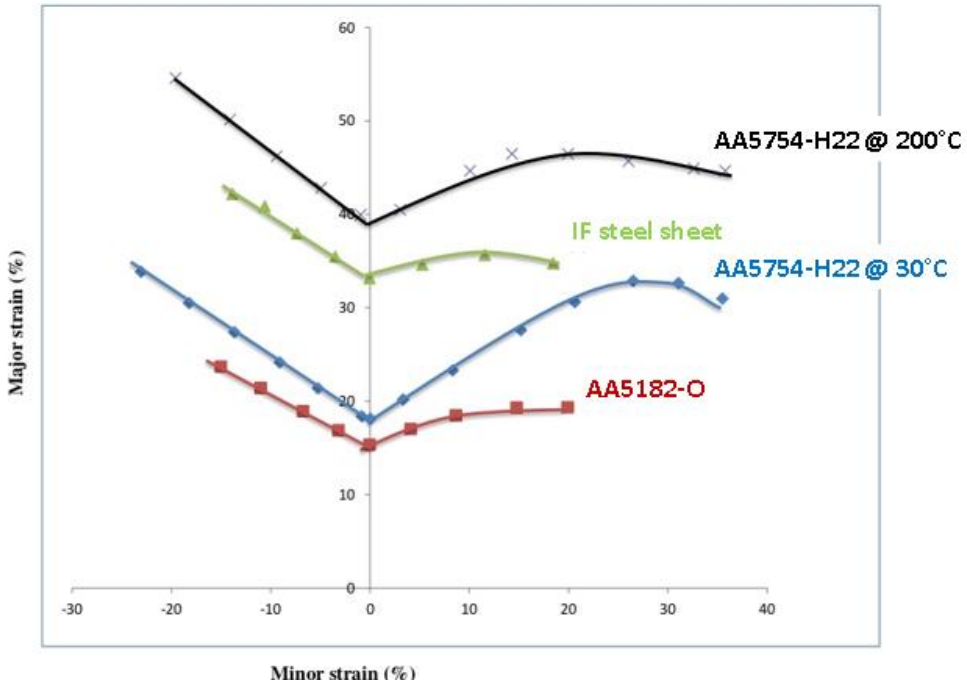

Figure 4: Comparison of forming limit for different aluminum alloys and 1mm thick IF steel sheet [14]

While elevated temperature forming processes will undoubtedly play a major role in increasing the process window for aluminum, friction and lubricant performance offers potential as well, as illustrated in Figure 5. In a deep drawing process, the limiting drawing ratio (LDR) – the ratio between the maximum blank diameter drawn without fracture and the punch diameter – can be increased if an effective lubricant or die coating facilitates material flow and delays plastic instability that would otherwise lead to material failure [15], [16].

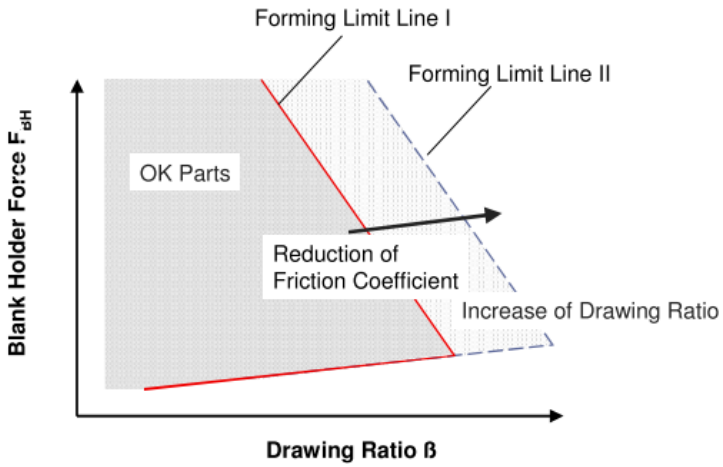

Figure 5: Influence of friction on process window [17]. A more effective lubricant or die coating delays localization that allows drawing of larger blanks or at higher binder loads without fracture. The forming limit of a given process, highlighted in red, can be extended to the dashed line under reduced friction conditions. Combining potentials from lubricant/ die coating choice with temperature-assisted forming is challenging considering their direct interaction; forming at elevated temperature, for example, impairs the lubricant lubricity and properties such as viscosity, whereas at the same time, industrial production conditions require a lubricant that is easy to apply and to clean-off for downstream processes.

For the development of new forming technologies, an integral characterization at the coupon level is required that accounts for the interaction of all correlating disciplines. The efforts and knowledge gains can then be reliably transferred to full-scale industrial components. Following this methodology for the process study on 6xxx and 7xxx series aluminum alloys, a three-stage approach was employed. Both the material and friction were characterized at coupon-level. Rahmaan [3] and DiCecco [2] performed tensile, through-thickness compression tests, and shear experiments that Abedini [18] utilized for calibration of the yield surface, and description of the thermo-viscous hardening model as part of this work. The TCT was utilized to characterize various lubricants and one die coating at warm forming temperatures. These efforts were evaluated in an experimental-numerical deep drawing study that also included a parameter study on anisotropic yield functions to accurately capture the material directionality. Finally, the gathered knowledge is transferred to a near-commercial structural rail with the purpose of defining the process window in terms of final part strength, surface quality, and thinning.

1.1 Aluminum Warm Forming

This section gives an overview on aluminum alloys, tempers, and their application. Material properties of aluminum alloys and temperature-induced changes to the microstructure, such as over-aging, are discussed.

1.1.1 Aluminum Alloys

The employed alloy designation system is based on the Aluminum Association [19] four-digit method for wrought aluminum. The first number identifies the major alloying element and defines the aluminum series, whereas the second one gives information on the modification number. The third and fourth digit are arbitrary numbers for identification of the specific alloy. An overview on these different series, their principal alloying element, and their industrial application is given in Table 1.

Table 1: Overview on different aluminum series and their characteristics [20], [21]

Series	Alloying element	Major characteristics	Industrial application samples
1xxx	Pure aluminum (min. 99.0%)	Strain hardenable, high formability, corrosion resistance, and electrical conductivity Ultimate tensile strength: 70 to 185 MPa Readily joined by welding, brazing, and soldering	Chemical piping (1060) Aluminum foil (1175) Electrical conductor wire (1350) Space mirror
2xxx	Copper	Heat treatable, can be precipitation hardened Ultimate tensile strength: 190 to 430 MPa Usually joined mechanically, but some alloys are weldable	External body sheet panel (2008) Vehicle hood, deck lids (2036) Aircraft wing structure (2024) Aircraft engine components (2618)
3xxx	Manganese	High formability and corrosion resistance Ultimate tensile strength: 110 to 285 MPa Readily joined by all commercial procedures	Air conditioner tube and heat exchanger (3003) Can bodies (3004) Building sheet, siding (3005, 3105)
4xxx	Silicon	Heat treatable, good flow characteristics Ultimate tensile strength: 175 to 380 MPa Easily joined, especially by brazing and soldering	Forged aircraft piston Weld filler alloy (4043)
5xxx	Magnesium	Strain hardenable, excellent corrosion resistance, toughness, and weldability Representative alloys: 5052, 5083, and 5754 Ultimate tensile strength: 125 to 350 MPa	Auto body and frame (5182, 5754) Auto inner panel (5083) Truck trailer bodies (5456) Offshore station tanks (5083)
6xxx	Magnesium-Silicon	Heat treatable, high corrosion resistance, and excellent extrudability Ultimate tensile strength: 125 to 400 MPa Readily welded by GMAW and GTAW methods	External vehicle body (6111) Truck beams (6070) Auto door beams (6061, 6063)
7xxx	Zinc	Heat treatable, very high strength Ultimate tensile strength: 220 MPa to 610 MPa Mechanically joined	Auto bumpers (7029, 7129) Aircraft wing and fuselage skin (7050, 7475) Aircraft wing structure (7050)
8xxx	Lithium and other elements	Heat treatable, high conductivity and hardness Ultimate tensile strength: 120 to 240 MPa	Aerospace applications

Pure aluminum was used in earlier days for “hand-made-bodies” but in the advent of mass production, it is not used due to its softness [22]. The addition of alloying elements enables aluminum alloys with favorable material properties in terms of strength, corrosion resistance, and conductivity. The aluminum alloy series can be further distinguished in terms of heatabilty that include 2xxx, 6xxx, and 7xxx series, with 4xxx depending on the specific alloy.

Following the alloying identification, the temper of the material is specified such as F (as fabricated), O (annealed), H (strain hardened), W (solution heat-treated) or T (thermally treated) that results in a stable condition in the latter case. In the scope of this study, thermally-treated alloys are utilized that are further specified in Table 2.

Table 2: Temper for heat treatment of wrought aluminum alloys [23], [19]

Temper	Definition
T1	Cooled from an elevated temperature shaping process and naturally aged
T2	Cooled from an elevated temperature-shaping process, cold worked, and naturally aged
T3	Solution heat treated, cold worked, and naturally aged
T4	Solution heat treated and naturally aged
T5	Cooled from an elevated temperature-shaping process and artificially aged
T6	Solution heat treated and artificially aged
T7	Solution heat treated and artificially over-aged
T8	Solution heat treated, cold worked, and artificially aged
T9	Solution heat treated, artificially aged, and cold worked
T10*	Cooled from an elevated temperature shaping process, cold worked, and artificially aged
	* T10 is designated in ANSI H35.1/H35.1(M) but not in EN 515 or ISO 2107

With the intention of influencing the corrosion response of formed heat-treated aluminum alloys, tempers between peak-aged (T6) and over-aged (T7) have been developed and are summarized in Table 3.

Table 3: Tempers for improved corrosion resistance [23]

Additional Digits for T7 Temper	Definition
T79	Very limited over-aging to achieve some improved corrosion resistance with limited reduction in strength as compared with the T6 temper.
T76	Limited over-aging to achieve moderate corrosion resistance with some reduction in strength. The T76 temper has lower strength and better corrosion resistance than the T79 temper.
T74	Over-aging to achieve good corrosion resistance with a greater reduction in strength than for T76. Strength and corrosion resistance of T74 are between those of T73 and T6 tempers.
T73	Full over-aging to achieve the best corrosion resistance of all T7 tempers with a greater reduction in strength than the T74 temper.
T77*	Aged condition providing strength at or near T6 temper and corrosion resistance similar to T75 temper. * T77 is designated in ANSI H35.1/H35.1(M)-2009 but not in EN 515 or ISO 2107.

1.1.2 Thermal Effect on Aluminum Alloys

Compensating for the inferior formability of aluminum, compared to mild steel, researchers [24]–[26] have been looking into alternative forming processes such as die quenching in that the material is first heated to elevated temperature (typically 470-560°C) to form a homogeneous solid solution, called solutionizing, and then rapidly formed in a cooled die. After die quenching the material is in a so-called W-temper and expensive natural aging treatments are required to reach full-strength that are costly and lengthy. As an alternative to die quenching, warm forming at temperatures below the material recrystallization temperature (typically less than 300°C) represents an attractive alternative [12].

Interest in warm forming dates back to the mid-19th century when researchers like Finch and Wilson [27], [28] found considerable potential in warm deep drawing annealed and hardened aluminum alloys at temperatures of 150°C. Shehata *et al.* [22] performed uniaxial and biaxial tension tests for aluminum alloys with different magnesium content (0 to 6.6%) over a temperature range from 20°C to 300°C and at different strain rates. They reported a drop in yield strength combined with an increase in ductility at higher temperatures that is more pronounced for higher m-values (rate sensitivity). The same observation was made by Ayres and Wenner [29] on tensile tests and hemispherical punch stretch tests on AA5182-O at temperatures up to 200°C and various strain rates. The strong impact of temperature and strain rate is demonstrated in Figure 6 for AA5182-O. The forming limit diagram at 130°C (left figure) predicts a similar critical major-to-minor strain ratio for all three punch speeds (50, 500, and 5,000 mm/min) whereas a major strain that is by about 28% higher, can be reached if formed at 50 mm/min instead of 5,000 mm/min. For the same alloy, van den Boogaard [30] reported strain-rate dependent flow stress behavior at temperatures higher than 125°C with higher stress values at increased strain rates, except for the temperature range between 25°C and 125°C for that a slightly negative strain-rate sensitivity was observed.

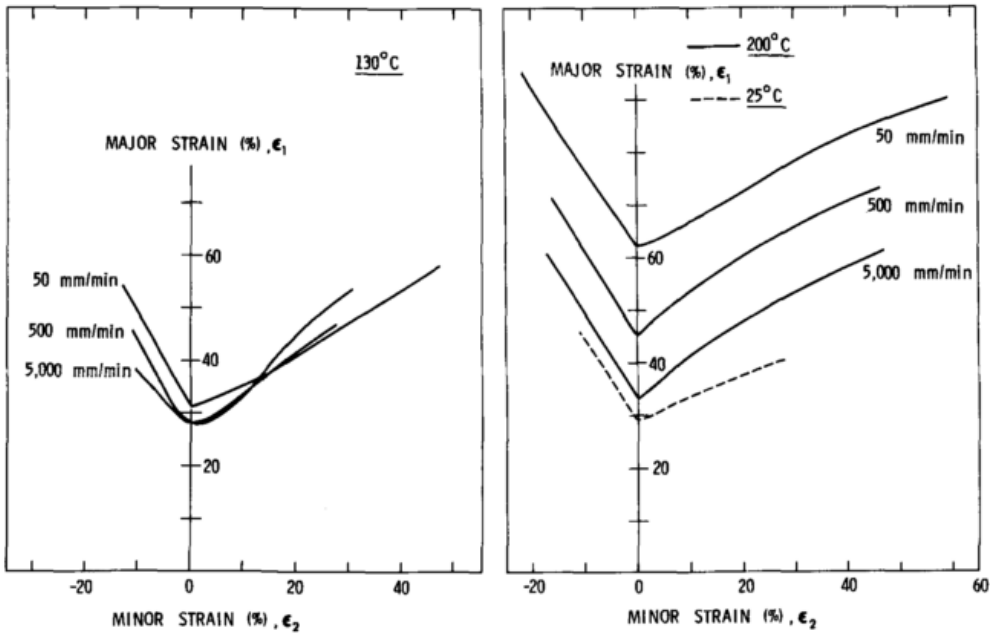

Figure 6: Temperature-dependent strain rate sensitivity for AA5182-O at 130°C (left figure) and 200°C (right figure) [29]

The positive strain-rate sensitivity in the temperature range of 200°C and 350°C was confirmed by Li and Gosh [31], [32] in biaxial and tensile tests on other 5xxx and 6xxx series aluminum alloys. They added that increased post-uniform elongation is mainly responsible for the increased ductility. Among the tested alloys, AA6111 T4 was found to exhibit the least increase in elongation, true fracture strain, and strain hardening exponent as illustrated in Figure 7 [32]. From his tensile study on aluminum alloys, Krajewski [33] identified alloy composition, heat treatment, and microstructure as key parameters impacting ductility at elevated temperature. A higher magnesium content and larger grains were found to increase total elongation at elevated temperature. Increased ductility was not found for age-hardenable aluminum alloys in either the T4 or T6 tempers.

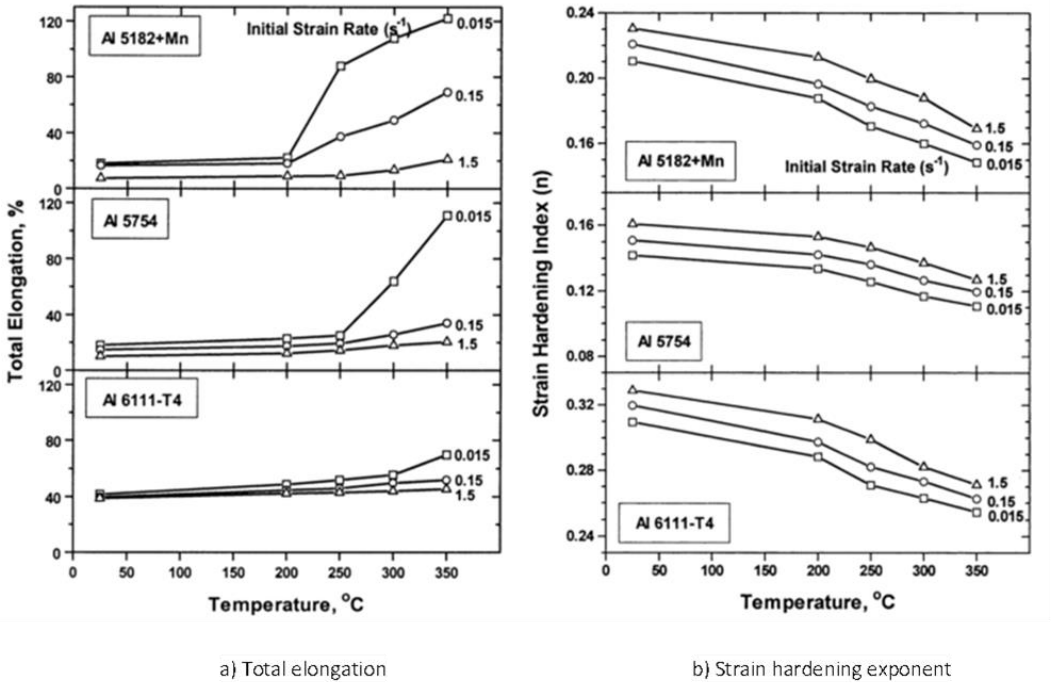

Figure 7: Effect of temperature and strain-rate on the total elongation and strain hardening exponent for different alloys [32]

Compared to conventional cold forming, elevated temperature forming incurs higher costs due to a more complex die design to incorporate electrical heaters, higher energy consumption, increased tool wear, and changing process parameters such as lubricant. Heating the blank and keeping the tooling at room temperature yields cost-savings and could extend the process window [7]. Niu *et al.* [34] demonstrated this on a magnesium ZEK 100 door inner part that they drew in one stroke by heating the blank to 215°C-260°C in a room temperature stamping die.

Naka and Yoshida [35] observed the same trend in cylindrical deep draws of AA6083-O at die temperatures between 20°C and 180°C while the punch was water-cooled. They explained the increasing LDR through the softer material showing less resistance to deformation in the flange section. The lowest LDR was found at 80°C that they explained through the presence of dynamic strain aging confirmed through serrated stress-strain curves in uniaxial tension tests. Independent of the die temperature, higher forming speeds negatively influenced the LDR.

Morris and George [12] transferred this knowledge to full-scale structural parts at the Chrysler Corporation for selected 5xxx series work-hardened alloys and peak-aged 6xxx and 7xxx series age-

hardened alloys. They highlighted the importance of short heating cycles (in the order of one to two minutes with an infrared heater) in combination with lubricant choice to prevent rapid cooling and found the black color of a resin bonded graphite lubricant beneficial in minimizing heat reflection. To prevent formability problems, the blank is to be formed fast enough before the temperature drops below a critical value. From tensile baseline studies, they found 200°C as an optimal forming temperature for age-hardened aluminum alloys in view of bending and drawing operations. They reported that the benefits were reduced in stretching operations of age-hardened alloys due to a reduced strain-rate hardening at elevated temperature that controls diffuse necking.

1.1.3 Forming Limitations

Limitations of a material or a forming process can appear in various forms such as part fracture, necking, wrinkling, distortion, springback, scratches on the sheet surface, or loss of material strength after forming. The occurrence of the latter, excessive strength loss, can be tremendous depending on heat exposure and might equate the strength of a costly 7xxx with a medium-strength 6xxx series aluminum alloy. This effect is addressed in the following.

In the peak-aged temper (T6), the aluminum alloy microstructure consists of finely dispersed metastable precipitates (η') within grains with coarser and densely-spaced precipitates along grain boundaries, whereas the lower-strength over-aged temper (T7) comprises coarser and thicker but more stable (η) precipitates inside the grain and more spaced precipitates along grain boundaries [89]. Stress corrosion resistance is said to be influenced by microstructure along grain boundaries with larger particles to be favoured in terms of reduced stress corrosion cracking [11], [36]. This behaviour explains why an over-aged temper (such as T76 or T73) is often used even though this temper is accompanied by a drop in strength of about 10% to 15% relative to the T6 condition [37].

Hui *et al.* [11] demonstrated partial strength recovery on peak-aged AA7075 tensile samples that were formed between 200°C and 260°C and exposed to a 30 min paint bake cycle at 177°C. The latter represents a thermal cycling process to cure the vehicle paint and to cause precipitation-hardening [11]. A forming temperature of 260°C or higher resulted in a considerable drop in both tensile strength and elongation to failure, that they associated with a change in the microstructure (structure of precipitates) due to the thermal exposure. Figure 8 [11] summarizes the effect of heat exposure on the mechanical properties (yield stress and micro hardness). For limiting dome height tests, they found

that formability increased between 140°C and 220°C whereas no remarkable change is noticed at 260°C. For deep-drawing, the highest LDR (2.0) was obtained at 180°C whereas blanks below 100°C fractured.

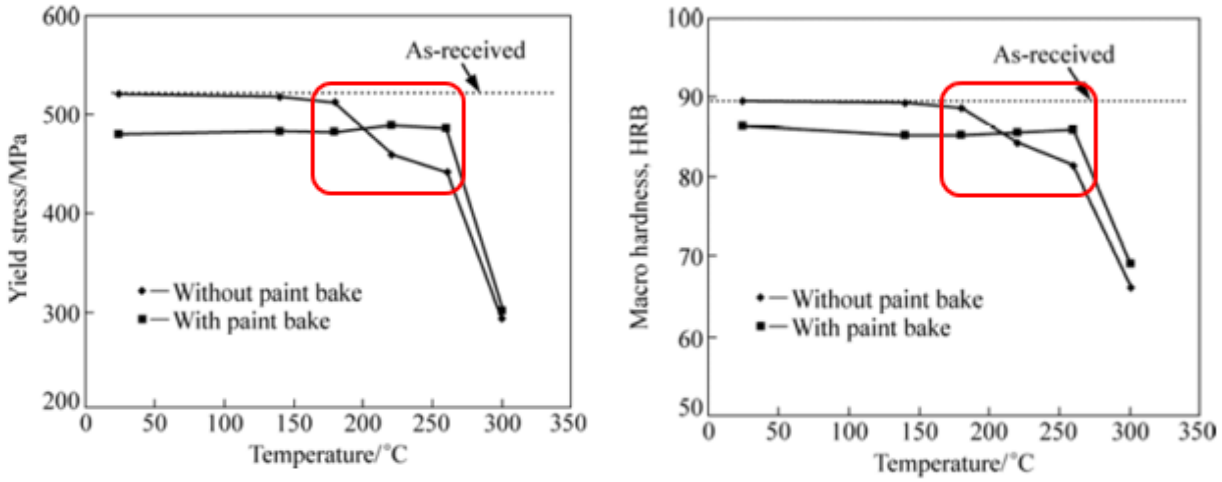

a) Yield stress b) Micro hardness

Figure 8: Effect of heat exposure on mechanical strength of AA7075 T6 [11]

The above-mentioned heat-treatment is summarized under the term retrogression and re-aging (RRA) treatment, that encompasses two thermal cycles applied to an alloy in T6 temper: exposure to higher temperatures to solutionize T6 precipitates, that is associated with a low strength (retrogression), followed by exposure to a lower temperature that facilitates re-precipitation and can bring back or surpass the initial mechanical strength (re-aging) [36]. The extent to that the strength can be recovered depends on the temperature and heat exposure time during the retrogression phase, as illustrated in Figure 9 [38]. The first phase is characterized through a rapid drop in strength, reaching a minimum value, followed by an increase in strength that allows partial recovery in RRA. The final stage records a strong drop in strength that is explained through precipitate coarsening. The critical retrogression time that allows full recovery or even exceeds the original strength decreases with increasing forming temperature [37].

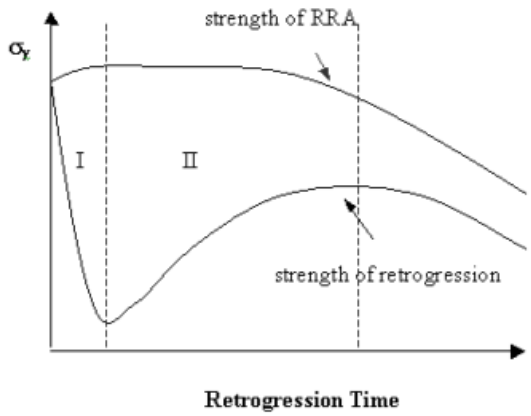

Figure 9: Effect of retrogression time on strength recovery in RRA [38]

Viana *et al.* [36] confirmed partial strength recovery and improved stress corrosion cracking resistance through RRA for AA7075 T6 that was subjected to a retrogression temperature between 160°C and 220°C followed by a re-aging cycle. From differential scanning calorimetry (DSC), they concluded the sequence of precipitate formation as follows:

SSS	→	GP zones	→	η’	→	η
(Saturated Solid Solution)		(Guinier Preston Zones)		(metastable precipitates)		(equilibrium precipitates)

After the retrogression stage, Viana *et al.* [36] reported a similar microstructure for all tested temperatures: the precipitate distribution inside the grain was similar to T6 with coarse precipitates along the grain boundaries comparable to the T7 temper. From selected area electron diffraction (SAED) and DSC, they concluded that the strength drop is associated with dissolution of less stable precipitates (Guinier Preston (GP) zones and smaller η’ particles), the extent of that is controlled through the heat exposure. After re-aging, the microstructure consists of densely-dispersed precipitates inside the grain (slightly coarser and denser than T6) with continuously growing precipitates along grain boundaries (similar to T7).

1.2 Constitutive Modeling

Finite Element (FE) models are commonly applied to predict material behavior in forming operations and therefore represent an important analysis tool. Accurate predictions of stresses and strains require a sophisticated material model that captures the experimentally-observed behavior such as strain

hardening, temperature-induced softening, and directionality. The root of plastic deformation lies in the crystal structure and the interaction of individual grains that motivates mathematically-driven crystal plasticity approaches. Unfortunately, the computational cost of crystal plasticity models makes them unattractive for full-scale forming simulations [39]. Therefore, a continuum-based approach with the use of phenomenological yield functions is often applied and used in the scope of this work.

Common building blocks for describing the deformation behavior of a material are the yield surface that determines plastic flow for a certain stress state, the hardening law that describes the evolution of the yield surface, and the flow rule that ties the strain to the stress increment [30].

1.2.1 Hardening Models

As demonstrated by Quan *et al.* [40] for AA7075, the hardening behavior of aluminum alloys has a strong correlation with temperature and rate of deformation. In an attempt to capture these effects, researchers have developed many different constitutive equations. While the following summary only covers selected models, a more detailed discussion is offered by Larour [41].

In agreement with the observed stress saturation for larger strains, implied by Voce [42], Hockett and Sherby [1] presented in 1974 the hardening model given as:

$$\sigma_{flow} = \sigma_{sat} - e^{\left(-(N\varepsilon_{pl})^{o}\right)}\left(\sigma_{sat} - \sigma_{y}\right) \tag{1}$$

that utilizes the saturation stress (σ_{Sat}), the yield stress (σ_{y}), the effective plastic strain (ε_{pl}), and the calibration parameters *o* and *N* where the latter describes the hardening characteristics. The absence of thermo-viscous effects limits the use of Equation 1 in its original form to quasi-static room temperature observations.

A thermo-viscous model was proposed by Johnson and Cook [43] in Equation 2, that represents the observed hardening behavior of 12 materials among that are steel and aluminum.

$$\sigma_{flow} = \left[A + B\ {\varepsilon_{pl}}^{n}\right]\left[1 + C\ ln\left(\frac{\dot{\varepsilon}}{\dot{\varepsilon}_{0}}\right)\right]\left[1 - \left(\frac{T - T_{0}}{T_{m} - T_{0}}\right)^{m}\right] \tag{2}$$

The stress is described through a power-law function in that *A* corresponds to the yield stress, *B* and *n* describe the hardening characteristics. Strain-rate and thermal effects are described through multiplicative terms in that *C* represents the rate sensitivity, $\dot{\varepsilon}_{0}$ the reference strain rate, *m* is a

measure for the thermal softening, T_m corresponds to the material melting temperature, and T_0 to the reference temperature. While the simplicity of the Johnson-Cook model promotes its popularity, it is occasionally criticized for poorly describing strain-rate effects of complex materials [43].

Owing to its simplicity, the phenomenologically derived thermo-viscous extended Nadai model [30], [44], [45] is often utilized as baseline comparison to physically-driven models such as the Bergström model. Just as in the Johnson-Cook model, the Nadai model uses a multiplicative strain rate function and has the following form:

$$\sigma_{flow} = C\left(\varepsilon_{pl} + \varepsilon_0\right)^n \left(\frac{\dot{\varepsilon}}{\dot{\varepsilon}_0}\right)^m \tag{3}$$

$$C(T) = C_0 + a_1\left[1 - e^{\left(a_2\frac{T-273}{T_m}\right)}\right]$$

$$n(T) = n_0 + b_1\left[1 - e^{\left(b_2\frac{T-273}{T_m}\right)}\right]$$

$$m(T) = m_0\, e^{\left(c\frac{T-273}{T_m}\right)}$$

where ε_0 represents the amount of pre-strain, C_0, a_1, a_2, n_0, b_1, b_2, m_0, and c are material constants.

The advantage of physically-based hardening models like the temperature- and rate-dependent model proposed by Bergström and Hallén [46] is the description of the hardening response through physical mechanisms of dislocation movement. The utilized description of the Bergström model for this work is based on the implementation by van den Boogaard [30]. The flow stress decomposes into strain and strain-rate independent stress σ_0, and stress due to evolution of dislocation density summarized under the term work hardening σ_w.

$$\sigma_{flow} = \sigma_0(T) + \sigma_w(p, T) \tag{4}$$

Contribution from the work-hardening term is determined through the dislocation density p, the material shear modulus G, and the Burgers vector b, and α is used as a scaling parameter of the order one.

$$\sigma_W = \alpha G(T) b \sqrt{p} \tag{5}$$

The evolution of the dislocation density is expressed through Equation 6:

$$\frac{dp}{d\varepsilon} = U(p) - \Omega(\dot{\varepsilon}, T) \tag{6}$$

$$\Omega(\dot{\varepsilon}, T) = \Omega_0 + C e^{\left(\frac{-mQ_v}{RT}\right)} \dot{\varepsilon}^{-m}$$

$$U(p) = U_0 \sqrt{p}$$

where the first term represents storage of mobile dislocations and the second expression describes dynamic recovery through remobilization and annihilation [30]. U_0 is the intrinsic immobilization rate, Ω_0 the low temperature high strain rate limit of remobilization probability, Q_v the activation energy for vacancy migration, R the gas constant, m is similar to the conventional strain rate sensitivity, and C is a calibration parameter [45]. The change in dislocation density is computed incrementally through Equation 7, from that the final flow stress assembles to Equation 8.

$$p_{i+1} = \left[\frac{U_0}{\Omega}\left(e^{(0.5\Omega\Delta\varepsilon)} - 1\right) + \sqrt{p_i}\right]^2 e^{-\Omega\Delta\varepsilon_{pl}} \tag{7}$$

$$\sigma_{flow} = \left(1 - C_T e^{\frac{-T_1}{T}}\right)\left(\sigma_0 + \alpha G_{ref} b \sqrt{p}\right) \tag{8}$$

where C_T and T_1 are calibration parameters. While the Bergström model generally captures the material response for aluminum alloys better than the extended Nadai model in view of the stress saturation, a major drawback of the Bergström model is the strain-rate independent description of the yield stress [30]. This can clearly be seen in Equations 7-8 since for the first time increment, the initial dislocation density is utilized – independent of the rate of deformation.

1.2.2 Yield Functions

The yield function ϕ in Equation 9, that is dependent on the Cauchy stress σ, the equivalent plastic strain increment ε_{pl}, anisotropy parameters α_i, and the yield exponent, describes whether deformation

is elastic (inside the yield locus) or plastic (on the yield locus). A stress state outside of the yield locus is not defined [30].

$$\Phi = \sigma_{eq} - \sigma_{flow} \tag{9}$$

According to Drucker's postulate, the plastic strain increments are normal to the flow potential ψ (σ, ε_{pl}, β_i) where β_i corresponds to a separate set of anisotropy coefficients and can be expressed through the product of a constant called the plastic multiplier (dλ) and the partial derivative of the flow potential with respect to the stress tensor [30].

$$d\varepsilon_{pl} = d\lambda \frac{\partial \psi}{\partial \sigma} \tag{10}$$

If the yield function is chosen as the flow potential, Equation 10 can be simplified and the term associative flow rule is employed.

The shape of the yield surface is influenced by the directionality of the yield stress under different loading conditions. The degree of anisotropy is commonly characterized using tensile tests at different angles θ from the rolling direction (RD). S_θ represents the ratio of stress along a particular material direction normalized by the corresponding stress along the RD:

$$S_\theta = \frac{\sigma_\theta}{\sigma_{RD}} \tag{11}$$

Other loading conditions, such as plane strain, biaxial or shear loading can also be utilized to characterize the anisotropy of the material stress response.

Strain- or plastic anisotropy is expressed through the well-known Lankford strain ratio (R-value) that measures the anisotropy between width (w) and thickness (t) strains [30] as defined in Equation 12, under the assumption of constant plastic strain. In forming, high R-values are favoured since they represent increased resistance to thinning whereas lower R-values correspond to larger strains in the thickness direction compared to strains in the width that promote thinning.

$$R_\theta = \frac{\varepsilon_y}{\varepsilon_z} = \frac{ln\left(\frac{w}{w_0}\right)}{ln\left(\frac{t}{t_0}\right)} \quad (12)$$

Deviations from an R-value of unity represent directionality. Depending on the evolution of the strain anisotropy with respect to the RD, ears might form in deep drawn cups. The material in directions of higher R-values delays material flow whereas draw-in is facilitated for low R-values. This observation is demonstrated on rolled AZ31 magnesium sheet in Figure 10 [47].

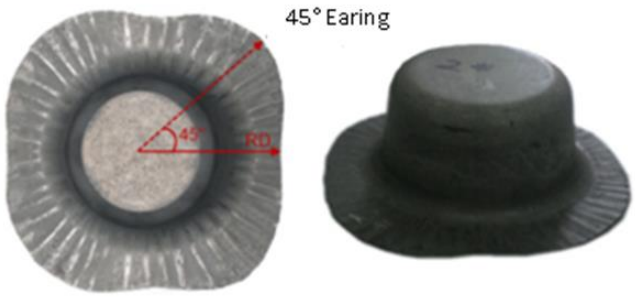

Figure 10: Presence of earing in deep drawing of rolled AZ31 magnesium sheet [47]

The Tresca and von Mises yield functions are the most popular criteria for isotropic materials, even though experimental data often lies between these two functions, closer to von Mises [48]. In an attempt to improve predictions, Hosford [5] suggested the non-quadratic yield function in Equation 13, expressed in a three-dimensional principal stress state, with *b* being an integer between one and infinity and σ_y the material yield stress in uniaxial tension. For *b* equal to one, Hosford's criterion reduces to von Mises whereas n equal to two yields Tresca [5].

$$\phi_{Hos} = (\sigma_1 - \sigma_2)^b + (\sigma_2 - \sigma_3)^b + (\sigma_1 - \sigma_3)^b = 2{\sigma_y}^b \quad (13)$$

The first anisotropic quadratic yield function was proposed by von Mises and was generalized and reduced to a material with three symmetric orthogonal axis and six anisotropy coefficients by Hill in 1948, called Hill48 [49]:

$$\phi_{Hill-48} = F(\sigma_{22} - \sigma_{33})^2 + G(\sigma_{33} - \sigma_{11})^2 + H(\sigma_{11} - \sigma_{22})^2 + 2L{\sigma_{23}}^2 + 2M{\sigma_{31}}^2 + 2N{\sigma_{12}}^2 = 0.5 \quad (14)$$

where *F*, *G*, *H*, *L*, *M* and *N* are the material anisotropy coefficients. While its user-friendly format and manageable number of required experiments are reasons for its popularity, poor accuracy is found for materials with low R-values such as aluminum alloys [48]. Further attempts such as Hill79 and Hill90 still failed to capture strongly anisotropic R-values whilst similar yield stresses in the RD and the TD [48]. The shortcomings of Hill48 can be seen in the R-value and stress ratio predictions in Figure 11 for high strength steel sheet of 780 MPa TS grade. Bong *et al.* [50] calibrated two versions of Hill48; utilizing the R-values for calibration of the anisotropy coefficients (denoted as Hill49-r) and utilizing the stress ratios (denoted as Hill48-σ). It can be seen from the figure that either R-values are well described with Hill49-r or stress ratios with Hill49-σ but neither one is capable of describing both material characteristics reasonably well.

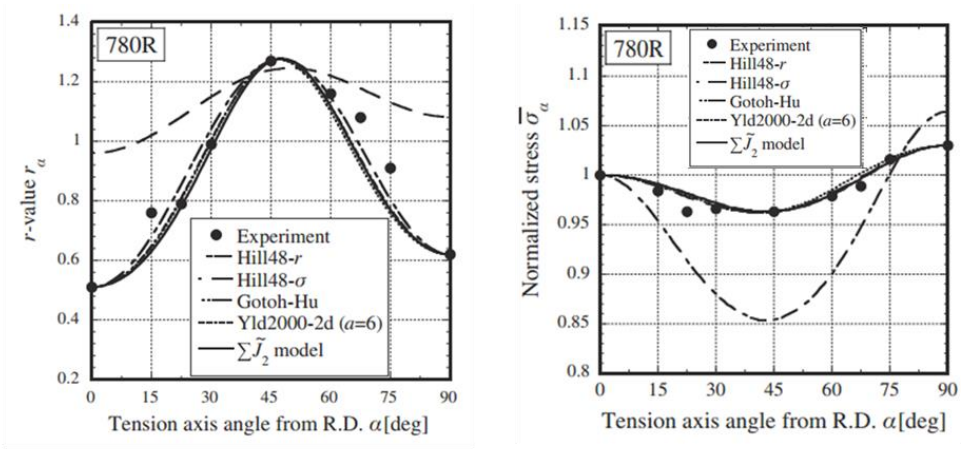

a) R-values b) Stress ratios

Figure 11: Comparison of R-value and stress ratio prediction for high strength steel sheets of 780 MPa TS grade [51]

In 1989, Barlat and Lian [52] modified Hosford's postulate to account for planar anisotropy under plane stress conditions, that they extended to general 3-D stress states in 1991 [53]. Barlat and coworkers proposed more yield functions such as YLD91 and YLD96, however, good experimental and crystallographic agreement was only found for aluminum alloys with low anisotropy and the accurate prediction of earing in aluminum deep drawing remained a challenge [48].

The yield function proposed by Barlat in 2000, called YLD2000-2d, utilizes two linear transformations of two isotropic yield functions that provide higher number of anisotropy coefficients and allow more detailed description of the material behavior:

$$\phi_{YLD2000-2d} = \phi'(X') + \phi''(X'') = 2{\sigma_{eff}}^{a} \tag{15}$$

where σ_{eff} is the effective material stress and a is chosen for the crystallographic structure of the material (normally 6 for body-centered cubic (bcc) materials and 8 for face-centered (fcc) materials). The anisotropic yield functions can be expressed as

$$\phi' = |{X'}_1 - {X'}_2|^a \tag{16}$$

$$\phi'' = |2{X''}_2 + {X''}_1|^a + |2{X''}_1 + {X''}_2|^a$$

The linearly-transformed stress components in principal plane stress space can be obtained through Equation 17 where L' and L'' represent transformation tensors of the form recorded in Equation 18 and 19.

$$X' = L' : \sigma, \quad X'' = L'' : \sigma \tag{17}$$

$$L' = \begin{bmatrix} {L'}_{11} & {L'}_{12} & 0 \\ {L'}_{21} & {L'}_{22} & 0 \\ 0 & 0 & {L'}_{66} \end{bmatrix}, L'' = \begin{bmatrix} {L''}_{11} & {L''}_{12} & 0 \\ {L''}_{21} & {L''}_{22} & 0 \\ 0 & 0 & {L''}_{66} \end{bmatrix} \tag{18}$$

$$\begin{bmatrix} {L'}_{11} \\ {L'}_{12} \\ {L'}_{21} \\ {L'}_{22} \\ {L'}_{66} \end{bmatrix} = \begin{bmatrix} 2/3 & 0 & 0 \\ -1/3 & 0 & 0 \\ 0 & -1/3 & 0 \\ 0 & 2/3 & 0 \\ 0 & 0 & 1 \end{bmatrix} \begin{bmatrix} \alpha_1 \\ \alpha_2 \\ \alpha_7 \end{bmatrix}, \begin{bmatrix} {L'}_{11} \\ {L'}_{12} \\ {L'}_{21} \\ {L'}_{22} \\ {L'}_{66} \end{bmatrix} = \frac{1}{9} \begin{bmatrix} -2 & 2 & 8 & -2 & 0 \\ 1 & -4 & -4 & 4 & 0 \\ 4 & -4 & -4 & 1 & 0 \\ -2 & 8 & 2 & -2 & 0 \\ 0 & 0 & 0 & 0 & 9 \end{bmatrix} \begin{bmatrix} \alpha_3 \\ \alpha_4 \\ \alpha_5 \\ \alpha_6 \\ \alpha_8 \end{bmatrix} \tag{19}$$

where α_i are anisotropic coefficients that are conventionally determined through uniaxial and equi-biaxial tension tests. In order to optimize deviations between experiment and calibrated yield surface, optimization techniques such as least-squares minimization are employed [4], [39]. Abedini *et al*. [54] highlighted deficiencies of conventional calibration methods since hydrostatic stresses are generated under in-shear loading conditions that violates mechanics of shear deformation. They suggest to constrain the ratio of principal strains to be equal and opposite for shear loading. This additional constraint upon calibration of the plastic potential might sacrifice accuracy in uniaxial and biaxial

regions for that they refer to yield functions with more calibration parameters or non-associative flow rules.

Figure 12 [50] demonstrates the difference in predictions by the isotropic von Mises yield function and the anisotropic YLD2000-2d model for ferritic stainless steel of 0.1 mm sheet thickness (Figure 12a) and 1 mm (Figure 12b). While onset of yielding under uniaxial tension in the RD is well captured by both yield criteria, von Mises slightly underpredicts yielding in the TD. Remarkable discrepancies are found for the thinner sheet under biaxial loading for that, in contrast to the von Mises model, the YLD2000-2d function correlates well with the experimental data point.

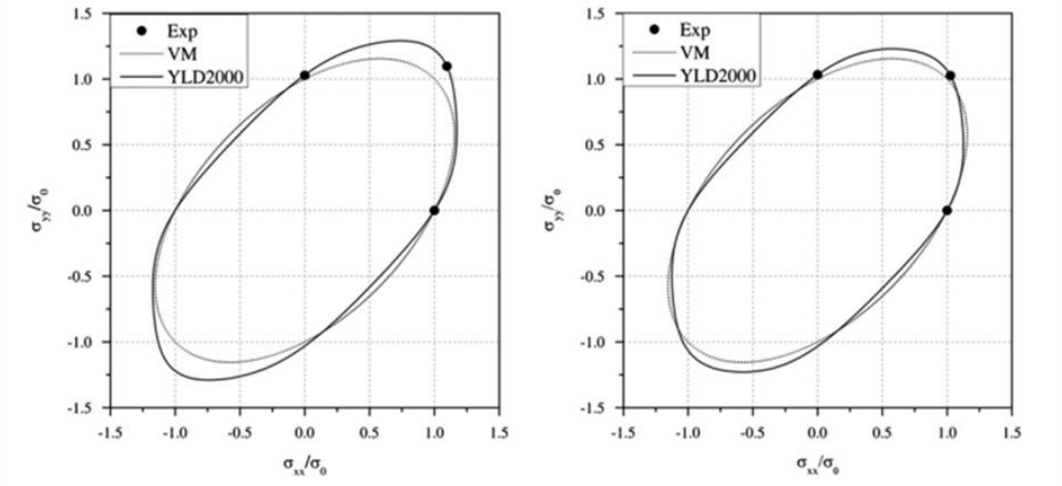

Figure 12: Comparison between experimental data points and predictions by von Mises and YLD2000-2d for ferritic stainless steel of different sheet thicknesses [50]

To demonstrate its advantage over the previously suggested yield surfaces, Barlat and coworkers [4] compared the yield surface of an aluminum alloy with 2.5 wt.% magnesium when setting the uniaxial yield stress in all directions and the balanced biaxial stress to unity. While YLD89 and YLD91 yielded an isotropic material behavior, YLD2000-2d accounted for the anisotropic R-values and was in very good agreement with experiments and polycrystal approaches.

Yoon *et al.* [55] implemented the YLD2000-2d constitutive model into a FE solver and performed deep drawn cup simulations for Al-5 wt.%. Experimental results for yield surface calibration were obtained from uniaxial tensile tests in the RD, the DD (diagonal direction), and the TD as well as bulge tests. Compared to previous Barlat yield surfaces, predictions using the YLD2000-2d locus matched the

experimental earing profile best whilst requiring reasonable CPU times (10%-increase compared to YLD91 e.g.). However, this constitutive model with adoption of an associated flow rule is limited to the simulation of four ears [56].

In 2005, Barlat and coworkers [39], [56] proposed a yield function for general tri-axial stress state, YLD2004-18p, of the form:

$$\begin{aligned} \phi_{YLD2004-18p} &= \phi\left(\tilde{S}', \tilde{S}''\right) \\ &= \left|\widetilde{S_1}' - \widetilde{S_1}''\right|^a + \left|\widetilde{S_1}' - \widetilde{S_2}''\right|^a + \left|\widetilde{S_1}' - \widetilde{S_3}''\right|^a \\ &+ \left|\widetilde{S_2}' - \widetilde{S_1}''\right|^a + \left|\widetilde{S_2}' - \widetilde{S_2}''\right|^a + \left|\widetilde{S_2}' - \widetilde{S_3}''\right|^a \\ &+ \left|\widetilde{S_3}' - \widetilde{S_1}''\right|^a + \left|\widetilde{S_3}' - \widetilde{S_2}''\right|^a + \left|\widetilde{S_3}' - \widetilde{S_3}''\right|^a = 4{\sigma_{eff}}^a \end{aligned} \tag{20}$$

that requires 18 anisotropy coefficients α_i for characterizing the material response. Setting all coefficients equal to unity leads back to Hosford's isotropic yield function defined in Equation 13. Further, if the exponent *a*, is set to two or four, the von Mises yield function results. When the two transformation matrices are coincident, hence only one linear transformation is performed, the yield function reduces to YLD91 given that six independent coefficients are imposed. For a reduction to plane stress, only 14 coefficients are required.

For calibration, uniaxial tensile tests in 15° increments relative to the rolling direction provide yield stresses and R-values in seven in-plane directions, as well as the yield stress and the R-value from balanced biaxial testing. The four remaining out-of-plane values are either computed from polycrystal models, assuming the crystallographic texture is known, or set to their isotropic values [39].

Yoon and coworkers [56] implemented YLd2004-18p in a umat subroutine and assessed its performance with circular cup drawing of AA2090-T3 and an imaginary highly anisotropic material. For the former material, the out-of-plane properties were computed from crystal plasticity equations. Volume solid elements were utilized to discretize the blank and an implicit time integration scheme was adopted. Whereas slight symmetric deviations were observed in the earing profile of the formed cups, that they explained through tooling alignment problems, very good agreement with simulation results was found and a total of six ears (AA2090-T3) and eight ears (fictitious material) could be predicted.

Park and Chung [57] implemented YLD2000-2d with a non-associative flow rule and a nonlinear isotropic-kinematic hardening model in ABAQUS/Explicit, that allowed them to assign a separate set of anisotropic coefficients for stress ratios and R-values. They performed circular cup draws and successfully modeled six and eight ears for AA2090-T3 and AA5042 respectively. It is worth mentioning that the simulation could only predict four ears when an associative flow rule with Hill48 or YLD2000-2d was utilized.

Summarizing from this overview of hardening models and yield functions, a lot of research has been conducted to improve strain and stress predictions by increasing the number of anisotropy coefficients to accurately capture the strain and stress directionality and by accounting for thermal softening and rate-effects in the description of the yield surface evolution. Considering all these efforts, friction has received only minor attention. As will be demonstrated in the model development in this thesis, even advanced anisotropic yield functions and non-associative flow rules can only predict accurate stresses and strains if other process conditions, such as friction, are described to the same level of accuracy. As will be addressed in the next section, friction plays a vital role in a forming process, particularly under thermal assistance and if long sliding distances are involved.

1.3 Tribology

This section is devoted to the influence of tribology on forming processes, including classification of lubrication regimes, tribological test methods, and lubricant performance, followed by a brief discussion of die coatings.

The importance of understanding and controlling tribological conditions in a forming process is demonstrated, for example, in roll forming, when friction allows the blank to be pulled into the die gap or in aluminum extrusion and closed-die forging where friction increases pressure and facilitates filling of die cavities [58]. Furthermore, the presence of friction prevents unconstrained grain deformation that could lead to orange peel effects [59] [60].

1.3.1 Parameters Affecting Friction

The complex nature of friction is captured in the following statement by Kalpakjian [61]:

"…every conceivable discipline has some effect on friction, wear and lubrication. […] from solid mechanics to organic chemistry, […] economics, occupational health hazards, ecology, and attendant legal considerations." [61]

Kim [62] structured these effects for advanced high-strength steels, that also applies to aluminum forming, into four main groups as illustrated in Figure 13. The tool material, surface finish and geometry (e.g. sharpness of radii and other tooling features) determines the hardness and therefore wear resistance but also influences the type of contact between the tool and sheet. In the same way, the mechanical properties and chemical composition of the sheet material are important since they determine its affinity to chemical reactions with the lubricant or the sliding partner. The sheet yield stress, hardness, and ability to strain harden are factors that determine the onset of plastic deformation and material behavior. Production conditions, such as load and forming speed, can also cause the tooling to heat up that has a direct influence on lubricant properties such as breakdown distance and viscosity. The latter exhibits an inverse relationship with heat, hence the viscosity and therefore its ability to maintain a lubricant film decreases at elevated temperature.

While the workpiece material, tool material, and production conditions are often fixed, the choice of lubricant and/or die coating offers considerable opportunity to improve lubricant performance, as well as significant risks. A lubricant that exhibits a high coefficient of friction (COF) or a short sliding distance to breakdown might be unable to separate the contacting surfaces from each other that results in scored surfaces or material transfer to the tooling. On the other hand, a particularly effective lubricant can reduce forming forces, improve surface quality, minimize springback, reduce interruptions to production for die maintenance (polishing and cleaning), or even decide between the part forming successfully or failing.

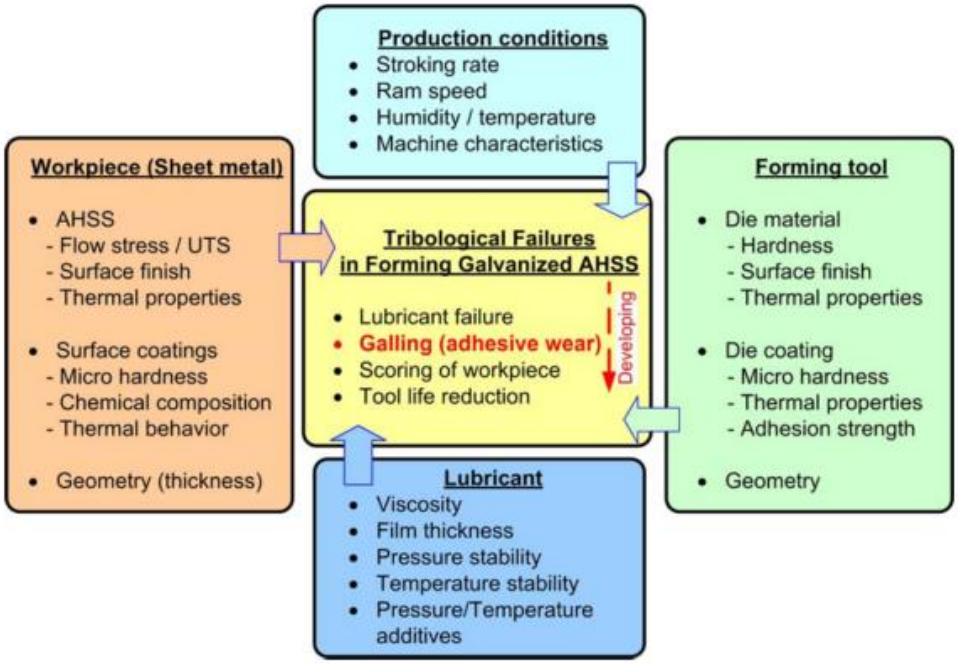

Figure 13: Overview on variables influencing friction [63]

1.3.2 Lubricant Regimes

Lubricants aim at forming a protective film layer that separates the two sliding surfaces from each other. In Figure 14, on a macroscale, the contact between the sliding partners, called the apparent contact area (A_{ap}), is perceived to be flat. However, upon a magnified view reveals that surface roughness is of key importance and that the contact is limited to selective regions, called asperities, that represent the true contact area (A_{tr}).

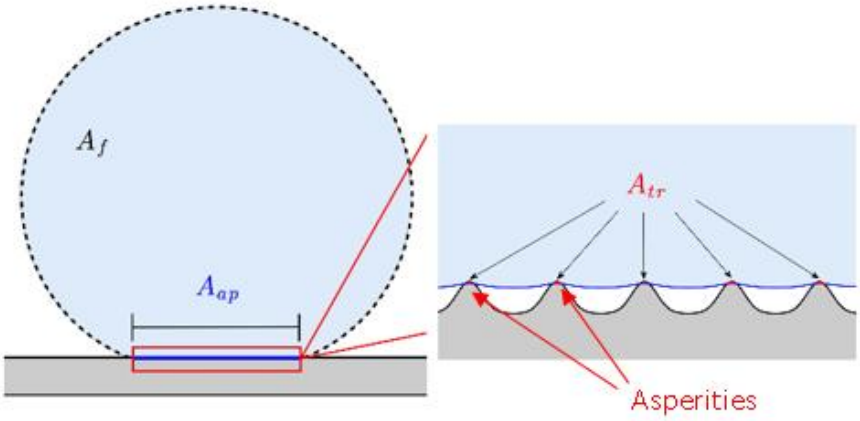

Figure 14: Apparent (A_{ap}) and true contact area (A_{tr}) of two sliding partners with free surface area (A_{fr}) [64]

The film thickness and lubricant consistency (liquid or solid) greatly influences the ratio of the load that is supported by asperities and the load that is carried by the pressurized lubricant in the asperity valleys. This idea allows a classification of the interface into different lubricant regimes that are illustrated in Figure 15. The Stribeck curve [62] is used to characterize how the transitions occur between the various lubricant regimes as a function of speed, viscosity, and pressure.

Relative motion under an unlubricated condition (Figure 15a) is characterized by high friction since localized adhesion between contacting asperities is not prevented [63]. Figure 15b represents boundary lubrication that exhibits thin adsorbed films on metal surfaces and asperity-dominated contact. The boundary film exhibits low shear stresses, prevents or delays the formation of junctions and bare metal to metal contact. As the process of adsorption is not instantaneous, the time between asperity contact plays an important role while lubricant properties such as viscosity are less important [62]. In the mixed regime in Figure 15c, lubricant between asperities offers partial load support. When asperity tips are deformed, lubricant in the valleys is entrapped and represents hydrostatic lubricant supply pockets that wet the contact during ongoing sliding. This behavior, described as “micro Plasto Hydrodynamic Lubrication”, was studied by Bech *et al.* [65] for aluminum with pyramidal-shaped lubricant pockets under deformation. Figure 15d illustrates full-film separation encountered in hydrodynamic lubrication. The complete load is supported by the lubricant and the resistance to sliding is defined by the lubricant shear stress that is a function of temperature, pressure, and strain rate [66]–[68].

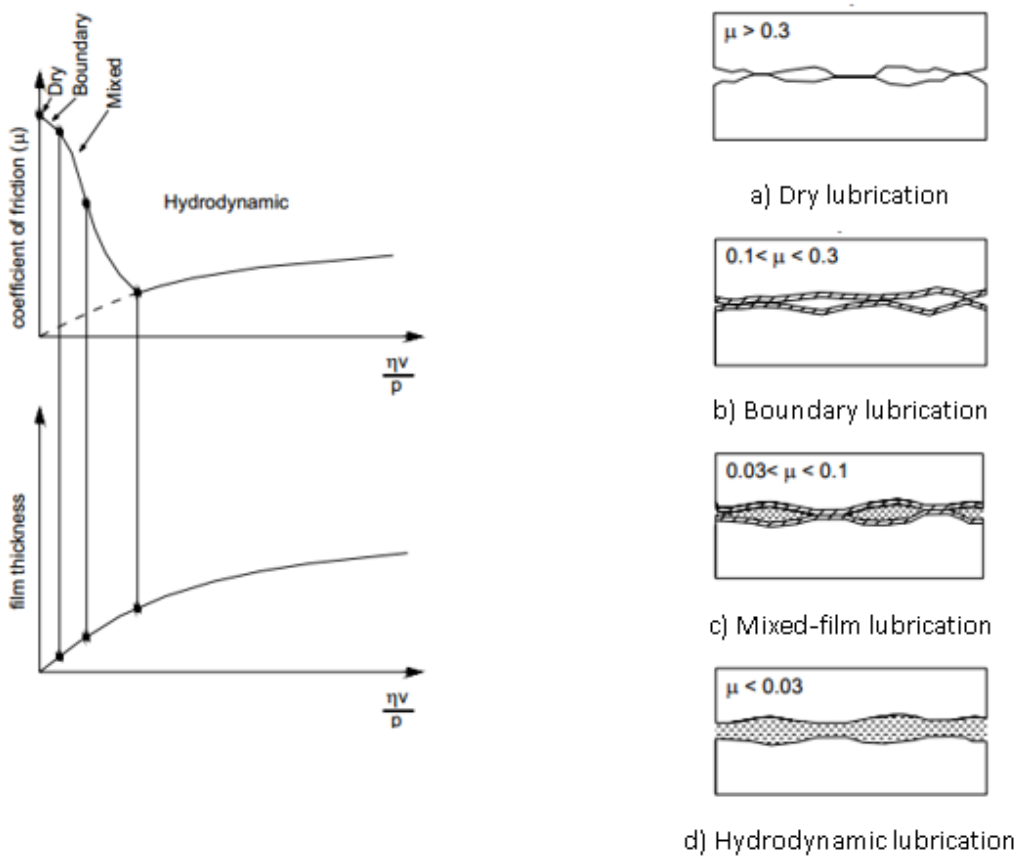

Figure 15: Stribeck curve (left) with different lubricant regimes (right) [63]

In a forming process, the discussed lubricant regimes rarely occur separately from each other that makes it difficult to decide on the major prevalent lubricant regime. DeMare and his colleagues [69] defined the boundary lubricant regime to be operative if 5%-10% contact is exceeded that is generally the case for metal stamping in that the true contact area is measured 25%-75% of the apparent contact area [70]. Darendeliler *et al.* [16] mainly confirm operation in the boundary lubricant regime for sheet metal forming operations such as deep drawing, that they obtained from numerical studies.

1.3.3 Friction Models

Experimental verification of friction laws dates back to Leonardo da Vinci (1452-1519) that were later confirmed by Amonton and Coulomb: the apparent contact area of the two sliding partners does not influence the friction force and, secondly, the friction force is proportional to the applied normal load. From these postulates, the complex nature of friction can be simplified to a non-dimensional number,

the well-known COF, that represents the ratio of the sliding force (F_{fric}) to the applied normal load (F_N) [67], [68].

$$COF = \frac{F_{fric}}{F_N} = \frac{\tau * A_{tr}}{F_N} \tag{21}$$

It is important to note that these laws only hold under the assumption that the true contact area increases when the load goes up. Bowden and Tabor [67], [68] demonstrated that for steel sliding on electronically polished aluminum, between loads from 0.037 g to 4,000 g, the COF was almost constant. Situations that can violate this condition include sliding in the presence of thin metallic or oxide films on the contacting surfaces, and for soft materials for that the friction is influenced by prior loading history.

Orowan [71] identified limitations of Coulomb's friction model since for high normal pressure, Equation 21 yields a friction shear stress (τ) that might exceed the material shear strength (k). To compensate for this deficiency, he suggested an extension of Coulomb's model for high pressures – known as the shear friction model – defined in Equation 22. It represents an upper limit of the friction shear stress with the material shear strength as maximum value.

$$\tau = m_{shear} * k \tag{22}$$

In this equation m_{shear} is the shear factor and can take values ranging from zero for no friction up to unity in the case of sticking friction (internal shearing without external sliding that is energetically more efficient once the material shear strength is reached) [62]. Wanheim and his colleagues [72] also confirmed the limitations of Coulomb's law at high normal pressures and suggested a general friction model that incorporates a correction factor for the ratio between real and apparent contact area. More advanced models account for lubricant interaction and include effects such as film thickness, viscosity, and sliding speed, but have limited application due to their complexity [73].

Standard Finite Element Method (FEM) solvers use Coulomb's friction model that assumes a constant COF over the blank geometry and during the whole forming process – an assumption that is criticized by a number of researchers. Wilson [59] emphasizes that the lubricant regimes can change during forming and vary in different areas due to the dynamic pressure conditions and contact times. Beynon [58] performed heat transfer measurements in a hot rolling facility and recorded enormous variations

from 18 kW/m^{2}K to 100 kW/m^{2}K, that directly influences frictional conditions. These observations explain the trend towards implementation of local- and time-dependent friction models in commercial FE solvers.

Hol *et al.* [74] implemented a multi-stage friction model in the boundary lubrication regime in a FE solver. The initial tool and workpiece surface topography is approximated through stochastic methods. The FE solver calculates parameters such as strain in the material, hardness of asperities and prevalent interface pressure that is used to calculate the flattening of the contact area due to normal loading and stretching. Asperity indentation and shear stress arising from ploughing and adhesion are obtained that finally lead to the COF. Even though realistic COFs are obtained in different zones, the conventional computational time for a deep drawing simulation undergoes a 200% increase when utilizing this friction model. A more accurate computation of the resulting shear stress is performed by Sigvant *et al.* [75] who simulated the Volvo XC90 door inner. They accounted for the load support from lubricant entrapped in pockets based on the lubricant film thickness. While some deviations were observed in selected areas, a remarkable aspect of the predictions in this study was the ability to capture details such as two minor wrinkles, as shown in Figure 16.

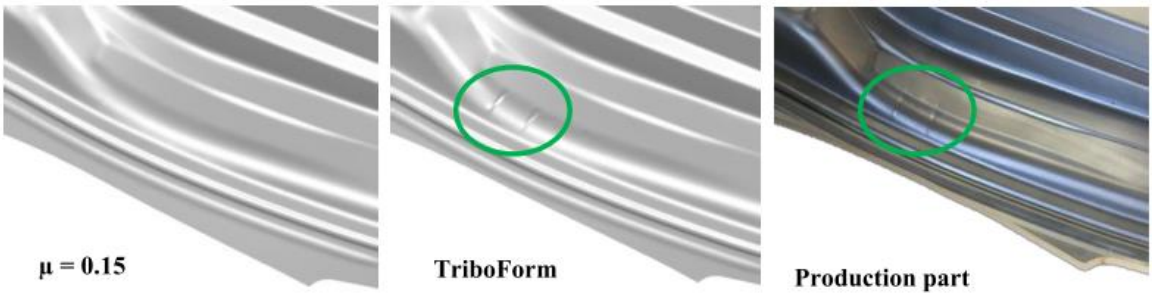

Figure 16: Results of different friction models of the Volvo XC90 door inner [75]

1.3.4 Lubricant Film Failure

Since the load is initially only supported by asperities, that represent a fraction of the apparent contact area, the carried load can easily exceed the material yield strength that plastically deforms the asperities. At the onset of sliding, depending on the presence and effectiveness of a lubricant, asperities of the contact partners interact with each other and the harder material deforms and plows through the softer material. The heat generated through plastic work causes temperature in the surrounding area to reach values equivalent to the metal melting temperature. If rupture of the

surface layer (e.g. oxide film) occurs, virgin material is exposed and interatomic forces cause adhesion such as welded junctions. Relative motion between the two contact surfaces requires force to shear off and break the bonding. Possible scenarios are transfer of these debris between contact surfaces (called pick-up), the formation of a protective lubricant film over the adhered particles resulting in low friction or, alternatively, the adhered particle becomes hard due to work hardening and oxidation and represents another asperity that causes scores on the neighbouring surface (called galling) [62], [67], [68].

Whilst lubricant film breakdown and its appearance on the part is evident, there is no straightforward approach to determine the exact time or sliding distance when the film lubricant breaks down. Skåre and Krantz [76] performed U-bend tests with installed Acoustic Emission (AE) sensors and found a proportional relationship between consumed energy due to frictional tool heating and AE signals. This set-up allowed ranking the performance of different lubricants unless phenomena such as stick-slip occurred. They emphasized caution since even though no wear is associated with this occurrence, high AE-effects are observed. In this case, careful examination of the punch force is required [76]. A more applied approach is the definition of a failure COF, that is determined from observations in laboratory tests or from experience [77], [78]. Comparison between severity of galling was performed based on qualitative visual inspection and classification into three different categories from no galling to most severe galling [77]. Dalton [70] presented a software that interrupts the test once failure is calculated based on the friction curve slope. Andreasen *et al.* [79] used the presence of a minimum of four scratches as a threshold to identify galling in their strip reduction test. Andreasen and his colleagues [80] utilized topographic methods to quantify galling and rated onset and severity of galling through presence and number of grooves.

1.3.5 Friction Tests

In view of the complexity of tribology and the numerous parameters involved, it is vital to select a friction test that replicates the forming process in terms of loading, material choice, and contact type [81]. While the production facility itself represents the most realistic testing equipment, the costs due to production stops, polishing after pick-up and cleaning when a new lubricant is introduced, combined with the risk of galling if lubricant amounts remain, is extremely expensive. This in turn highlights the need for friction tests that mimic the physical forming process [82], [83]. Figure 17 illustrates this point

and gives an overview of commonly used tests for sheet metal forming processes as a function of part location [83]. From this observation it is not surprising that different friction tests, associated with different contact mechanisms, yield diverse COF values that makes a quantitative comparison between them challenging [81], [84].

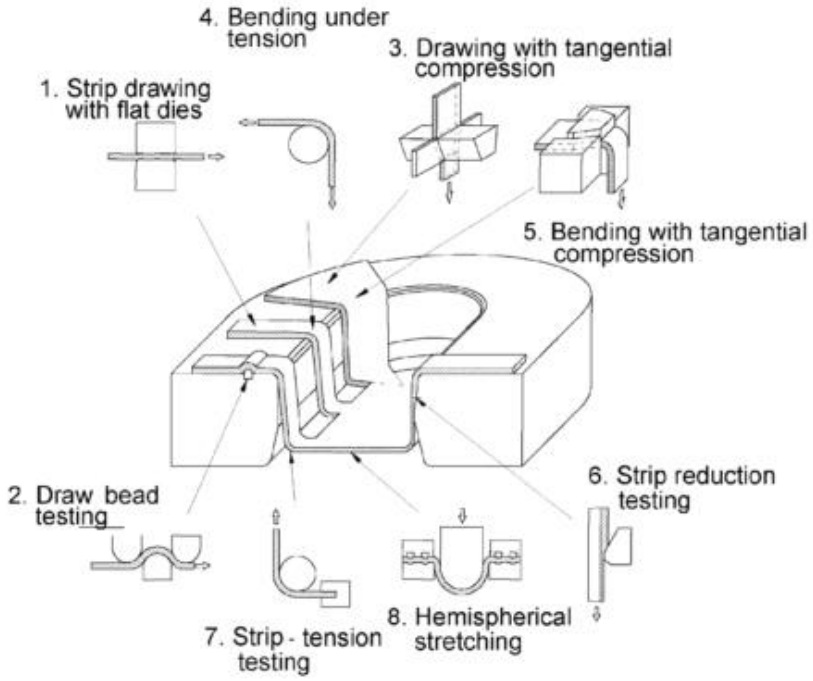

Figure 17: Overview of commonly used tribotests in sheet metal forming [83]. In the flange: flat die tester with (1) or without (3) tangential compression or draw-bead simulator (2). In the die radius: Bending under tension (4) or with tangential compression (5). In the sidewall: strip reduction test (6). In the punch nose: strip-tension test (7) or limiting dome height test (8)

Bay and his colleagues [83] suggested a classification of tribotests into two categories: (i) simulative or laboratory tests in that the testing conditions can be far from a forming operation and are intended to gather an improved understanding of tribological mechanisms; and, (ii) process tests, that are closely related to a physical forming process. Various test methods are discussed in the following.

1.3.5.1 Laboratory Friction Tests

Pin-on-disk test

Figure 18 illustrates the set-up of a pin-on-disk test: the sheet material (circular disk) is clamped to a support plate and a tool pin with a radius tip is positioned perpendicular to the sheet. After the pin is

pressed onto the disk, either the pin or the disk starts rotating. The normal load and friction forces are measured that allows calculation of the COF according to Coulomb's law [85]. The small contact area and therefore limited asperity interaction is seen as a drawback of this testing method [70].

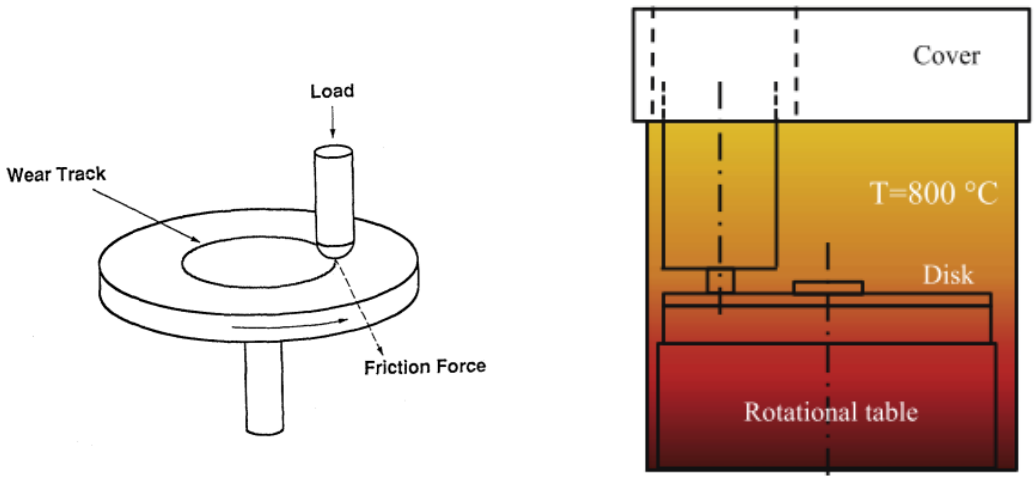

Figure 18: Experimental set-up of a pin-on-disk test [86] (left) and modified for testing at elevated temperature (right) [87]

Ghiotti *et al.* [87] present a modified pin-on-disk tester, in Figure 18 (right), equipped with a heating chamber that allows friction testing under hot stamping conditions of complete forming cycles (heating, testing, and cooling of the pin). Based on measured normal pressure and torque, in the case of manganese boron steel with an Al-Si layer and no lubricant, a mean COF of 0.51 was found after 400 forming cycles.

Flat die test

The flat die tester operates in the mixed or boundary lubricant regime and closely simulates the contact mechanism between binder and sheet [66]. The blank is clamped at a normal load (F_N) and pulled at a constant drawing speed through a set of flat dies. The required pulling force (F_{draw}) is recorded and allows calculation of the COF as per Equation 23 that contains the factor 0.5 since friction occurs on the upper and lower side of the die. A schematic outline of a flat die tester that also facilitates elevated temperature testing is illustrated in Figure 19. To prevent scatter and vibration in the data due to elastic deformation of the test equipment, a rigid construction of the apparatus is vital [34].

$$COF_{Flat\ die} = \frac{1}{2}\frac{F_{draw}}{F_N} \tag{23}$$

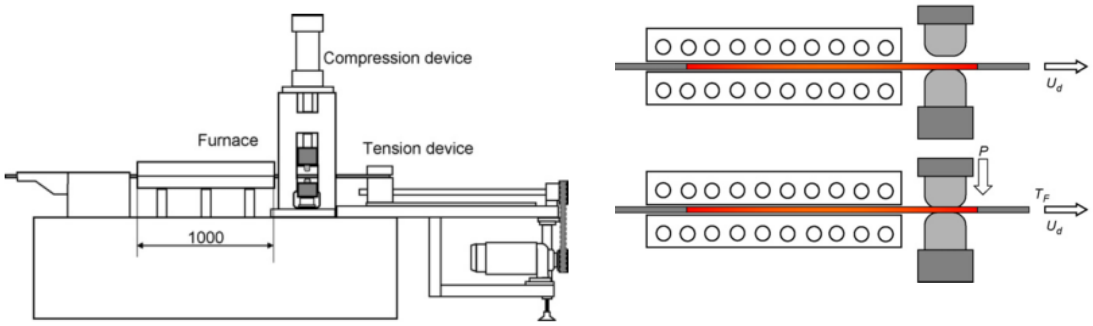

Figure 19: Modified flat die tester for friction testing at elevated temperature [88]

Szakaly and Lenard [34] found, with the flat die tester, a decrease in the COF at higher speeds for that they make reduced contact time for junction formation responsible. Compared to bare steel, hot-dip galvanized steel mostly exhibited a higher COF to that they attributed to earlier onset of micro Plasto Hydrodynamic Lubrication. Scanning electron microscope (SEM) revealed that due to increased number of channels and valleys for lubricant entrapment, tool steel is a superior die material to cast iron.

Yanagida and his colleagues [88], [89] modified the conventional flat die tester to obtain friction coefficients for hot stamping in FEM (Figure 19). The blank is heated in a furnace and pulled through the compression zone once the target temperature is reached. In a study on two water-based forging lubricants that were sprayed on preheated dies at 200°C, the mean COF was reduced by a maximum of 48% for manganese boron steel and by 65% for hot rolled steel. The less effective performance with manganese boron steel was explained by the presence of an aluminum base coating.

Twist Compression Testing

The Twist Compression Test (TCT) was developed at the University of Waterloo around 1960 by Schey [62]. This experiment is illustrated in Figure 20: an annular test cup is pressed onto a clamped sheet specimen and starts rotating at a constant sliding speed. The resistance to sliding, measured as a reaction torque (T), is utilized to calculate the COF based on the cup contact area (A_{ap}) , the medium cup radius (r_m), and the applied interface pressure (P) as per Equation 24.

$$COF_{TCT} = \frac{T}{r_m \, P \, A_{ap}} \tag{24}$$

The TCT offers good control over the interface pressure and eliminates any influence from sheet orientation (e.g. anisotropy) [90]. It is relatively quick to perform and serves to rate lubricant performance under lubricant depleting conditions. Operation in the boundary regime requires flat-to-flat contact between the cup and the sheet, that prevents fresh lubricant from entering the contact zone and ensures lubricant starvation. Additionally, there are no limitations on testing distances since the cup can slide (rotate) continuously over the same tested specimen surface. On the downside, the TCT is often criticized for its absence of plastic deformation that represents a strong deviation from a real forming process [81].

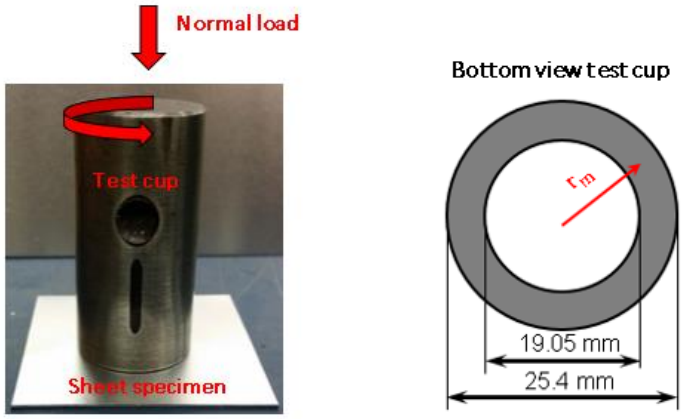

a) Methodology b) Geometric dimensions

Figure 20: Twist Compression Test

Kim *et al.* [91] performed TCT and utilized qualitative ranking of powdering and galling, surface roughness, optical and atomic force microscopy, and time to reach an absolute COF of 0.3 to successfully rank coated and uncoated advanced high strength steels under lubricated conditions. They concluded that a predicted increase in temperature to 75°C, obtained from an experimentally-validated FE model, is not severe enough to decrease lubricant effectiveness. A sharp pressure increase (by about 135%) on the cup outer edge might provoke faster film reduction and therefore earlier onset of galling.

Bending under tension and draw-bead simulator

Bending tests emulate mild friction conditions with the presence of forming strains. The draw-bead simulator (DBS), see Figure 21, was developed by Nine [92] and represents a superposition of friction and bending forces that requires two sequential tests to be performed. Initially, the fixed draw-bead and groove shoulders are replaced with rollers and the material strip is pulled through it to measure the force (F_{roller}) for bending and unbending in the absence of friction. In the next step, the test is repeated with fresh material (from the same batch) and fixed draw-bead/groove shoulders that measure the pull force (F_{fixed}) and the force in the draw-bead (F_{bead}). Based on Coulomb's law and under the assumption of constant pressure around the draw-bead, the COF can be calculated using Equation 25. Drawbacks of these bending tests are the absence of surface expansion, measurement error, and stochastic variation resulting from two separate tests for one condition, particularly if a good lubricant is used and the magnitude of the deformation and friction force is comparable [83].

$$COF_{DBS} = \frac{1}{\pi} * \left(\frac{F_{fixed} - F_{roller}}{F_{bead}}\right) \tag{25}$$

Schey and Dalton [93] concluded from the flat die tester that directionality in tool surface has the most powerful impact on the COF and acknowledged that generalizing the friction behavior for a class of steel or a certain lubricant is challenging since even standardized coatings from the same supplier but different batches can greatly alter test results.

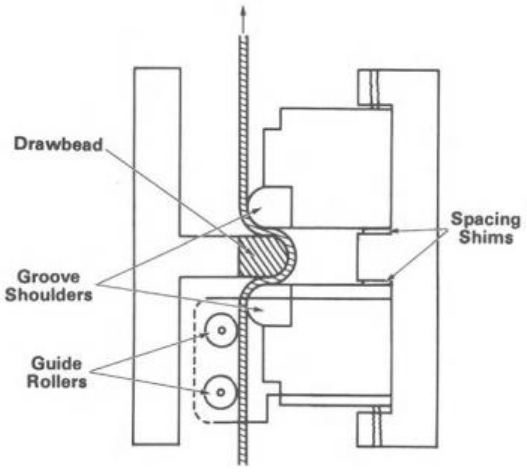

Figure 21: Experimental set-up of a draw-bead simulator [68]

Xu [90] acknowledged that friction is a function of the sliding system and that different gauges and materials within one test method can only be compared if the same pressure distribution is prevalent. The DBS recorded lower COFs for thicker samples (change in contact pressure) and the TCT also showed a strong pressure-dependency for that he made the lubricant responsible. At low contact pressure, present in the DBS, the lubricant does not contribute to load support and asperity interaction occurs that leads to a constant COF. With increasing load, however, the pressurized lubricant delays the growth of the true contact area that causes Coulomb's law to collapse – the COF decreases.

Noting the drawbacks regarding comparison of two separate tests (requiring the same lubrication regime), Bay et al. [83] modified a conventional bending under tension and DBS to measure front and back tension in combination with the torque load during one test.

Stretch forming test

In the stretch forming test, such as the limiting dome height test (LDH) illustrated in Figure 22, a hemispherical punch deforms a blank that is clamped between the die and a hold down ring or binder. In some cases, draw beads are used to hold the sheet in place and to prevent material draw-in towards the punch. The test stops when the sheet fractures.

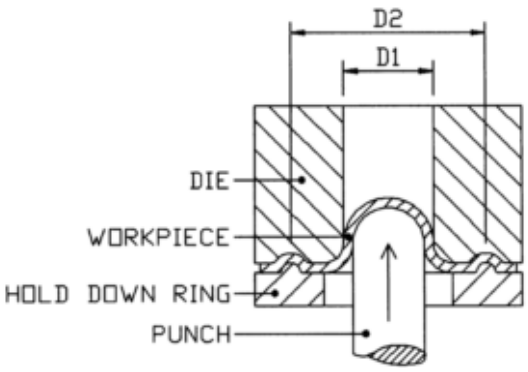

Figure 22: Experimental set-up of a stretch forming test [94]

Rao and Wei [94] found from stretch forming tests and deep draws on AA1100, AA5052, and AA6061 that boric acid is comparable to the lubricity features of commercially available lubricants but has advantages in terms of price, solubility in water, and non-toxic nature. They also observed enhanced repeatability in punch force for the better performing lubricants.

1.3.5.2 Process Tests

When plastic deformation occurs, the thin adherent oxide layer of aluminum may fracture that results in direct contact between the two metal surfaces and yields a significant increase in both friction and heat transfer coefficient [58]. This observation justifies the importance of friction tests that incorporate an appreciable level of plastic deformation.

Deep drawing

A schematic outline of a deep drawing operation is illustrated in Figure 23. A circular blank is clamped between a die and a binder and stretched by a flat punch. Contrary to a pure-stretch forming test (as in Figure 22), the periphery of the blank is not fully constrained and the applied binder load acts to control the material flow and suppress wrinkling during drawing. From a tribological perspective, the flange area represents the most severe condition since it affects thickness reduction in the sidewall that may lead to material failure [84]. The severity of the tribological condition can be controlled through the die entry radius, blank diameter, forming speed, binder load, and temperature [80].

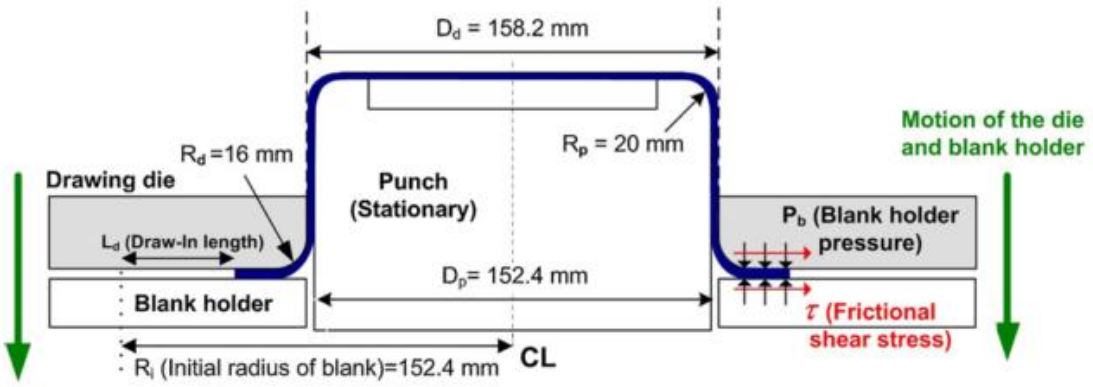

Figure 23: Schematic set-up of deep drawing [81]

Kim *et al.* [81] demonstrated that deep drawing is a sensitive friction test if process parameters such as binder load and drawing ratio are selected to provoke fracture for cups formed with less effective lubricants and successful forming for best lubricants. The lubricant ranking in terms of forming forces was confirmed by the size of the flange perimeter (maximum deviation of about 11 mm between best and least effective lubricant) and the draw-in length (minor changes) for a 80 mm cup depth. The draw-in length corresponds to the difference between the initial to the as-formed flange diameter. For

clarification, please refer to Figure 24. FE simulation was used for inverse modeling: a constant COF was adjusted to make the predicted punch force match the measured value.

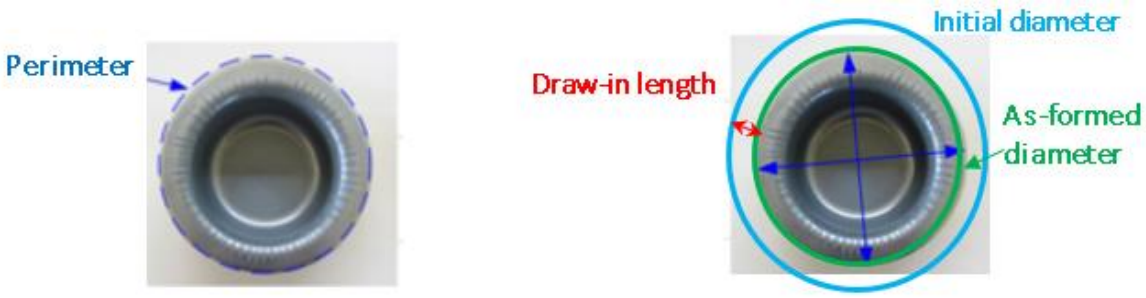

Figure 24: Perimeter (left) and draw-in length (right) of cups drawn to a target depth of 80 mm [81]

With the intention of facilitating friction testing for hot stamping, Geiger *et al.* [95] presented a modified cup deep draw tool set that incorporates cartridge heaters. The blank is heated in a furnace to its austenitization temperature, manually transferred to the press, and drawn. The COF is determined in an analytical-experimental-numerical approach.

1.3.6 Die coatings

Lubricants can often reduce or prevent die pick-up to an extent; however, die coatings and alternative tooling materials can offer further benefit. Tool materials that are not prone to material sticking such as ceramic tools, tool surface treatments such as die coatings or intentional surface texturing of the tool or sheet represent attractive options [96] for reducing die pick-up.

One aspect of this thesis focuses on die coatings that represent a thin layer on the original surface applied through Physical Vapor Deposition (PVD) or Chemical Vapor Deposition (CVD). Table 4 gives an overview on commonly used PVD and CVD coatings.

Table 4: Common die coatings deposited through PVD or CVD methods [97]

Coating	PVD or CVD	Typical Coating Thickness, µm	Hardness, HV	Adhesion[1]
TiN	PVD	1 – 5	2,300 – 2,900	70
TiCN	PVD	1 – 5	3,000 – 3,500	62
Diamond-like carbon (DLC)	PVD	1 – 10	1,000 – 5,000	Unknown
MoST®[2]	PVD	2 – 5	1,500 – 2,100	>120
TiC	CVD	7 – 10	3,000 – 3,200	Unknown
TiC/TiN	CVD	7 – 10	2,600 – 2,800	110

[1] Critical normal force (newtons) required to remove coating from substrate in scratch test
[2] MoS_2/Ti composite coating developed by Teer Coatings and licensed to IonBond

At higher forming pressures these coatings are not sufficiently durable if deposited as a single layer. Hence, surface treatment of the tool surface or interlayers prior to coating deposition is required. Minimum requirements of 1000 HV surface hardness can be met by nitriding that is performed at low temperatures (500°C to 570°C) and results in a compound layer of iron and a nitrogen diffusion zone. The presence or the thickness of this compound layer depends on the nitriding process parameters. However, it has been reported that the presence of such a layer can influence the tribological conditions due to its brittle and porous character [98].

Lee and his colleagues [99] found that for deep draws of pure aluminum with uncoated and PVD TiN-coated tooling, a combination of uncoated punch and coated dies yielded the highest LDR (increase by 4.6% compared to uncoated dies) and considerably reduced punch force (by 13.4% at the LDR). The use of an uncoated punch (with coated die) was beneficial since stretching in the critical punch nose zone was reduced.

Podgornik and Hogmark [100] highlighted the importance of pre-treatments on the die coating performance. They found that compared to hardened tool steel, plasma nitriding sustained higher loads before onset of galling but only if the surface roughness is not altered during nitriding or reground to its initial absolute value. The PVD coating TiN recorded a comparable threshold length to uncoated hardened steel. The "[..] WC doped hydrogenated diamond like carbon with a multilayer structure of WC and C […]" showed a significant decrease in recorded COF (0.19 compared to 0.6 (TiN) and 0.74 (uncoated)) over the whole load range. This coating could sustain loads by about a factor six higher than the uncoated or TiN coated tooling before galling was initiated.

Several researchers have reported on the excellent performance of diamond-like carbon (DLC) coatings [101]–[103]. Horiuchi *et al.* [104] recorded an average COF of 0.03 for the best DLC coating,

0.34 for the oil-based lubricant GM100 lubricant, and 0.73 under unlubricated condition with AA5052 at 200°C. In deep drawing, dry-formed cups (using only the DLC coating) recorded considerably lower punch forces, as recorded in Figure 25, and less thinning.

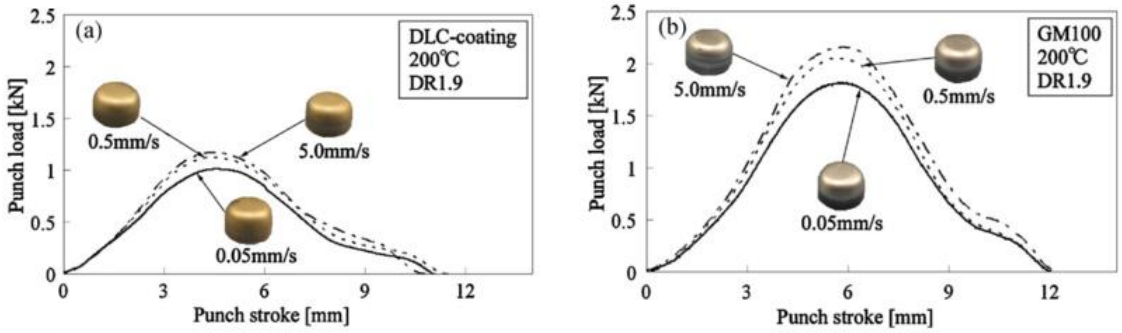

a) With DLC coating

b) Uncoated with GM100 lubricant

Figure 25: Punch force in deep drawing [104]

In a performance comparison of DLC to PVD coatings in deep drawing of AA5000-series aluminum alloys, Murakawa *et al.* [105] observed adhesion of aluminum on the die after dry deep drawing of one cup for the uncoated die steel, the TiCN, and the CrN coatings, that resulted in material rupture after the first few runs whereas the DLC coating allowed forming up to 1560 parts before fracture. The coating adhesion was improved by replacing the die steel with substrate material of WC-Co alloy that allowed forming up to 6190 parts when the coating came off locally.

Friction, particularly determination of lubricant breakdown, is still a controversial topic that is influenced by many other factors such as temperature, material choice, interface pressure, sliding speed, lubricant choice, surface finish, contact mechanism, and lubricant regime. Hence, a large number of experimental and numerical characterization methods exist that all aim at mimicing the target forming process at coupon level. The drawback of utilizing numerical models to determine the prevalent COF in a tribotest is the dependency on model input parameters. Deficiencies in the description of the material model or simplified boundary conditions directly influence the friction coefficient that is then utilized as a scaling parameter to balance other shortcomings. While the implementation of multi-stage friction models in commercial FEM solvers exists, the incurred increase in computation time limits the use in industrial applications. Hence, the work presented in this thesis

utilizes an experimentally-driven approach to separately characterize warm friction from the material anisotropy.

1.4 Summary of Previous Work and Scope of Current Work

As demonstrated in the literature review, remarkable research has been conducted for 7xxx series aluminum alloys with the main focus on AA7075 in light of its application in aerospace industry. While most efforts are focused on die quenching to control deficiencies like excessive springback and strength loss due to over-aging, selected attempts to study warm forming are either limited to coupon-level testing or are restricted to one specific topic and do not consider related issues such as the effect of peak strength on corrosion resistance. While the importance of friction characterization has received more attention over the years, most friction studies are either at room temperature or for steel; elevated temperature testing focuses on hot stamping that operates in a temperature regime far above conventional warm forming temperatures. Hence, there remains a need to study the warm forming process of high-strength aluminum alloys by looking at the larger picture to account for correlating effects.

The research presented in this thesis is part of a larger project undertaken by the University of Waterloo in collaboration with several automotive and materials companies, including Honda R&D Americas Inc., Arconic Ground Transportation Group, and Promatek Research Centre. The overall goal of this larger research project is to develop elevated temperature forming processes suitable for fabrication of automotive sheet components using high-strength aluminum alloy sheet with optimized final properties in terms of corrosion resistance, formability, mechanical strength, and crash performance. The work presented in this thesis addresses the warm forming behaviour of several medium (AA6013 T6) and high strength (AA7075 T6 and AA70XX T76) aluminum alloys; here, AA70XX refers to a developmental 7000 series alloy. Of particular interest is the development and validation of models of the deep draw behaviour of these alloys at temperatures up to 233°C. As part of this effort, a detailed investigation of their elevated temperature frictional behaviour was undertaken, considering several lubricants and one die coating on the as-formed surface quality. The material flow behavior is described through a temperature- and rate-dependent hardening model that was derived from the Hockett-Sherby model. A key aspect of the work, is application of the gathered knowledge from coupon testing to a near-commercial structural rail that was utilized to study the post-forming

strength/hardness of these alloys, as well as their surface condition (presence of scoring or galling) and amount of thinning.

The objectives of this Master thesis are threefold:

(i) Characterize the thermo-viscous material hardening behavior and friction response for different lubricants and a die coating
(ii) Evaluate these efforts through an experimental-numerical warm cup draw study
(iii) Define the process window for studied alloys on a near-commercial structural rail in terms of final part strength, thinning, and surface quality

The balance of this thesis is organized as illustrated in Figure 26. The second chapter deals with material characterization and summarizes experimental efforts by DiCecco [2] and Rahmaan [3] that were utilized by Abedini [18] for calibrating the yield surface and the thermo-viscous hardening model as part of this work. Elevated temperature friction for different lubricants and one die coating was characterized in the TCT and is discussed in Chapter 3. These efforts were evaluated in an experimental-numerical deep draw study; the experimental set-up for deep drawing is covered in Chapter 4 whereas Chapter 5 is devoted to the model development. Chapter 6 represents the knowledge transfer from coupon-level testing to a near-commercial structural rail. Micro hardness measurements, thinning, and surface quality were utilized to define the process window. The thesis closes with conclusions and recommendations for future work in Chapter 7.

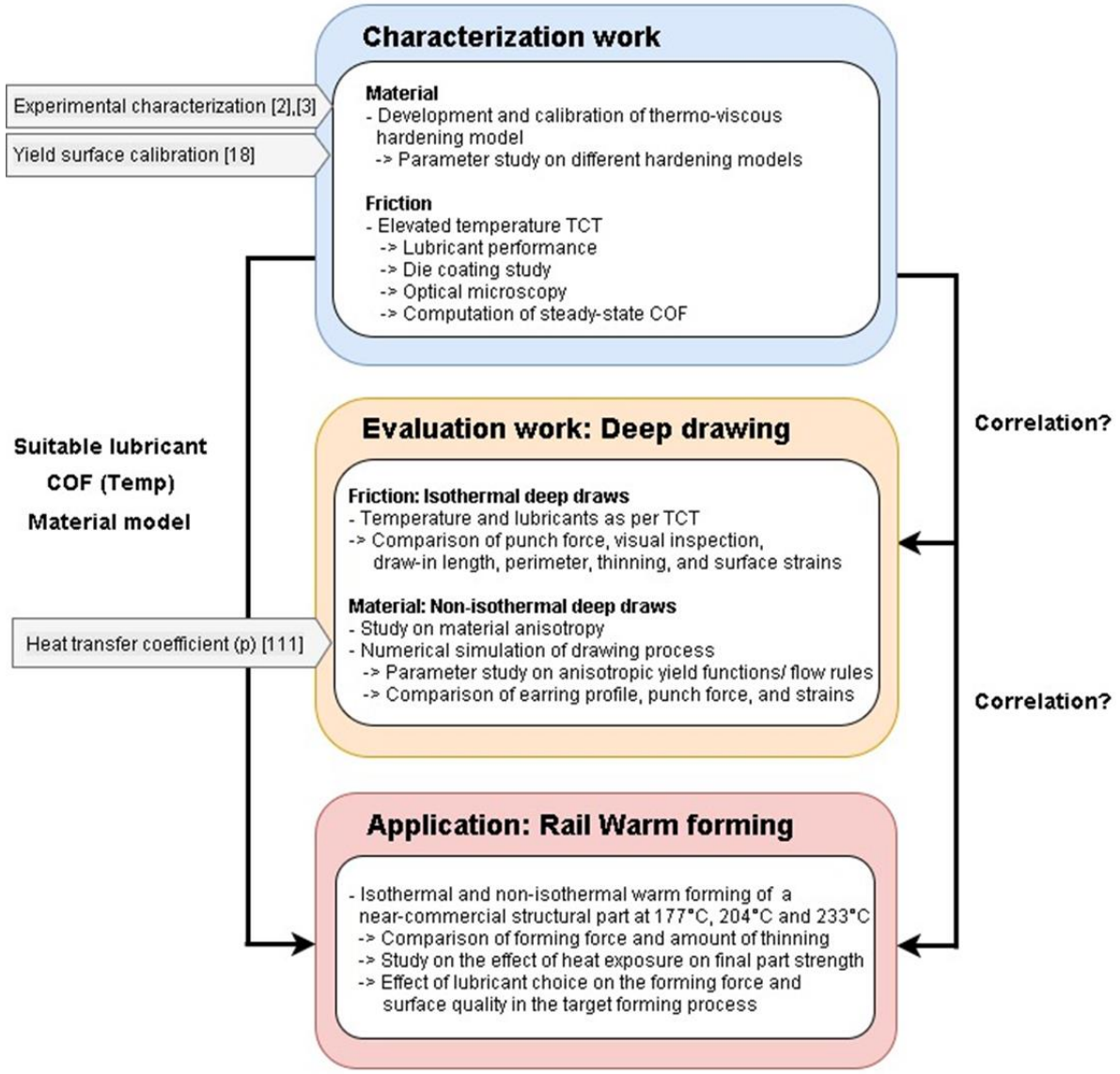

Figure 26: Overview of thesis structure

2 Material Characterization

This chapter presents the mechanical properties of the studied aluminum alloys and an anisotropic constitutive model. The actual experimental material characterization was performed in separate studies by DiCecco [2] and Rahmaan [3] and the yield surface calibration was performed by Abedini [18]. The primary contribution in terms of material characterization stemming from the current thesis research is the development of a temperature- and rate-sensitive hardening model.

2.1 Studied Materials

In this research, three high-strength aluminum alloys were investigated. AA6013 T6 was selected as a medium strength (380 MPa [3]) baseline alloy to which the performance of two higher strength alloys, AA7075 T6 (565 MPa [3]) and a developmental alloy, AA70XX T76 (520 MPa [3]), were compared. Most of the testing was done for all three alloys whereas on some occasions, the emphasis was placed on the more novel AA70XX-T76 alloy. It is also worth noting that the as-received temper for AA70XX was over-aged, aiming at improved corrosion resistance, whereas the AA6013 and AA7075 were supplied in peak-aged condition. The as-received material consisted of 2mm-thick rolled sheets.

The nominal chemical composition of theses alloys is recorded in Table 5. Compared to AA6013, AA7075 and AA70XX have a higher content of both zinc and magnesium that is responsible for their increased strength. The higher chromium content for AA7075 (0.18%-0.28%) compared to 0.04% for AA70XX offers better control over grain growth during hot rolling or heat treatments but on the other hand, makes the AA7075 more quench-sensitive and narrows the process window in die quenching [106].

Table 5: Nominal chemical composition in weight percent of studied aluminum alloys [107]

	Alloy		
Alloying element	AA6013	AA7075	AA70XX
Silicon (Si)	0.6%-1.0%	0.4%	0.06%
Iron (Fe)	0.5%	0.5%	0.08%
Copper (Cu)	0.6%-1.1%	1.2%-2.0%	1.3%-2%
Manganese (Mn)	0.2%-0.8%	0.3%	0.04%
Magnesium (Mg)	0.8%-1.2%	2.1%-2.9%	1.2%-1.8%
Chromium (Cr)	0.1%	0.18%-0.28%	0.04%
Zinc (Zn)	0.25%	5.1%-6.1%	7.0%-8.0%
Titatnium (Ti)	0.1%	0.2%	0.06%
Zirconium (Zr)	negligible	negligible	0.08%-0.15%

2.2 Experimental Material Characterization for AA70XX T76

The experimental work described in this section was performed by DiCecco [2] and Rahmaan [3]. Consequently, only a brief summary of experimental set-up, utilized methodology, and obtained results for AA70XX T76, a 7xxx series aluminum alloy under development, is presented.

2.2.1 Tensile and Shear Testing

The tensile tests were performed to obtain: (i) R-values and stress ratios from tests at different angles relative to the RD; and (ii) true stress-strain for calibration of the constitutive behavior.

For calibration of advanced yield functions and non-associative flow rules, tensile data in 15° increments relative to the RD was required. Rahmaan [3] obtained these mechanical properties from room temperature quasi-static tensile tests using the so-called mini-dogbone tensile geometry presented in Figure 27a. For characterization of the hardening behavior, DiCecco [2] performed quasi-static tensile tests at elevated temperature (150°C, 190°C, and 240°C) using the ASTM E8 geometry in Figure 27b. For the strain-rate sensitivity study, DiCecco [2] performed tensile tests at 200°C at two additional strain rates, 0.001 s^{-1} and 0.1 s^{-1}.

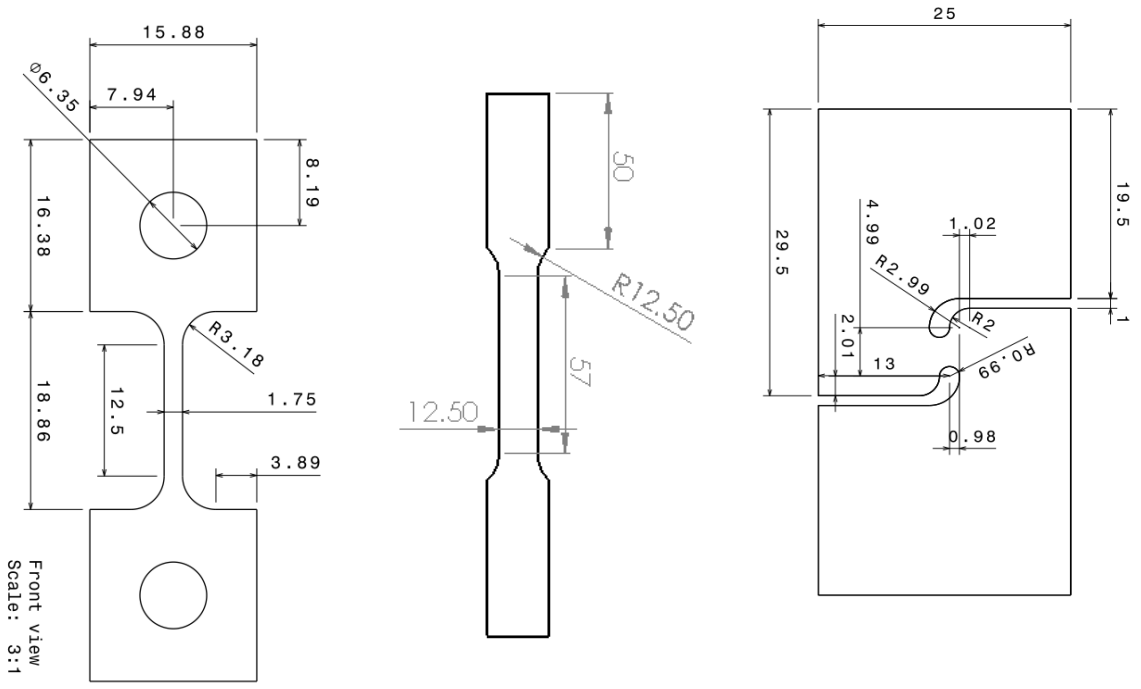

a) Mini-dogbone specimen [2] b) ASTM E8 specimen [103] c) Mini shear specimens [2]

Figure 27: Utilized sample geometry, of 2 mm thickness, for material characterization experiments

Tensile tests have the disadvantage of early onset of localization that transforms the prior uniaxial stress state into a tri-axial state. Strain values from tensile tests (up to localization) usually provide strain values on the order of 5%-10% [108] that gives limited confidence for calibration of the hardening model and extrapolation to higher strains. In view of the absence of localization, shear tests were performed by Rahmaan [108] and provide larger strain levels.

For the shear tests, Rahmaan [3] also utilized miniature shear specimens, illustrated in Figure 27c, developed by Peirs *et al.* [108], that can be tested in a conventional tensile apparatus. Abedini *et al.* [108] demonstrated its effective use for constitutive plastic and fracture characterization on ZEK100. The advantage of a shear test is that a through-thickness localization does not occur and plane stress conditions prevail even at large strain levels.

2.2.2 Apparatus for Tensile and Shear Testing

Both tensile and shear experiments at all strain rates were performed on the MTS criterion Model 45 testing frame illustrated in Figure 28. For elevated temperature testing, a heating chamber was placed

around the grip system that held the tensile specimen and ensured constant temperatures during testing.

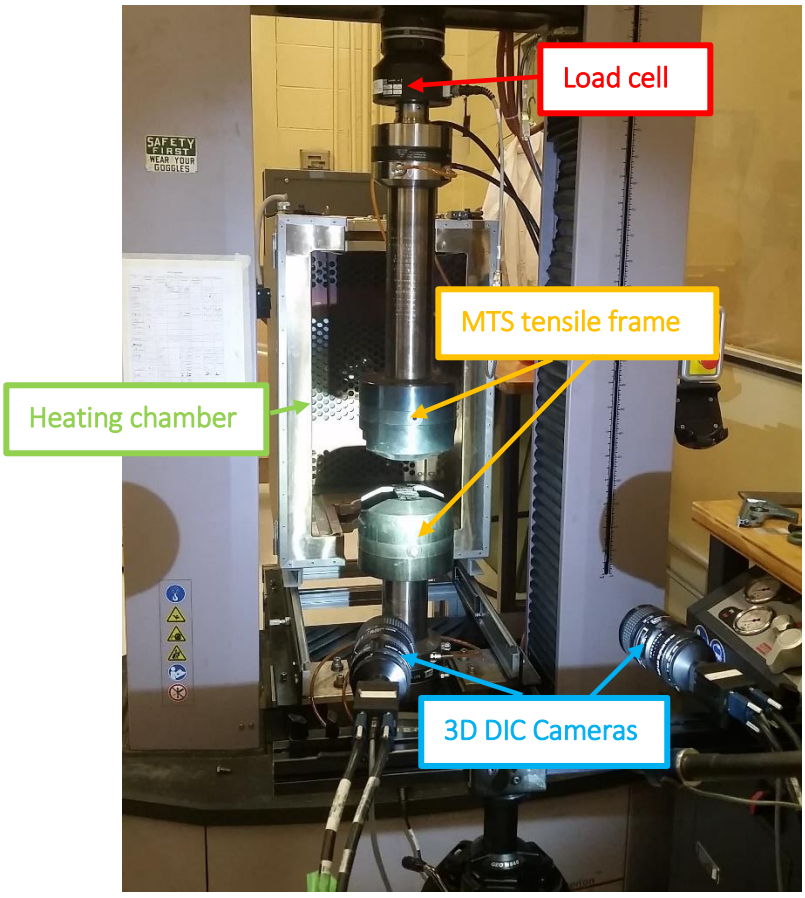

Figure 28: Test set-up for tensile and shear testing

2.2.3 Through-Thickness Compression Experiments

For calibration of the yield function, aside from tensile data, equi-biaxial R-values and stress ratios were required. Rahmaan [3] performed through-thickness compression tests (TTCT) using an Instron model 1331 servo-hydraulic test equipment. Specimen preparation was performed as per the method outlined by Steglich *et al.* [109] who verified that this test method can yield equivalent results to the popular bulge test.

2.2.4 Methodology and Results

Full-field strain measurements in both the tensile and shear tests were captured through the Digital Image Correlation (DIC) technique. This optical method computes deformation through tracking of

surface points in two consecutive images. A detailed description of the DIC methodology is given by Sutton *et al.* [109].

Tensile experiments

For conversion of the experimentally obtained engineering stress-strain data into true stress (σ_{true}) and true strain (ε_{true}), Equations 26-27 [110] are employed in the conventional approach. These equations, however, are only valid until the onset of localization.

$$\sigma_{true} = \sigma_{eng}\left(1 + \varepsilon_{eng}\right) \tag{26}$$

$$\varepsilon_{true} = ln\left(1 + \varepsilon_{eng}\right) \tag{27}$$

In the elevated temperature data, DiCecco [2] observed diffuse necking shortly after the onset of yielding and the aforementioned equations were not applicable. Hence, DiCecco [2] employed the area reduction technique outlined by Omer *et al.* [110]. The instantaneous area is computed from the stereoscopic DIC data by dividing the minimum cross-section into increments from which the current cross-sectional area is approximated using a trapezoidal rule. This method assumes that the material is necking in a symmetric fashion as only one surface of the specimen is measured using the DIC. By approximating the instantaneous area of the minimum cross-section, the true stress can be estimated to larger strain levels although the local strain rate will increase and triaxial loading conditions will develop during strain localization.

For input into the numerical model, the true strain was further converted to plastic strain by subtracting the elastic strain portion in Equation 28 [110], where *E* is denoted as the Young's Modulus recorded in Table 6, calculated as an average of at least three repeats.

$$\varepsilon_{pl} = \varepsilon_{true} - \left(\frac{\sigma_{true}}{E}\right) \tag{28}$$

Table 6: Temperature-dependent Young's Modulus obtained from quasi-static tensile experiments by DiCecco [102]

	Temperature (°C)			
	25	150	190	240
Young's Modulus (GPa)	68	64	59	49

Figure 29 illustrates flow stress versus effective plastic strain at temperatures between 25°C and 240°C with a reference strain rate of 0.01 s^{-1} and two additional rates, 0.001 s^{-1} and 0.1 s^{-1}, at 200°C. Note that 240°C was selected as the upper test condition considering the maximum rail forming temperature of 233°C studied in this work.

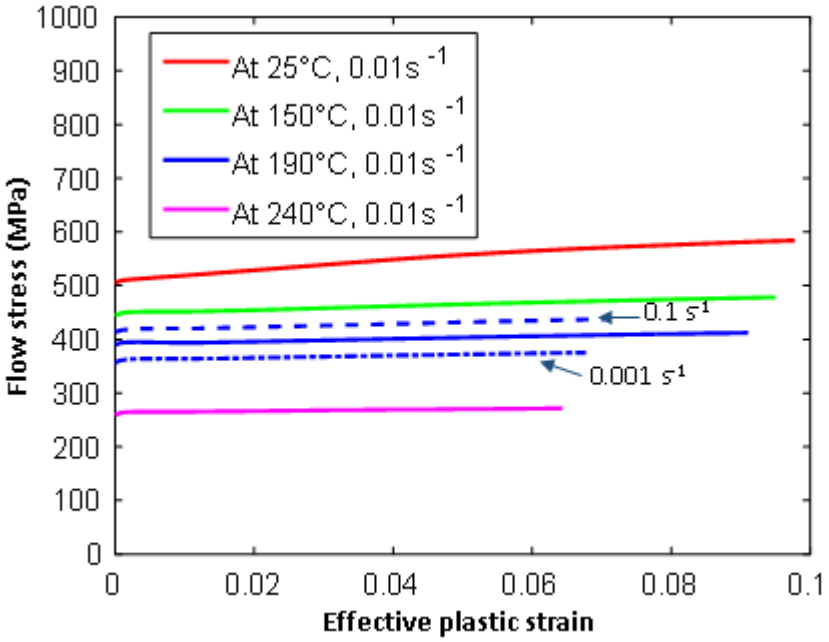

Figure 29: Elevated temperature flow-stress versus effective plastic strain from tensile data by DiCecco [2]

Good repeatability was confirmed by the standard deviation of the average stress between 0.02% and 0.08% plastic strain in Table 7. DiCecco [2] hypothesized that the larger deviation at 240°C might be associated with precipitate coarsening and increased thermal-sensitivity.

Table 7: Standard deviation of the average stress between 0.02%-0.08% plastic strain [2]

	Test temperature			
	25°C	150°C	190°C	240°C
Standard deviation	0.23%	0.46%	0.42%	1.44%

Plotted flow stress curves in Figure 29 indicated hardening at room temperature that steadily decreased with an increase in temperature. At 240°C, the yield stress was almost equal to the saturation stress. A strongly positive rate sensitivity was recorded at 200°C. It is worth noting that the range of plastic strain was limited to below 10% at room temperature and around 6% at the highest temperature. Shear data could provide more insight in the flow-stress history beyond this range but was not performed at elevated temperatures.

As discussed in section 1.2.2, strain and stress directionality is expressed through the stress ratio and the Lankford parameter in Equation 11-12, respectively. From quasi-static room temperature tensile tests in 15° increments relative to the RD, Rahmaan [3] obtained the ratios listed in Table 8 and visualized in Figure 30. Please note that plotted lines represent the evolution trend between experimental data points that are marked with circles. While the stress exhibited negligible directionality along the RD, a significant strain directionality was observed for the Lankford parameter in red color.

Table 8: R-values and stress ratios (defined as the ratio of stress along a particular material direction normalized by the corresponding stress along the RD) obtained from quasi-static room temperature tensile tests by Rahmaan [3]

	Angle along the RD						
	0°	15°	30°	45°	60°	75°	90°
R-values	0.68	0.56	0.78	1.43	1.40	1.29	1.87
Standard deviation R-values	0.05	0.036	0.06	0.13	0.15	0.08	0.31
Stress ratios	1.00	0.99	1.00	0.98	1.00	1.02	1.00
Standard deviation stress ratios	0.005	0.015	0.015	0.015	0.015	0.015	0.015

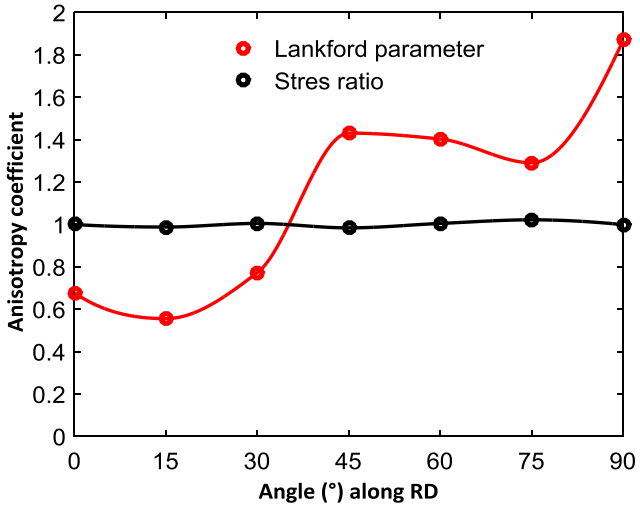

Figure 30: Visualized anisotropy for AA70XX T76; data obtained by Rahmaan [3]

Omer [111] performed experiments at 470°C (for die quenching) and confirmed negligible thermal effects on anisotropy for AA70XX T76 and AA7075 T6.

Yoon *et al.* [56], [112] found a correlation between the variation in strain and stress directionality with sheet orientation obtained from tensile tests and the shape of the earing profile. They interpreted the earing profile as a mirror image of the R-value evolution with respect to the TD; maximum and minimum cup height corresponds to a peak and valley R-value respectively. Since the material at the blank rim is exposed to radial compressive strains, the material behavior at a certain angle is controlled through the material properties at the respective angle rotated by 90°. Considering this reported behavior, the R-value distribution suggests that circular cup draws for AA70XX T76 record multiple ears. Comparison to experimental observations are discussed in Chapter 4.

Shear experiments

Calibration of a constitutive model that reasonably captures the true material response is challenging if measured strain only reaches 6%-10% (at least for the studied AA70XX T76). However a material under shear loading can sustain much higher deformation before fracture and gives a detailed insight into the material hardening response.

For comparison to tensile data or calibration of the constitutive model, a conversion to equivalent plastic strain is required. Rahmaan *et al.* [108] proposed computation of the work-conjugate equivalent

plastic strain under the assumption of plastic work equivalence without adopting a yield criterion. The shear stress is computed from the measured force (F), shear gage length (L_S), and the sample thickness (t) as shown below:

$$\tau_{12} = \frac{F}{L_s\, t} \tag{29}$$

Owing to the decomposition of the logarithmic strain tensor into an elastic and plastic part and under the assumption of plane stress (σ_2 = - σ_1, σ_3 = 0), Hooke's law is utilized to compute principal elastic and plastic strain in Equation 30, that is based on the assumption that, compared to the shear components, the magnitude of the normal stresses are negligibly small.

$$\varepsilon_{1,el} = \frac{\tau_{12}}{2G} \qquad \varepsilon_{1,pl} = \varepsilon_1 - \frac{\tau_{12}}{2G} \tag{30}$$

Under the assumption of plastic work equivalence, the plastic work increment is defined in Equation 31, from that the work conjugate equivalent plastic strain increment in Equation 32 follows.

$$dw_{\,pl,shear} = \int 2\,\tau_{12}\, d\varepsilon_{1,pl} = \sigma_{eq} d\varepsilon_{eq,pl} \tag{31}$$

$$d\varepsilon_{eq,pl} = 2\left(\frac{\tau_{12}}{\sigma_{eq}}\right)\left(d\varepsilon_1 - \frac{d\tau_{12}}{2G}\right) \tag{32}$$

The expression τ_{12}/σ_{eq} represents the normalized shear stress ratio with respect to the reference direction in the tension test. Rahmaan [3] found a ratio of 0.577 +-0.02 standard deviations for AA70XX T76.

For this study, Rahmaan [3] utilized a plastic work level of 36 MJ/m^3 at which the stress levels for shear conversion were obtained. Figure 31 compares converted shear flow stress data obtained from Rahmaan [3] to tensile data from DiCecco [2], both performed at room temperature. Tensile data plotted in green color was performed at a quasi-static strain rate of 0.01 s^{-1} that was in good agreement with the respective converted shear curve in red. While minor differences were observed at the onset of yielding, the hardening behavior was similar. It is worth pointing out that the strain range from the shear experiment was five times larger than the strain from the tension test. The black curve

represents converted shear data at a strain rate of 0.001 s^{-1} and coincided with the experiment at 0.01 s^{-1}, that demonstrated rate-insensitive behavior of AA70XX T76 at room temperature

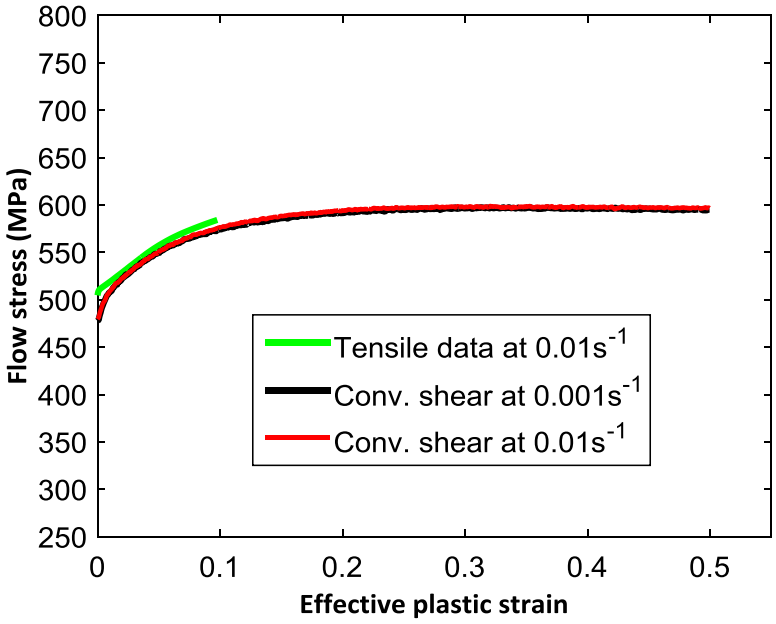

Figure 31: Comparison of room converted shear data by Rahmaan [3] to tensile data by DiCecco [2]

Equi-biaxial tests

Strain ratios under biaxial loading were obtained by Rahmaan [3] in the Marciniak test and computed at the same plastic work level (36 MJ/m^3) utilized for tensile and shear calculations. The strain ratio, R_b, is recorded in Equation 33 [4], where ε_{RD} and ε_{TD} refer to the strain in the RD and TD direction, respectively.

$$R_b = \frac{\varepsilon_{TD}}{\varepsilon_{RD}} \tag{33}$$

The stress ratio, obtained from through-thickness compression tests, was computed from Equation 34, that represents the normalized stress ratio in the TD with respect to the RD.

$$S_b = \frac{\sigma_{TD}}{\sigma_{RD}} \tag{34}$$

Results for AA70XX T76 are recorded in Table 9.

Table 9: Stress and strain ratios for equi-biaxial loading for AA70XX T76 obtained by Rahmaan [3]

	Ratio	Standard deviation
R_b	0.9	+-0.04
S_b	1.037	+-0.02

2.3 Calibration of Yield Function

As shown in Figure 30, AA70XX T76 exhibits a strong strain directionality. Isotropic yield functions like von Mises or Hosford are not suitable for accurate description of the material response. In the scope of this thesis, a parameter study on different yield surfaces and flow rules was performed; an overview on test conditions is given in Table 10. As discussed in Section 1.2.2, the associative flow rule (AFR) assumes that both yield stress function and plastic potential are described by one set of anisotropy coefficients. Assigning a separate set of anisotropy coefficients to each the yield stress function and the plastic potential allows more accurate description of the material response. The latter is summarized under the term non-associative flow rule (Non-AFR). Note that the first case in Table 10, associative Hosford, serves as baseline comparison to that the advanced Barlat YLD2000-2d is compared.

Table 10: Overview on studied yield functions and flow rules

Case #	Flow rule	Yield stress function	Plastic potential
1	AFR	Hosford (isotropic)	Hosford (Isotropic)
2	AFR	YLD2000-2d	YLD2000-2d
3	Non-AFR	YLD2000-2d	YLD2000-2d
4	Non-AFR	Hosford (isotropic)	YLD2000-2d

The studied yield surfaces were calibrated by Abedini [18] who employed the proposed shear constraint by Abedini *et al.* [54] that is discussed in Section 1.2.2. For minimizing deviations between function prediction and experimental data, Abedini utilized a genetic algorithm implemented in the software MATLAB.

For calibration of AFR YLD2000-2d, the following data is required [55]:

(i) Yield stress ratios in the RD, DD, and TD

(ii) Yield stress ratios under equi-biaxial loading

(iii) R-value in the RD, DD, and TD

(iv) R-value under equi-biaxial loading

For calibration of non-AFR YLD2000-2d, the following data is required [57]:

(1) Yield stress function

(i) Yield stress ratios in 15° increments relative to the RD

(ii) Yield stress ratios under equi-biaxial loading

(2) Plastic potential

(iii) R-value in 15° increments along the RD

(iv) R-value under equi-biaxial loading

For improved description of the material behavior, shear stress ratios were added to the conventional eight input parameters. The input data was obtained by Rahmaan [3] in room temperature mini-dogbone tensile tests, through-thickness compression and Marciniak tests, and mini-shear tests at a plastic work level of 36 MJ/m^3. Table 11 summarizes these results. Since Omer [111] demonstrated negligible temperature effects on the anisotropy of AA70XX T76, studied yield surfaces were calibrated with room temperature R-values and stress ratios.

Table 11: Utilized experimental data [3] at a plastic work level of 36 MJ/m^3 for yield surface calibration; see Table 8 for standard deviations in uniaxial tension, Table 9 for standard deviation in equi-biaxial testing, and for shear the standard deviation is +-0.02

	Normalized stress ratio	R-value
Uniaxial tension in RD	1.00	0.68
Uniaxial tension 15° relative to RD	0.99	0.56
Uniaxial tension 30° relative to RD	1.01	0.77
Uniaxial tension 45° relative to RD	0.98	1.43
Uniaxial tension 60° relative to RD	1.01	1.40
Uniaxial tension 75° relative to RD	1.02	1.29
Uniaxial tension 90° relative to RD	1.9	1.87
Equi-biaxial loading (Through-thickness compression + Marciniak tests)	1.037	0.90
Shear testing	0.577	-

Calibrated yield surfaces [18] for the Barlat YLD2000-2d model are plotted in Figure 32 for both AFR (blue) and non-AFR (green). The results are based on a yield exponent of eight that is conventionally used for FCC materials. The left figure, Figure 32a, shows minor differences in stress ratio predictions between AFR and non-AFR. Both flow rules captured the mild stress anisotropy well. A considerably different prediction is observed for R-values. It is important to recall that in view of the limited number of anisotropy coefficients for AFR YLD2000-2d (eight for both plastic potential and yield stress function), only strain ratios at 0°, 45°, and 90° were utilized as input, that was well captured by the model. Looking at experimental data in between, the AFR could not describe the complete material response. In contrast, the non-AFR, for that R-values and stress ratios in 15 ° increments were utilized in view of the increased calibration parameters (eight for each plastic potential and yield stress function), captured the R-value variation fairly well. Some discrepancy were present between the DD and the TD that could be attributed to the additional shear constraint, that was utilized for yield surface calibration, as discussed in [54]. From Figure 32b it can be seen that the predicted yield loci in stress space had a similar shape for both AFR and non-AFR YLD2000-2d and captured the yield stress for equi-biaxial and shear loading well. Calibrated anisotropy coefficients [18] are summarized in Table 12.

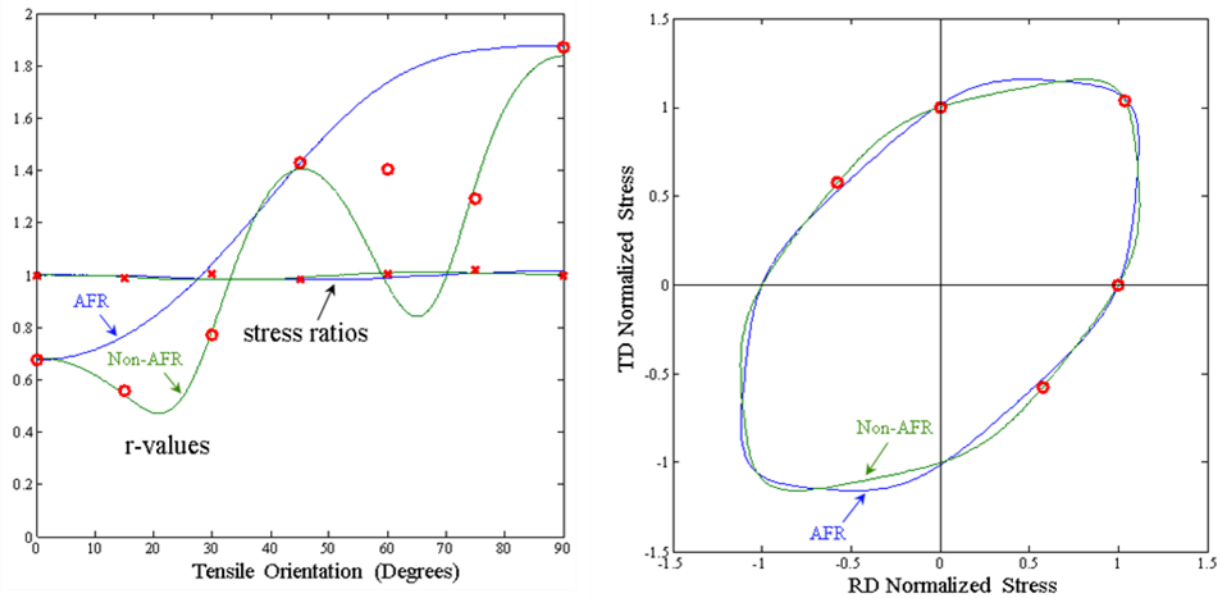

a) Measured and predicted stress and strain ratios

b) Yield surface in stress space

Figure 32: Calibrated yield surfaces [18] for Barlat YLD2000-2d with associative flow rule (blue) and non-associative flow rule (green). Red circles represent experimental strain and stress ratios.

Table 12: Calibrated anisotropy coefficients [18] for studied yield functions and flow rules

	YLD 2000-2d AFR	YLD 2000-2d Non-AFR, Yield function	YLD 2000-2d Non-AFR, Plastic potential
α_1	0.8376	1.2698	0.6859
α_2	1.1344	0.6131	-0.7087
α_3	1.0503	1.9426	0.8257
α_4	0.9424	0.5602	0.0627
α_5	0.9880	0.3226	-0.0755
α_6	0.8253	1.9306	0.6709
α_7	1.0360	1.0371	0.4637
α_8	1.0443	0.9926	0.4540

Since the current implementation of constitutive models in the solver LS-DYNA is limited (only associative Barlat YLD2000-2d is supported), Prof. Butcher [6] implemented the discussed yield criteria and flow rules in a user-defined material sub-routine (umat) that is discussed in Chapter 5 of this thesis.

2.4 Calibration of Temperature and Rate-dependent Constitutive Model

Consideration of thermo-viscous effects in the material flow behavior plays a key factor in accurate prediction of the material response. While experimental data is essential, the hardening model aims at mimicing the material flow behavior beyond the measured strain range [41]. This section discusses three different hardening models that all account for rate and temperature effects of AA70XX T76, a 7xxx series aluminum alloy under development. Calibration was performed on the converted flow stress versus effective plastic strain curves obtained from tensile and shear tests by DiCecco [2] and Rahmaan [3], discussed in Section 2.2. The Least Squares method in the software Excel was utilized to optimize calibration parameters which are discussed for each hardening model separately, followed by a discussion on their performance at various temperatures and strain rates.

2.4.1 Extended Nadai Model

The extended Nadai model is discussed in section 1.2.1 and is given as Equation 5. This model is often utilized as a baseline comparison to physically-driven models [30], [44], [45] and enjoys popularity among users in view of its compact form. For the studied AA70XX T76, optimized calibration parameters are recorded in Table 13. The melting temperature T_m was set to 633°C [113]. For this study, the average correlation coefficient serves as measure of agreement between model prediction and experiment. A value of unity is perceived optimal.

Table 13: Optimized calibration parameters for the extended Nadai model for AA70XX T76

C_0	21.980 MPa	n_0	0.347	c	519.096
a_1	15.800 MPa	b_1	-0.382	ε_0	1.26
a_2	10.822	b_2	-3.144	m_0	3.37E-4

As demonstrated in Table 14, correlation coefficients close to unity were found for most test temperatures except for room temperature results.

Table 14: Average correlation coefficient for the extended Nadai calibration for AA70XX T76

Test temperature	25°C		150°C	190°C			240°C
Strain rate	0.001 s^{-1}	0.01 s^{-1}	0.01 s^{-1}	0.001 s^{-1}	0.01 s^{-1}	0.1 s^{-1}	0.01 s^{-1}
Correlation Coefficient	0.762	0.758	0.996	0.966	0.992	0.9991	0.957

2.4.2 Bergström Model

The physically-driven Bergström model is discussed in section 1.2.1 and shown as Equations 4-8. This model was selected because it offers more insight into the material behavior. Since the dislocation density is described through an evolution function, model calibration requires more material properties. Calibration results for σ_0, C, m, Ω_0, C_T, and T_1 are listed in Table 15 where italic parameters are either material properties or were taken from literature for annealed AA5754 [30].

Table 15: Optimized calibration parameters for the Bergström model for AA70XX T76

σ_0	472.735 MPa	m	0.370	p_0	*1E+12 m^{-2}*
α	*1.0*	U_0	*6.093E+8 m^{-1}*	G_{ref}	*27576 MPa*
b	*2.87E-10 m*	Ω_0	38.022	C_T	560.240 K
C	8.052E+5	Q_v	*1.092E+4 J/mol*	T_1	3657.167 K

Computed correlation coefficients summarized in Table 16 showed good experimental correlation at lower temperatures but seemed to fail at capturing rate effects at 200°C.

Table 16: Average correlation coefficient for the Bergström calibration for AA70XX T76

Test temperature	25°C		150°C	200°C			250°C
Strain rate	0.001 s^{-1}	0.01 s^{-1}	0.01 s^{-1}	0.001 s^{-1}	0.01 s^{-1}	0.1 s^{-1}	0.01 s^{-1}
Correlation Coefficient	0.995	0.996	0.930	0.794	0.779	0.929	0.799

2.4.3 Proposed Model

The third phenomenological hardening model was developed as part of this research and utilizes a reduced Hockett-Sherby model (see Equation 1) that was made temperature and rate-dependent, as

shown below, where *n* corresponds to the hardening exponent and *r* represents a rate-dependent term defined in Equation 39.

$$\sigma_{flow}(T, \varepsilon_{pl}, \dot{\varepsilon}) \ = \left[\sigma_{sat} - \left(\sigma_{sat} - \sigma_y\right) \exp\left(-n\ \varepsilon_{pl}\right)\right] r \tag{35}$$

Experimental observations for AA70XX T76 in Figure 29 and Figure 31 recorded hardening at room temperature that gradually decreased as temperature rose. The suggested model accounts for this effect through the exponential function in Equation 36 that describes the rate at that the yield stress approaches the saturation stress. n_1 and n_2 are calibration parameters.

$$n(T) = n_1 * \exp(-n_2 * T) \tag{36}$$

A strongly inverse correlation was observed for the yield stress, saturation stress, and temperature. As temperature increased, both yield stress and saturation stress experienced a drop. Additionally, the difference between yield stress and saturation stress decreased exponentially as a function of temperature. Hence, the thermal effect on both stress terms were coupled. The yield stress is described as shown below:

$$\sigma_y(T) = \ \sigma_{y,ref} - \frac{y_1}{1 + \exp(-y_2(T - y_3))} \tag{37}$$

The temperature-induced drop in the yield stress is subtracted from the reference yield stress ($\sigma_{y,ref}$), that corresponds to the test condition at the lowest temperature. While this function is somewhat more complex and requires calibration of three parameters (y_1, y_2, and y_3), it ensures stress saturation at higher temperatures (beyond test conditions in this study). A so-called sigmoid curve (also known as “S-curve”) captures this behaviour well.

In analogy to the observed temperature-dependent hardening behavior described through the hardening function *n*, the decreasing difference between saturation stress and yield stress as a function of temperature is to be considered as well. The suggested model describes this behavior through a constant term, that is the yield stress at the respective temperature, and a variable term, that decreases as temperature rises. An exponential function with calibration parameters s_1 and s_2 is utilized.

$$\sigma_{sat}(T) = \sigma_y + s_1 \exp(-s_2 T) \tag{38}$$

Despite the phenomenological character of this model, convergence of the yield and saturation stress as a function of temperature, demonstrated in Figure 33, is physically-motivated as the hardening of the material will vanish at sufficiently high temperatures.

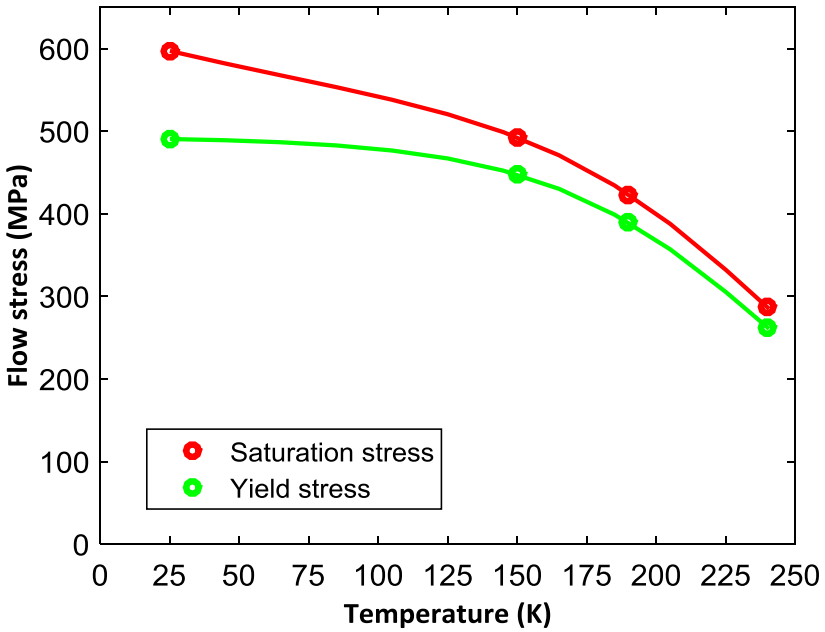

Figure 33: Predicted correlation between yield stress and saturation stress as a function of temperature

The significant temperature-dependent strain-rate sensitivity was demonstrated through shear tests [3] at room temperature and tensile tests [2] at 200°C. The existence of no rate effects at room temperature and positive rate sensitivity at elevated temperature were modeled through a multiplicative term that scales the computed flow stress at the reference strain rate as shown below

$$\mathrm{r}(\mathrm{T}, \dot{\varepsilon}) = \exp\left(ln\left(\frac{\dot{\varepsilon}}{\dot{\varepsilon}_{ref}}\right) m \left(\frac{T - T_0}{T_m}\right)\right) \tag{39}$$

In a similar way to the Zerilli-Armstrong model, the strain rate is expressed through a logarithmic function that is embedded in an exponential function. To ensure absence of rate-effects at room temperature, a temperature term is included that becomes zero if the current temperature is equal to

the reference temperature (T_0). The alloy melting temperature T_m is obtained from literature [113]. The parameter *m* in Equation 39 represents the thermally-induced strain-rate sensitivity.

Calibration results for AA70XX T76 are summarized in Table 17 where the italic parameters were obtained from literature or represent physical material properties.

Table 17: Optimized calibration parameters for the proposed model for AA70XX T76

n_1	44.445	y_3	517.140 K	T_m	*906 K*
n_2	3.379E-3	s_1	831.385 MPa	$\sigma_{y,ref}$	*493 MPa*
y_1	485.201 MPa	s_2	6.893E-3		
y_2	2.409E-2	m	1.777E-1		

Based on the computed correlation coefficients in Table 18, the proposed model seems to be capable of capturing the material behavior at both lower and upper temperatures including rate-effects.

Table 18: Average correlation coefficient for suggested model calibration

Test temperature	25°C		150°C	200°C			250°C
Strain rate	0.001 s^{-1}	0.01 s^{-1}	0.01 s^{-1}	0.001 s^{-1}	0.01 s^{-1}	0.1 s^{-1}	0.01 s^{-1}
Correlation Coefficient	0.998	0.999	0.992	0.968	0.984	0.988	0.962

2.4.4 Comparison of Calibrated Constitutive Models

The results at room temperature are plotted for a strain rate of 0.001 s^{-1} and 0.01 s^{-1} in Figure 34a and Figure 34b, respectively. The solid black line represents converted shear data [3] at room temperature and the grey solid line plots the experimental tensile data [2] at 0.01 s^{-1}. Predictions by the Bergström model are presented by the blue dashed line, the green dotted curve represents the extended Nadai model, and the red solid line summarizes predictions by the proposed model. While all models produced reasonable results in predicting rate-insensitive flow behavior at room temperature, yield stress predictions varied somewhat. The extended Nadai model strongly overpredicted the yield stress by about 15% and converged to the measured saturation stress only after 30% plastic strain. Both the Bergström and the new model accurately predicted onset of yielding and subsequent hardening behavior of the material.

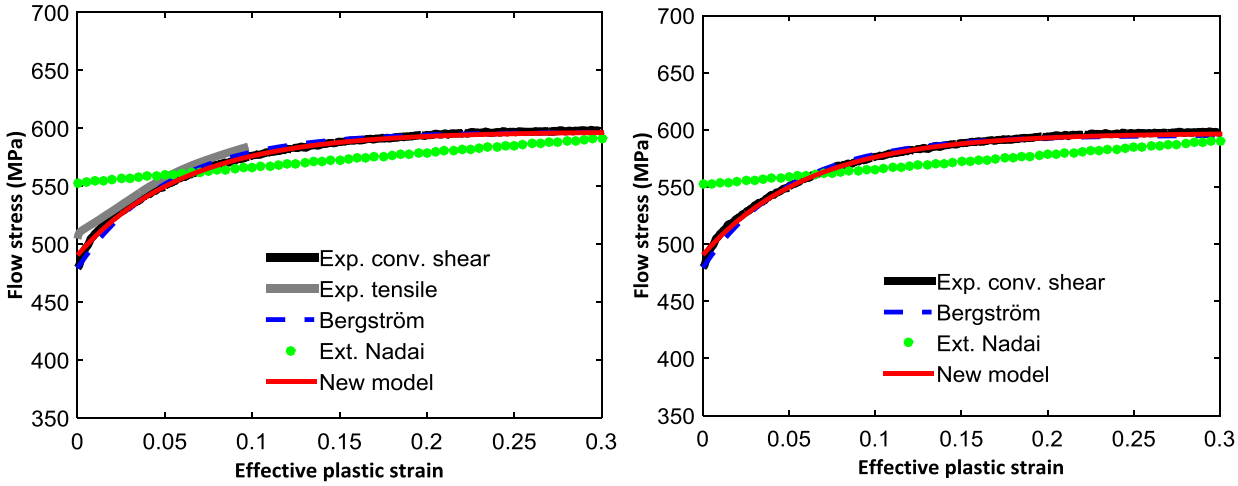

a) At 25°C, at a strain rate of 0.001 s^{-1} b) At 25°C, at a strain rate of 0.01 s^{-1}

Figure 34: Comparison of different hardening models with experimental data at room temperature. The black curve represents experimental converted shear data, grey experimental tensile data, dashed blue curve the Bergström model, green dotted line the extended Nadai model, and red line the proposed model.

While quasi-static flow stress predictions at 150°C and at 250°C, in Figure 35, were in good experimental agreement, results at 200°C, in Figure 36, offer a better insight into model predictions in view of strain-rate effects.

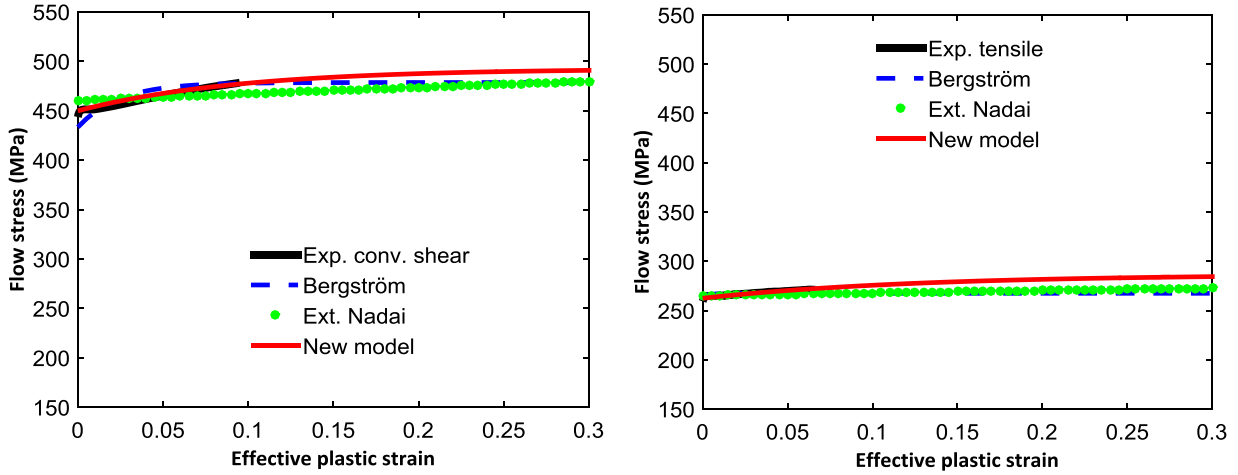

a) At 150°C, at a strain rate of 0.01 s^{-1} b) At 250°C, at a strain rate of 0.01 s^{-1}

Figure 35: Comparison of different hardening models with experimental data at 150°C and 250°C

The shift in flow stress due to thermally-induced rate sensitivity was well-captured by both the extended Nadai model and the proposed model whereas poor experimental correlation was found for

the Bergström model at a strain rate of 0.1 s^{-1} in Figure 36c. A major drawback of this model is the rate-insensitive yield stress discussed in Section 1.2.1.

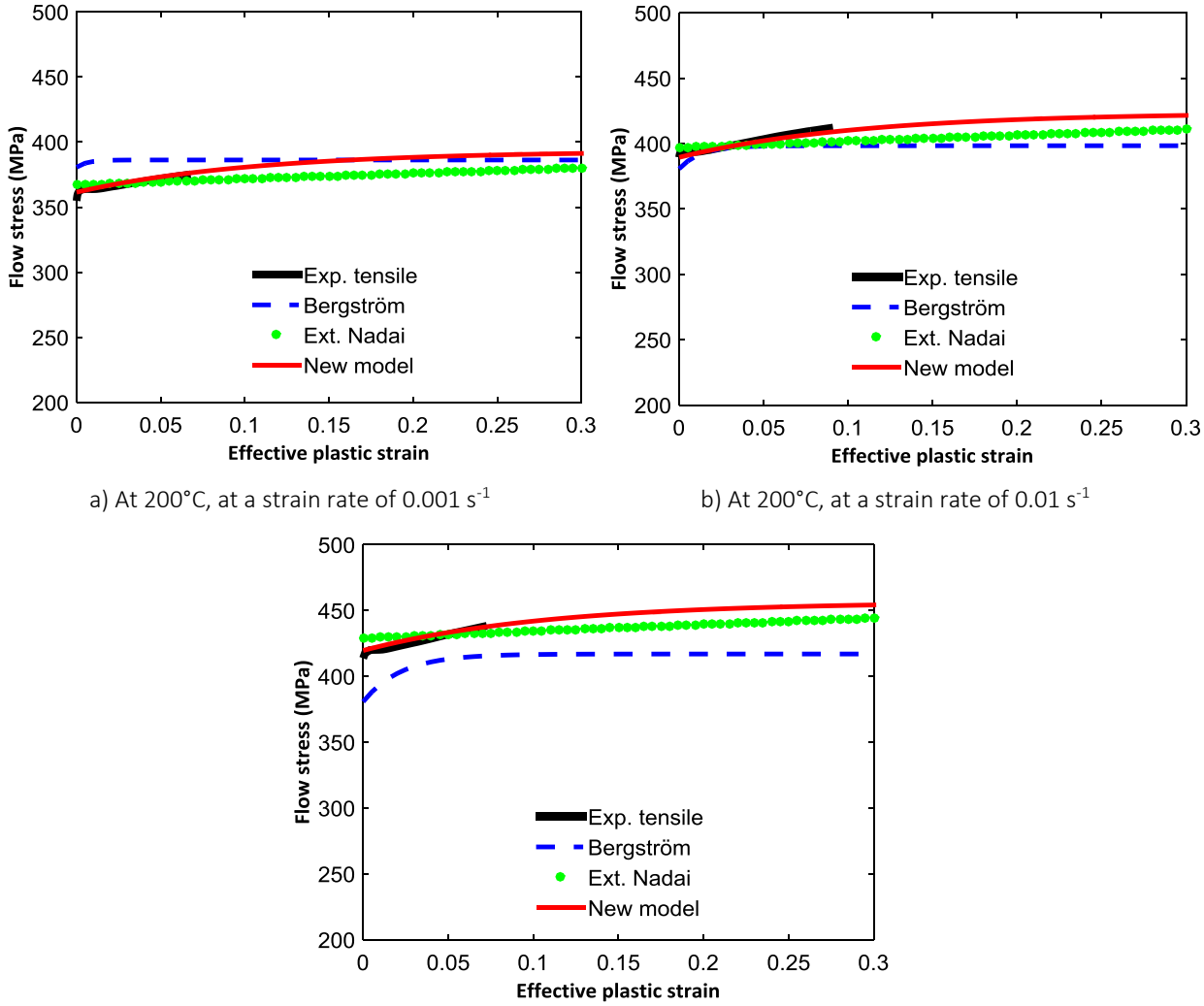

a) At 200°C, at a strain rate of 0.001 s^{-1}

b) At 200°C, at a strain rate of 0.01 s^{-1}

c) At 200°C, at a strain rate of 0.1 s^{-1}

Figure 36: Comparison of different hardening models with experimental data at 200°C at strain rates ranging from 0.001 s^{-1} to 0.1 s^{-1}

Concluding from these observations, among the studied hardening models, the proposed model more accurately described the observed behavior of AA70XX T76 and was utilized for numerical modeling of circular cup draws in Chapter 5.

3 Friction Characterization

This chapter discusses the experiments performed to characterize the warm friction behavior of the AA70XX T76 developmental alloy using the Twist Compression apparatus at the University of Waterloo. First, the experimental set-up of the test equipment is presented, followed by a description of the adopted test parameters and the rationale for their selection, including the lubricants, contact pressure, and maximum sliding distance during testing. The choice of contact pressure and sliding distance was based on consideration of the characteristics of the warm forming processes studied (rail forming in Chapter 6). Finally, the test results are presented.

3.1 Twist Compression Apparatus

As part of another research project, George [114], a research engineer in Prof. Worswick's group, performed modifications to the TCT apparatus to enable elevated temperature testing. A schematic of the test apparatus is given in Figure 37.

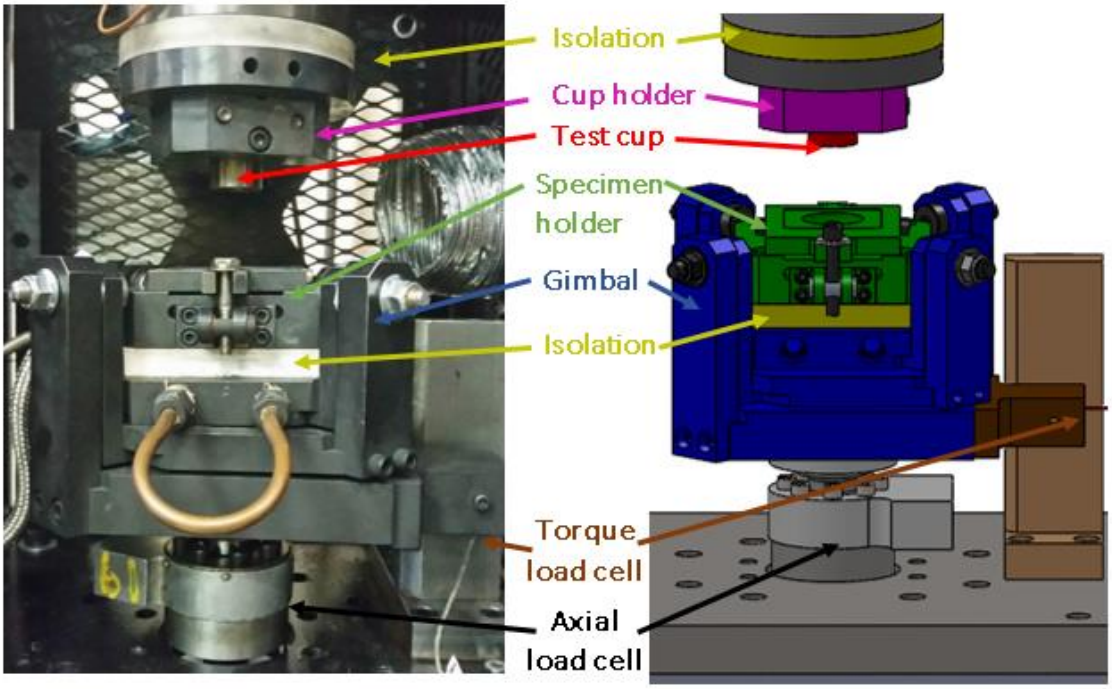

Figure 37: TCT equipment in the laboratory (left) and in the CAD software (right) [114]

The test cup (highlighted in red) is positioned through a screw in the cup holder (pink) that prevents movement during testing. The specimen holder is highlighted in green and positions the blank; the

optional clamp prevents buckling for testing of thin sheets. The gimbal, highlighted in blue, aligns the test cup surface with the specimen to ensure parallel contact and precludes entrance of fresh lubricant during testing. The resistance to sliding is measured by a 45.5 kg-load cell (brown) located on the torque arm that presses against the rod during testing. In order to measure the applied interface pressure, a 2270 kg-capacity load cell is installed between the actuator and the gimbal.

Two 300 W cartridge heaters are installed in each the cup and specimen holder that allows testing at temperatures up to 430°C. Cooling channels and isolation plates are installed to prevent surrounding electrical components from overheating. Instantaneous temperature control is realized through thermocouples installed in both the cup and specimen holder.

3.2 Friction Test Parameters

With the aim to get a better understanding of the tribological conditions, such as the forming pressure and sliding distances, the warm forming process was modelled using FE simulations. Approximate determination of the forming pressure in the target process serves as guidance for selection of interface pressure in the friction test.

The predicted contact pressure distribution in the die during forming is shown in Figure 38 that corresponds to a punch depth of 29.4 mm. For a description on the model set-up, please refer to Appendix B. It is evident from the figure that the highest contact pressure occurs at the die entry radius. Averaging the forming pressure along the die length in 0.1 s increments yields the time-dependent evolution summarized in Figure 39. The forming pressure varies considerably during the process and peaks as the blank surface slides over the die entry radius region prior to forming the channel sidewall. Forming pressures as low as 12.4 MPa and as high as 30.1 MPa were predicted. The average value over all time increments corresponded to roughly 22.5 MPa.

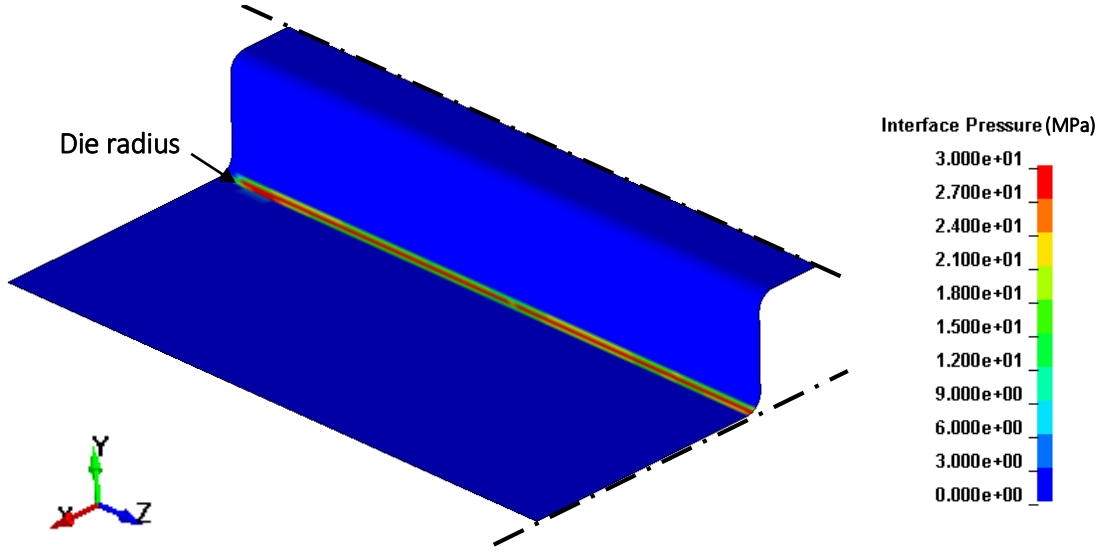

Figure 38: Predicted pressure values in the die at 29.4 mm punch displacement

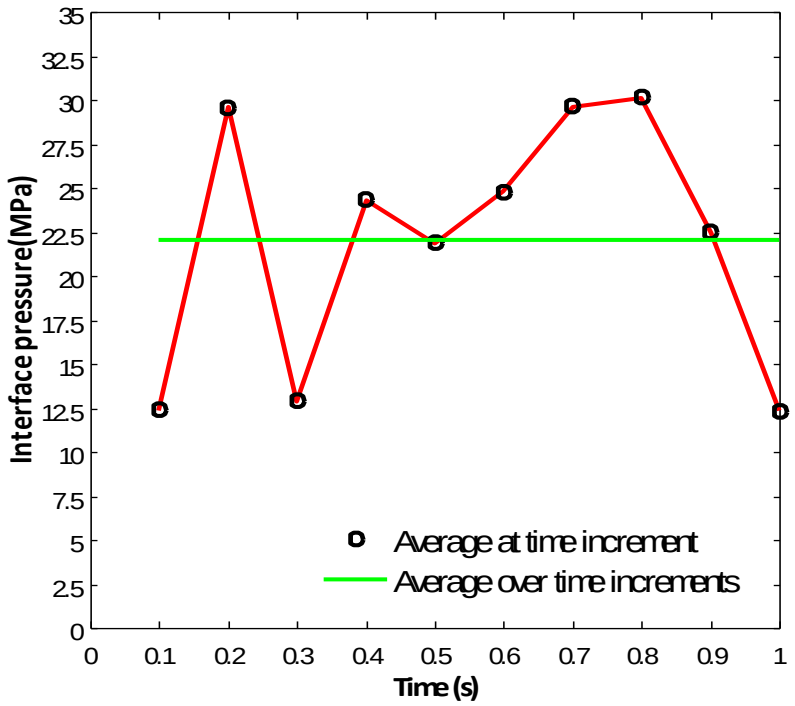

Figure 39: Evolution of the forming pressure in the die radius, predicted by the FE model

The time-history data indicates that the material that flows around the die entry radius into the rail sidewall experiences the highest contact pressure. In addition, this material experiences a sliding distance of about 50 mm. Given this large sliding distance and contact pressure, combined with

elevated forming temperature, the warm Twist Compression Test (TCT) was concluded to be suitable for the friction characterization studies.

Four commercially available lubricants were considered:

Forge Ease AL278 (hereinafter referred to as Fuchs)

Fuchs is a synthetic lubricant that is liquid when applied to the blank and requires about 20 min dry time in ambient room temperature. Its recommended dilution ratio is four parts lubricant and one part water and its service temperature is up to 350°C, although lubricity can be impaired at temperatures above 275°C that represents the melting temperature of a wax ingredient [115], [116]. Initial tests showed that replacing water with alcohol resulted in a more even wetting of the blank and faster curing. Therefore, a dilution ratio of four parts alcohol and one part lubricant was utilized.

OKS 536 (hereinafter referred to as OKS)

OKS is a water-based graphite-bonded coating with a service temperature of -35°C to 600°C. The physical lubricant condition is liquid and requires a minimum of 30 min drying time. The maximum recommended dilution ratio is one part lubricant and five parts water [117]. The lubricant film is water-soluble whereas graphite particles deposited to the surface after forming can only be removed by mechanical treatment. In the current friction study, three parts lubricant and one part water were mixed.

LPS Dry Film PTFE Lubricant (hereinafter referred to as PTFE Spray)

The PTFE-Spray is a liquefied gas supplied in a pressurized container. The lubricant was sprayed onto the sheet specimen, however, its quick evaporation rate allowed only limited control over the applied lubricant amount. Its solubility in water is below 10% that makes lubricant removal after forming difficult. The service temperature is between -40° to 260°C [118].

Teflon film

Teflon film is a dry film synthetic, fluorocarbon-based polymer with a thickness of 0.1 mm, that is rated for forming up to 260°C [119]. Note that this lubricant is tested from a research perspective since use of such a film lubricant is not appropriate for a high-volume industrial process.

Table 19 gives an overview of the outlined test matrix from that can be seen that AA70XX T76 was selected as the lead alloy and that experiments for AA7075 T6 and AA6013 T6 were restricted to room

temperature using Fuchs. In view of mechanical limitations of the utilized TCT equipment, 170°C was the temperature limit for studying the friction response under unlubricated conditions.

Table 19: Test matrix for warm friction characterization in the TCT

		Lubricant				
Test temperature (°)	Alloy	Fuchs	OKS	PTFE Spray	Teflon film	Unlubricated
25	AA70XX T76	3	3	3	3	3
	AA7075 T6	3				
	AA6013 T6	3				
170	AA70XX T76	3	3	3	3	3
200	AA70XX T76	3	3	3		
230	AA70XX T76	3	3	3		

The square test specimen (50.5 mm length) was deburred and cleaned with acetone before the lubricant was applied. Due to the thin lubricant film and the small specimen dimensions, a high-precision scale with a resolution of +- 0.01 g was unable to capture the lubricant weight. In order to still ensure consistent testing conditions, Fuchs was applied with a paint roller, OKS with two lubricant pumps and evenly spread with a brush, PTFE Spray was sprayed for 3 s from a distance of 10 cm and the Teflon film was cut into equal squares. A minimum of three repeats were performed to ensure good reliability but in some cases, more repeats were required to ensure reliable test results.

Tooling Material and Coating

As will be demonstrated in the presentation of the friction test results in Section 3.6, the tested lubricants were only able to prevent die pick-up to a limited extent. As a result, additional experiments were performed using a die coating, Ionbond35 [120] that is a CrWN PVD-die coating intended for aluminum warm forming.

In order to mimic the target forming process (rail forming in Chapter 6), the TCT tooling (here referred to as test cups) were made of the same die material, Dievar tool steel [121], hardened to 53 HRC (Rockwell hardness), that is equivalent to roughly 560 VH (Vickers hardness), and polished to a surface roughness of about 0.13 µm. The Ionbond35 coating has a hardness of 3000 to 3200 VH that makes it

wear-resistant but, at the same time, could cause adhesion problems in view of the large hardness gradient between the cup material and the coating as discussed in Section 1.3.6. To compensate for this difference, a duplex treatment was selected: ion nitriding with a roughly 110 µm case depth followed by application of the 5 µm thick CrWN deposited through a PVD arc method process. The Ionbond35 coating exhibits a COF of 0.3 when sliding over dry steel and is deposited at approximately 350°C. The rather low deposition temperature prevents geometric distortion or reduction in tooling strength. The specified service temperature is 800°C that accommodates temperature ranges for aluminium die quenching [120].

To explore the effectiveness of the die coating, TCT was performed at room temperature, 170°C and at 230°C, as summarized in Table 20. Testing under unlubricated condition had the intention of studying die pick-up whereas die coating in addition with the, among tested lubricants most effective lubricant in preventing galling, aimed at reducing the friction coefficient.

Table 20: Test matrix for die coating study on AA70XX T76

		Lubricant	
Test temperature (°C)	Alloy	Unlubricated	Recommended lube
25°C	AA70XX T76	3 repeats	3 repeats
170°C	AA70XX T76	3 repeats	3 repeats
230°C	AA70XX T76	-	3 repeats

3.3 Methodology

For input into conventional FE solvers, an average COF is required. The straight-forward approach of averaging the COF over the sliding distance appears to be an attractive solution. However, Coulomb's friction law in Equation 21 only holds while the friction force is proportional to the applied load – which breaks down once galling occurs. Hence, the point of lubricant breakdown is to be determined, the curves cropped and the COF averaged up to the point of failure.

As discussed in Section 1.3.4, determination of lubricant breakdown is not always obvious and agreement on reliable detection methods are still under development. Interrupted tests, as suggested by Dalton [70], would allow direct assessment of the specimen and cup surfaces once a certain COF is

reached. However, since the current TCT equipment does not allow instantaneous test interruption, a failure COF of 0.1 was selected as a threshold to indicate the onset of lubricant breakdown. As will be presented in Section 3.6, this number was chosen considering that observed onset of galling for the Fuchs lubricant, when tested at 230°C, recorded peak COFs of about 0.1. Admittedly, this is a low value for failure and is somewhat arbitrary, however, bearing in mind that the tested lubricants are rated for heavy duty forming, the chosen limit was felt to be justified.

The ASTM G115 Standard guide for Measuring and Reporting Friction Coefficients [122] recommends that a steady-state COF be reported since initial contact of sliding partners (summarized under the term running-in) might cause friction force spikes. Following this recommendation, the steady-state COF was computed as visualized in Figure 40:

(i) Determination of sliding distance that records a steady-state COF

(ii) Determination of sliding distance that records a COF of 0.1

(iii) Averaging of COFs within this range

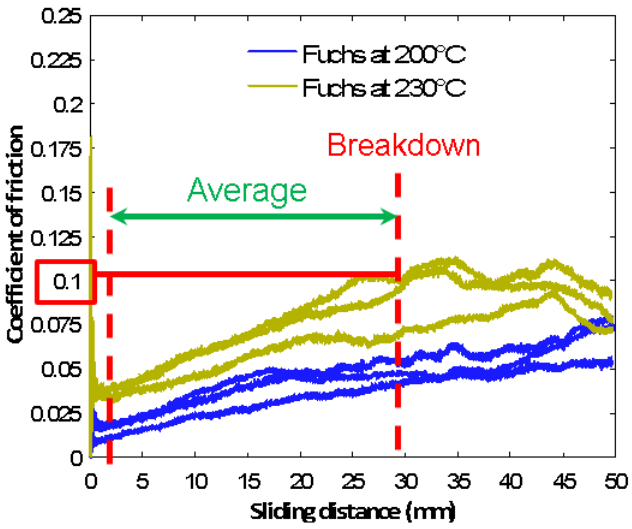

Figure 40: Visualized procedure to compute the average COF based on a failure COF of 0.1

3.4 Pre-study

The effect of various test parameters on the friction response was investigated in the pre-study with AA70XX T76 sheet using the Fuchs lubricant. The sliding distance was set to 50 mm (corresponds to a

260° rotation) that represents the approximate sliding distance during forming. The interface pressure and sliding speed were varied.

The results for three repeats at a low interface pressure of 5 MPa and a sliding speed of 10 mm/s are recorded in Figure 41a. A strongly oscillating COF over the sliding distance and an antisymmetric cup imprint (see Figure 42a) on the tested sheet specimen were observed. From this observation was concluded that an interface pressure of 5 MPa was not sufficient to activate the self-alignment mechanism of the gimbal.

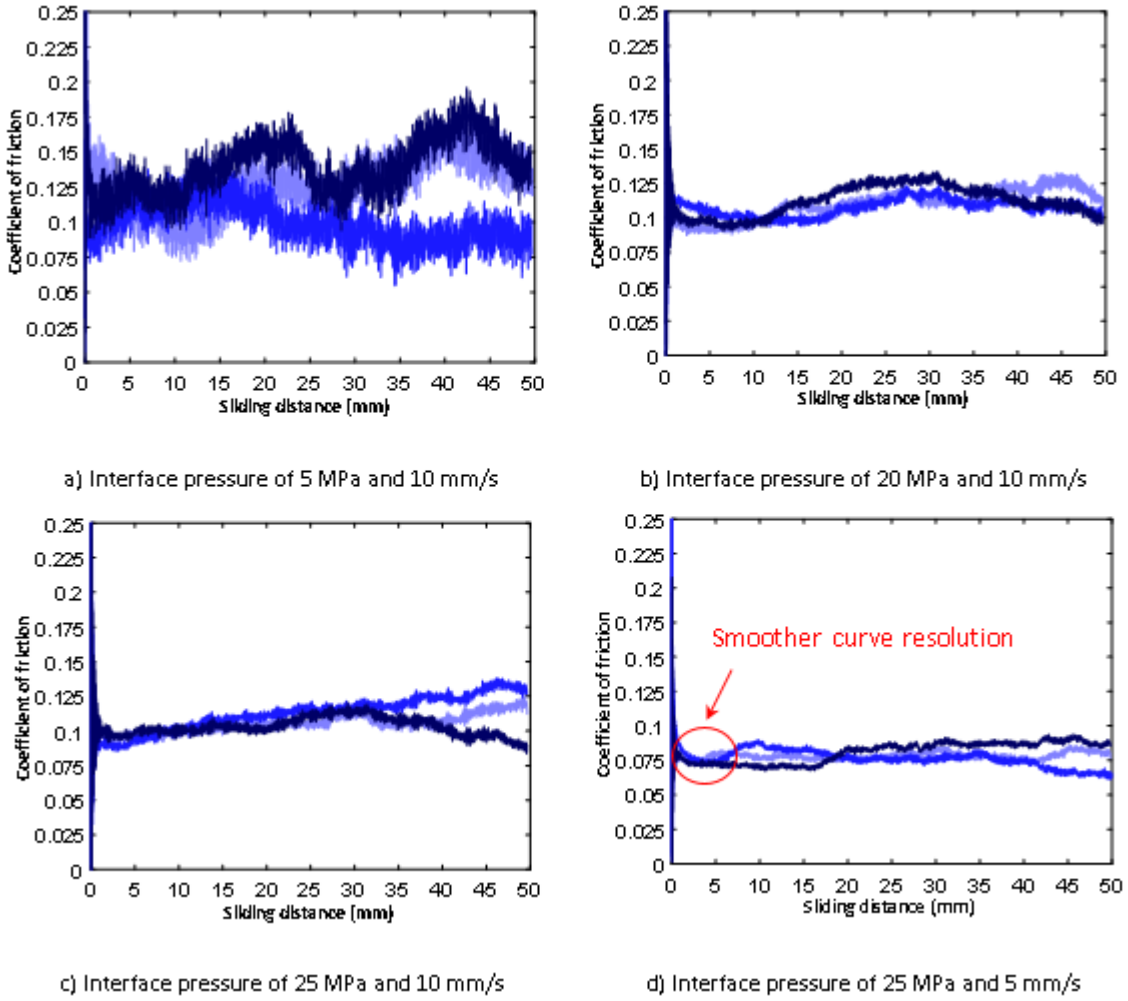

a) Interface pressure of 5 MPa and 10 mm/s

b) Interface pressure of 20 MPa and 10 mm/s

c) Interface pressure of 25 MPa and 10 mm/s

d) Interface pressure of 25 MPa and 5 mm/s

Figure 41: COF over sliding distance for AA70XX T76 utilizing Fuchs

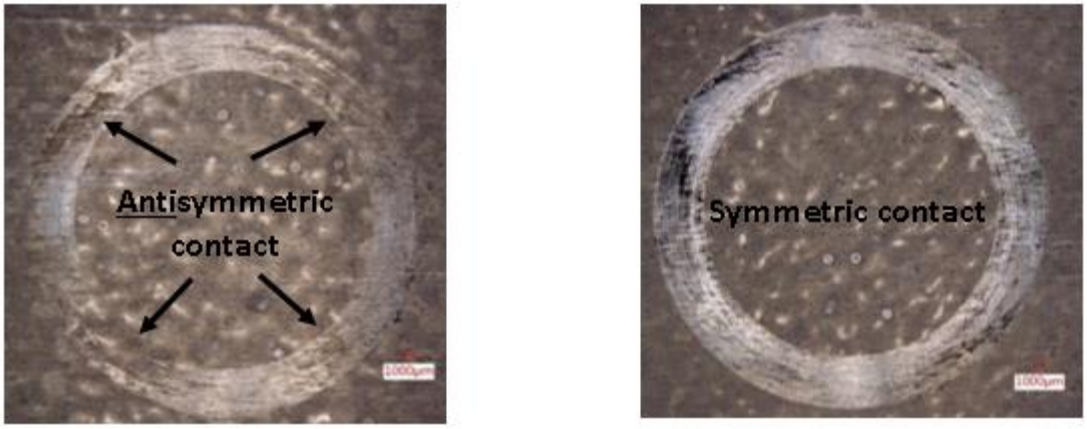

a) At an interface pressure of 5 MPa

b) At an interface pressure of 20 MPa

Figure 42: Cup imprint on tested sheet specimen at different interface pressure

An increase to 20 MPa in Figure 41b resulted in a more stable friction coefficient and a better repeatability between three tests that is also reflected in a symmetric cup imprint as confirmed in Figure 42b.

Testing at 25 MPa at the same sliding speed as for the previous two test conditions caused negligible changes in the recorded absolute COF, that was in accordance with expectations. As one recalls from Coulomb's friction law, the frictional force is proportional to the applied normal load. At higher loads, increased asperity interaction leads to higher friction forces that balances the higher normal load and therefore results in a constant COF. In view of the predicted average forming pressure of about 22.5 MPa with peak values of approximately 31 MPa, testing at 25 MPa seemed to be adequate.

3.5 Alloy Comparison

Before the elevated temperature performance of different lubricants is discussed, room temperature tests with Fuchs are presented (Figure 43) for all three alloys AA6013 T6 (grey), AA7075 T6 (yellow), and AA70XX T76 (blue).

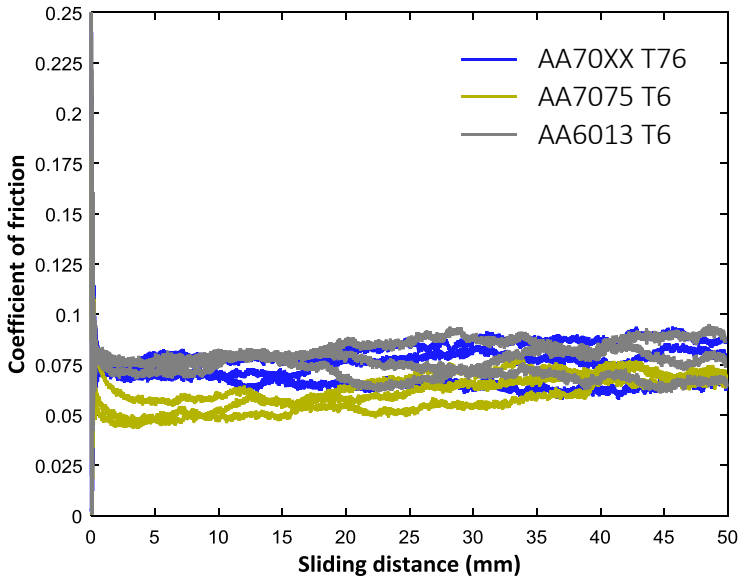

Figure 43: COF over sliding distance with Fuchs for different alloys

For quantitative comparison, the average COF for thee repeats is computed as outlined in the methodology in Section 3.3 and is recorded in Table 21 together with the standard deviation.

Table 21: Average COF for studied aluminum alloys

Alloy	Average COF	Standard deviation
AA6013 T6	0.077	0.004
AA7075 T6	0.061	0.005
AA70XX T76	0.075	0.008

Interestingly, AA7075 T6 records a lower COF up to a sliding distance of about 30 mm while the COF values for AA70XX T76 and AA6013 T6 are similar. In view of the strength levels of these three alloys, one would have expected AA7075 T6 and AA70XX T76 to report comparable results since AA6013 T6 exhibits lower strength. The chemical composition and hence influence on the affinity to chemical reaction with the sliding partner was also considered since 7xxx-series alloys contain more zinc whereas 6xxx-series exhibit a higher weight percent of silicon and magnesium. However, again, as AA6013 T6 and AA70XX T76 report a similar COF, this reason did not serve as plausible explanation for the observation. Taking surface roughness measurements on the initial sheet condition revealed a

smoother surface for AA7075 T6 (Ra 0.23 µm) whereas an average Ra value of 0.88 µm and 0.93 µm is recorded for AA70XX T76 and AA6013 T6, respectively. The positive effect of smoother surfaces on the COF was confirmed by Schey [123] who investigated the effect of surface roughness on the friction response in the TCT .

3.6 Comparison of Lubricant Performance

This section presents a comparison of the four lubricants (Fuchs, OKS, PTFE Spray, and Teflon film) tested under room temperature and elevated temperature (230°C) conditions. Considering that Fuchs is already being applied in industry to form aluminum alloys, it was adopted as a baseline to that the performance of other lubricants was compared.

3.6.1 Friction Results at Room Temperature and 170°C

The performance of the Fuchs lubricant is first compared to an unlubricated condition in Figure 44. At room temperature (Figure 44a), testing without lubricant (orange curves) resulted in a moderate initial COF of about 0.16 followed by a gradual increase to a steady coefficient of approximately 0.38 after roughly 18 mm sliding distance. While the initial COF at 170°C (see Figure 44b) is comparable to the values at room temperature, the increase to its steady state value occurs at a much faster rate, after 6 mm of sliding. Surprisingly, the absolute value of the constant COF is very similar to what is observed at room temperature even though higher friction was expected at elevated temperature.

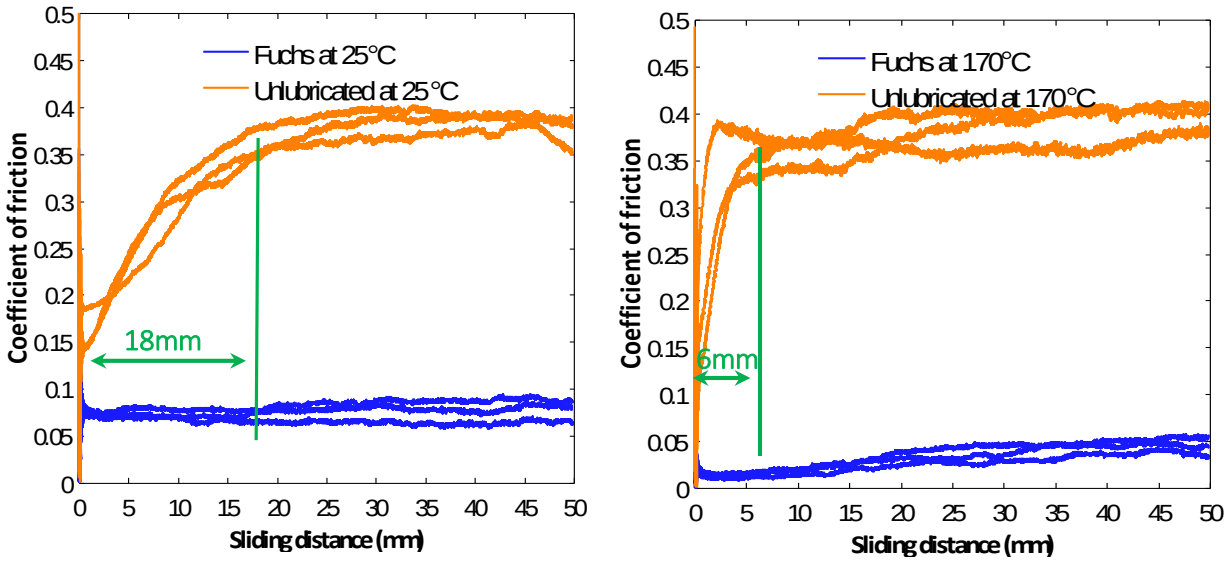

a) At 25 °C

b) At 170 °C

Figure 44: COF over the sliding distance for AA70XX T76 in unlubricated condition (orange) and utilizing Fuchs (blue)

Inspection of the sheet specimen after testing at room temperature is recorded in Figure 45 and serves as possible explanation for comparable absolute COFs at room and elevated temperature for dry testing. A magnified section of the contact area revealed that localized regions were excluded from interaction with the cup surface and were less scored. It seems that due to the absence of a protective film separating the two sliding partners from each other, the asperities that were initially in contact formed junctions that were subsequently sheared off. Adhered particles separated contacting surfaces and limited the frictional interaction to only localized spots. The same mechanism is expected at 170°C, however, considering the thermal softening of aluminum at elevated temperature, the earlier increase in the COF could be explained through earlier onset of junction formation. Sheet and test cup condition after testing were unacceptable in view of surface quality and tool wear. The effectiveness of the lubricant Fuchs was highlighted by a five-fold and nine-fold decrease in the steady-state COF at 25°C and 170°C, respectively, compared to unlubricated condition.

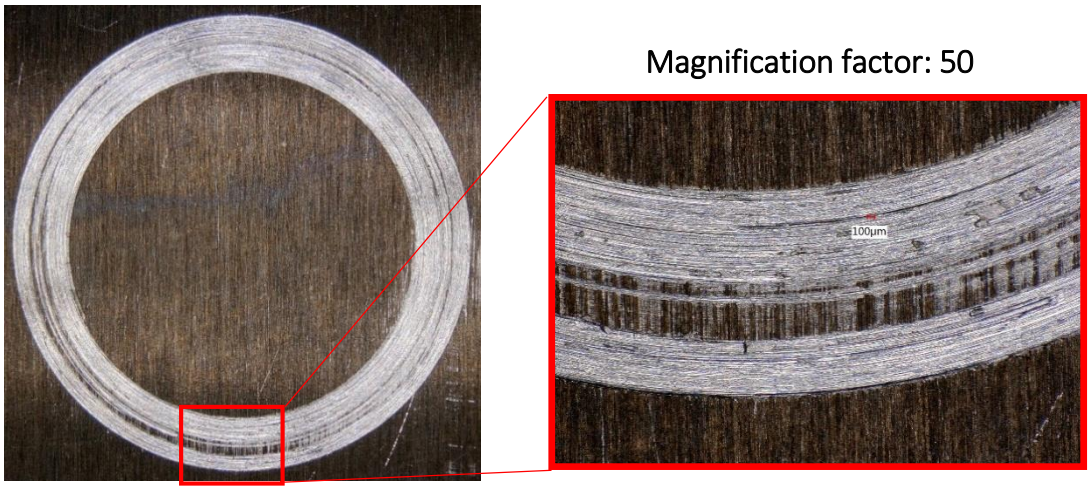

Figure 45: Visual inspection of the AA70XX T76 sheet specimen after testing at room temperature under dry condition

Figure 46 serves to compare the performance of the OKS (pink curves) and Fuchs (blue curves). At room temperature (Figure 46a), at the onset of sliding, both lubricants exhibited an initial COF of about 0.08 followed by a stable response for the first 22 mm sliding distance in that OKS slightly outperformed Fuchs. During further sliding, however, the OKS exhibited an increasing COF whereas the Fuchs was more stable. At 170°C (Figure 46b), both lubricants recorded enhanced performance and experienced a drop in the initial COF to roughly 0.025, followed by a steady increase over the sliding distance that was more pronounced for the OKS. The presence of lubricant additives in both Fuchs and OKS explained the improved effectiveness at elevated temperature. Unfortunately, no details on the exact additives are available since they are considered proprietary. Even though both lubricants were capable of maintaining their lubricant film over the whole sliding distance and therefore successfully prevented scored surfaces, the more pronounced increase for the OKS suggested either partial consumption of the protective layer or a delay in the reformation of the separating layer once asperity contact caused interruption.

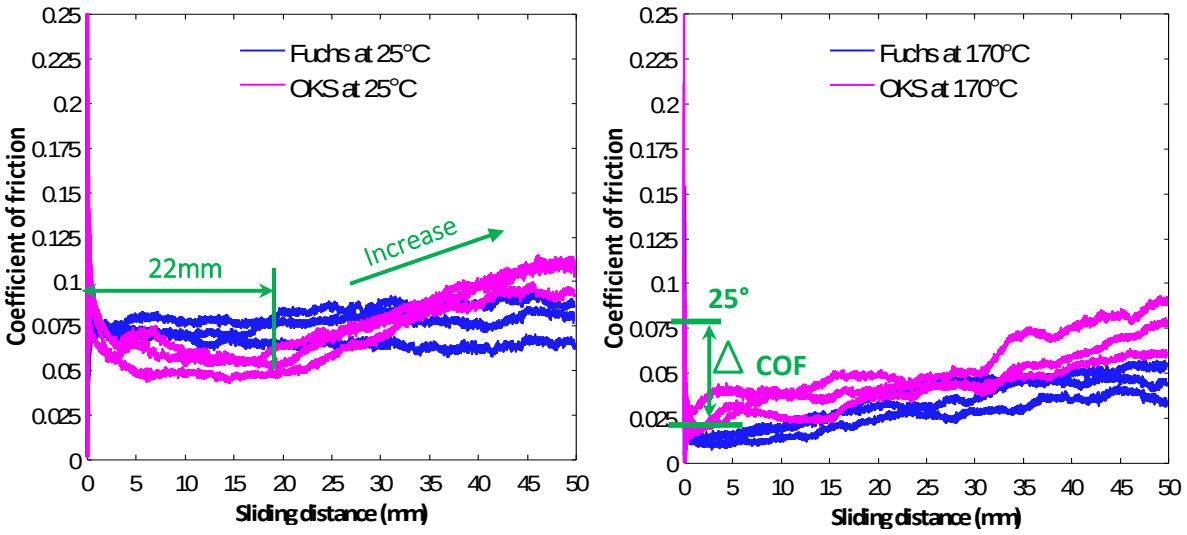

a) At 25 °C

b) At 170 °C

Figure 46: COF over the sliding distance for AA70XX T76 with OKS (pink) and Fuchs (blue)

A summary of the COF over the sliding distance obtained with the PTFE Spray (highlighted in turquois) is given in Figure 47. When looking at room temperature results in Figure 47a, PTFE Spray clearly outperformed Fuchs for shorter sliding distances. The COF evolution for longer sliding distances varied from slightly to moderately increasing curves. In the latter case, scratches were detected on the tested specimen whereas in other instances no sign of galling was visible. The occasionally poor repeatability between tests could be explained through the application method. Spraying the lubricant onto the sheet specimen gave only limited control over the lubricant amount. Compared to room temperature testing, enhanced lubricant performance was recorded for PTFE Spray at 170°C. While the COF up to 20 mm sliding distance was comparable to Fuchs, for longer sliding distances the PTFE Spray was characterized through a severe increase in the COF that was reflected on the sheet specimen as illustrated in Figure 48.

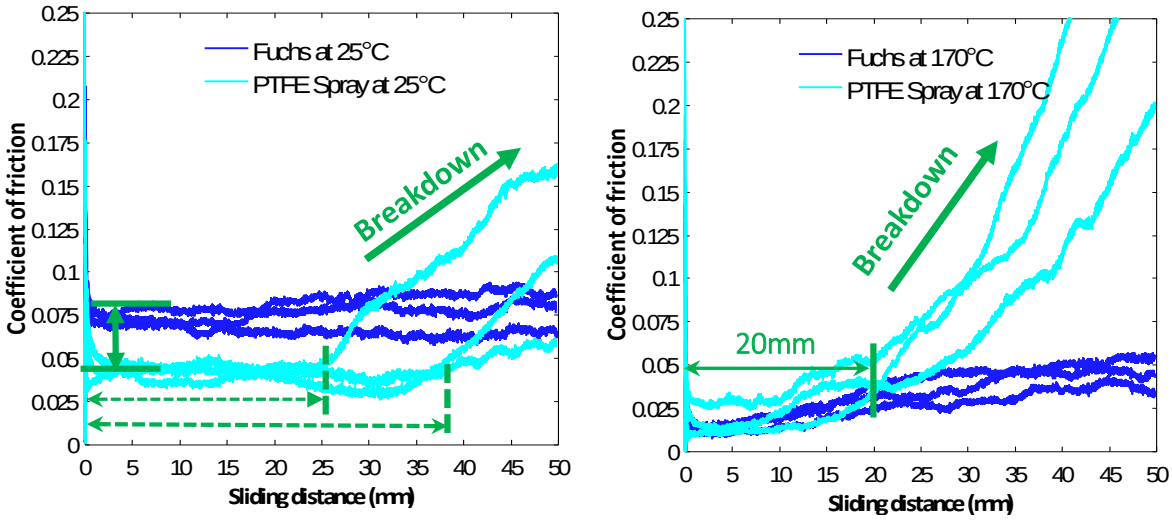

a) At 25 °C

b) At 170 °C

Figure 47: COF over the sliding distance for AA70XX T76with PTFE Spray (turquois) and Fuchs (blue)

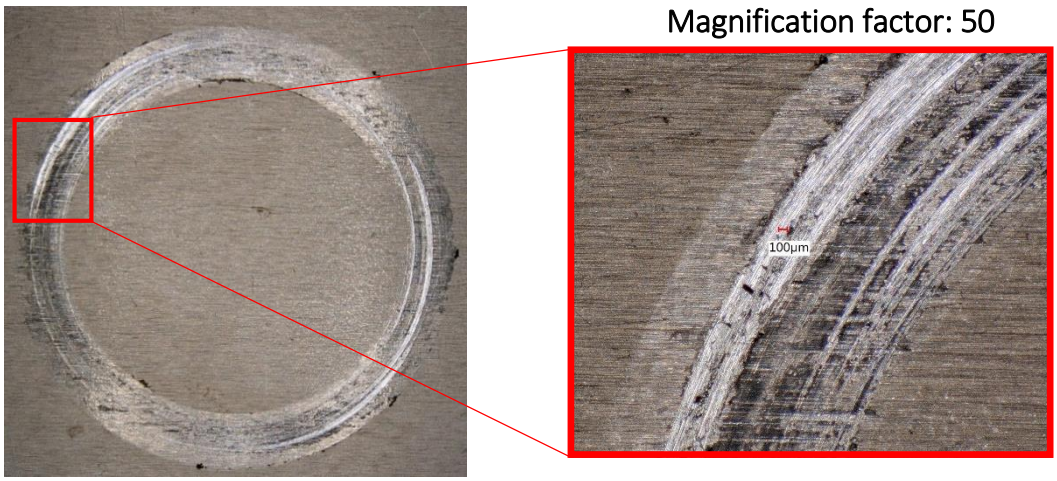

Figure 48: Visual inspection of the AA70XX T76 sheet specimen after testing at 170°C using PTFE Spray

Figure 49 presents the COF over the sliding distance for Teflon film, highlighted in red, and Fuchs in blue color. At room temperature (Figure 49a), the Teflon film exhibited a COF that is approximately one-half of the value for Fuchs.

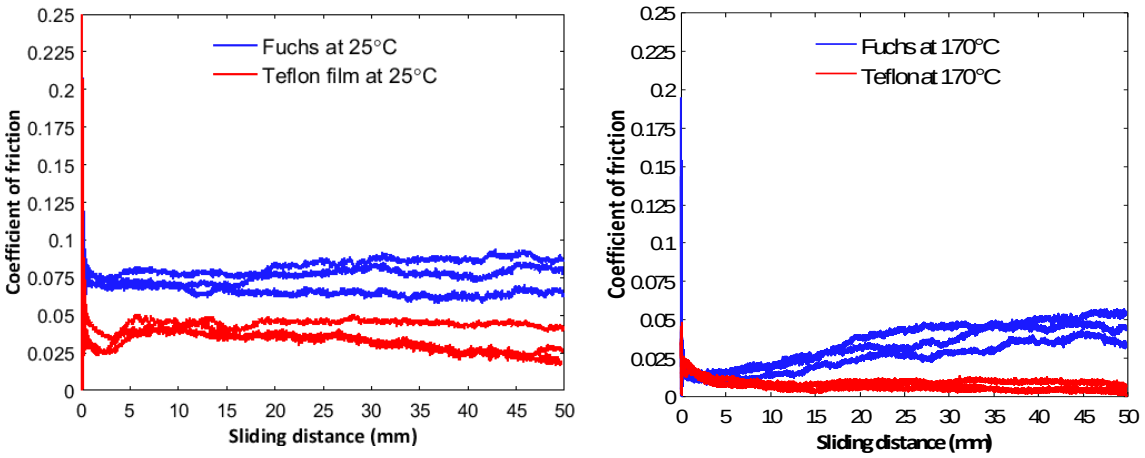

a) At 25 °C

b) At 170 °C

Figure 49: COF over the sliding distance for AA70XX T76 with Teflon film (red) and Fuchs (blue)

The average computed COF of 0.037 compared well with the reference value of 0.03 from Figure 50 for sliding speeds below 10 mm/s and an interface pressure between 2.8 MPa-24.8 MPa [119]. Figure 49b demonstrates the superior performance of Teflon film over Fuchs at 170°C. An extremely low COF of below 0.01 was recorded over the whole sliding distance.

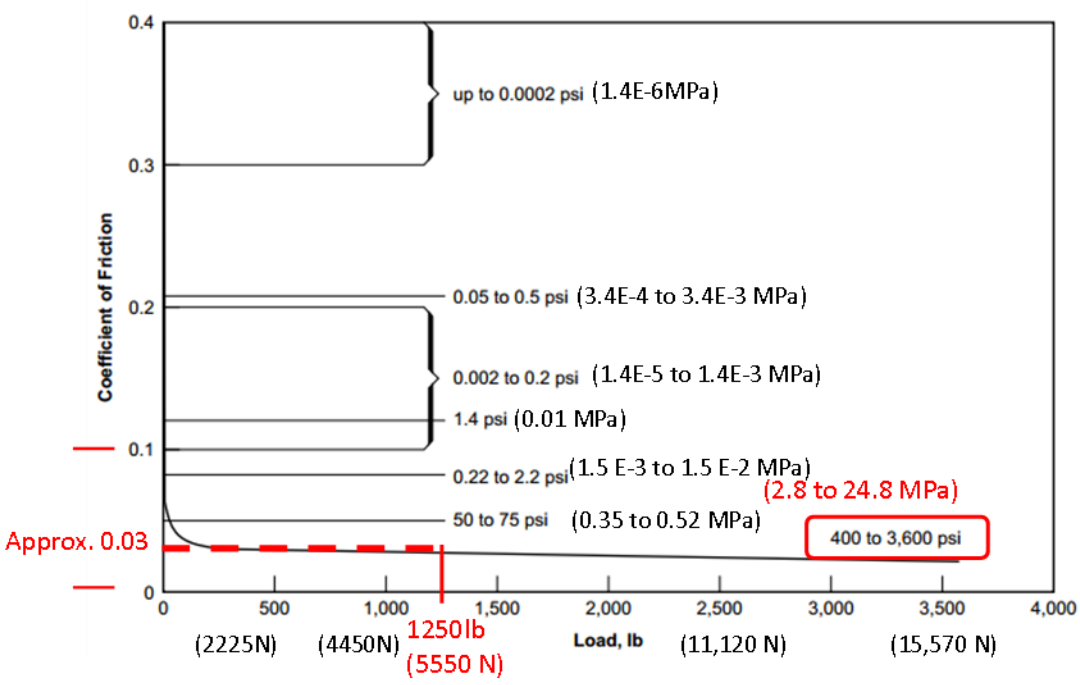

Figure 50: Specified COF for Teflon film [119] (Note that units are from original source).

In an attempt to understand this observation, it is important to recall the different lubricant regimes outlined in Section 1.3.2. Considering the 0.1 mm thickness of the Teflon film, complete separation of contacting surfaces was ensured that implied operation in the hydrodynamic lubricant regime. Surface inspection of the sheet specimen after testing confirmed this assumption. While the test cup imprint was pressed into the Teflon film, after peeling the layer off, the sheet specimen showed good surface quality with no scratches or signs of asperity interaction (see Figure 51). This observation was made for both testing temperatures.

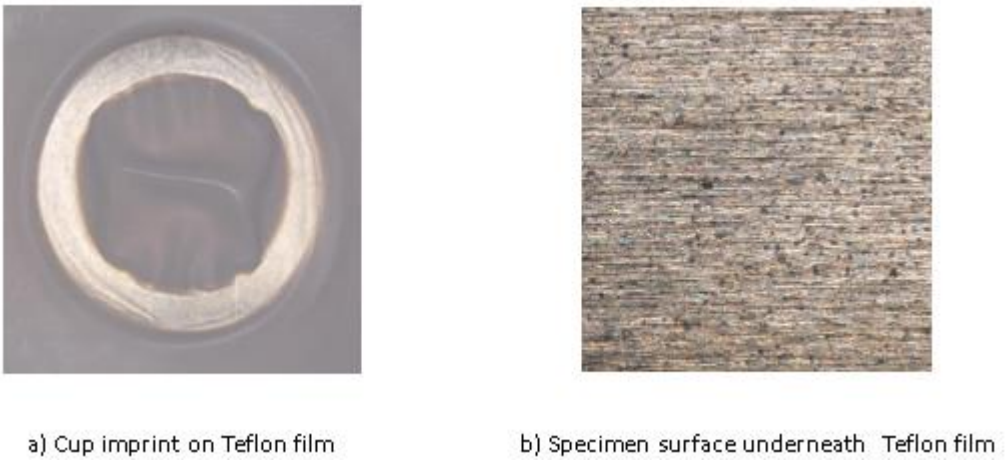

Figure 51: Visual inspection of AA70XX T76 sheet specimen after testing with Teflon film at 170°C

In the hydrodynamic lubricant regime, friction is a function of the lubricant shear stress that is strongly dependent on temperature. Figure 52 shows this behavior for Teflon film that experiences a 50% reduction in the shear stress from room temperature to 100°C. This lubricant property underlines the significant drop in the COF for Teflon film at 170°C. Additionally, it might also serve as explanation for the decreasing COF towards the end of the 50 mm sliding distance recorded for room temperature testing in Figure 49a. Frictional heating induced through ongoing sliding causes the temperature to rise that could alter the lubricant performance of the Teflon film.

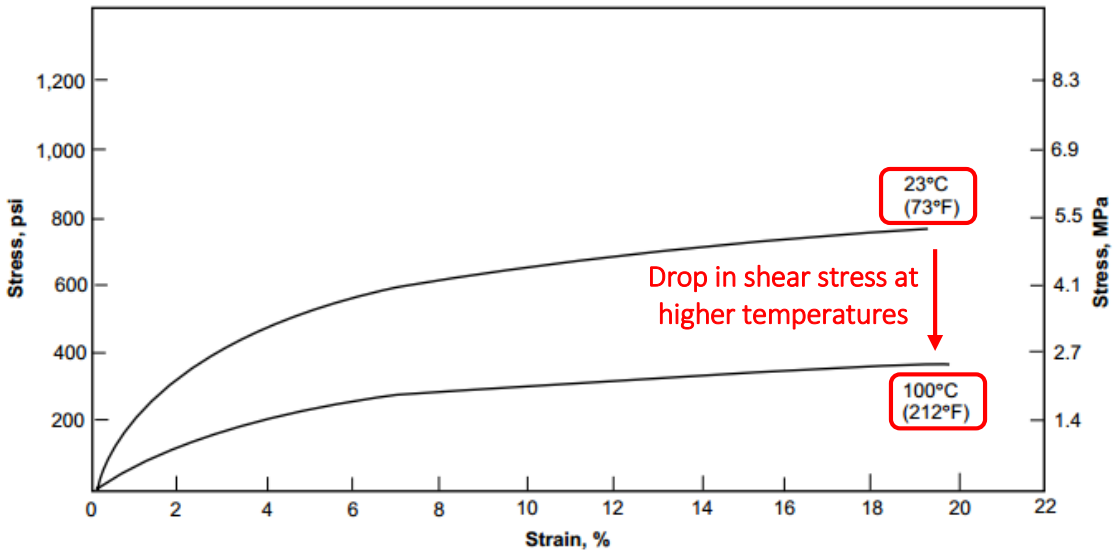

Figure 52: Shear stress of Teflon film as a function of temperature [119]

3.6.2 Friction Results at 200°C

Summarizing from test results at room temperature and 170°C, only the Fuchs and OKS lubricants were able to either maintain a protective lubricant film over the whole sliding distance and are of industrial interest in view of lubricant application. Consequently, subsequent elevated temperature TCT at 200°C were only performed for Fuchs and OKS. The results are illustrated in Figure 53.

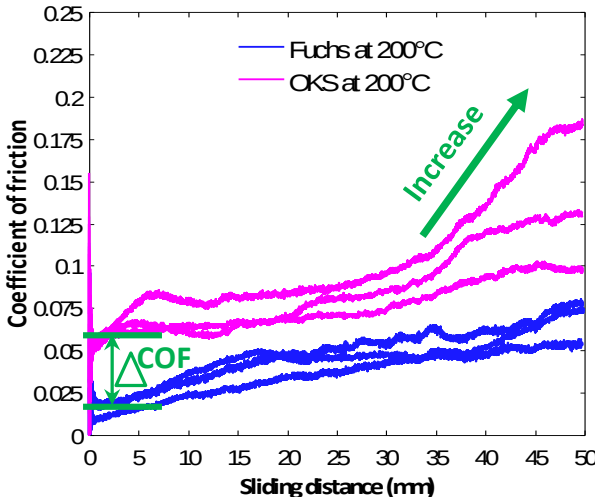

Figure 53: COF over the sliding distance for AA70XX T76 with OKS (pink) and Fuchs (blue) at 200°C

The COF for the Fuchs lubricant at 200°C, plotted as blue curves, showed a similar performance observed at 170°C with a slightly more pronounced increase in the COF over the sliding distance and no visual scratches on the sheet specimen. In contrast, the OKS data showed inferior performance compared to 170°C. While the initial COF of OKS was comparable to the initial COF recorded at 170°C, the COF evolution at 200°C was characterized through an initial short increase, followed by a constant plateau that terminated with a moderate to strong increase. Compared to Fuchs, OKS consistently recorded higher COFs. The higher magnification images, shown in Figure 54, from the surface of as-tested sheet specimens confirmed localized galling and the presence of accumulated metal particles.

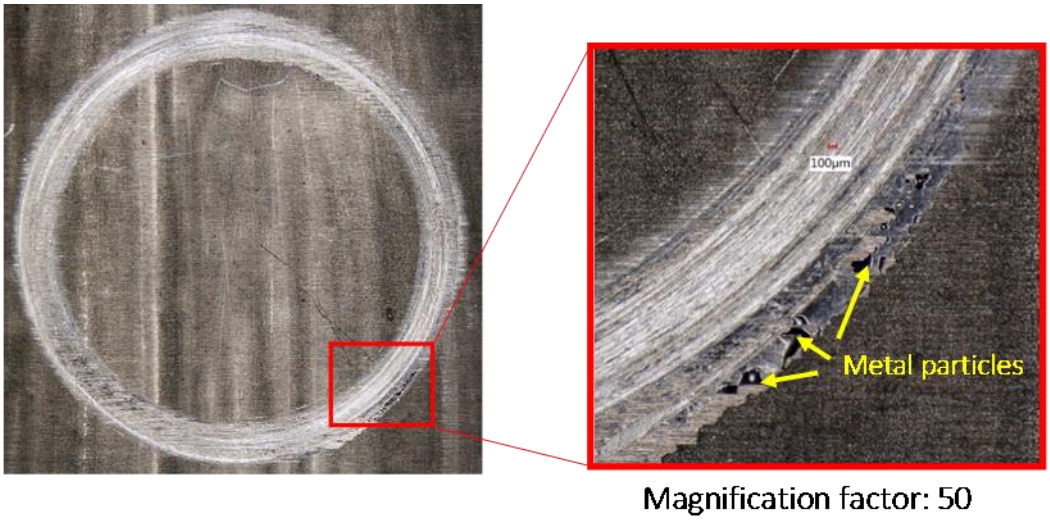

Figure 54: Visual inspection of the AA70XX T76 sheet specimen after testing with OKS at 200°C

3.6.3 Friction Results at 230°C

Initiation of galling at 200°C excluded the OKS from further warm friction testing. TCT was also performed with Fuchs at 230°C that represents the highest forming temperature in the rail forming process. From Figure 55, a decreasing performance was observed at 230°C, highlighted in yellow color. The curve started with a higher initial COF that was followed by instabilities after a sliding distance of about 22 mm. There are several possible mechanisms that might explain this observation, such as asperity interaction due to localized film breakdown or friction instabilities due to stick-slip. In some instances, scoring was observed on the tested sheet specimen as shown in Figure 56.

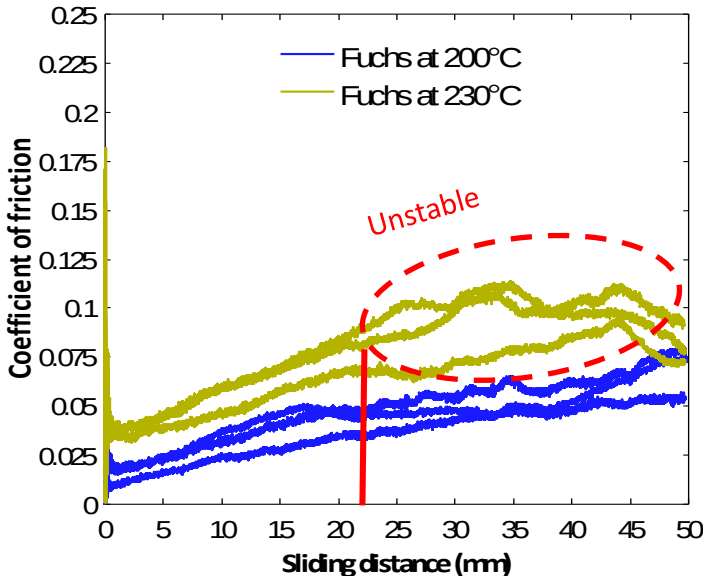

Figure 55: COF over the sliding distance for AA70XX T76 with Fuchs at 200°C (blue) and at 230°C (yellow)

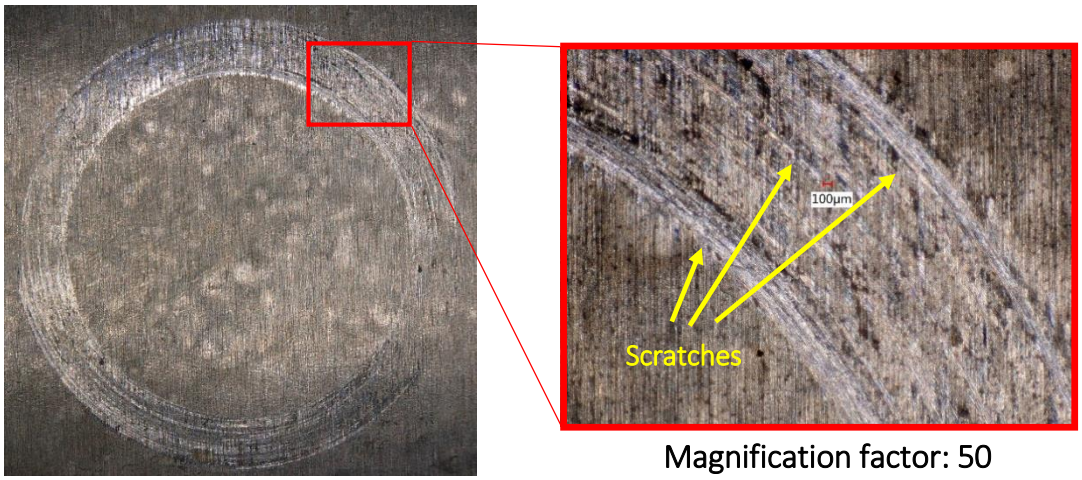

Figure 56: Visual inspection of the AA70XX T76 sheet specimen after testing with Fuchs at 230°C

3.7 Steady-state COF

While Section 3.6 focuses on lubricant performance over the sliding distance, for input into most commercial FEM solver, a steady-state COF is required. Following the methodology discussed in Section 3.3, a failure COF of 0.1 was employed in this study considering that the onset of galling for the Fuchs lubricant, when tested at 230°C in Figure 55, recorded peak COFs of about 0.1. Averaging

the COFs between running-in of the contact partners (onset of steady-state COF) and failure, yielded the steady-state COFs for studied lubricants at various temperatures in Figure 57. Note that plotted error bars correspond to the highest and lowest COF among three repeats for each condition. The COF for the unlubricated sliding is averaged over the whole sliding distance since the initial COF already exceeded the failure criterion of 0.1. These values and standard deviations are listed in Appendix A.

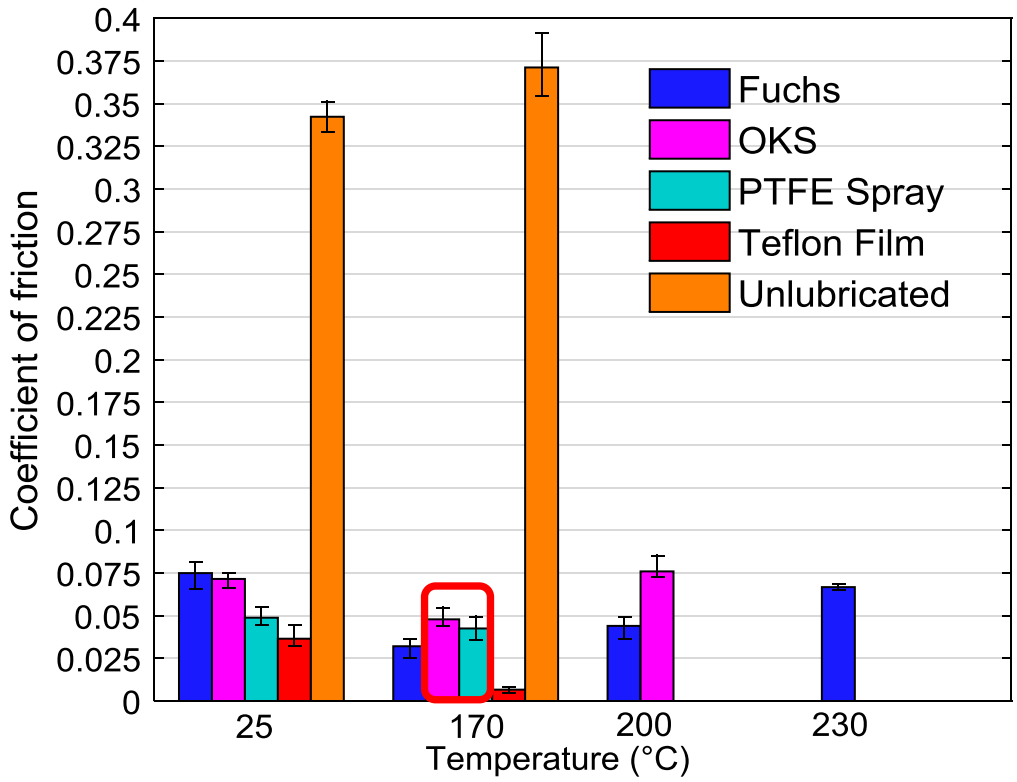

Figure 57: Steady-state COF as a function of temperature and lubricant; error bars correspond to upper and lower COF among three repeats

The error bars demonstrate the presence of some scatter for all lubricants. It would have been expected that the PTFE Spray (turquois bars) exhibits larger variations in view of limited control over applied lubricant amount. Following this theory, excellent repeatability would have been expected for Teflon film (red bars), that is not reflected in Figure 57 (at least not for room temperature results). From the complex nature of friction, discussed in Section 1.3.1, it is concluded that a combination of several parameters such as initial condition of sheet specimen and test cup contribute to the observed scatter in the steady-state COF.

Interestingly, from Figure 57, the COF of the OKS and PTFE Spray at 170°C, surrounded by the red box, predict a very similar lubricant performance that is not in agreement with the COF evolution over the sliding distance shown in Figure 58 and the breakdown distance plotted in Figure 59. While OKS could maintain an almost constant COF throughout sliding, PTFE Spray was characterized through breakdown, reflected in a sharp increase in slope in the last half of sliding. Under the assumption of a failure COF of 0.1, the PTFE Spray breaks down after approximately 34.5 mm sliding distance, whereas no lubricant failure was observed for the OKS over the whole 50 mm sliding distance. This in turn highlights the importance of looking at the complete friction evolution instead of relying on a single average value.

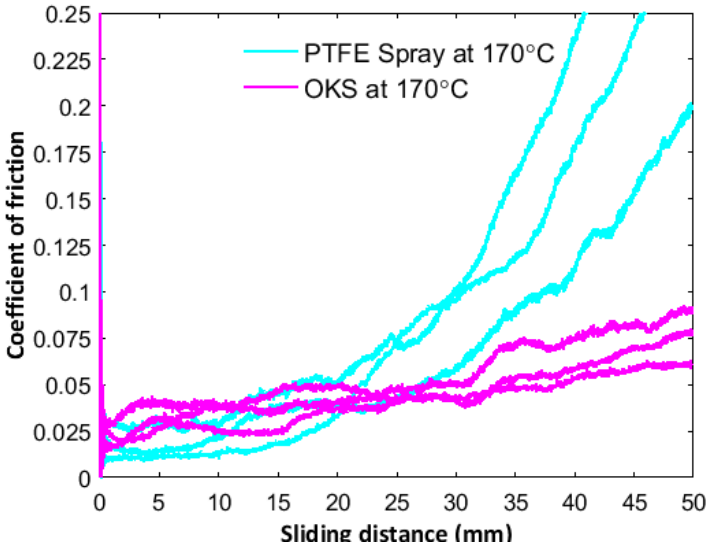

Figure 58: COF over the sliding distance for PTFE Spray (turquois) and OKS (pink) at 170°C

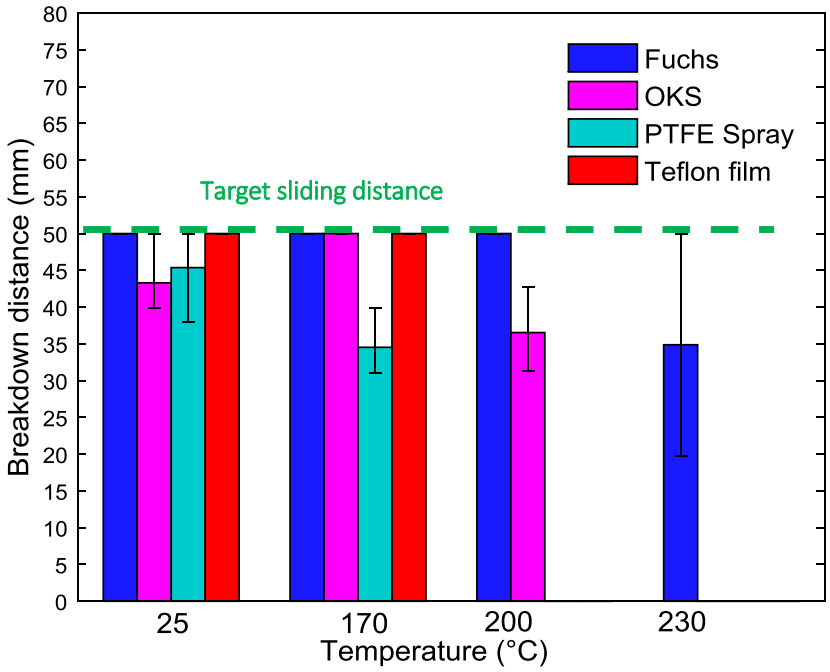

Figure 59: Lubricant breakdown distance for AA70XX T76 with different lubricants and at temperatures between 25°C and 230°C; a failure COF of 0.1 was utilized; error bars correspond to upper and lower breakdown distances among three repeats

Admittedly, the lubricant breakdown distance in Figure 59 presents large scatter bands between earliest and latest lubricant failure distance among three repeats. This observation might be attributed to the choice of a failure COF. Nevertheless, there is a clear trend of shorter lubricant breakdown distances as a function of temperature. The PTFE Spray broke down after roughly 45.4 mm at room temperature compared to 34.5 mm at 170°C. The same trend is recorded for the OKS with a threshold distance of 50 mm at 170°C and 36.5 mm at 200°C. The strong correlation between temperature and lubricant film breakdown was confirmed by Andreasen *et al.* [79] in a lubricant study with the strip reduction test (simulates ironing by forcing a reduction of the sheet thickness). They commented on the presence of large scatter bands that were reduced at higher temperature in view of breakdown following test start. It is worth noting that in the discussion in Section 3.6.1 was stated that no scratches were observed after testing with OKS at room temperature that contradicts the recorded threshold distance of 43.3 mm for OKS at 25°C (see Figure 59). This occurrence might indicate that adopting a failure COF for lubricant breakdown is to be debated.

3.8 Effect of Die Coating

The lubricant comparison over a temperature range from 25°C to 230°C revealed that among tested lubricants, Fuchs performed reasonably well at temperatures up to 200°C, but showed onset of scratches at 230°C at an interface pressure of 25 MPa, a sliding speed of 5 mm/s, and a sliding distance of 50 mm. Hence, the performance of the CrWN PVD-die coating Ionbond35, specifically for aluminum warm forming, was studied. For deposition of the Ionbond35 PVD die coating [120], ion nitriding was selected as a pre-treatment to balance the hardness gradient between test cup material (560 VH) and the die coating (3000 to 3200 VH). Initial tests on duplex-treated TCT cups revealed that the presence of a brittle white layer from ion nitriding caused the Ionbond35 [120] coating to buckle that was believed to impair the friction response as reported by Podgornik *et al.* [98]. Hence, in a second attempt, the coating was deposited as a single treatment.

The lubricant study revealed that, compared to the OKS and PTFE Spray, Fuchs is more effective in preventing galling. Since the Fuchs revealed no significant change in lubricant performance from 170°C to 200°C, the die coating was tested in an unlubricated condition and with Fuchs at room temperature, 170°C, and 230°C. Experiment parameters such as sliding speed (5 mm/s), interface pressure (25 MPa) and sliding distance (50 mm) corresponded to the settings for the lubricant comparison study in Section 3.6.

Results at room temperature

Figure 60 illustrates room temperature results for unlubricated testing in Figure 60a and with Fuchs in Figure 60b. For direct comparison, the COF over the sliding distance for the coated cup, plotted in black, is plotted together with results under the same testing conditions without coating, plotted in blue for the Fuchs and in orange for unlubricated condition. While there was no noticeable difference in the constant COF between coated and uncoated tests, an earlier increase in the COF was observed for the die coating. With Fuchs, the die coating exhibited a slightly higher COF compared to uncoated results in blue color.

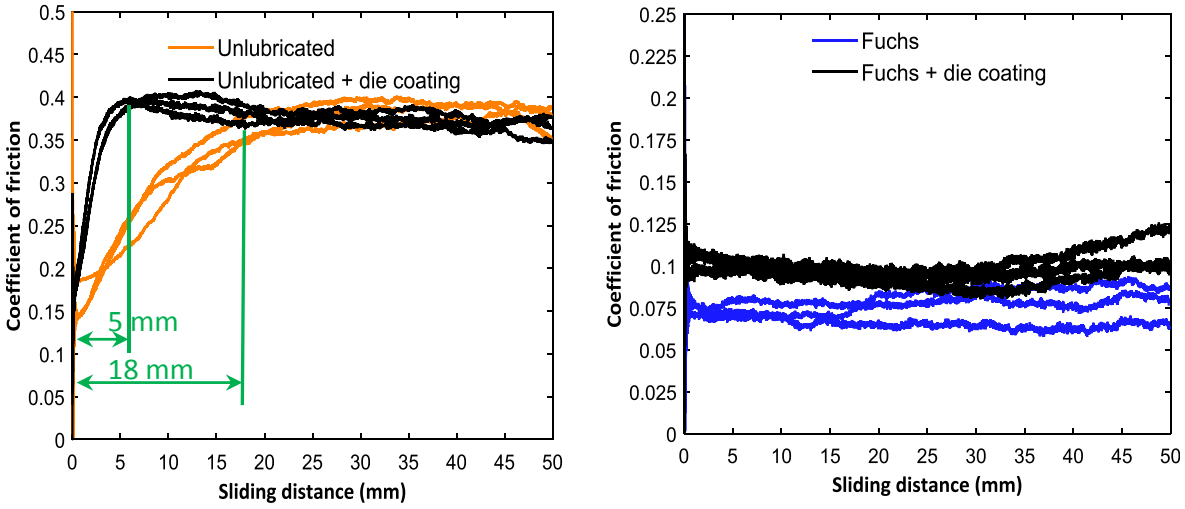

a) Unlubricated b) Fuchs

Figure 60: COF over sliding distance for different lubrication conditions with AA70XX T76 at 25°C

Results at 170°C

The trend of a higher COF or faster increase of the COF with coated cups was confirmed at 170°C. In both cases for unlubricated sliding in Figure 61a and with Fuchs in Figure 61b, the die coating exhibited a higher COF at the onset of sliding. This observation was particularly pronounced for dry testing when the peak COF reached values of about 0.6 followed by a sharp decrease to the steady COF comparable to what was found for uncoated testing. Also, the fact that the three repeats were almost coincident emphasized the reliability of the test findings. For dry forming at both temperatures, 25°C and 170°C, material transfer from aluminum to the test cup could not be prevented, as confirmed by visual inspection under the microscope in Figure 62.

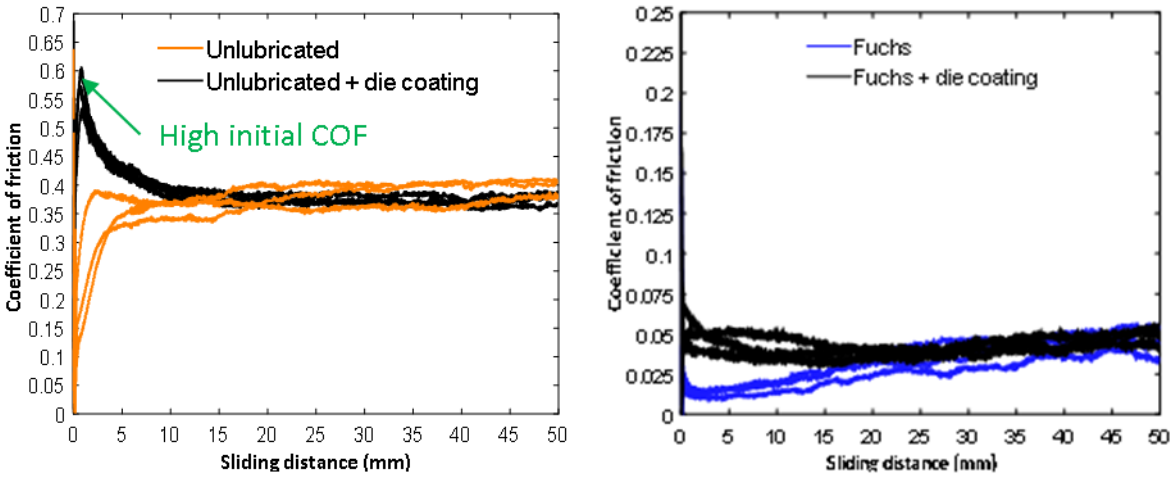

a) Unlubricated b) Fuchs

Figure 61: COF over sliding distance for AA70XX T76 under different lubrication conditions at 170°C

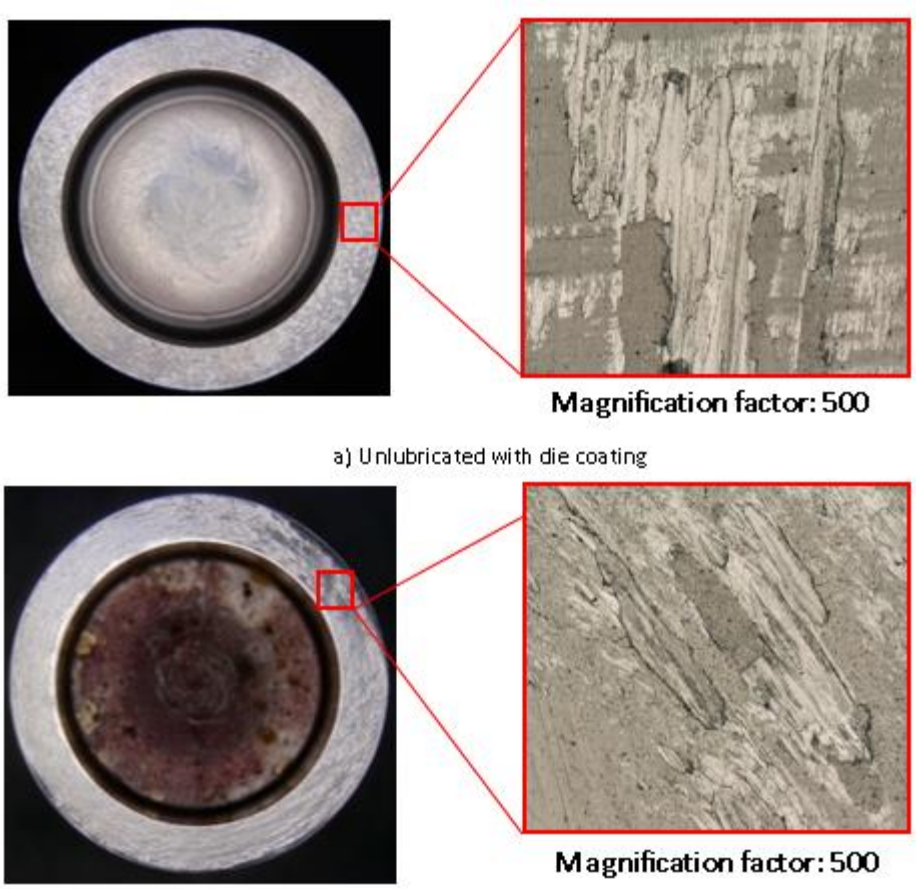

Figure 62: TCT cup surface after testing at 170°C under dry conditions

The observations made of the die coating performance at 25°C and 170°C were somewhat surprising, particularly the high initial COF at the onset of sliding. Surface roughness measurements were taken and confirmed a comparable Ra value of 0.13 µm for both the coated and uncoated cup that was specified to ensure similar testing conditions. Visual inspection under the microscope of the as-received cup, shown in Figure 63, revealed a different texture indicated by the red arrow. Note that this photo was created with the optimal microscope KEYENCE VHX 5000. The difference in surface texture might explain why the die coating initially experienced higher friction than the uncoated cups. After the sliding partners have run-in, the texture will have changed and other factors like surface hardness and material properties dominate the friction response. Nevertheless, considering that the coating is almost six times harder than the base material, less wear would have been expected on coated cups.

Magnification factor: 500

a) Uncoated test cup

Magnification factor: 500

b) Coated test cup

Figure 63: Surface texture of as received test cups

Results at 230°C

In view of mechanical limitations of the testing equipment, testing at 230°C was only performed using the Fuchs lubricant (dry tests were not performed at this temperature). Both the coated and uncoated conditions, plotted in Figure 64, exhibited an identical initial COF; however, the evolution over the sliding distance differed considerably. The uncoated condition exhibited a sharp increase in COF after only 5 mm of sliding and met the breakdown COF threshold of 0.1 after approximately 35 mm. In contrast, the coated condition remained quite stable with a relatively low COF over the entire sliding distance of 50 mm. As discussed, the Fuchs lubricant without die coating resulted in scratched specimen surfaces (Figure 56) that corresponds to the unstable friction curve shape in Figure 55. Signs of galling on the cup surface were confirmed by optical microscope in Figure 65a. In contrast, the Fuchs lubricant with die coating resulted in an almost constant COF over 50 mm sliding distance and the COF was approximately halved. At 230°C, the coated cup in combination with Fuchs could prevent die pick-up. The milky deposits on the cup test surface recorded in Figure 65b seemed to be wax particles accumulated from the Fuchs lubricant. These observations suggest that the die coating performance is strongly dependent on the service temperature.

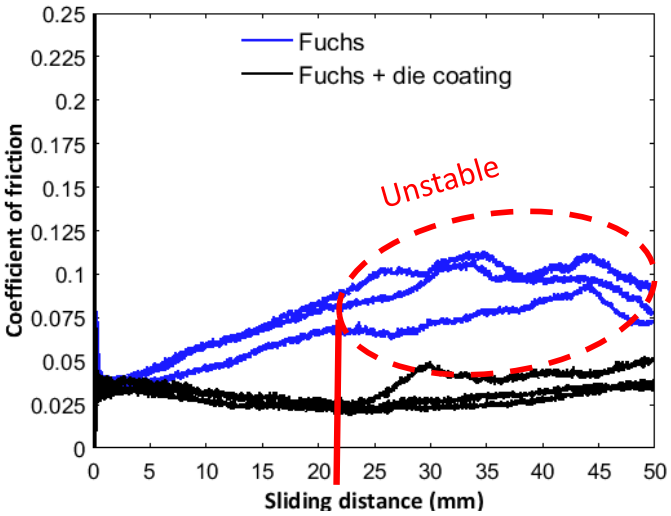

Figure 64: COF over sliding distance with Fuchs with (black) and without die coating (blue) at 230°C

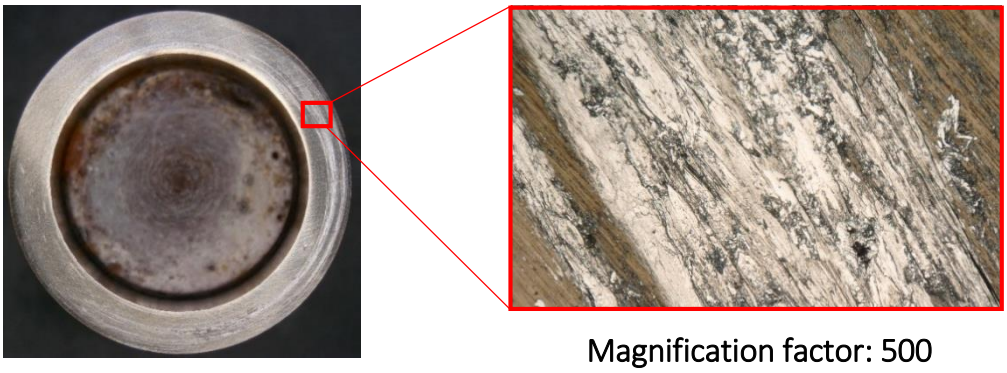

a) Fuchs without die coating

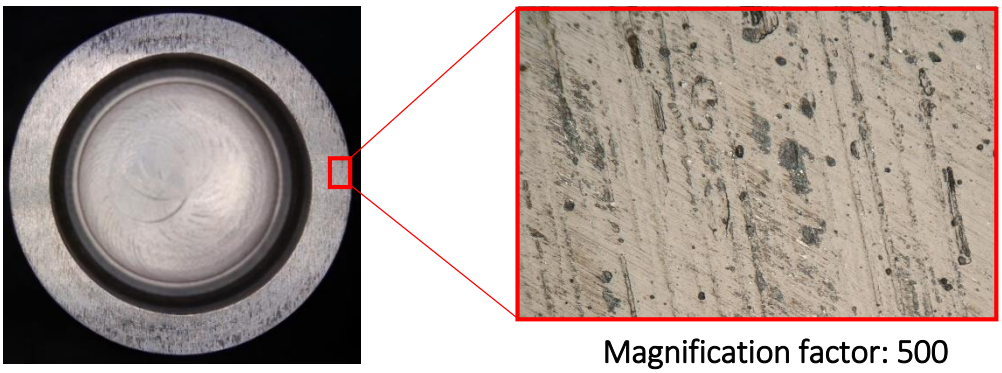

b) Fuchs with die coating

Figure 65: TCT cup surface after testing with Fuchs at 230°C

3.9 Summary of Friction Characterization

A modified TCT apparatus [114] was utilized to characterize the warm friction behavior of AA70XX T76, which refers to a 7xxx series aluminum alloy under development. Pre-tests were determined utilizing AA70XX T76 with Fuchs to determine a suitable sliding speed (5 mm/s) and interface pressure (25 MPa), where the latter was approximated through a FE simulation of the target forming process in Chapter 6. The sliding distance was set to 50 mm and corresponds to the rail sidewall.

Room temperature tests with Fuchs revealed slightly lower friction for AA7075 T6 compared to both AA70XX T76 and AA6013 T6 that showed a similar behavior. The lower surface roughness for AA7075 T76 was identified as possible reason for this observation. A study of four different lubricants (Fuchs, OKS, PTFE Spray, and Teflon film) revealed that Fuchs is the only lubricant that is of industrial interest in view of lubricant application method and could maintain its lubricant film over the complete sliding distance of 50 mm up to 200°C. Utilizing Fuchs at 230°C, onset of galling was observed on the tested sheet specimen that could be prevented if tested in combination with PVD coated (Ionbond35 [120]) test cups. Below a service temperature of 230°C and under unlubricated condition, the tested die coating has proven to neither prevent pick-up nor reduce the COF.

4 Deep Drawing

For the production of automobile vehicles, deep drawing is a key technology that produces components like the roof reinforcement, the engine bonnet, the mudguard, and the door inner part. During drawing, the material undergoes a complex strain history from shear in the cup edge, to plane strain in the sidewall, where it transitions into a plane strain state along the hat radius. Factors like the die entry and punch radius, blank size, forming speed, draw depth, and the binder load can decide over successful part forming or fracture. The binder load is a critical process parameter that controls the material flow; while a clamping load that is too high causes excessive stretching that might lead to part fracture, material flow that is little constrained results in undesired wrinkling in the final part. The material anisotropy is also reflected in the part, for example, instead of a perfectly circular cup, a high anisotropy can delay or facilitate the material draw-in in certain directions and form ears as discussed in Section 1.2.2.

Considering these observations, circular cup draws were felt to be well-suited for validation of the characterized material model in Chapter 2 and warm friction in Chapter 3. Isothermal deep draws were performed for AA6013 T6 and the developmental AA70XX T76 alloy. The experiments considered the same thermal conditions used in the TCT experiments. The lubricant performance was ranked based on visual inspection of the sheet surface, punch force, thickness change, flange draw-in length, flange perimeter, and strain distribution. For validation of the characterized material model, a numerical-experimental approach was selected; circular cups under non-isothermal conditions were deep-drawn since it yields larger strains that are well-suited for validation of the material anisotropy. These efforts were simulated for AA70XX T76 in a FE model that is discussed in Chapter 5.

The chapter opens with a description of the utilized test apparatus followed by an outline on the test scope. Steps for blank preparation, such as thermal validation and strain measurements, are covered in Section 4.3. Finally, results are presented for both isothermal and non-isothermal deep draws.

4.1 Equipment and Tooling for Deep Drawing

The utilized tool set for this study is illustrated in Figure 66 and composes a punch, binder, and die. The binder and die have flat surfaces (no draw beads) with the die having a 110.6 mm inner diameter

and a die entry radius of 12 mm. The cylindrical punch has a 12 mm radius in the punch nose and a 101.9 mm diameter that provides an effective clearance of 2.4 mm for the tested 2 mm-thick blanks. Hardened H13 tool steel is utilized for the tooling that is mounted to a die set and installed in a servo-hydraulic press. The die is kept stationary while the binder is load-controlled and the punch displacement-controlled. The punch force is measured by a load cell that is installed between the actuator and the respective tooling and the punch displacement is recorded by linear variable differential transformers (LVDT). The actuators are controlled by an MTS 407 controller that communicates with a Labview program. For elevated temperature testing, four 1000 W resistance cartridge heaters and two thermocouples are installed in both the die and binder mounting plate. The punch is equipped with six 450 W cartridge heaters and two thermocouples for temperature control. In order to prevent heating of the surrounding, ceramic isolation plates are used. The reliability of this press set-up and control system has been demonstrated by Boba *et al.* [13] who utilized thermal cameras to validate heat distribution in the blank for definition of forming limits on ZEK100.

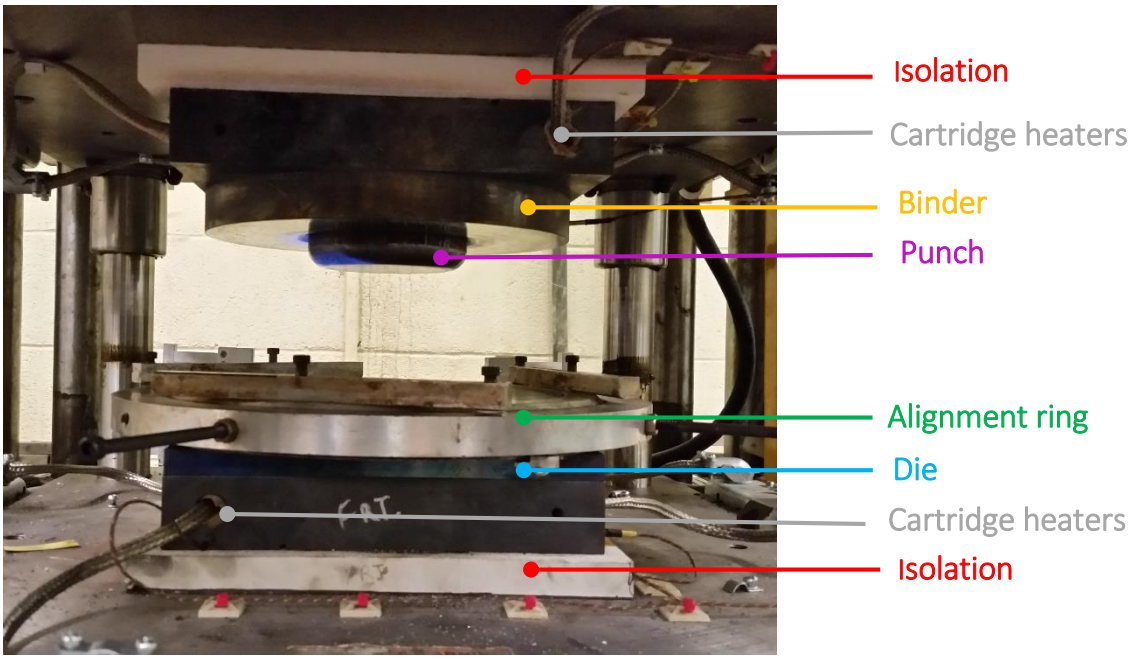

Figure 66: Experimental set-up of deep drawing test

With the aid of an alignment ring, the room temperature blank was centered relative to the punch and die. The binder closed, the clamping load was applied, and the punch was displaced to contact the

blank. Three minutes were allocated for the blank to reach the target temperature that was adopted from previous studies. Once the time limit was reached, the punch was displaced and formed the cup.

4.2 Deep Draw Test Parameters

Analogous to the thermal conditions in the TCT, isothermal deep draws at 170°C were performed for validation of warm friction characterization in Chapter 2. Circular cup draws were selected in view of their resemblance to a physical forming process.

In a similar fashion outlined by Kim *et al.* [77], [84], two series of experiments, recorded in Table 22, were performed. In the first series, deep drawing of AA6013 T6 203.2 mm (8 in) diameter blanks, corresponding to a drawing ratio of 2.0, were performed at a binder load of 70 kN. The second series considered drawing of AA70XX T76 circular cups at a binder load of 80 kN, that representd more severe tribological conditions due to the higher strength of the AA70XX alloy. The binder loads correspond to an initial interface pressure of about 3.9 MPa and 4.4 MPa and a peak value of approximately 16.8 MPa and 19.2 MPa at the end of the forming process for AA6013 T76 and AA70XX T76, respectively. Parameters like binder load and blank diameter were determined in FE simulations and pre-trials to prevent premature fracture (if the binder load is too high) and wrinkling (if the binder load is too low). The punch ram speed was set to a value of 1 mm/s that was adopted from the ISO12004-2 standard for creating forming limit diagrams with a hemispherical or cylindrical punch.

Table 22: Test matrix for isothermal deep drawing for friction validation

	Lubricant			
Alloy	Fuchs	OKS	Teflon film	PTFE Spray
AA6013 T6	3 repeats	3 repeats	3 repeats	3 repeats
AA70XX T76	3 repeats	3 repeats	3 repeats	3 repeats

Kim *et al.* [84] identified blank surface roughness, thickness measurements, punch force, flange draw-in length, and perimeter as important parameters for lubricant ranking. These parameters were utilized for the following friction study as well except for surface roughness since visual inspection of the sidewalls was felt to be more decisive than roughness values that are usually associated with large scatter bands. Additionally, the strain distribution along the cup profile was measured using optical strain measurement techniques (Argus).

Note that the selected draw depth of 55 mm, in this study, did not produce fully-drawn cups but left a flange of approximately 20 mm width. The remaining flange aided to extract the formed part and also enabled use of a scanner to capture the flange perimeter and draw-in as a function of sheet orientation. Additionally, since in this study the distance between the die, blank, and die was controlled through the clamping load instead of shims (called spacers) between the die and the binder, the flange section would undergo severe thinning towards the end of the drawing process due to decreasing contact area under constant binder load.

After deburring and cleaning of the machined blanks, the lubricant was applied on both sides since sliding occured between the binder, blank, and die. While lubricant weight could not be captured for the PTFE Spray, the Fuchs weight was approximately 0.08 g and the weight of OKS applied to the blank surface was 0.13 g. Note that the tooling was cleaned prior to every forming trial with 2400 grit sandpaper and water.

For validation of the characterized material model, non-isothermal circular cup draws were formed. As discussed in the literature review in Section 1.1.2, forming over a temperature gradient allows drawing of larger blanks (here 228.6 mm diameter (9 in)), that was well-suited for this study to evaluate the presence of earing in view of larger plastic strains. The punch ram speed was set to 1 mm/s and a clamping load of 70 kN, 80 kN, and 100 kN was found suitable for AA6013 T6, AA7075 T6 and AA70XX T76, respectively. A cup depth of 75 mm (with a 20 mm wide flange) was targeted for that pre-tests were performed to determine tooling temperature that facilitates forming without fracture. As summarized in Table 23 three repeats per alloy were formed with the Fuchs lubricant and one repeat with the Teflon film to study the effect of lubricant choice on the earing profile.

Table 23: Test matrix for non-isothermal deep drawing to evaluate the material model

	Lubricant	
Alloy	Fuchs	Teflon film
AA6013 T6	3 repeats	1 repeat
AA7075 T6	3 repeats	1 repeat
AA70XX T76	3 repeats	1 repeat

4.3 Blank Preparation for Deep Drawing

This section opens with a discussion of strain measurements on formed cups that served to distinguish between lubricant performances in isothermal deep draws and to assess FE model predictions of non-isothermal deep draws for characterization of the material anisotropy. The section closes with thickness measurements and blank preparation for recording the thermal history during forming.

4.3.1 Strain Distribution

Grid marking is a common and simple way for strain analysis in sheet metal forming. Small circles or square grids are etched onto the sheet specimen and deform with the blank. Automated or manual measurement of the deformed grid allows calculation of the major and minor strains. Whether the grid pattern is permanently deposited to the sheet specimen such as electrochemical etching or only temporary painted is dependent on process conditions such as friction and lubrication, and extent of surface strains, for example [124].

In view of lubricant application on both blank sides and limited accessibility for cameras during forming, conventional DIC technique was not applicable to this study. Instead, the GOM optical measurement system, ARGUS, for 3D strain and forming analysis was utilized. For electrochemical etching of blanks and subsequent post-processing, Natural Resources Canada – CanmetMATERIALS – kindly provided the equipment and personnel for performing these measurements.

The methodology for etching is outlined in Figure 67 and comprises a stencil (grid pattern template), a felt pad soaked in etching solution (LNC-5 by the company LECTROTECH CO.), and a power supply that is attached to an electrode wheel. In this study, 1 mm diameter dots in a constant distance of 2.5 mm were etched onto the sheet prior to forming through the following procedure [124]:

(i) Position stencil on cleaned blank surface

(ii) Place felt pad, soaked in etching solution, on stencil

(iii) After applying the voltage, reciprocate electrode wheel on felt pad

Since the etching solution and the current can pass the stencil only through the grid pattern, the template is etched onto the sheet surface. After etching, a neutralizing solution was utilized to clean

blanks. The etched grid pattern does neither cause distortion nor stress concentration in the sheet metal. [124].

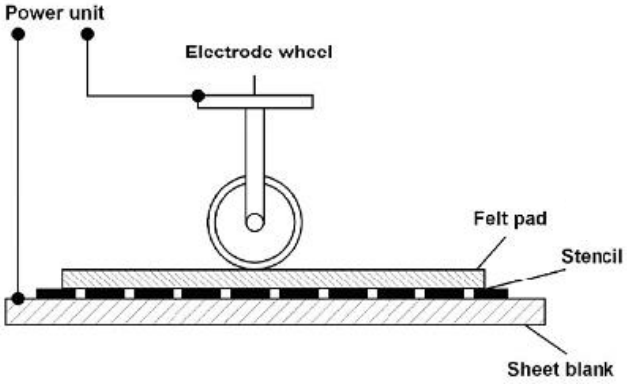

Figure 67: Methodology of electrochemical etching for strain measurements [124]

After forming, the part was positioned on the calibration table and photos at different angles were taken and imported into the software. From calibration cubes (labelled in Figure 68), the software detects camera position and angle from that the photo is taken and calculates strain distribution based on displacement of the initial equally-spaced dots. It is worth noting that, in contrast to the DIC, the optical strain measurement with Argus does not provide a strain history and instead provides the final strain state in the part. In deep drawing, the cup hat, for example, undergoes a proportional strain path whereas the sidewall experiences bending, unbending, and uniaxial stretching of that only the latter, the final strain state, is captured by Argus.

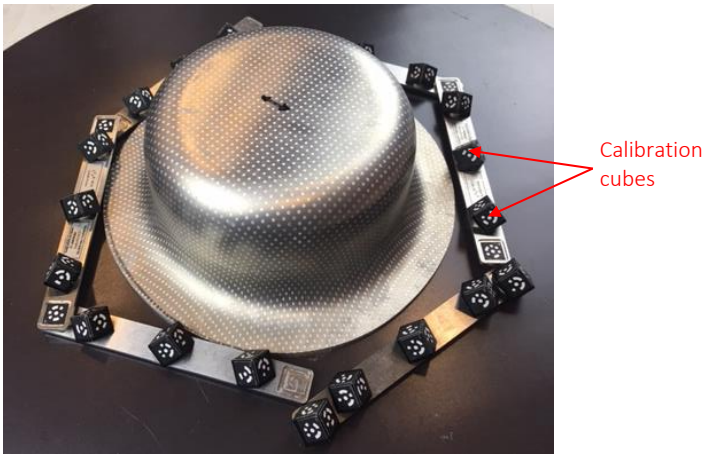

Figure 68: Post-processing of strain measurements

4.3.2 Thickness Measurements in Deep Drawing

The change in thickness on drawn cups was utilized for the lubricant study on isothermal deep draws to rank tested lubricant performances. Before forming, thickness measurements at four different positions of the blank were taken with the StressTel ultrasonic thickness measurement device and a 5 mm probe diameter. An average value was calculated and represents the blank thickness to that measurements after forming along the cup contour at positions outlined in Figure 69 and in 45° increments in radial direction were compared.

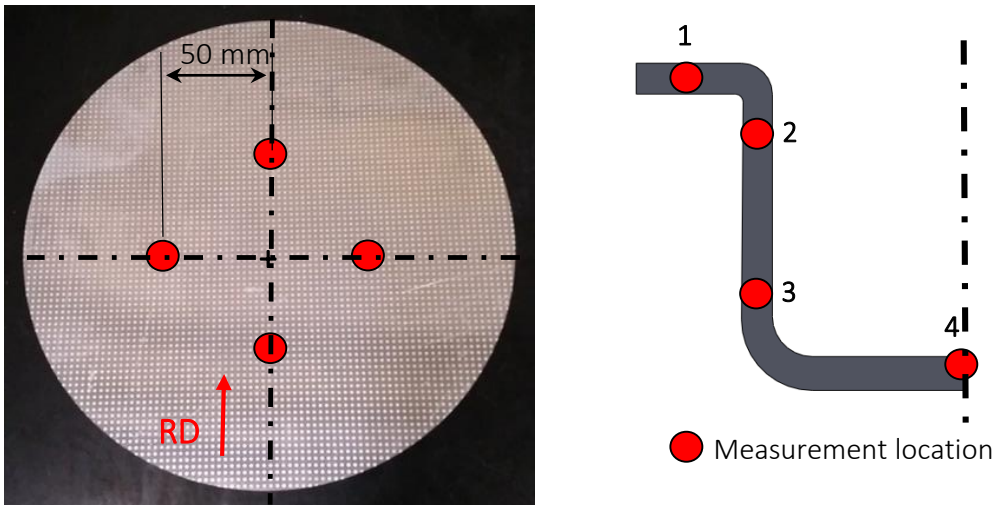

a) Before forming b) After forming

Figure 69: Thickness measurement locations on disk and drawn cup

4.3.3 Thermal History in Deep Drawing

For material model evaluation in addition to drawing non-isothermal circular cup draws, a FE model was developed that utilizes the calibrated yield surface by Abedini [18] and the proposed thermo-viscous hardening model discussed in Chapter 2. Thermal conditions are critical parameters in a forming process, particularly under non-isothermal conditions, since they greatly influence the material flow stress. Hence, accurate experimental data for validation of the simulation model is vital. For this purpose, a high-temperature resistant tape was utilized to attach thermocouples to the blank as pictured in Figure 70. The positions of these three thermocouples corresponds to the as-formed cup flange, sidewall, and center. Note that this temperature evaluation was performed for AA7075 T6 and assumed to be applicable to AA70XX T76 considering their similar thermal material properties.

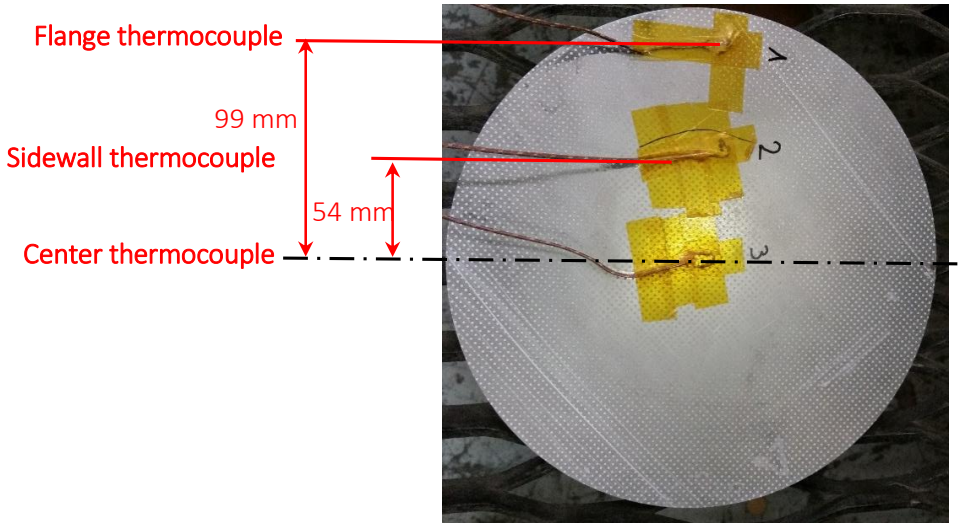

Figure 70: Thermocouple positions on AA7075 T76 deep drawing disk

4.4 Image Processing for Draw-in Length and Perimeter

For the study on isothermal deep draws, the perimeter and the draw-in length were utilized to distinguish between the performances of different lubricants. A more effective lubricant, for example, represents less resistance to sliding, hence enhanced material flow yields a smaller flange perimeter and an increased draw-in length. For non-isothermal deep draws that serve as evaluation of the characterized anisotropic material model, the draw-in length as a function of sheet orientation is required to quantify the earing profile.

The observed earing profile that was particularly pronounced for AA70XX T76, due to the anisotropic material characteristics, gave reason for concern that manual measurements of perimeter and draw-in length might not be sufficiently accurate. Therefore, flange profiles were scanned using a flatbed scanner and digital image processing tools in MATLAB were utilized. For post-processing purposes, two jigs were utilized to align the flanges relative to the material RD during scanning.

A custom MATLAB script was written that imports the scanned flange profiles and converts them into binary files. The distance between data points served to calculate the perimeter of the as-formed cup flange. For the draw-in length, a reference line in the RD is created and an algorithm employed that finds the closest common y-data point for the closest common x-value within a tolerance of 0.2 mm. Figure 71b shows the cup contours detected by the script. Manual measurements of the draw-in length (51 mm) on one cup showed very good agreement with the values predicted by the script (51.2 mm).

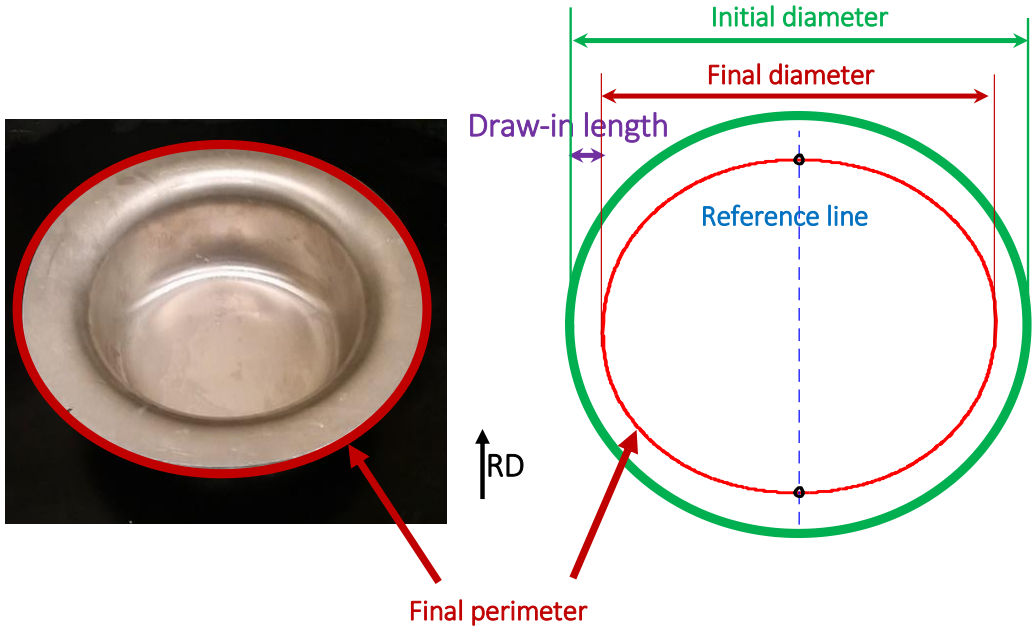

a) Formed part with flange

b) Post-processed contours

Figure 71: Image processing in MATLAB to compute draw-in length and perimeter; illustrated is an AA6013 T6 cup isothermally formed at 170°C utilizing Teflon film; initial blank diameter corresponded to 203.2 mm

4.5 Isothermal Deep Drawing Results

The purpose of these tests was to examine correlations between the lubricant ranking obtained in the TCT as a laboratory test and deep drawing as a process test that better resembles a physical forming process. In accordance with thermal conditions utilized for the lubricant study in the TCT, circular cups were drawn under isothermal conditions at 170°C with the Fuchs, OKS, PTFE Spray, and Teflon film. For post-processing purposes (measurement of draw-in length and perimeter), AA6013 T6 and AA70XX T76 (a 7xxx series aluminum alloy under development) blanks were drawn to a target depth of 55 mm resulting in a 20 mm cup flange. Considering an initial blank diameter of 203.2 mm, the drawing ratio corresponded to 2.0. The lubricant ranking parameters surface quality, forming force, flange perimeter, draw-in length, change in thickness, and strain distribution are discussed.

4.5.1 Surface Quality

Figure 72 shows sidewall sections of circular cups drawn with different lubricants. Note that the surfaces were cleaned after forming to examine the blank surface on scratches. The sidewall was chosen for comparison since it represents the material section that slides between the binder and the die when the punch pulls the material inwards. Hence, the lubricant performance will be reflected in the surface quality of the sidewall. While AA6013 T6 showed a similar trend, AA70XX T76 is illustrated in Figure 72 since the performance of less effective lubricants were better reflected considering the higher strength level of AA70XX T76 that caused more challenging tribological conditions (a stronger material is more reluctant towards material flow and deformation).

Cups with Fuchs (Figure 72a), OKS (Figure 72b), and Teflon film (Figure 72c) could be drawn and easily extracted from the tooling whereas the PTFE Spray in Figure 72d adhered to the die and required assistance with extraction. The cup sidewall with Teflon film had impeccable surface quality with no visible signs of tool contact. The etched surface grids for Argus strain measurement were slightly faded for cups drawn with Fuchs and OKS. While one cup drawn with the PTFE Spray resulted in fracture, on two more repeats severe scratches and scraped off sidewall surfaces confirmed high resistance to sliding.

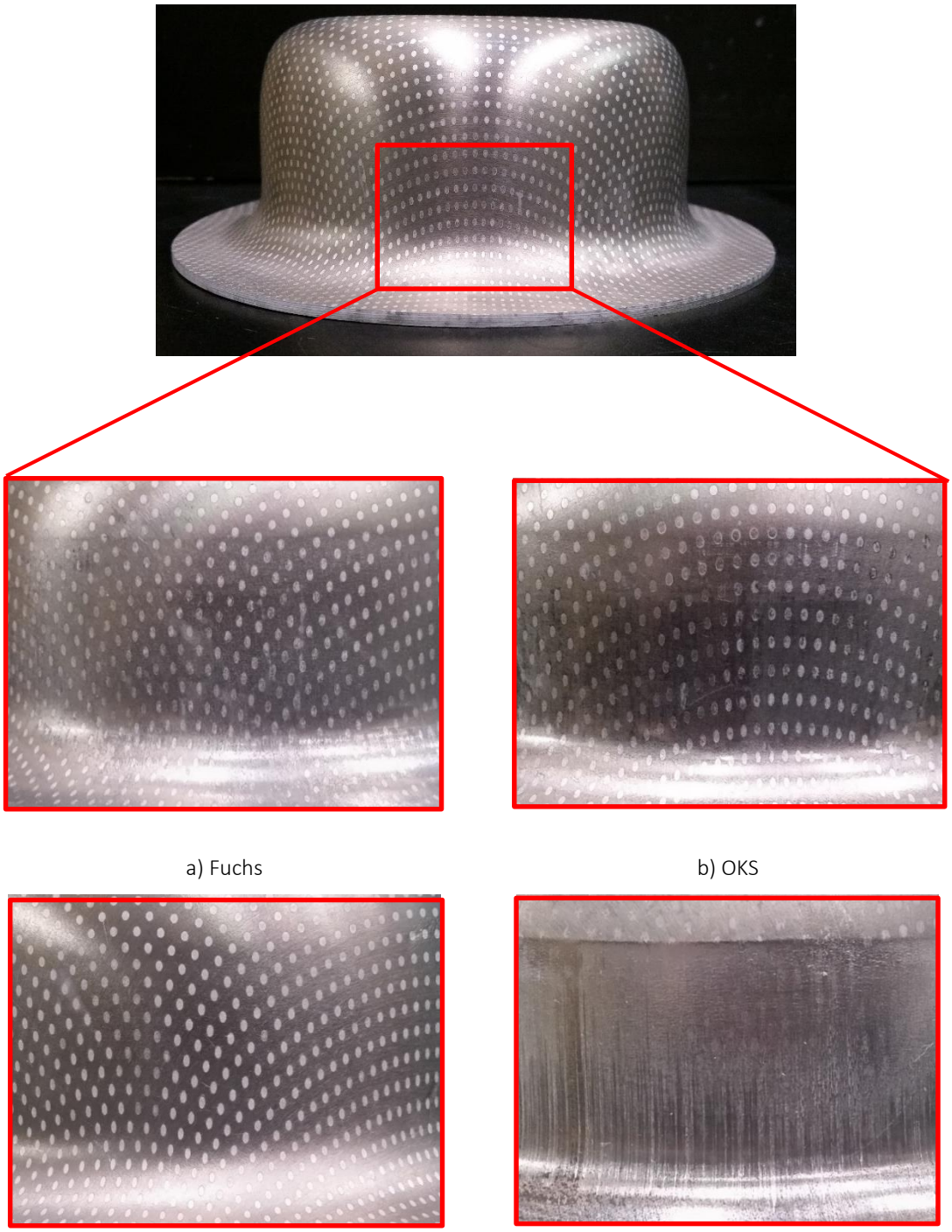

Figure 72: Visual inspection of circular cup sidewall (after cleaning) for AA70XX T76. Cups were drawn under isothermal conditions at 170°C to a target depth of 55 mm. The initial blank diameter corresponded to 203.2 mm, resulting in a drawing ratio of 2.0, the cup target depth was 55 mm.

4.5.2 Punch Force

Figure 73 gives an overview on the force evolution during isothermal deep drawing as a function of punch stroke. Results for the peak-aged AA6013 utilizing the Fuchs (blue curve), OKS (pink curve), PTFE Spray (turquois curve), and Teflon film (red curve) are plotted in Figure 73a, whereas corresponding results for AA70XX T76 are illustrated in Figure 73b. Except for AA6013 T6 with PTFE Spray, where some discrepancy was observed, excellent repeatability among three parts under the same condition was demonstrated. Interestingly, the peak force in deep drawing occurred before the target cup depth was reached, that explains why, in the case of part failure, cups fractured at an early stage of the drawing process. This was observed for one AA70XX T76 cup formed with the PTFE Spray when fracture occurred at a cup depth of approximately 18.7 mm.

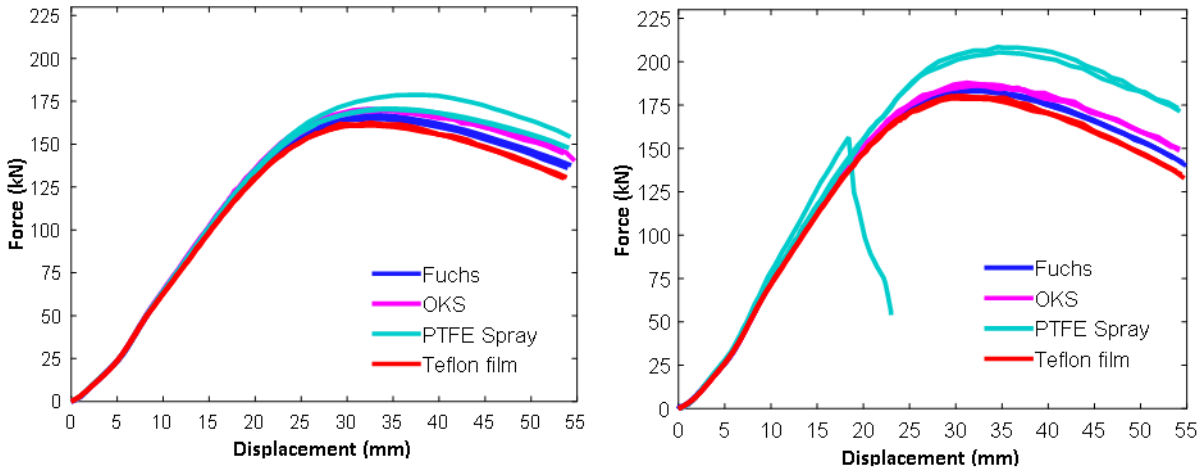

Figure 73: Force-displacement for isothermally-formed AA6013 T6 and AA70XX T76 cups at 170°C. The initial blank diameter corresponded to 203.2 mm and the target depth was 55 mm resulting in a drawing ratio of 2.0.

Peak punch forces for AA6013 T6 and AA70XX T76 are summarized in Figure 74. For all lubricants, higher forming forces were recorded for AA70XX T76, that can be explained through the 10 kN higher binder load in combination with the higher strength level. The lubricant ranking from absolute force values showed the same trend as for visual inspection. Compared to the most effective lubricant, the Teflon film, PTFE Spray required roughly 7% and 14. 9% higher forces for AA6013 T6 and AA70XX T76 respectively. From the error bars, that represent maximum and minimum values among three repeats, large scatter bands were recorded for PTFE Spray whereas very good repeatability was observed for

the other lubricants. While visual inspection showed almost negligible differences between Fuchs and OKS, the punch force was found to be a very sensitive parameter since, compared to OKS, Fuchs recorded roughly 4.4 kN and 3.4 kN lower forces for AA6013 T6 and AA70XX T76, respectively.

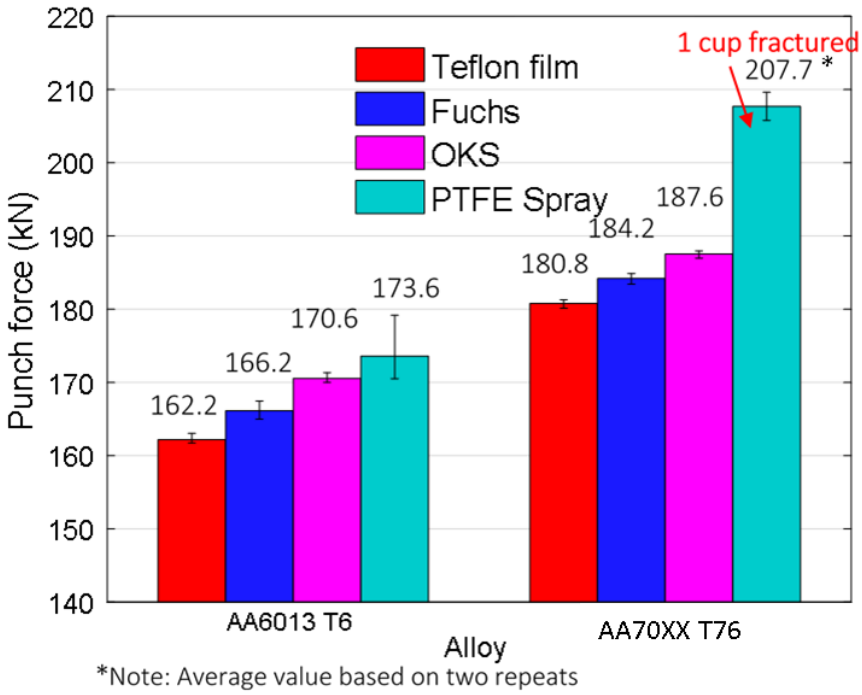

Figure 74: Peak punch force in deep drawing of AA6013 T6 and AA70XX T76 formed with different lubricants. Cups were drawn under isothermal conditions at 170°C to a target depth of 55 mm. The initial blank diameter corresponded to 203.2 mm and the target cup depth was 55 mm resulting in a drawing ratio of 2.0.

4.5.3 Flange Perimeter

A higher forming force implies more resistance to sliding through the die-binder interface. Whereas a more effective lubricant facilitates material flow, a less effective lubricant will resist sliding. Since higher punch forces were recorded for the PTFE Spray, the expected larger flange perimeter of the drawn cup was confirmed by summarized values in Figure 75. The smallest perimeter was observed for the cup formed with the Teflon film that also recorded the lowest forming forces for both alloys. While cups drawn with the Fuchs and OKS exhibited a larger perimeter than the Teflon film, their scatter bands between maximum and minimum value among three repeats were overlapping. Contrary the PTFE Spray with a 7.2 mm larger perimeter for both alloys clearly distinguished itself from cups drawn with the Teflon film. This finding is visualized in Figure 76. The use of alignment jigs when

scanning the profiles allowed overlaying flanges of cups formed with the PTFE Spray in turquois and with the Teflon film in red color.

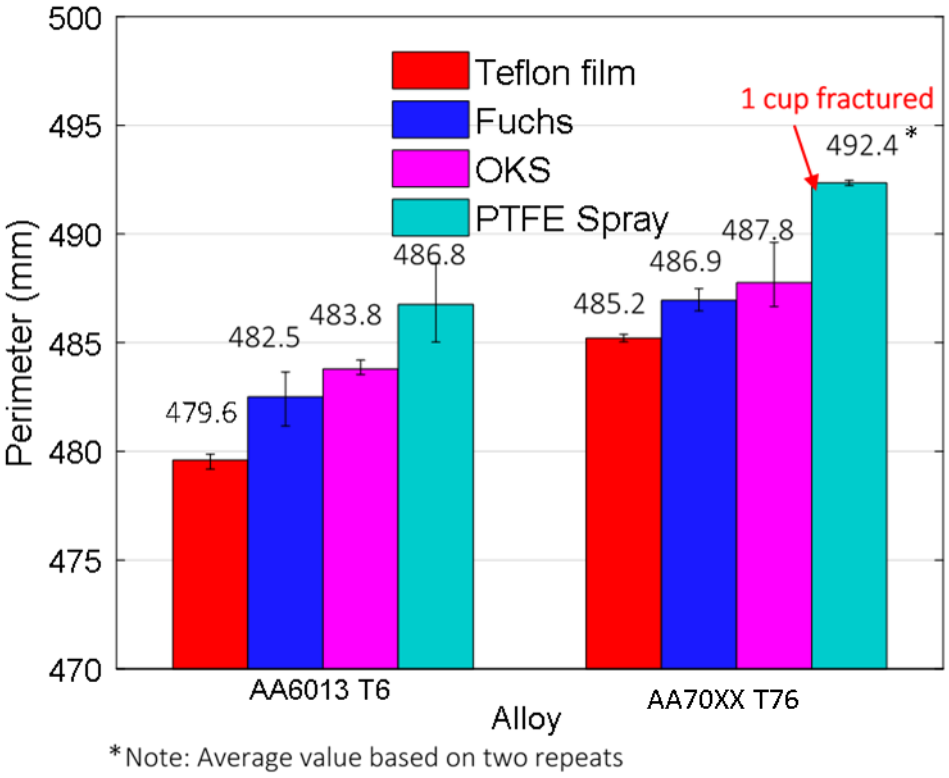

Figure 75: Perimeter of cup flange of AA6013 T6 and AA70XX T76 formed with different lubricants. Cups were drawn under isothermal conditions at 170°C to a target depth of 55 mm. The initial blank diameter corresponded to 203.2 resulting in a drawing ratio of 2.0.

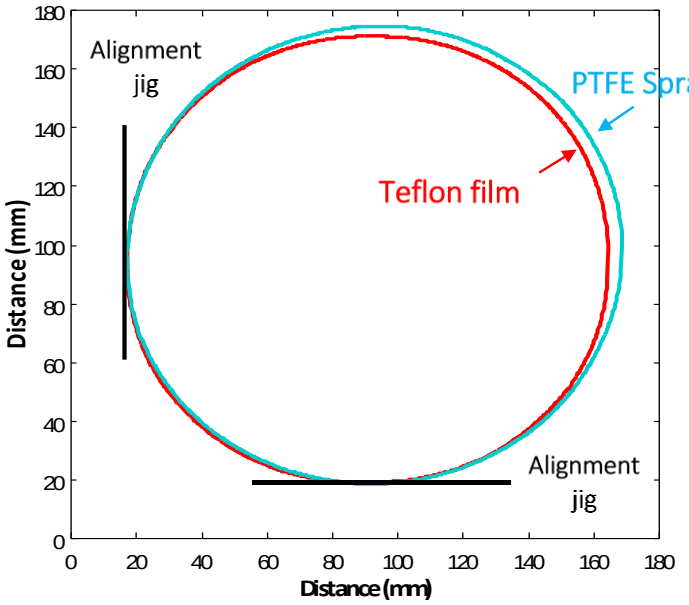

Figure 76: Overlaid flange profile for AA6013 T6 formed with Teflon film (red) and PTFE Spray (turquois). Cups were drawn under isothermal conditions at 170°C to a target depth of 55 mm. The initial blank diameter corresponded to 203.2 mm, resulting in a drawing ratio of 2.0.

4.5.4 Draw-in Length

The draw-in length describes the difference in the initial blank diameter to the final flange diameter. Owing to reduced sliding resistance for a more effective lubricant, material flow is facilitated; hence, an increased draw-in length is expected for a more effective lubricant.

The draw-in length in the RD for AA6013 T6 and AA70XX T76 is summarized in Figure 77. Average values showed the same lubricant ranking as observed for the aforementioned parameters. The Teflon film experienced largest draw-in, however, differences among lubricants were minor, at least for AA6013 T6, and scatter bands were occasionally overlapping. With a 2.3 mm and 4.4 mm difference between the PTFE Spray and Teflon film for AA6013 T6 and AA70XX T76, respectively, the draw-in length was found not to be as sensitive as the perimeter or the punch force. Striking was the more pronounced scatter for AA70XX T76 formed with the Teflon film for that lubricant application method could not be the reason since punch forces showed excellent repeatability. Alignment during scanning of the flange profiles could serve as a reasonable explanation. In view of earing for AA70XX T76, slight deviations may have significant influences on measurement positons and values obtained.

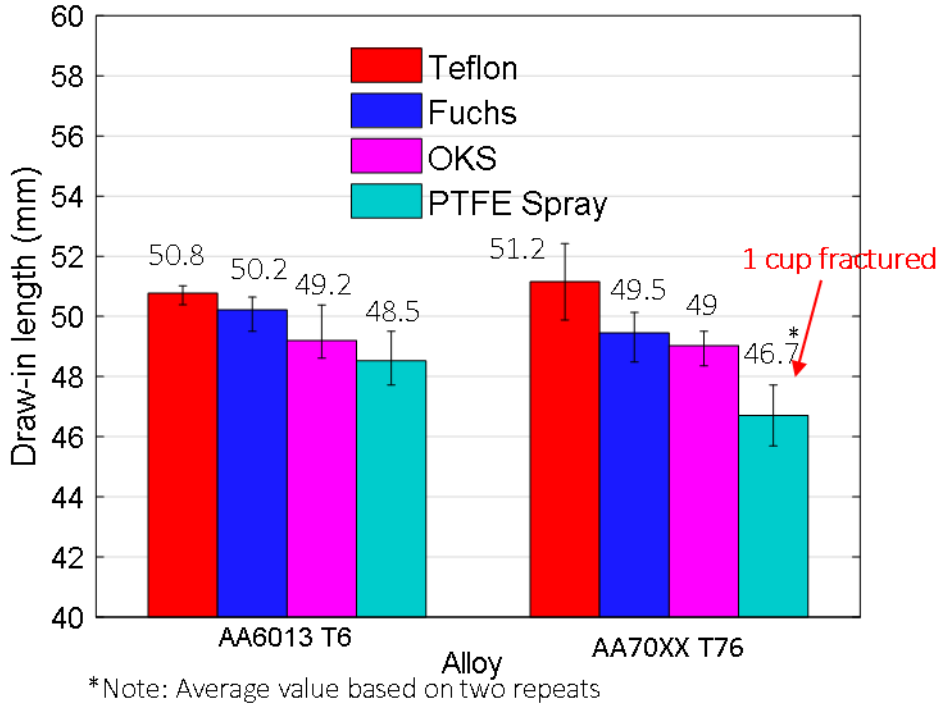

Figure 77: Draw-in length in the RD of cup flange of AA6013 T6 and AA70XX T76 formed with different lubricants. Cups were drawn under isothermal conditions at 170°C to a target depth of 55 mm. The initial blank diameter corresponded to 203.2 mm resulting in a drawing ratio of 2.0.

4.5.5 Change in Thickness

The effect of lubricant performance on thickness change and strain distribution is discussed in the following. Figure 78 summarizes the percent thickness change for the PTFE Spray (turquois bars) and the Teflon film (red bars) at different measurement locations. Since visual inspection, punch force, perimeter, and draw-in length identified the Teflon film and PTFE Spray as the upper and lower bound lubricant, respectively, possible thickness changes were assumed to be most significant for this lubricant comparison. Measurement location 1 represents the flange section for that approximately 6.6% and 8.1% thickening was recorded for AA70XX T76 drawn with the PTFE Spray and the Teflon film, respectively. More thickening would have been expected for a more effective lubricant since there is less resistance to the radial compressive strains. In fact, the Teflon film recorded a slightly greater increase, however, considering the absolute value of 0.03 mm, this observation was likely due to measurement error. Compared to AA70XX T76, higher percent flange thickening was found for AA6013 T6 cups that were formed at a lower binder load, hence, combined with the lower material strength, constrained the material less.

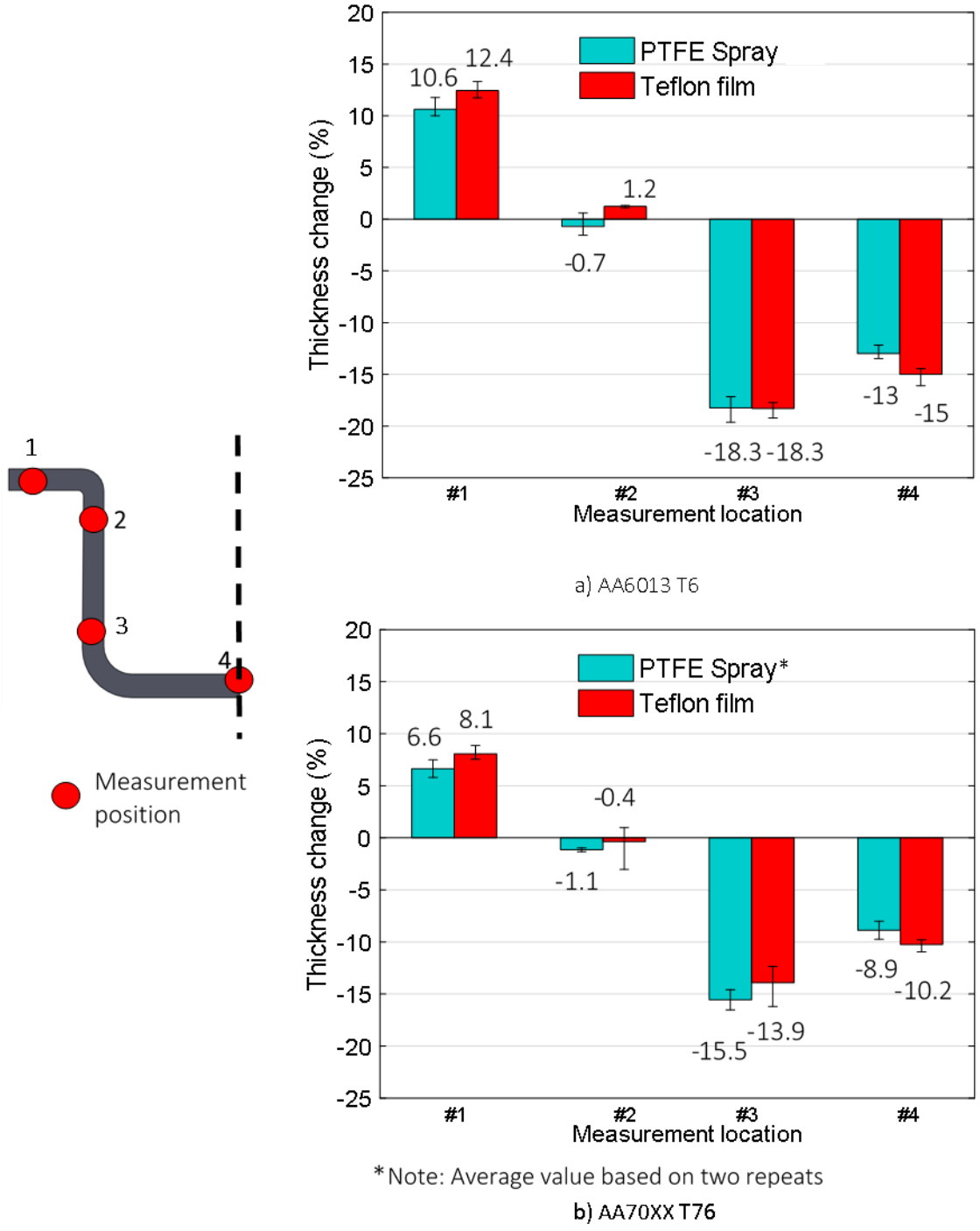

Figure 78: Thickness change of drawn cups for AA6013 T6 and AA70XX T76 formed with the Teflon film (red bars) and PTFE Spray (turquois bar). Cups were drawn under isothermal conditions at 170°C to a target depth of 55 mm. The initial blank diameter corresponds to 203.2 mm, resulting in a drawing ratio of 2.0.

Thickness changes in the flange radius, represented by measurement position 2, were below 1.5% and were assumed to be negligible. Thinning in the order of 15.5% and 13.9% for AA70XX T76 with the PTFE Spray and Teflon film, respectively, occurred in the lower sidewall of measurement location 3. This material section was subjected to stretching that was assumed to be less severe with more effective lubricants. According to this theory, PTFE Spray should experience more thinning than Teflon film that was confirmed by measurements for AA70XX T76 whereas equal values for AA6013 T6 contradicted this claim. The center point in the hat section reported 1.3% and 2% less thinning for the PTFE Spray of AA70XX T76 and AA6013 T6, respectively. In view of the small numbers and scatter bands among repeats, negligible differences and measurement error might explain occasionally contradicting results. Summarizing from these findings, thickness reduction was not found to be sensitive to serve as lubricant ranking parameter. Hence, no additional thickness measurements were taken for the Fuchs and OKS.

4.5.6 Strain Distribution

Strain distribution and magnitude governs the location and extent to that thickness changes occur in the cup. Since no remarkable discrepancies were observed between tested lubricants, similar results were expected for the strain distribution. An exemplary major strain distribution on an AA70XX T76 cup drawn using the Teflon film is plotted in Figure 79. The pink line indicates a section defined along the RD, along that the major strain distributions were compared. The results for the different lubricants are shown in Figure 80. Note that the flange geometry and the line resolution are strongly dependent on the condition of the etched grid pattern on the as-formed cup surface. For some lubricants, particularly the PTFE Spray, the grids on the sidewall and part of the flange surface were scraped off preventing strain measurement in those regions (as indicated in the plots).

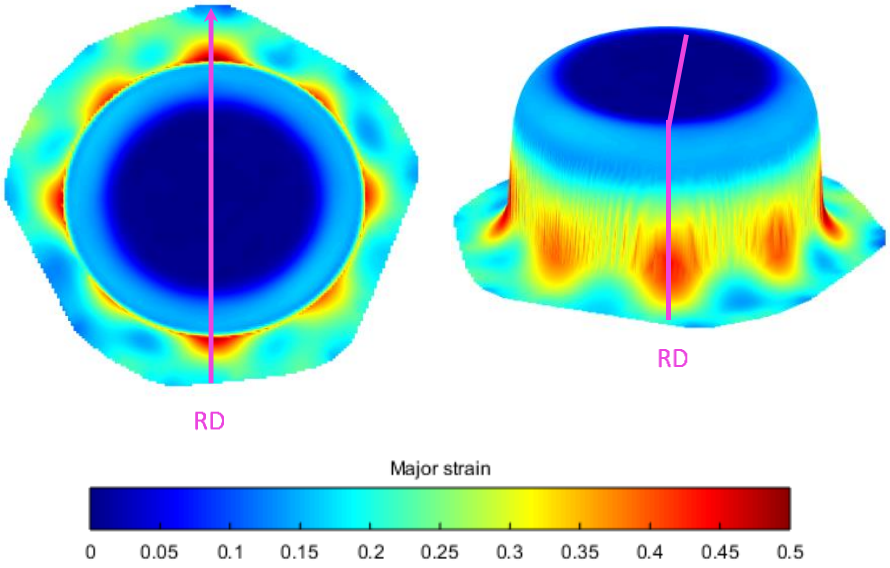

a) Top view b) Side view

Figure 79: Major strain fringe plot of AA70XX T76 drawn with Teflon evaluated with Argus and plotted in the software MATLAB; Cup was isothermally drawn at 170°C to a target depth of 55 mm. The initial blank diameter was 203.2 mm and corresponds to a drawing ratio of 2.

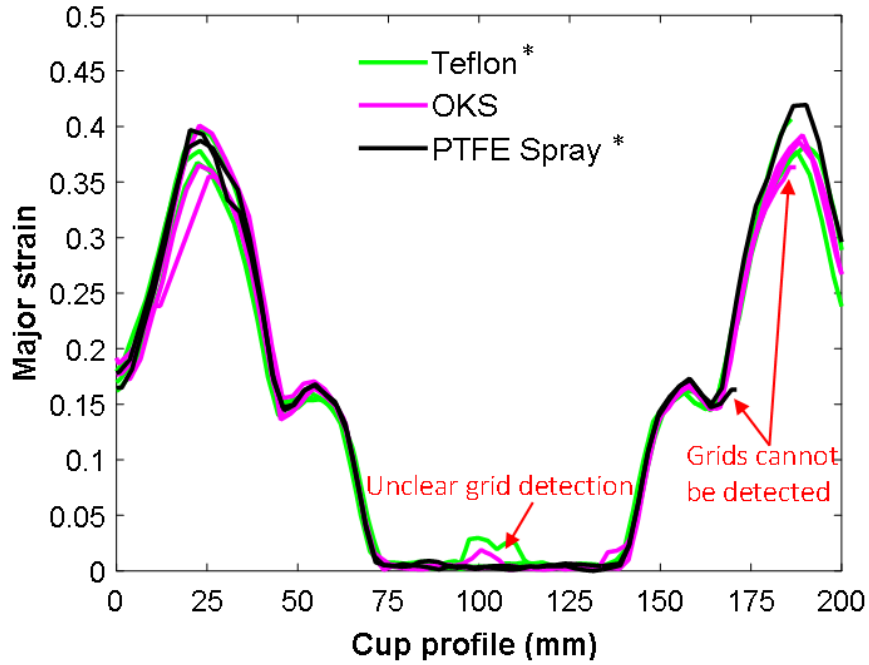

* Note: 2 repeats (Teflon), 2 repeats (PTFE Spray)

a) AA6013 T6

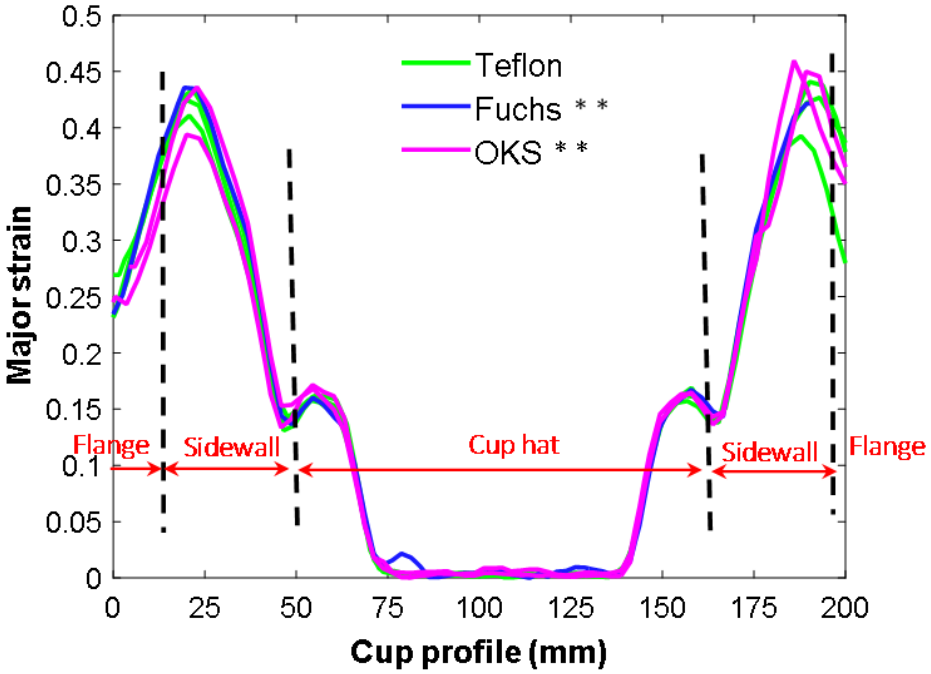

** Note: 1 repeat (Fuchs), 2 repeats (OKS)

b) AA70XX T76

Figure 80: Major strain along cup contour in the RD for AA6013 T6 and AA70XX T76 isothermally formed at 170°C to a target cup depth of 55 mm. The initial blank diameter corresponded to 203. 2 mm resulting in a drawing ratio of 2.

The cup hat region exhibited almost negligible strain whereas the hat radius and the cup sidewall were characterized by a sharp increase in strain. Referring to Figure 79, peak major strains on the order of approximately 40% to 45% occurred near the die entry radius at the transition from the sidewall to the flange. From the major and minor strains the thickness change can be readily computed from the assumption of plastic volume conservation. The thickness distribution for an AA70XX T76 cup drawn under isothermal conditions with the Teflon film lubricant is shown in Figure 81. Percent thickness reduction in Figure 81c demonstrates peak values of approximately 15% in the cup bottom radius that corresponds to measurement position number three for ultrasonic thickness measurements performed in Section 4.5.5. Measurements recorded 13.9% thinning, that is in very good agreement with the obtained thickness change through optical strain measurements.

Cups formed from both alloys using all lubricants exhibited similar strain distributions over the cup profile. It was concluded that comparison of the strain distribution in the final part is difficult because it requires preservation of the etched grid pattern that requires mild tribological conditions and/ or limited surface expansion. Instantaneous strain recording during cup drawing, e.g. use of DIC, could reveal that a more effective lubricant delays peak strains or distributes them more evenly.

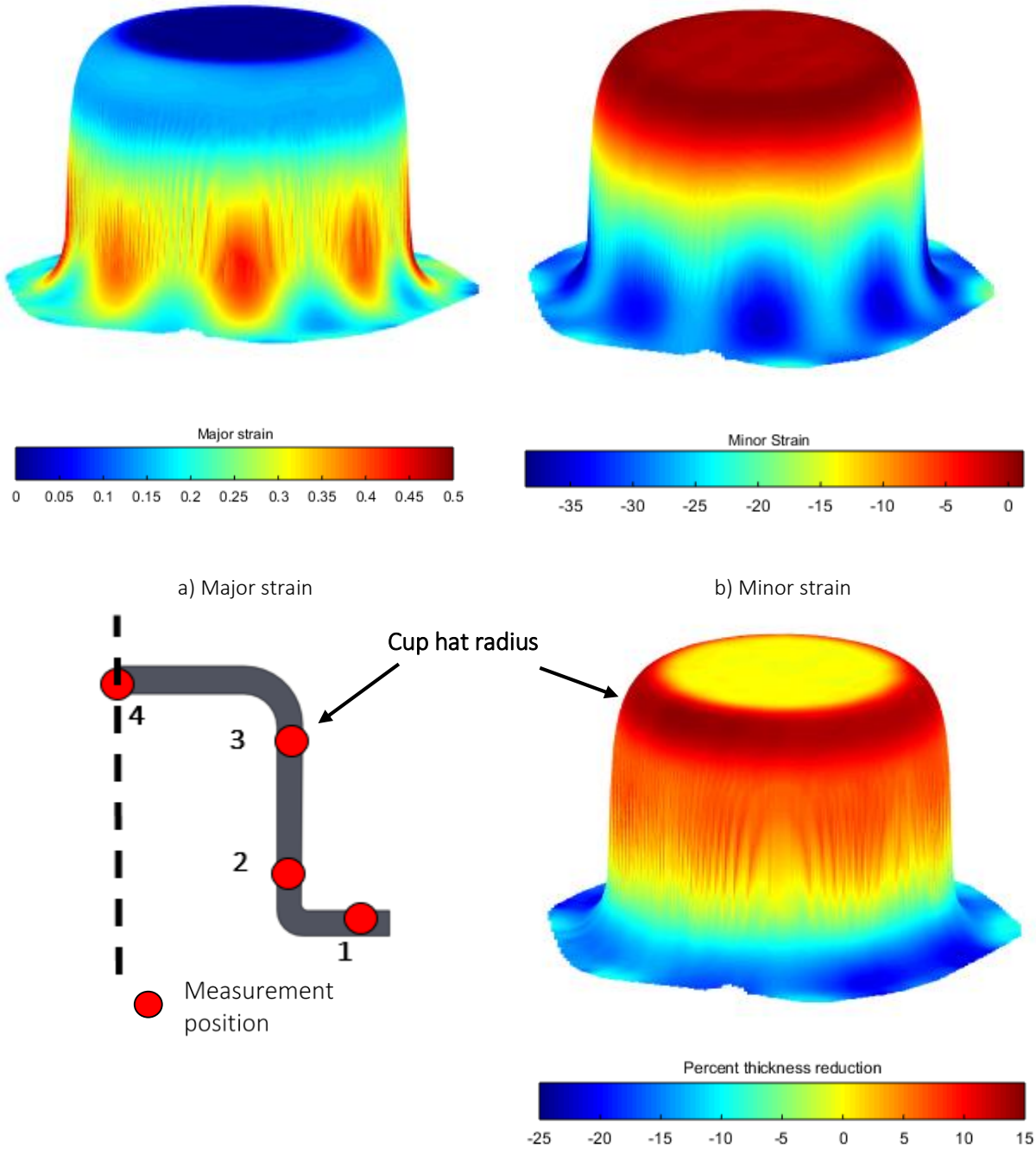

Figure 81: Major and minor strain distribution, and thickness change on an AA70XX T76 cup formed under isothermal conditions at 170°C utilizing the Teflon film. The target cup depth was 55 mm, whereas the initial blank diameter corresponded to 203.2 mm resulting in a drawing ratio of 2.0.

4.5.7 Summary of Isothermal Deep Drawing

In light of the resemblance to a physical forming process, deep drawing was selected as a process test to evaluate the friction efforts in Chapter 3. Initial 203.2 mm diameter AA6013 T6 and AA70XX T76 (a 7xxx series aluminum alloy under development) blanks were drawn to a target depth of 55 mm (leaving a 20 mm wide flange) under isothermal conditions and at 170°C, analogous to the thermal condition in the TCT. In general, the lubricant ranking correlated well with predictions in the TCT: the Teflon film was superior followed by the Fuchs, OKS, and PTFE Spray. Six different metrics were studied and their reliability to distinguish between lubricant performances as well as measurement efforts were rated in Table 24. Visual inspection can be seen as an intuitive metric that allowed distinction between the PTFE Spray and Teflon film whereas distinction between Fuchs and OKS was unclear. In contrast, the punch force was easy to obtain and revealed a high level of sensitivity since it recorded a superior performance of Fuchs compared to OKS (4.4 kN and 3.4 kN lower process forces for AA6013 T6 and AA70XX T76, respectively). Comparison of the perimeter and draw-in length involved some efforts since flange profiles were scanned and a custom MATLAB script utilized for improved repeatability. While the general lubricant ranking was confirmed, the discrepancy among the lubricants was moderate and occasionally accompanied with overlapping error bars. Thickness change and strain distribution yielded no noticeable differences between tested lubricants and were associated with considerable efforts considering etching of the blanks prior to forming and post-processing.

Table 24: Rating of utilized metrics for evaluation of lubricant performance in isothermal deep draws

	Sensitivity				Measurement effort			
Metric	Low			High	Low			High
Visual inspection								
Punch force								
Flange perimeter								
Draw-in length								
Thickness change								
Strain distribution								

4.6 Non-isothermal Deep Drawing Results

Since the warm friction has been characterized and evaluated, the efforts are now devoted to the assessment of the material anisotropy. Non-isothermal deep draws were selected for this purpose because forming over a temperature gradient facilitates drawing of larger cups that involve higher plastic strains. The hat radius in the formed cup represents the critical contact point with the punch radius when the material is pulled inwards. With the intention to prevent that excessive stretching in the cup radius causes fracture, the punch was set to a lower temperature and provided cooling that directly influenced the material flow stress. Hence, tailored properties could be achieved along the cup profile that allowed strong material sections in regions of high stretching and soft material in the blank rim that was pulled inwards. Considering long sliding distances, large plastic strains, temperature differentials, and strain-rate sensitivity, non-isothermal deep draws represent a forming process that is well-suited for this study since it combines friction efforts with the work performed on the thermo-viscous constitutive model and yield function calibration.

For all three alloys, non-isothermal circular 228.6 mm diameter blanks were drawn to a target depth of 75 mm (leaving a 20 mm wide flange), that corresponded to a drawing ratio of 2.25. Initial trials revealed that a clamping load of 70 kN, 80 kN, and 100 kN was suitable to draw AA6013 T6, AA7075 T6 and AA70XX T76 (a 7xxx series aluminum alloy under development) blanks, respectively. While the punch ram speed was set to 1 mm/s, the effect of tooling temperature was studied in pre-tests that are discussed in the following

4.6.1 Determination of Tool Temperature

The experiments served to examine the effect of a temperature differential between the punch and die/binder on achievable draw depth. Thermal settings were validated through attached thermocouples to the blank during forming.

Figure 82 provides an overview of the experimental outcomes. Isothermal forming at 25°C, 170°C and 200°C resulted in early fracture at draw depths of only 19.2 mm, 23.6 mm, and 21.2 mm, respectively. Fracture occurred at the punch profile radius indicating that the material in this region is unable to support the load required to draw the large flange into the die. Lowering the punch temperature to 170°C and keeping the die and binder at 200°C still resulted in fracture but allowed a draw depth of

31.3 mm to be reached. A further decrease of the punch temperature to 150°C (with die and binder at 200°C) resulted in the target cup depth of 75 mm to be reached. One other condition was considered where the punch was not heated and the binder and the die were held at 200°C. In this case, the heat is conducted from the binder and die into the punch and a steady state temperature of 100°C was reached in the punch. Since these conditions also resulted in the targeted cup depth of 75 mm to be achieved without fracture, these temperature settings were utilized for the balance of the non-isothermal deep draw study.

Cup height: 19.2 mm

a) Punch, die, and binder at 25 °C

Cup height: 23.6 mm

b) Punch, die, and binder at 170 °C

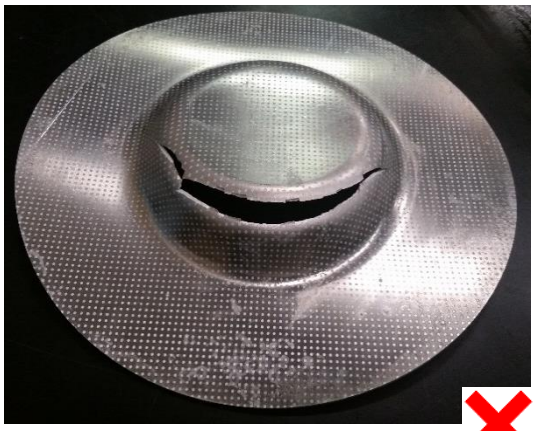

Cup height: 21.2 mm

c) Punch, die, and binder at 200 °C

Cup height: 31.3 mm

d) Punch at 170 °C, binder and die at 200 °C

Cup height: 75 mm

e) Punch at 150 °C, binder and die at 200 °C

Cup height: 75 mm

f) Punch at 100 °C, binder and die at 200 °C

Figure 82: Influence of tooling temperature on cup height in deep drawing of 228.6 mm diameter AA7075 T6 blanks utilizing the Fuchs lubricant

Thermal recordings are desirable for two reasons, first, to validate that thermal settings in the equipment are correct, and, second, to compare the thermal history to predictions by the numerical model, that is discussed in Chapter 5. For this purpose, three thermocouples were attached to the AA7075 T6 blank at locations that correspond to the as-formed hat, sidewall, and flange section, as discussed in section 4.3. Figure 83 shows conditions after forming and confirms that, in contrast to the centre thermocouple, the flange and sidewall thermocouple came off when the material was pulled inwards. Nevertheless, temperature recordings are available for all three thermocouples until the onset of forming and for the complete forming cycle in the blank center. Figure 84 records the thermal evolution over the punch stroke from the attached thermocouples.

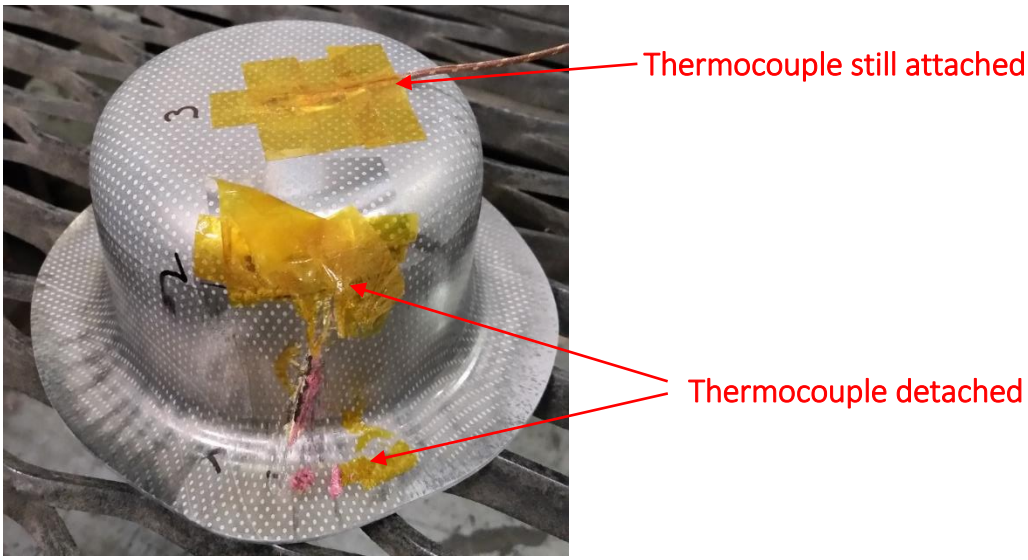

Figure 83: Circular cup (AA7075 T6 utilizing Fuchs) with thermocouples attached during non-isothermal forming (punch at 100°C, die and binder at 200°C) to a target depth of 75 mm. The initial blank diameter corresponded to 228.6 mm resulting in a drawing ratio of 2.25.

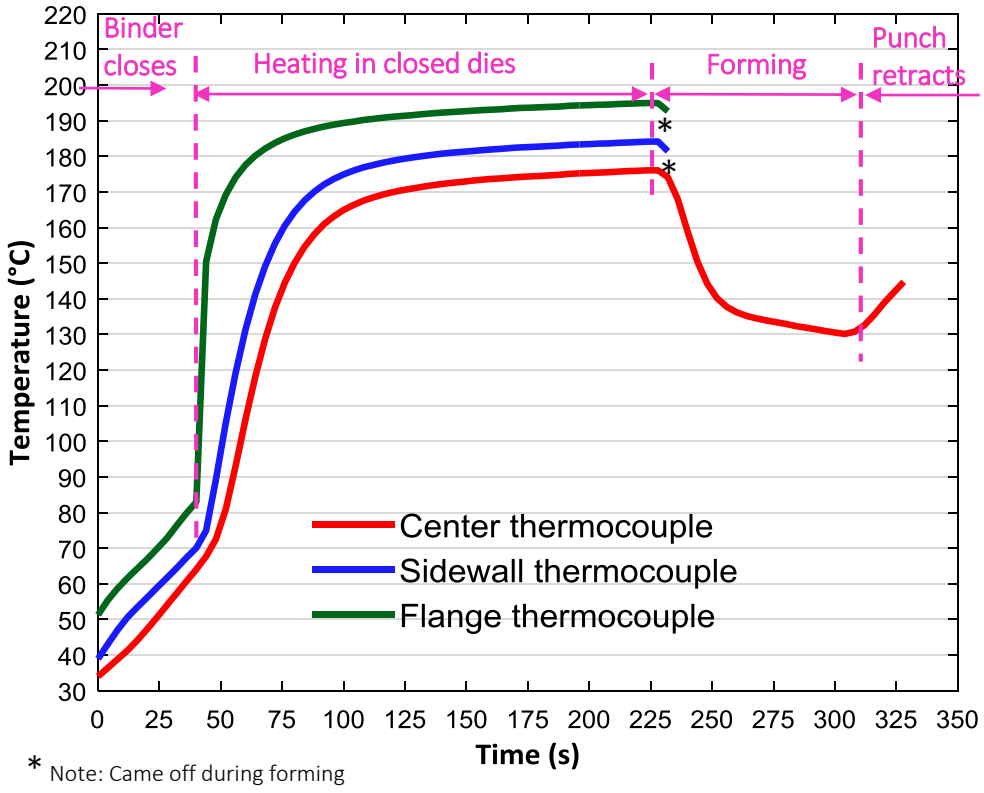

Figure 84: Thermal evolution over the punch stroke during non-isothermal deep drawing of an AA7075 T6 228.6 mm diameter blank to a target depth of 75 mm. Three thermocouples were attached at positions corresponding to the as-formed hat, sidewall, and flange section.

Figure 84 demonstrates a sharp increase in temperature after approximately 35 s when the 200°C hot binder closed and contacted the room temperature blank. A total of 180 s were allocated to heat the blank when the punch was displaced and pulled the blank inwards. At the onset of forming, a temperature of 176°C, 184°C, and 195°C was recorded in the blank centre, sidewall, and flange section, respectively. A temperature gradient over the blank profile was expected considering the 200°C hot binder and die and the 100°C punch. Measured temperature values at different locations in the blank were applied as thermal boundary conditions to the simulation model discussed in Chapter 5. Since the flange and sidewall thermocouple came off during forming, temperatures during drawing were only recorded for the center thermocouple. Due to contact with the punch, the blank center cooled down to approximately 130°C at the stroke end when the punch retracted.

4.6.2 Force-displacement of Non-isothermal Cup Draws

Figure 85 plots the force evolution over the punch stroke for AA6013 T6, AA7075 T6, and AA70XX T76 formed under non-isothermal conditions utilizing Fuchs (three repeats) and Teflon film (one repeat), respectively. Excellent repeatability was observed for all cups formed with the Fuchs lubricant. Compared to AA6013 T6, 2.9% and 15.5% higher punch forces were required for AA70XX T76 and AA7075 T6 respectively. The higher forming force for AA7075 T6, compared to AA70XX T76, is most likely associated with the initial temper and hence the higher material strength; AA7075 T6 was peak-aged whereas AA70XX T76 was supplied in an over-aged temper with the intention of improving the corrosion performance. While forming with the Teflon film resulted in lower process forces for both AA7075 T6 (brown curve) and AA6013 T6 (purple curve), AA70XX T76 (turquois curve) recorded a slightly higher peak force compared to the Fuchs lubricant (blue curve). Since the difference is minor, this observation was believed to be due to process variation and more repeats with the Teflon film are work in progress.

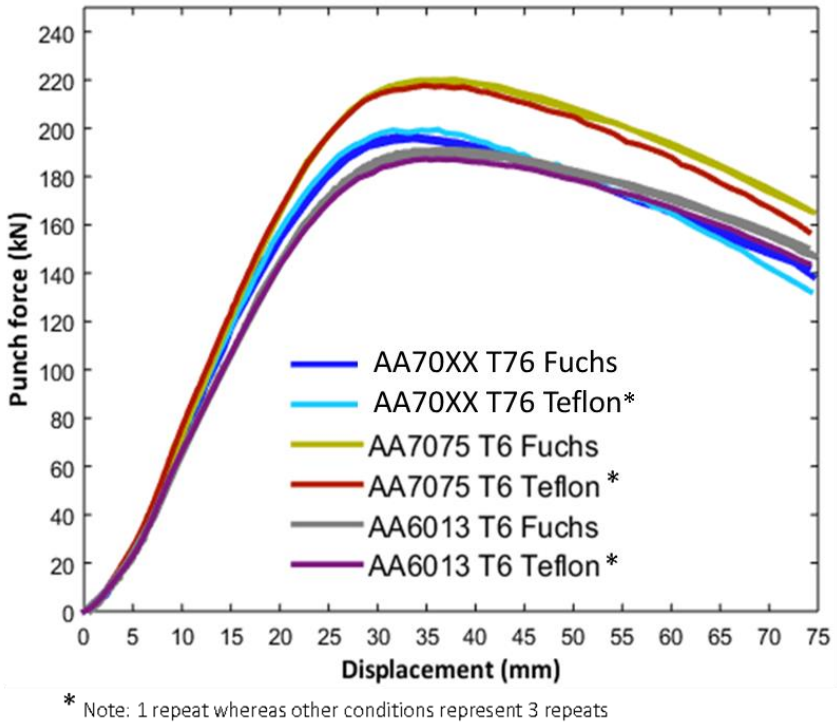

Figure 85: Force-displacement for 228.6 mm diameter blanks drawn to a target depth of 75 mm under non-isothermal conditions (die and binder at 200°C with the punch at 100°C) utilizing the Fuchs lubricant ant the Teflon film)

4.6.3 Earing Profile

In a perfectly isotropic material, the flange of a drawn cup with a circular blank geometry will exhibit a circular flange profile, in contrast to a directional material in that the flow behavior is a function of the anisotropy and loading direction. A high R-value, for example, represents a high resistance to thinning that results in reduced draw-in of the material whereas low R-values facilitate material flow. These opposing processes will be reflected in the presence of earing in the cup flange that is discussed in Section 1.2.2.

With the intention of performing experiments under industrial conditions, the Fuchs lubricant was initially utilized in the non-isothermal draw experiments. Visual inspection of drawn cups, however, revealed excessive burnishing of the etched grid pattern in the flange region, as can be seen for AA70XX T76 in Figure 86b. In contrast, cups formed with the Teflon film, under identical process conditions, resulted in better grid quality for subsequent strain measurements (Figure 86a). As a result, Teflon film was adopted as the lubricant for the balance of the non-isothermal cup draw experiments.

A striking feature of the experiments utilizing Teflon film was that the earing profile was significantly more pronounced than was observed for the Fuchs-lubricated cups, as can also be seen for AA70XX T76 in Figure 86. It would appear that the burnished regions experienced higher sliding resistance that supressed the degree to that anisotropy is reflected in the final part. There was also a lower degree of symmetry in the earing profiles of the cups formed with the Fuchs that may be due to press misalignment or irregular lubricant application, for example. The degree of asymmetry in the cups lubricated with the Teflon film was less.

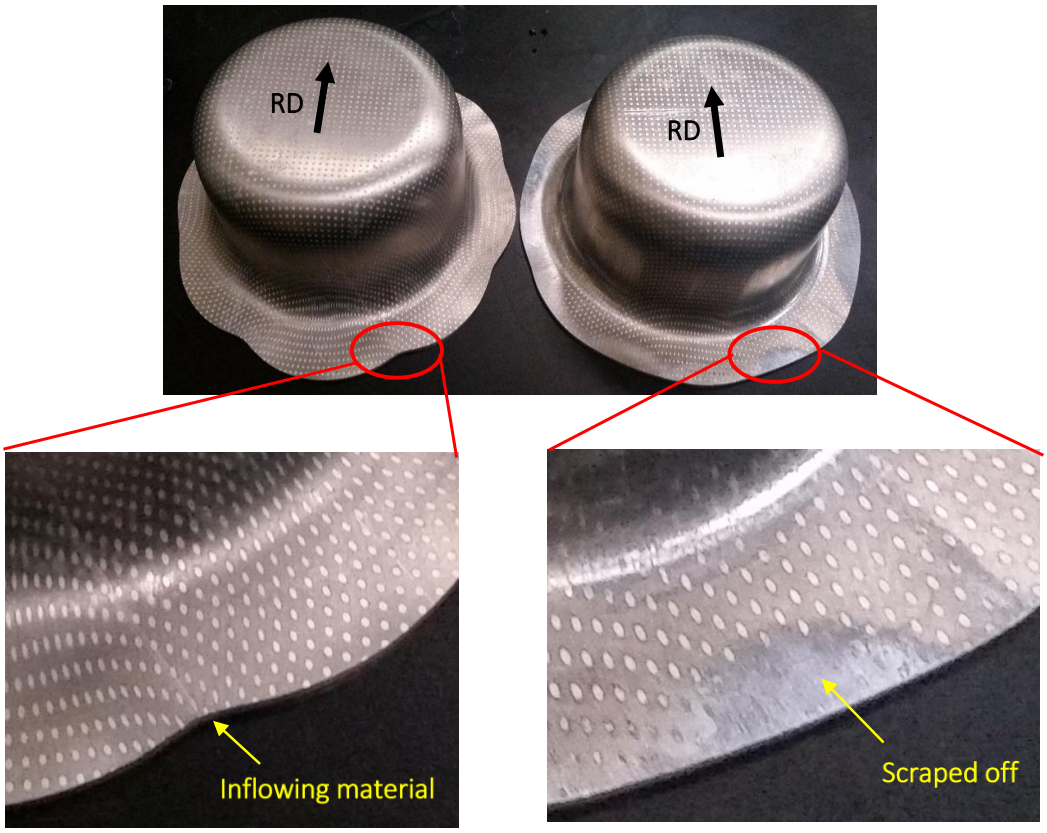

a) Formed with Teflon film b) Formed with Fuchs

Figure 86: Effect of lubricant choice on degree of earing on an AA70XX T76 cup formed under non-isothermal conditions (die and binder at 200°C with the punch at 100°C)

The earing profile for circular cups drawn using 228.6 mm diameter AA70XX T76, AA7075 T6, and AA6013 T6 blanks is illustrated in Figure 87, that demonstrates that the degree of strain anisotropy, reflected in the number and extent of ears, varies considerably. AA6013 T6 showed very mild earing with a slightly ellipsoidal-shaped flange profile, whereas eight slightly pronounced ears were observed for AA7075 T6 and eight clearly defined ears for AA70XX T76. Yoon *et al.* [56] and van den Boogaard [30] found a strong correlation of the strain anisotropy with the earing profile in circular cup drawings. Rahmaan [3] conducted room temperature tensile tests oriented in 15° increments relative to the RD for all three alloys, AA6013 T6, AA7075 T6, and AA70XX T76. Since Omer [111] confirmed negligible thermal effects on the material anisotropy of studied alloys, R-values and stress ratios at room temperature were utilized to explore the observation by Yoon *et al.* [56]. For this purpose, the cup flange was scanned and the draw-in length computed with image processing technique, discussed in

Section 4.4. Figure 88, Figure 89, and Figure 90 show the scanned flange profile of the AA70XX T76, AA7075 T6, and AA6013 T6 cup, respectively.

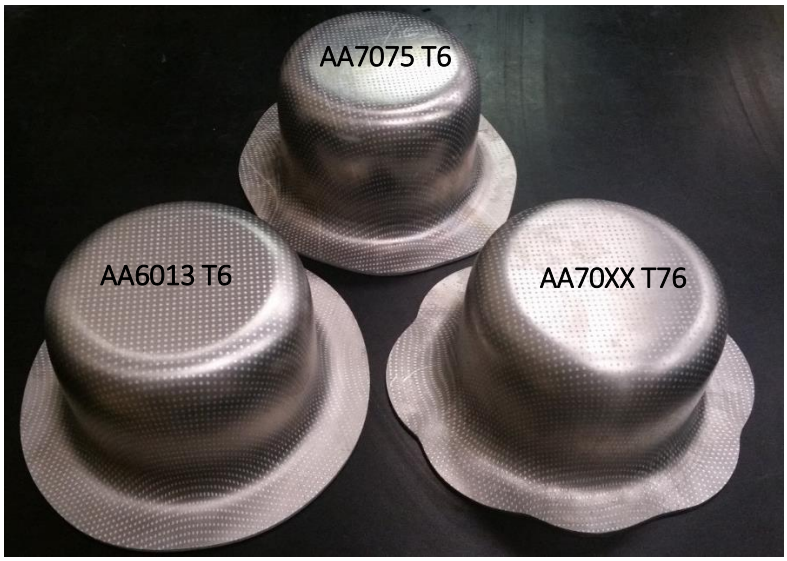

Figure 87: Circular cups drawn under non-isothermal conditions (die and binder at 200°C with the punch at 100°C) utilizing Teflon film. The initial blank diameter was 228.6 mm and the cup was drawn to a target depth of 75 mm, corresponding to a drawing ratio of 2.25.

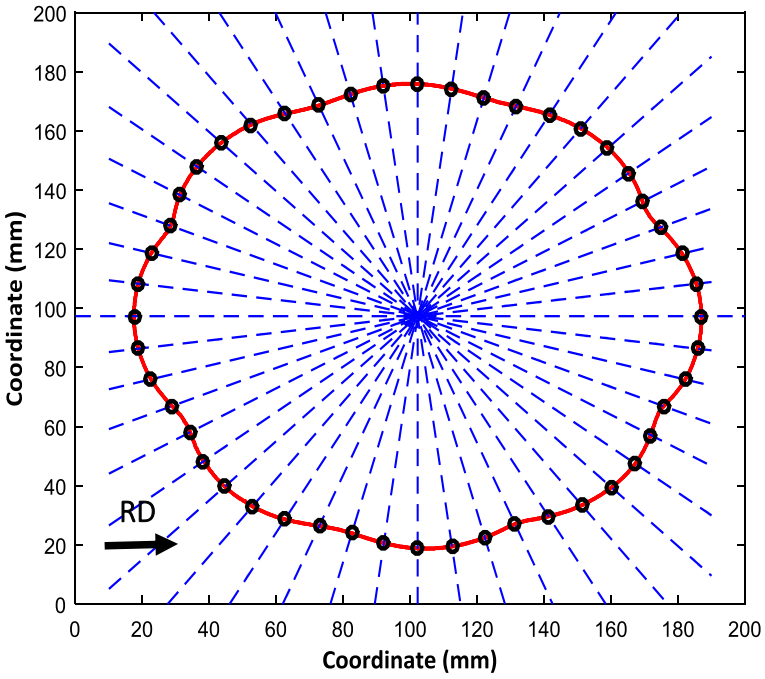

Figure 88: Scanned profile of an AA70XX T76 cup drawn under non-isothermal conditions utilizing the Teflon film

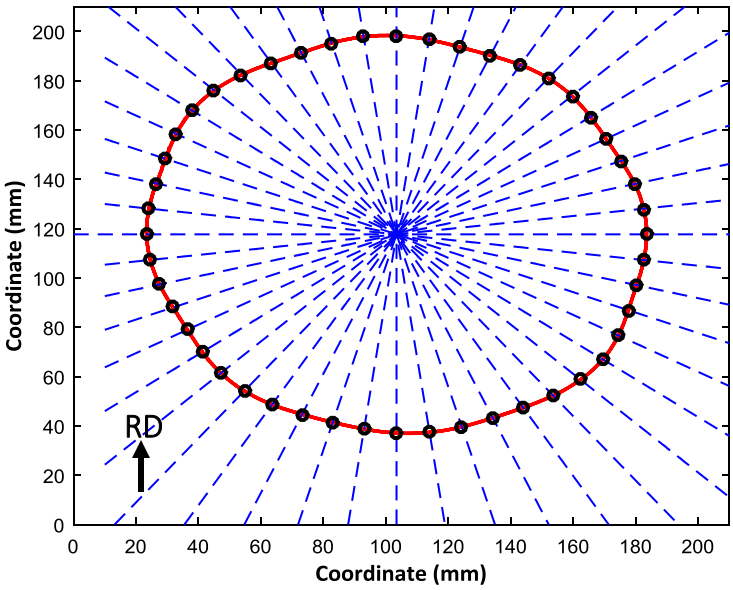

Figure 89: Scanned profile of an AA7075 T6 cup drawn under non-isothermal conditions utilizing the Teflon film

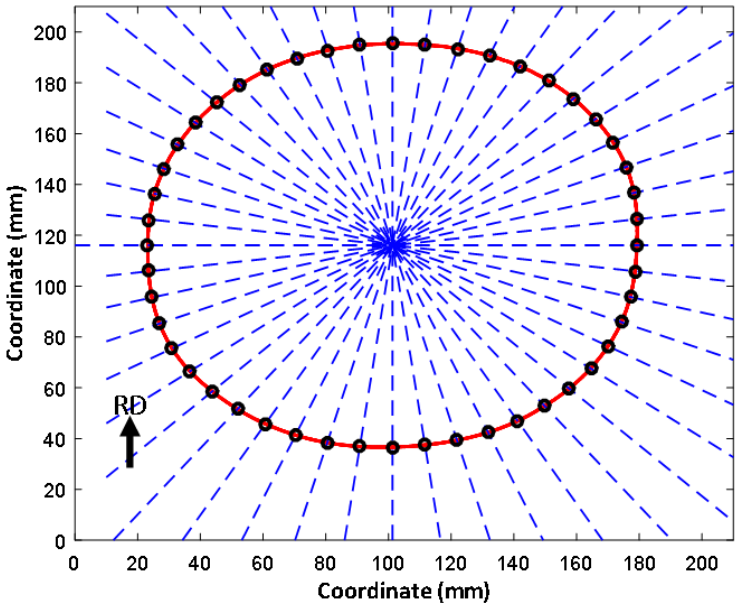

Figure 90: Scanned profile of an AA6013 T6 cup drawn under non-isothermal conditions utilizing the Teflon film

To facilitate comparison of the earing profile among the three alloys, the draw-in length is normalized with respect to the RD and plotted together with the R-value and stress ratio evolution relative to the RD. Results for AA70XX T76 are plotted in Figure 91, where experimental data points are marked with

circles and stars and solid/ dashed lines highlight the trend. It is important to note that for visualization purposes, in this figure as well as for the results for AA7075 T6 (Figure 92) and AA6013 T6 (Figure 93), the R-values and stress ratios were mirrored about the 90° symmetry line.

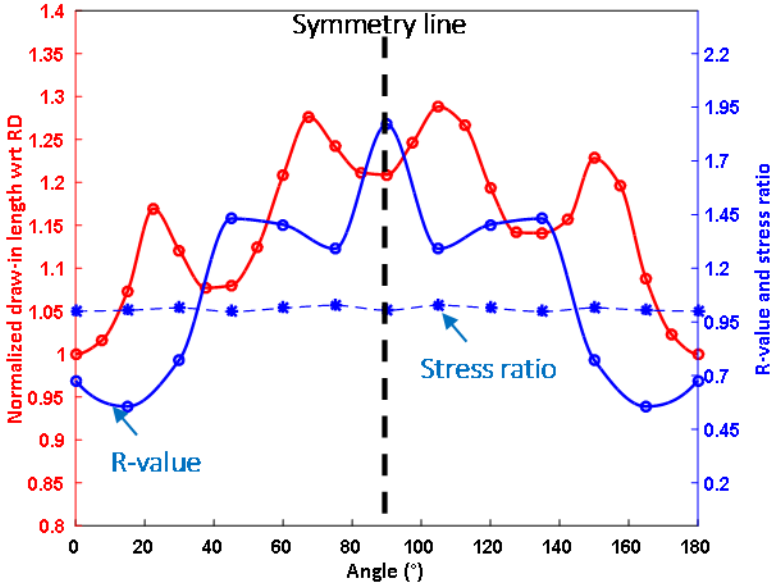

Figure 91: Measured draw-in length for AA70XX T76, normalized with respect to the RD (red solid curve), is compared to the variation in the R-value (solid blue line) and stress ratio (dashed blue line) in 15° increments relative to the RD obtained by Rahmaan [3]. The cup was drawn under non-isothermal conditions utilizing the Teflon film; the drawing ratio corresponded to 2.25; note that the strain and stress ratios are mirrored about 90°.

From the assumption of an orthotropic material, the earing appearance between 0°C to 90°C should be identical to the profile in the 90° to 180° quadrant [56]. While, for AA70XX T76, good agreement was found for the ear in the TD, some asymmetry was found for the ear in the DD. Several factors could account for this asymmetry, including alignment of the blank centre with the die and punch, as the alignment when scanning the flange profile. For the purpose of this study, the accuracy of the earing profile for comparison with FE model predictions was considered acceptable. As observed by Yoon *et al.* [56], the R-value in a certain direction correlated well with the earing profile in the same direction rotated by 90°. The high R-value in the TD represents increased resistance to thinning, hence less material flow that resulted in a lower draw-in length in the RD.

Figure 92 depicts the earing profile for the AA7075 T76 cup. Even though asymmetry in the earing profile was observed, the trend and number of ears correlated well with the R-value evolution; a

reduced draw-in length, hence the presence of an ear, was recorded for peak R-values such as in the DD and TD. While the material in the second quadrant was somewhat off, the total number of eight ears was in good agreement with measured strain anisotropy by Rahmaan [3].

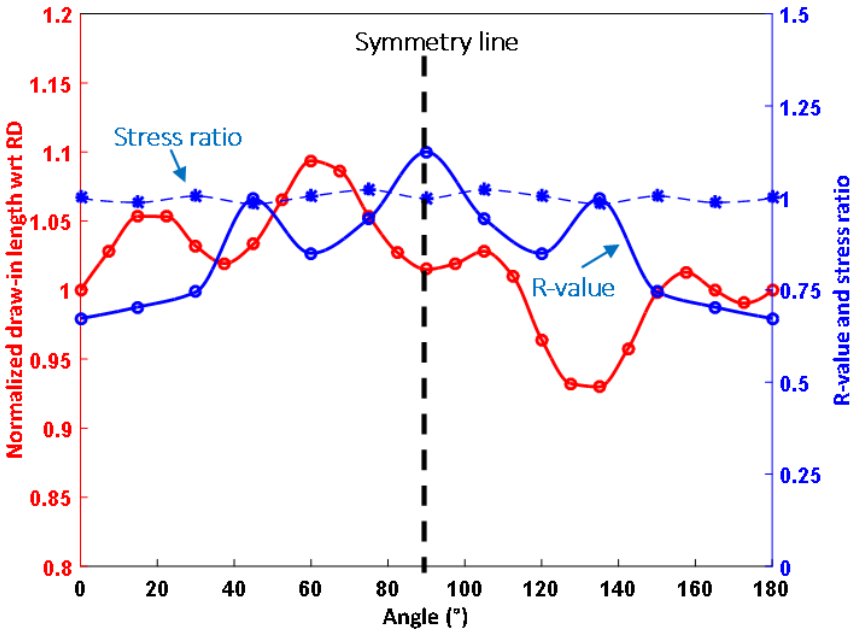

Figure 92: Measured draw-in length for AA7075 T6, normalized with respect to the RD (red solid curve), is compared to the variation in the R-value (solid blue line) and stress ratio (dashed blue line) in 15° increments relative to the RD obtained by Rahmaan [2]; note that the strain and stress ratios are mirrored about 90°.

Compared to AA70XX T76 and AA7075 T6, peak-aged AA6013 differed least from a perfect circular flange profile. As shown in Figure 93, mild asymmetry between the first and the second quadrant was observed for this alloy as well. A somewhat poor correlation between draw-in length and the variation in R-value along the RD was found. In contrast to AA70XX T76, that exhibits a large variation in R-value from the RD (0.68) to the TD (1.87), AA6013 T6 only varies from 0.8 (RD) to 1.0 (TD). Accounting for the standard deviation of 0.04 and 0.13 in the RD and the TD, respectively, AA6013 T6 seems to exhibit almost planar isotropy (R-values which deviate from unity but do not vary in the plane). This behavior might explain the somewhat poor correlation with observed R-values.

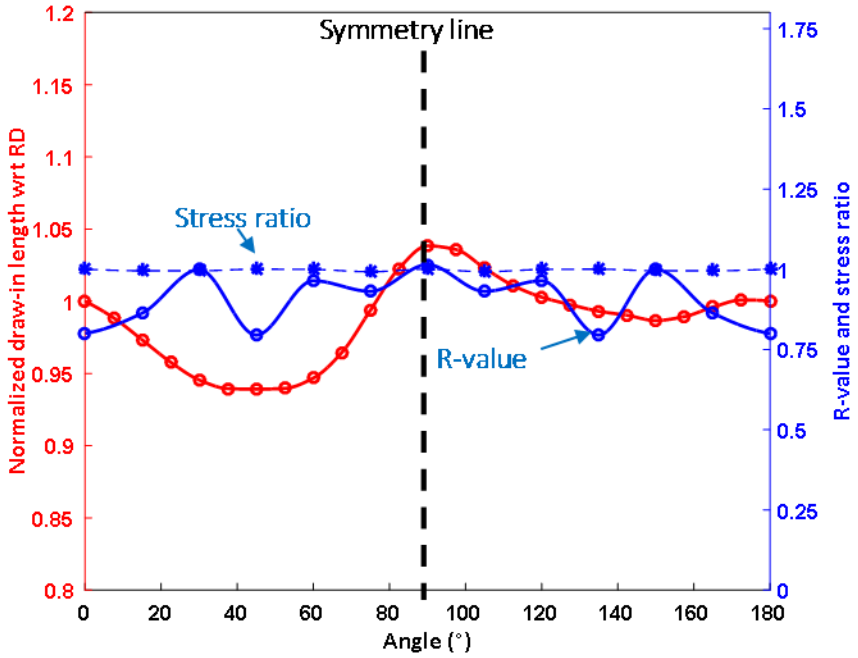

Figure 93: Measured draw-in length for AA6013 T6, normalized with respect to the RD (red solid curve), is compared to the variation in the R-value (solid blue line) and stress ratio (dashed blue line) in 15° increments relative to the RD obtained by Rahmaan [2]; note that the strain and stress ratios are mirrored about 90°.

4.6.4 Surface Strains

Optical measurements with Argus, provided major and minor strain distributions for the final AA70XX T76, AA7075 T6, and AA6013 T6 cup and are plotted in Figure 94, Figure 95, and Figure 96, respectively. Major strain in the RD and along the cup profile are plotted in Figure 97 and demonstrates a symmetric strain distribution. Whereas AA6013 T6, represented by the yellow curve, recorded a peak major strain in the transition from cup flange to sidewall of roughly 59%, AA7075 T6 (turquois curve) and AA70XX T76 (blue curve) exhibited 67% and 101%, respectively.

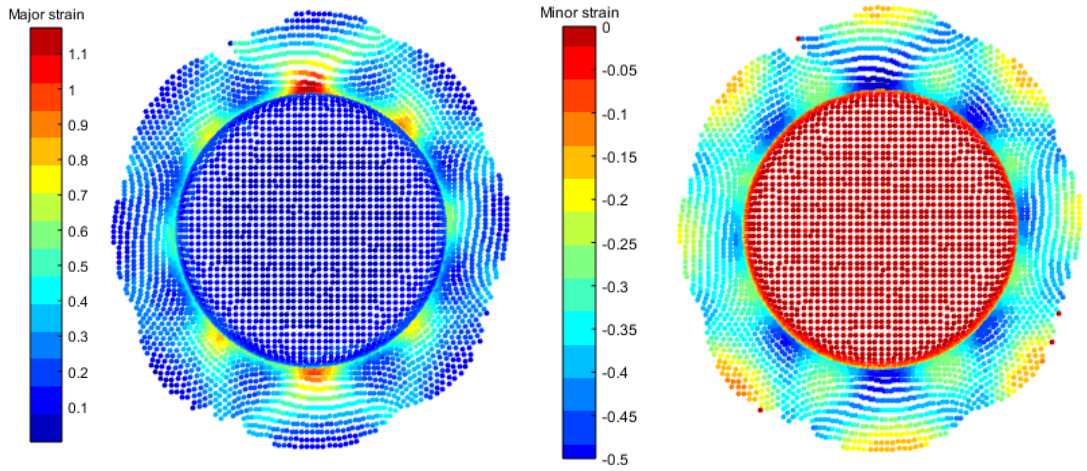

a) Major strain b) Minor strain

Figure 94: Strain distribution in the AA70XX T76 cup formed under non-isothermal conditions utilizing Teflon film.

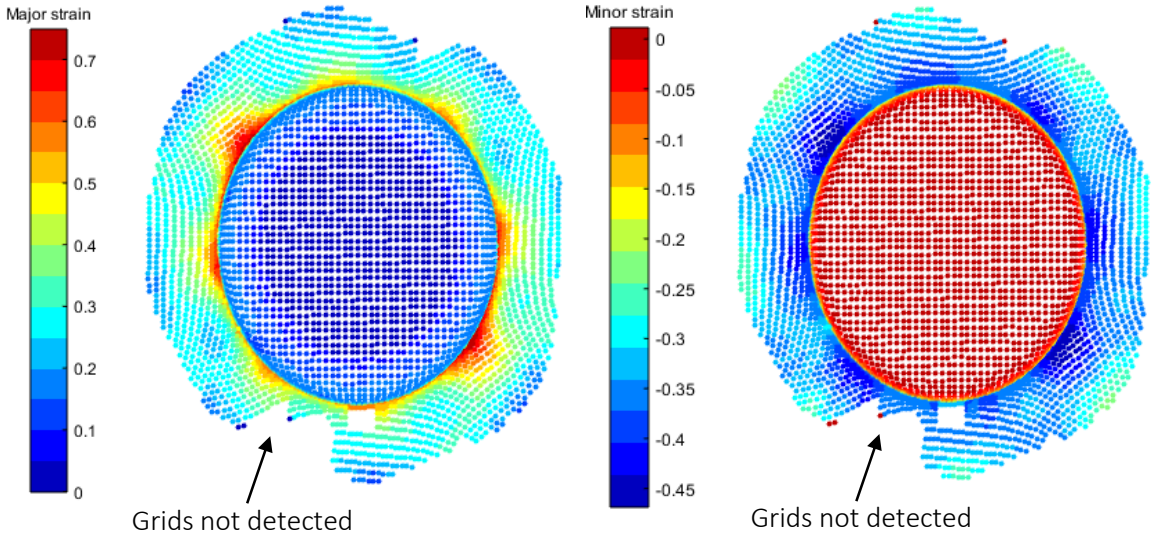

a) Major strain b) Minor strain

Figure 95: Strain distribution in the AA7075 T6 cup formed under non-isothermal conditions utilizing Teflon film.

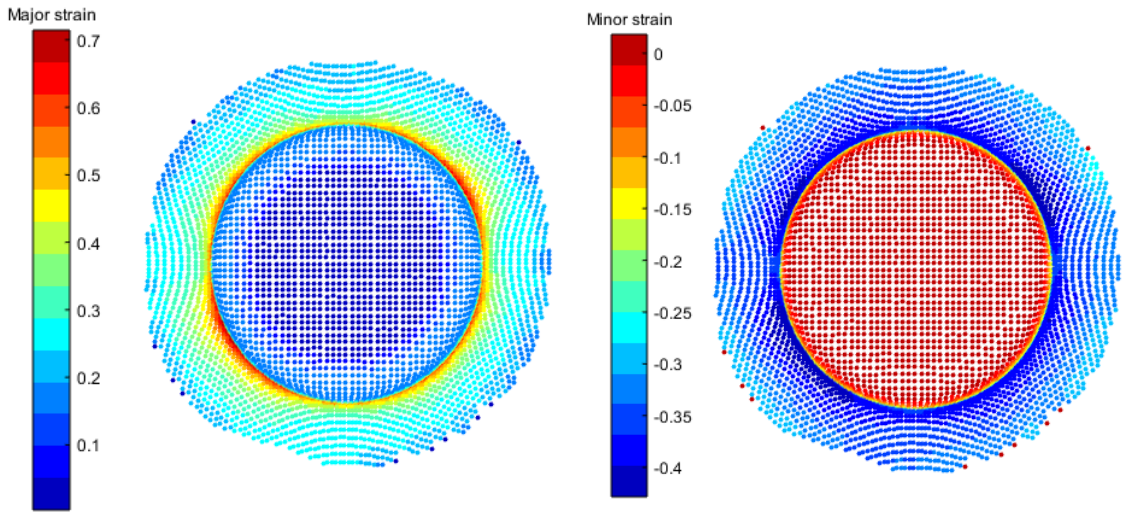

a) Major strain b) Minor strain

Figure 96: Strain distribution in the AA6013 T6 cup formed under non-isothermal conditions utilizing Teflon film.

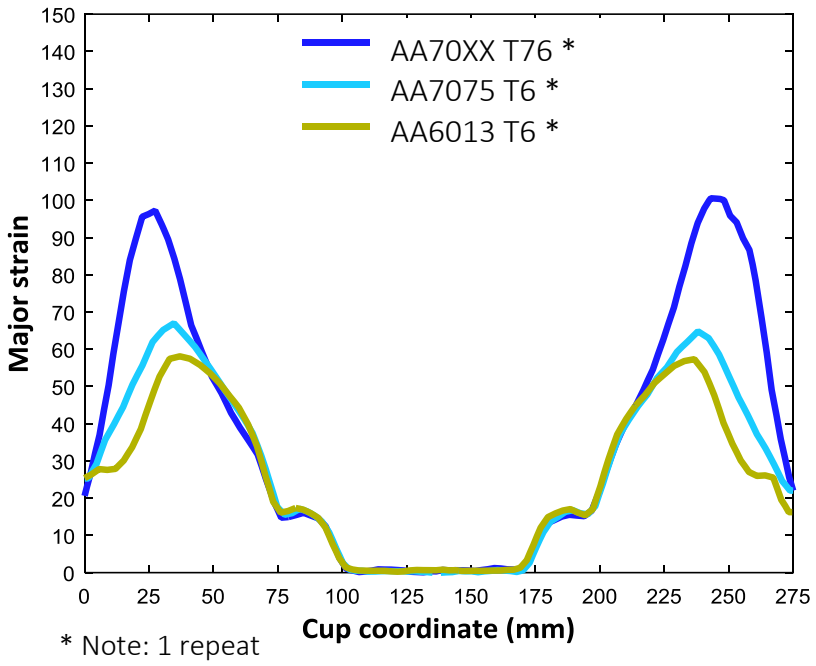

Figure 97: Major strain distribution along the cup profile in the RD. Cups were formed under non-isothermal conditions (die and binder at 200°C with the punch at 100°C) utilizing the Teflon film.

With the intention of gaining insight into the strain state at different locations on the drawn cup, the minor to major strain ratio was computed for a line path aligned with the RD along the cup profile,

illustrated in Figure 98. Note that since the cup hat region exhibited negligible strain (see also Figure 94b), the strain ratios were only plotted up to the punch profile radius.

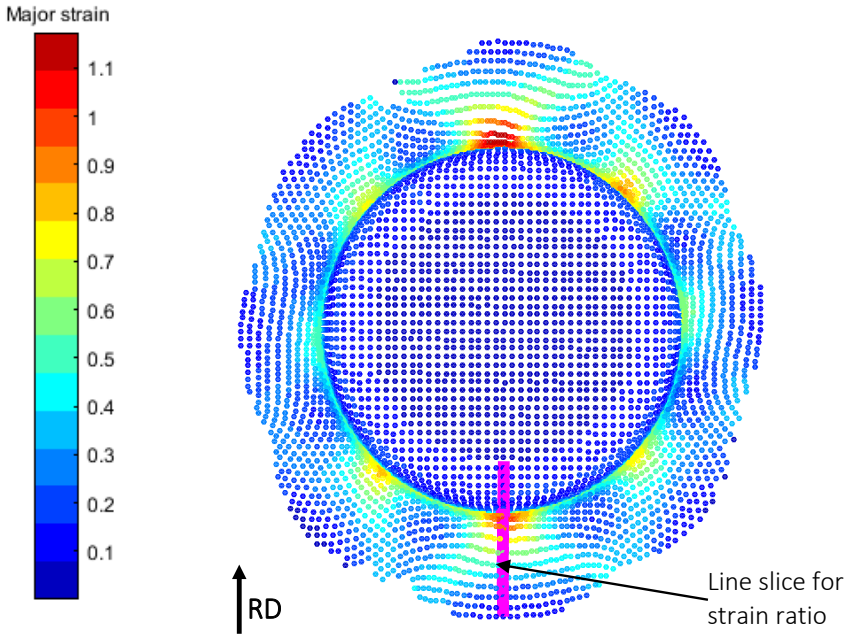

Figure 98: Major strain distribution and position of the line slice (pink color) aligned with the RD of the AA70XX T76 cup drawn under non-isothermal conditions using the Teflon film.

From the strain plots in Figure 99 and Figure 100 it can be seen that the flange region was characterized by a state of shear that was confirmed by a strain ratio close to -1, whereas the sidewall was subjected to uniaxial tension and then transitioned to plane strain in the hat radius. It is important to note that these strains reflected total values and did not provide a history of the strain evolution. The sidewall, for example, did not undergo a proportional strain path, but incurred bending and unbending before it finally transitioned into a uniaxial strain state.

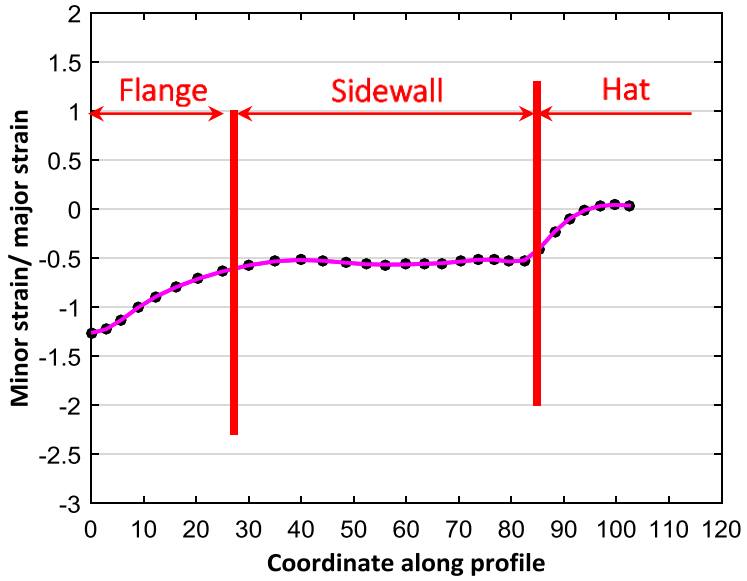

Figure 99: Ratio of minor to major strain along the cup profile of AA70XX T76 formed under non-isothermal conditions using the Teflon film; strain ratios refer to final state in the formed part

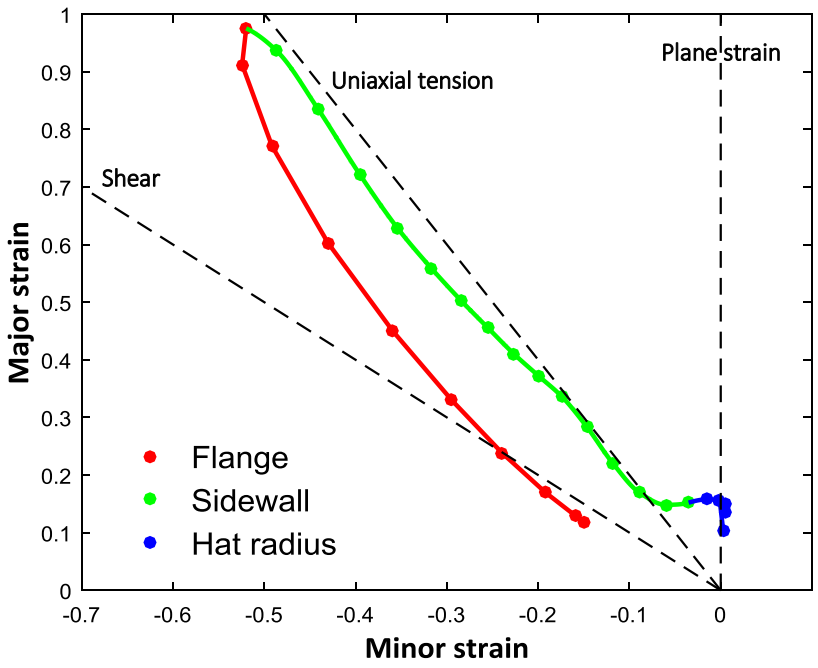

Figure 100: Major strain over minor strain for grid points along the profile of an AA70XX T76 circular cup formed under non-isothermal conditions utilizing the Teflon film; strain ratios refer to final state in the formed part

4.6.5 Summary of Non-isothermal Deep Drawing

Non-isothermal deep draws with the die and binder at 200°C and the punch at 100°C were performed since cooling, and hence strengthening, of the contact zone between punch radius and blank facilitated drawing of larger blanks yielding higher plastic strains. This observation, in addition to longer sliding distances and temperature gradients, was felt to be well-suited for evaluation of the material anisotropy and warm friction response in an experimental-numerical study. This chapter discussed the experimental work whereas Chapter 5 elaborates on the model development. AA70XX T76 (a 7xxx series aluminum alloy under development), AA7075 T6, and AA6013 T6 blanks with an initial diameter of 228.6 mm were drawn to a target depth of 75 mm (leaving a 20 mm wide flange). The observed earing profile on formed cups correlated well with the R-value evolution for AA70XX T76 and AA7075 T6; a total of eight strongly pronounced ears and eight slightly defined ears for AA70XX T76 and AA7075 T6, respectively. For AA6013 T6, R-value evolution suggested near planar isotropic properties for that a slightly ellipsoidal flange was observed. Compared to AA6013 T6, AA70XX T76 and AA7075 T6 required approximately 2.9% and 15.5% higher process forces, respectively. The thermal history has a key impact on the material flow stress and represents an important metric for the simulation model. From attached thermocouples to the blank, a temperature drop from 176°C to 130°C was recorded for the blank center, at the stroke end. Surface strains in the RD, on the final cup, revealed peak major strain values of 101%, 67%, and 59% for AA70XX T76, AA7075 T6, and AA6013 T6, respectively.

5 Model Development

The motivation for developing a constitutive model and for evaluating its performance at coupon-level lies in the cost and time savings for designing full-scale industrial components and forming operations. Cup drawing with a target depth of 75 mm and under non-isothermal conditions allowed the combined evaluation of several disciplines studied in this work. Large plastic strains facilitated study of the material anisotropy, long sliding distances involved friction, and forming over a temperature gradient highlighted the need for a thermo-viscous constitutive model. In light of its novelty, AA70XX T76 – a 7xxx series aluminum alloy under development – was selected for the model development in this work. Considering the observed eight ears in the cup flange, material characteristics of AA70XX T76 suggest high directionality that required advanced material models to accurately capture this behavior. Models were developed of blanks with an initial diameter of 228.6 mm, drawn to a target depth of 75 mm (leaving a 20 mm flange for post-processing). To facilitate forming without fracture, a die and binder temperature of 200°C with the punch at 100°C was found suitable. Measured earing profile, force-displacement, thermal history, and surface strain data from the Argus optical strain measurements were adopted as validation parameters to assess the numerical model.

The chapter is structured into three sections and opens with the adopted material model, followed by a discussion on the FE model set-up. Finally, model predictions are compared to experimental measurements from Section 4.6. For this study, LS-DYNA, LS-PrePost, and HyperMesh were utilized as solver, pre- and post-processor, respectively.

5.1 Material Model

The implemented material model was retrieved from material characterization efforts discussed in Chapter 2. Rahmaan [2] and DiCecco [1] performed tension, shear and through-thickness compression tests from that R-values and stress ratios in 15° increments relative to the RD, as well as flow stress curves were extracted. As was demonstrated through the presence of eight ears in circular cup draws of AA70XX T76, the alloy exhibits a high level of in-plane anisotropy and requires advanced anisotropic yield functions to accurately capture this behavior. Hence, earing prediction utilizing the following yield functions and flow rules was studied in a parametric fashion:

(i) Associative Barlat YLD2000-2d [4]

(ii) Non-associative Barlat YLD2000-2d [4]

(iii) Non-associative Barlat YLD2000-2d [4] and Hosford [5]

The first case represents the standard version that is also available as a built-in function in LS-DYNA. While this case assumes that the plastic potential and the yield stress function are described through one common set of calibrated anisotropy coefficients, the non-associative flow rule offers more flexibility. For the latter, a separate set of eight coefficients is available for each the plastic potential and the yield stress function; hence, the material anisotropy can be described in more detail. Instead of adding complexity and effort by calibrating YLD2000-2d for the plastic potential and the yield stress function, the isotropic Hosford yield function is suggested for the latter in light of the very mild stress anisotropy observed for all studied alloys in this work. Calibration of studied yield surfaces was performed by Abedini [18] and the results are plotted in Section 2.3 in Figure 32; anisotropy coefficients are documented in Table 12.

Flow-stress curves obtained from DiCecco [2] and Rahmaan [3] suggested a rate-insensitive material response at room temperature and a strongly rate-dependent yield and flow stress at elevated temperature. It has been demonstrated in Section 2.4 that, compared to the physically-driven Bergström and the phenomenologically-derived extended Nadai model, the developed model in this thesis captures the observed material behavior more accurately. The proposed model utilizes a simplified Hockett-Sherby model that describes the saturation stress as a function of the material yield stress and hardening exponent that are both a function of the temperature. To account for rate-effects, the flow stress term is scaled through a temperature-sensitive term. Optimized calibration coefficients for AA70XX T76 are summarized in Table 17.

Simulation results revealed that the strain rate during the studied deep drawing operation ranged from an average of about 0.1 s^{-1} to peak values of 0.3 s^{-1} within a temperature window of 130°C to 205°C. Model predictions for this process window are plotted in Figure 101.

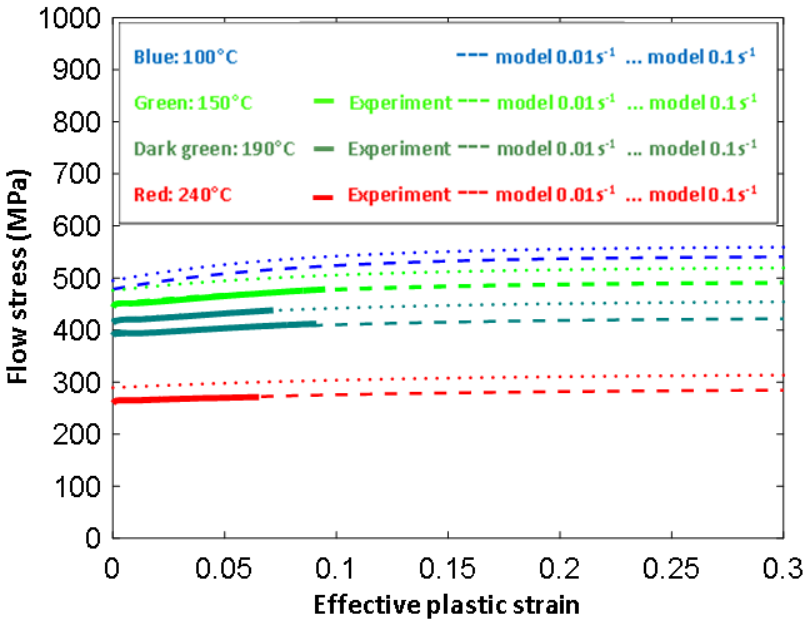

Figure 101: Model predictions for material flow stress within the temperature and strain rate range of the deep drawing operation; a developed model derived from the Hockett-Sherby model is utilized

The current implementation of constitutive models in the solver LS-DYNA supports the Barlat YLD2000-2d yield function, however, it does not consider temperature-dependency of the hardening behaviour of the material. The current work is focussed on elevated temperature forming, for that a temperature- and strain rate-sensitive hardening model is of critical importance. Hence, in the following study a user-defined material sub-routine (umat), implemented by Prof. Butcher [6], was utilized.

The umat constitutive routine [6] uses an incremental plasticity approach that is passed in initial stress state, strain increment, and history variables of the previous time step as initial conditions of the new step. Under the initial assumption of elastic deformation and with the use of the material elasticity tensor, a so-called trial stress is computed. At the same time, the size of the yield surface is calculated based on the employed hardening law. In the next step the location of the trial stress with respect to the yield surface is checked. If the stress state is inside, the assumption of elastic deformation is valid and the trial stress is set equal to the actual stress. Violation implies plastic deformation for that the trial stress is iteratively returned to the yield surface through a standard return-mapping algorithm [125] until a prescribed tolerance of $1*10^{-6}$ times the yield stress is met. Note that the code structure accommodates the plastic potential being same as the yield function (associative flow rule) or different from the yield function (non-associative flow rule).

The thermal material response of the blank and the tooling is computed through an isotropic material model. The tooling is assigned an isotropic rigid material with properties of Dievar tool steel [121] for which neither strain nor stresses are computed with the intention of enhancing computational efficiency. Material properties are listed in Table 25.

Table 25: Material properties assigned to the tooling and the blank in the FE model

	Blank (AA70XX T76 [113])	Tooling (Dievar tool steel [121])
Density	$2.81*10^3$ kg/m^3	$7.8*10^3$ kg/m^3
Young's Modulus	see Table 6	$2.1*10^5$ MPa
Heat capacity	$9.6*10^4$ J/kg K	$4.6*10^2$ J/kg K
Thermal conductivity	130 W/m K	31 W/m K

5.2 Model Set-up

The geometry of the simulation model is shown in Figure 102 and comprises a blank, binder, punch, and die. Note that for visualization of the blank position, the first few rows of elements within the binder have been removed. In addition, only one-quarter of the geometry was simulated due to symmetry about the x- and z-axes. This feature is a convenient way of enhancing the computational efficiency, however, to prevent any resulting changes to the deformation behavior of the blank, appropriate symmetry conditions were enforced.

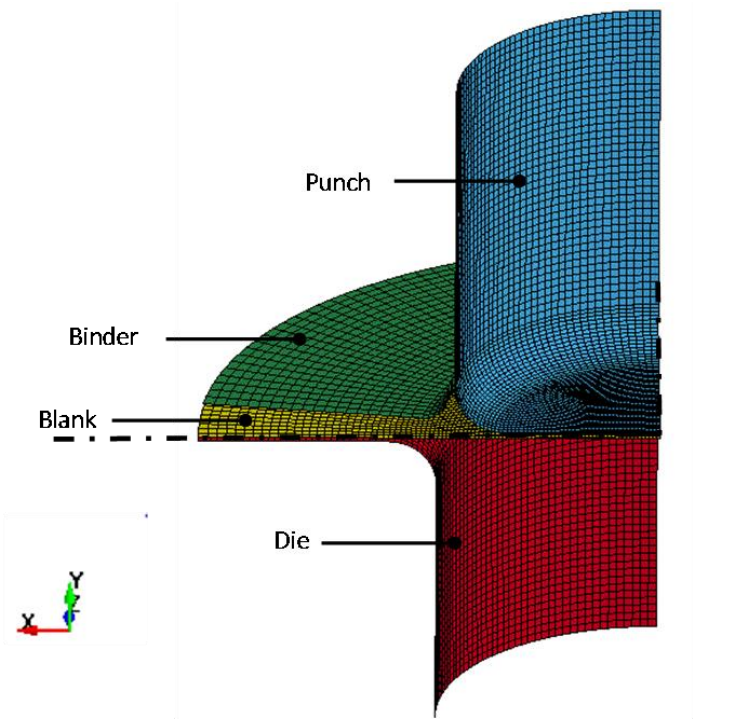

Figure 102: Geometry of the simulation model for deep drawing

The 2 mm thick blank had a diameter of 228.6 mm and was discretized with quadrilateral shell elements ranging from 0.8 mm to 3.4 mm in length. For the tooling, 1.6 mm quadrilateral elements were utilized along the radius to ensure proper contact detection. A thick thermal shell formulation was utilized that computes a temperature gradient through the shell thickness and therefore captures the temperature history of the blank more accurately. With respect to integration, instead of the standard Gaussian integration rule, the Lobatto method, with five through thickness integration points, was selected. The reason for this choice lies in the position of the inner and outer integration points on the surface that facilitated one-to-one comparison to surface strains from Argus optical strain measurements.

The constant die and binder temperature of 200°C, in the physical forming process, were replicated in the simulation model through a prescribed thermal boundary condition that was enforced throughout the simulation. In contrast, the punch was only prescribed an initial temperature of 100°C and experienced an increase in temperature during forming. Recorded thermocouple readings (attached during deep drawing, discussed in Section 4.3.3), confirmed a temperature gradient along the blank

profile. Measured temperature values at the onset of forming were assigned to the respective blank sections: 176°C, 184°C, and 195°C in the blank center, sidewall, and flange, respectively. Figure 103 illustrates this point and records the initial fringe plot issued by the numerical model.

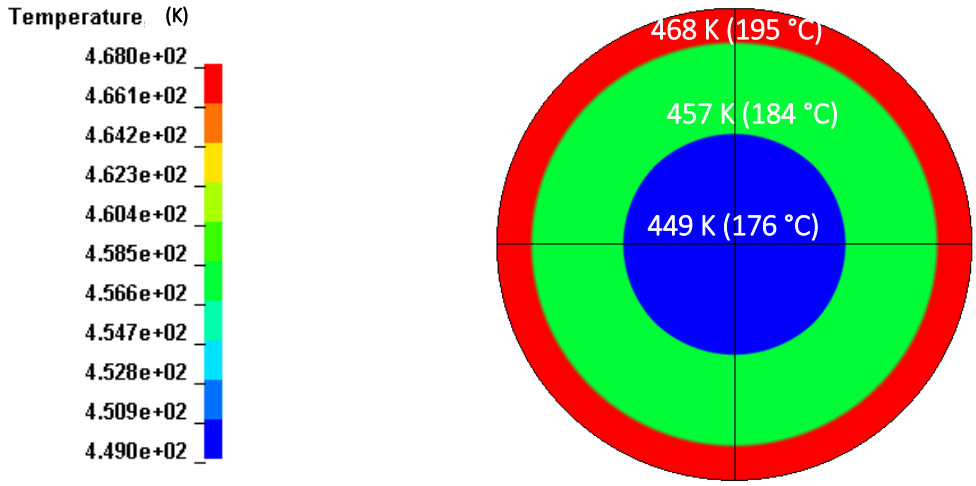

Figure 103: Initial temperature assigned to the blank in the FE model, obtained from attached thermocouples during forming

During the forming process, the die translational and rotational degrees of freedom were fully constrained whereas the binder and the punch were allowed translational displacement in the y-direction. To prevent inertial effects, the binder load of 25 kN was applied through a linear ramp function. Note that this magnitude refers to only one quarter of the total load in view of the quarter-symmetry assumption. An additional constraint was applied to the binder that constrained its movement to 0.1 mm/s with the intention of keeping the binder closed during forming. Punch movement was realized through a velocity-controlled boundary condition that utilizes 5% of the punch stroke time to accelerate and decelerate the punch to and from a peak simulation velocity of 500 mm/s. Note that the experimental punch speed corresponded to 1 mm/s and that use of time-scaling was made in the simulation model. Thermal properties and strain rates were scaled accordingly. A two-way thermo-mechanical penalty-based contact algorithm was utilized between the blank and tooling. The friction coefficient was input as a function of temperature obtained from the TCT (see Appendix A) and the frictional shear stress was limited to the factor 0.58 of the material yield stress that would correspond to a galling condition. Values for heat contact conductance as a function of contact

pressure were experimentally obtained for AA70XX T76 by Omer *et al.* [111] and are summarized in Table 26.

Table 26: Heat transfer coefficient as a function of contact pressure for AA70XX T76 [111]

Contact pressure	Convection in air	2 MPa	5 MPa	12.5 MPa	25 MPa	40 MPa	60 MPa
htc (W/m^2K)	20.5	355	501	620	750	1010	2800

In view of the open die design (see Figure 104), during forming, the lower blank surface cooled down through convection with the ambient air. This temperature loss was accounted for in the simulation model with a convection boundary condition that was applied to the outer blank shell section that was not in contact with the tooling.

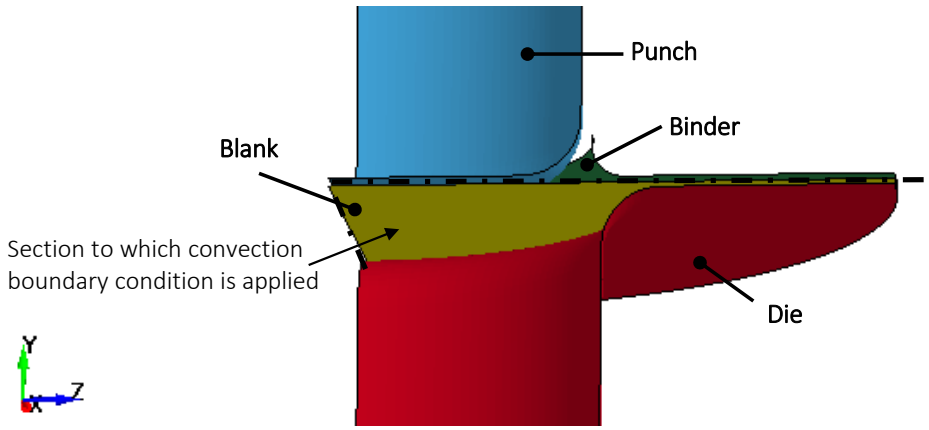

Figure 104: Blank section to that a convection boundary condition was applied in the numerical model

The distance for thermal contact detection was set to 0.05 mm that was found to correlate well with recorded thermocouple readings in the blank center in Figure 105. The simulation underpredicted the cooling behavior by approximately 11°C, as seen in Figure 105, which might be associated to the discretization of the punch with shell elements instead of volume elements. Nevertheless, since the thermal deviation was moderate, it was assumed that the effect on the material flow behavior was minor and that the simulation model predicted the thermal behavior reasonably well.

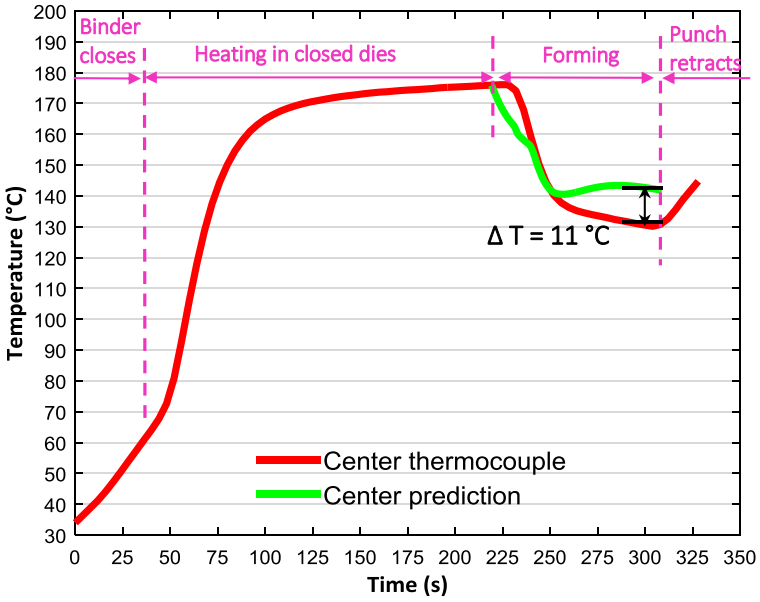

Figure 105: Comparison between measured and predicted temperature evolution in the blank center during circular cup drawing of AA70XX T76 under non-isothermal conditions (die and binder at 200°C with the punch at 100°C)

A coupled thermo-mechanical simulation was performed within LS-DYNA. For the thermal solver a fully implicit solution algorithm with a symmetric direct solver and a flexible time step, that was restricted to a maximum temperature change of 2.5°C, was selected. In view of the nonlinearities such as curved geometry, contact, and considerable plastic deformation, a dynamic explicit mechanical solver was selected. Mass scaling was utilized to improve computational efficiency by prescribing a timestep of $1*10^{-6}$ to the lower bound of the explicit timestep.

Considering the fine mesh and applied boundary conditions to the blank, initial simulation run-times revealed that computational times of the thermal solver were unreasonably high. As a result, the following simplifications were employed. Instead of computing the heat transfer between the blank and the tooling, a time-dependent thermal history was prescribed to the blank. Conditions for thermal loading were obtained from the computed thermal history of a thermo-mechanical analysis, with a von Mises material model, under the aforementioned boundary conditions. Resulting temperatures in the respective flange, sidewall, and hat section were averaged and prescribed to the blank in the form of a time-dependent temperature evolution, shown in Figure 106. This simplification allowed a reduction to a structural instead of a thermo-mechanical analysis. Hence, simulation times were

approximately 3.5 hours that were within reasonable time windows to perform the yield surface parameter study discussed at the beginning of this chapter.

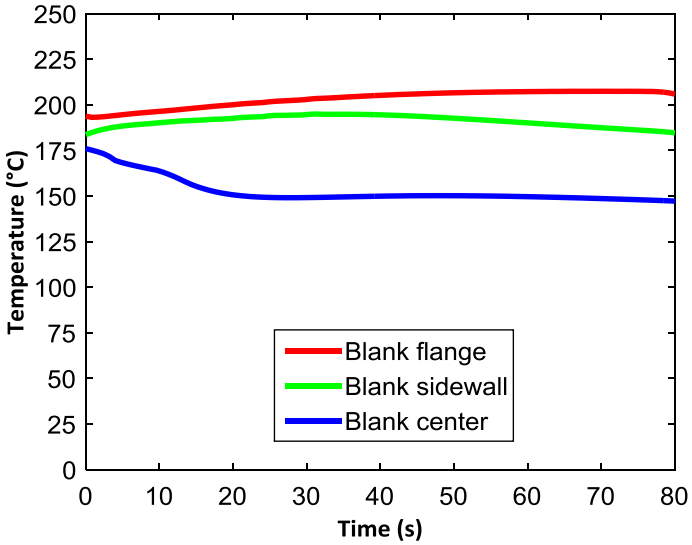

Figure 106: Applied thermal history to respective sections in the blank in the FE model with the intention to run a structural instead of a thermo-mechanical analysis

5.3 Simulation Results

This section compares the model predictions with experimental results from Section 4.6 for non-isothermal deep drawing of AA70XX T76, a 7xxx series aluminum alloy under development, utilizing the Teflon film. First, the predicted number of ears were utilized to downselect the yield function/ flow rule that could predict all of the observed eight ears. In a second round, the draw-in length along the RD was studied and the yield function/ flow rule that most accurately captured the experimental draw-in length, was selected for force-displacement comparison and discussion of surface strains from the Argus optical strain measurements.

5.3.1 Prediction of Earing Profile

Figure 107 illustrates the equivalent plastic strain and the earing profile for the studied yield functions and flow rules. Note that for visualization purposes, the quarter model was mirrored to plot as a full cup. Figure 107a represents a perfectly circular cup predicted by the isotropic yield function Hosford, that was initially selected to validate the umat. The predictions by the associative Barlat YLD2000-2d (Figure 107b) exhibited four ears; this deviation from the observed eight ears was somewhat expected.

Since the associative flow rule only provides eight anisotropy coefficients to describe the material strain and stress directionality, the detail to that the material response can be described is limited. This shortcoming was demonstrated in Section 2.3; for associative YLD2000-2d the variation in R-values between the RD and the DD, and the DD and the TD was not well-captured. In contrast, both non-associative Barlat YLD2000-2d (Figure 107c) and non-associative Hosford-Barlat YLD2000-2d (Figure 107d) predicted eight ears. The predicted R-value evolution by non-associative Barlat YLD2000-2d in Section 2.3, Figure 32a, demonstrated the improved accuracy by assigning a separate set of anisotropy coefficients to each the plastic potential and the yield stress function. Localized peak plastic strain values of roughly 1.2 were recorded for some elements in the flange contour that was caused by severe element distortion.

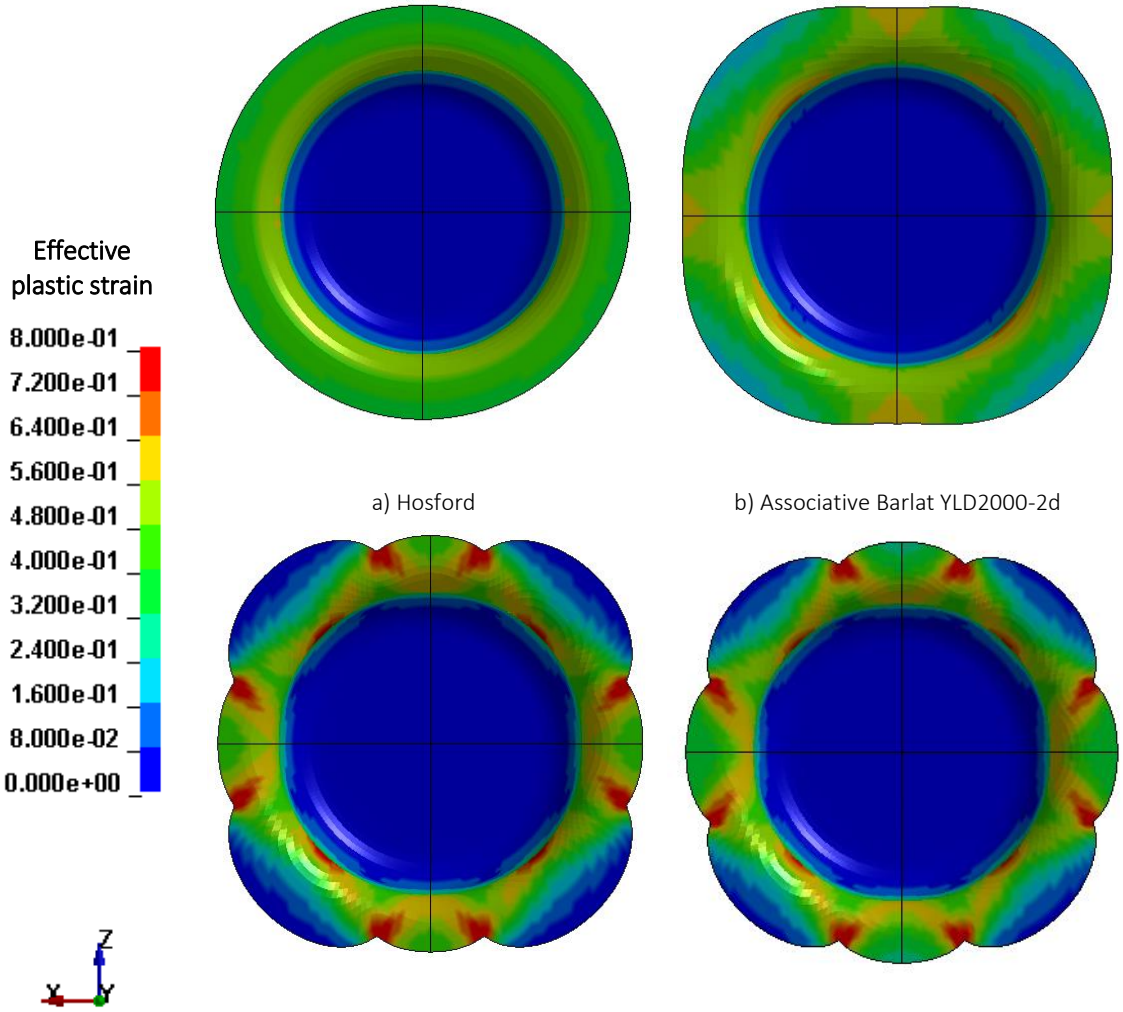

a) Hosford

b) Associative Barlat YLD2000-2d

c)Non-associative Barlat YLD2000-2d

d)Non-associative Barlat YLD2000-2d and Hosford (yield stress function)

Figure 107: Predicted earing profile by various yield functions and flow rules for AA70XX T76 under non-isothermal conditions; the drawing ratio corresponded to 2.25.

Since only the models utilizing a non-associative flow rule predicted eight ears, the draw-in length of these two cases was studied further. The developed script in Section 4.5.4 for computation of scanned flange profiles of circular cups was utilized to capture the draw-in length in 7.5° increments relative to the RD. The detected flange profile for the non-AFR Barlat YLD2000-2d and Non-AFR Hosford-Barlat YLD2000-2d is plotted in Figure 108 and Figure 109, respectively, from that the draw-in length could be extracted.

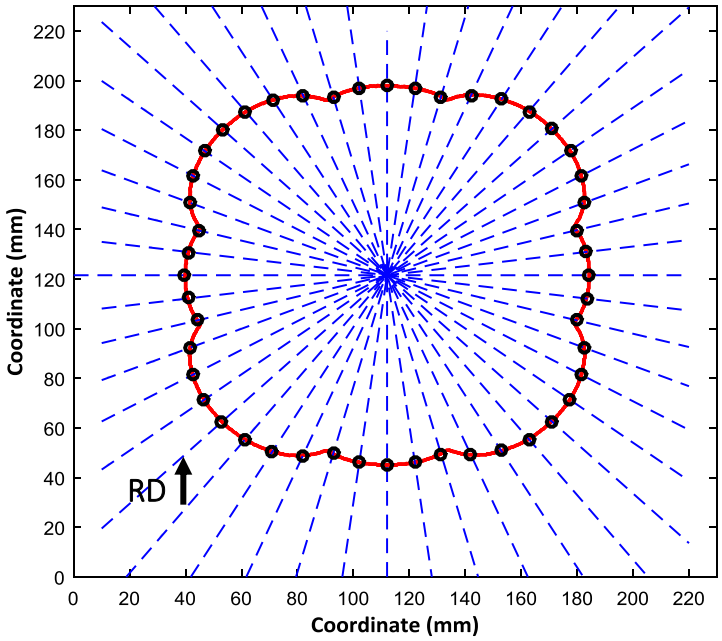

Figure 108: Scanned flange profile of an AA70XX T76 cup simulated under non-isothermal conditions utilizing non-associative Barlat YLD2000-2d

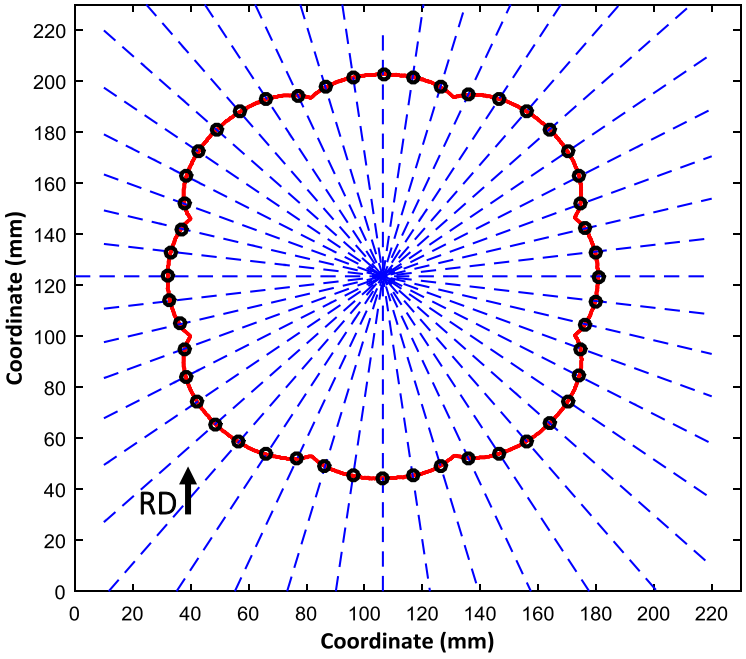

Figure 109: Scanned flange profile of an AA70XX T76 cup simulated under non-isothermal conditions utilizing non-associative Hosford-Barlat YLD2000-2d for the the yield stress function and for the plastic potential, respectively

Figure 110 plots the draw-in length in 7.5° increments relative to the RD where measurement points are marked with circles. While the trend was generally captured by non-associative Barlat YLD2000-2d, in green color, the ears in the DD and TD are somewhat deviating from the experiment. The predicted earing profile using the non-associative Hosford-Barlat YLD2000-2d model for the yield stress function and for the plastic potential, in blue color, was in better agreement with the experiment. The draw-in length in the RD and the TD was overpredicted by both yield functions that might be due to boundary conditions such as friction and prescribed thermal history. To explore this potential source of error, the earing profile was computed under the assumption of a COF of 0.03, that corresponds to Fuchs at 170°C for a sliding distance of 50 mm, obtained in the TCT in Appendix A, and imaginary higher COF of 0.06 for comparison purposes. For the latter, localized straining in the sidewall elements was observed and is therefore not included in the results in Figure 111.

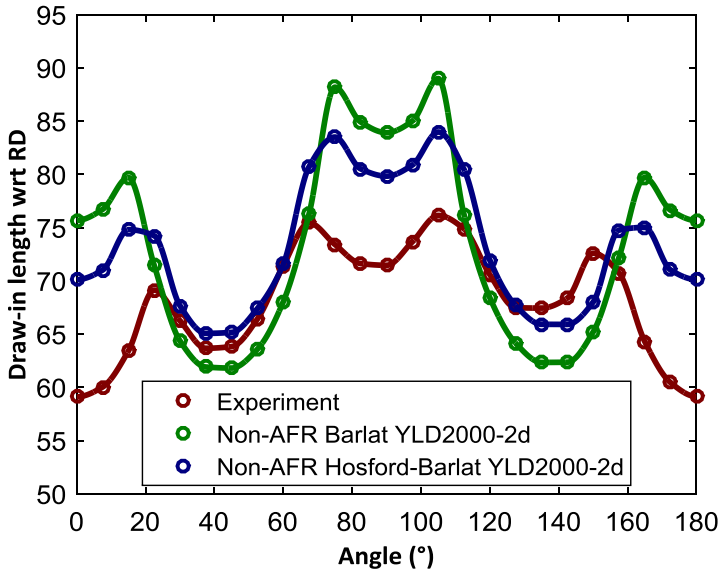

Figure 110: Draw-in length with respect to the RD measured (red color), predicted by non-associative Barlat YLD2000-2d (green color) and by non-associative Hosford-Barlat YLD2000-2d (blue color) for the yield stress function and the plastic potential, respectively

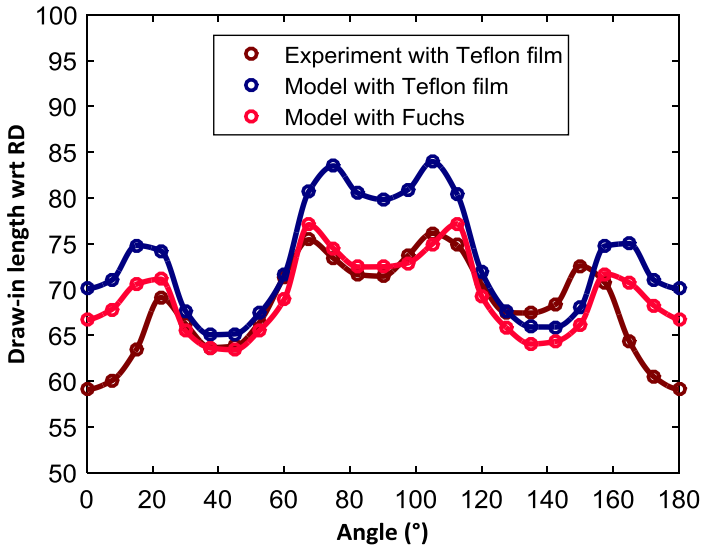

Figure 111: Draw-in length with respect to the RD measured (red color) and predicted by non-associative Hosford-Barlat YLD2000-2d for the yield stress function and the plastic potential, respectively, under different frictional conditions (COF 0.007 for Teflon film and 0.03 for Fuchs)

The pink curve in Figure 111 represents model predictions for Fuchs whereas the predicted earing profile utilizing Teflon film is depicted in the blue curve. Even though both lubricants have a very low friction coefficient (0.007 for the Teflon film and 0.03 for the Fuchs), the effect on the draw-in, particularly in the TD, was significant and reflected experimental observations made earlier. Cups formed utilizing the Fuchs, in Section 4.6.3, exhibited a supressed earing profile compared to deep draws utilizing the Teflon film. It is worth noting that the COF utilized for Fuchs and Teflon film were obtained in the TCT at a temperature of 170°C and for a sliding distance of 50 mm (corresponding to conditions of the target warm forming process), whereas the cup depth for this study was 75 mm under varying thermal conditions. This occurrence highlights the importance of a combined modeling approach, hence accurate description of the material model as well as friction characterization.

5.3.2 Force-displacement Prediction

Since the non-associative Hosford-Barlat YLD2000-2d model captured the observed earing profile most accurately, force-displacement and surface strain are discussed for this yield function and flow rule with the Teflon film lubricant. Figure 112 compares the measured punch force (brown curve) to the predicted force in blue color. While the solid blue line accounted for rate effects in the constitutive model, the dashed line corresponded to force predictions under the assumption of a rate-independent

material behavior (flow-stress curves at the reference strain rate of 0.01 s^{-1} were utilized). Interestingly, the peak force of approximately 200 kN was in very good agreement with predictions by the rate-insensitive model (3% difference) whereas the force was overpredicted by roughly 11% when accounting for rate-effects. Considering that the average strain rate in the simulation was predicted 0.1 s^{-1} with peak values of 0.3 s^{-1}, the higher process forces by accounting for these effects were reasonable. At the same time, these observations emphasize the importance of a rate-sensitive constitutive model. The somewhat different force evolution in the second stroke part is believed to be due to the thermal boundary conditions in the simulation model. With the intention to speed up simulation times, the punch speed was time-scaled and a time-dependent thermal history was prescribed to the flange, sidewall, and hat section; hence, no computation of heat transfer was required that simplified the thermo-mechanical analysis to a structural analysis. As part of work in progress, a thermally-coupled model in the absence of time-scaling will be performed.

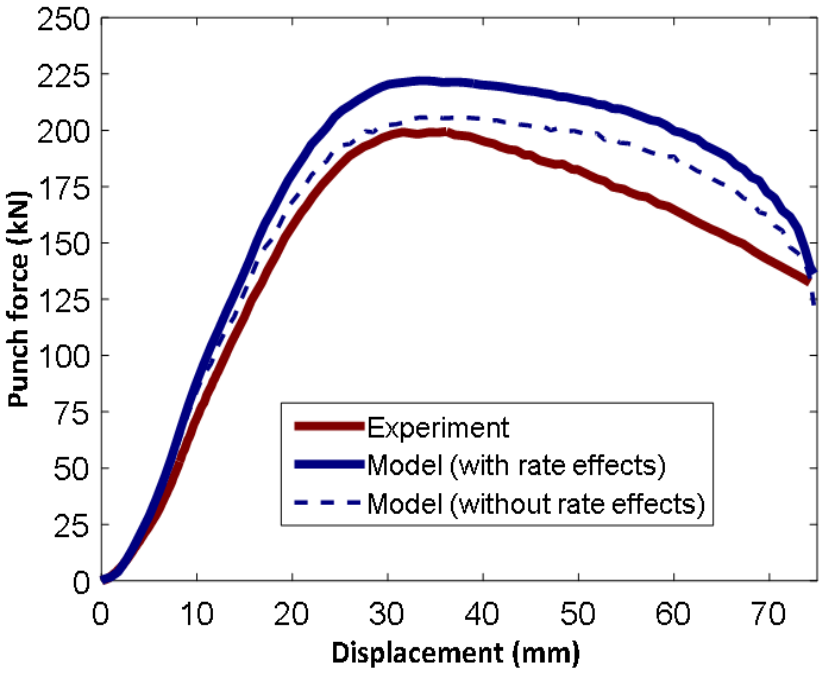

Figure 112: Measured punch force (brown) and predicted force (blue) by non-AFR Hosford-Barlat YLD2000-2d for the yield stress function and the plastic potential, respectively, for deep drawing an AA70XX T76 circular cup to a target depth of 75 mm under non-isothermal conditions

5.3.3 Predicted Surface Strains

Figure 113 and Figure 114 compare the major strain distribution between the surface strain from the Argus optical strain measurements and predictions using the non-associative Hosford-Barlat YLD2000-2d model. While acceptable agreement was observed for the major strain in the TD in Figure 114b, the major strain in the RD was somewhat underpredicted. Coupling the currently mechanical analysis with the thermal solver will yield a more realistic temperature distribution in the blank profile that directly influences the flow stress.

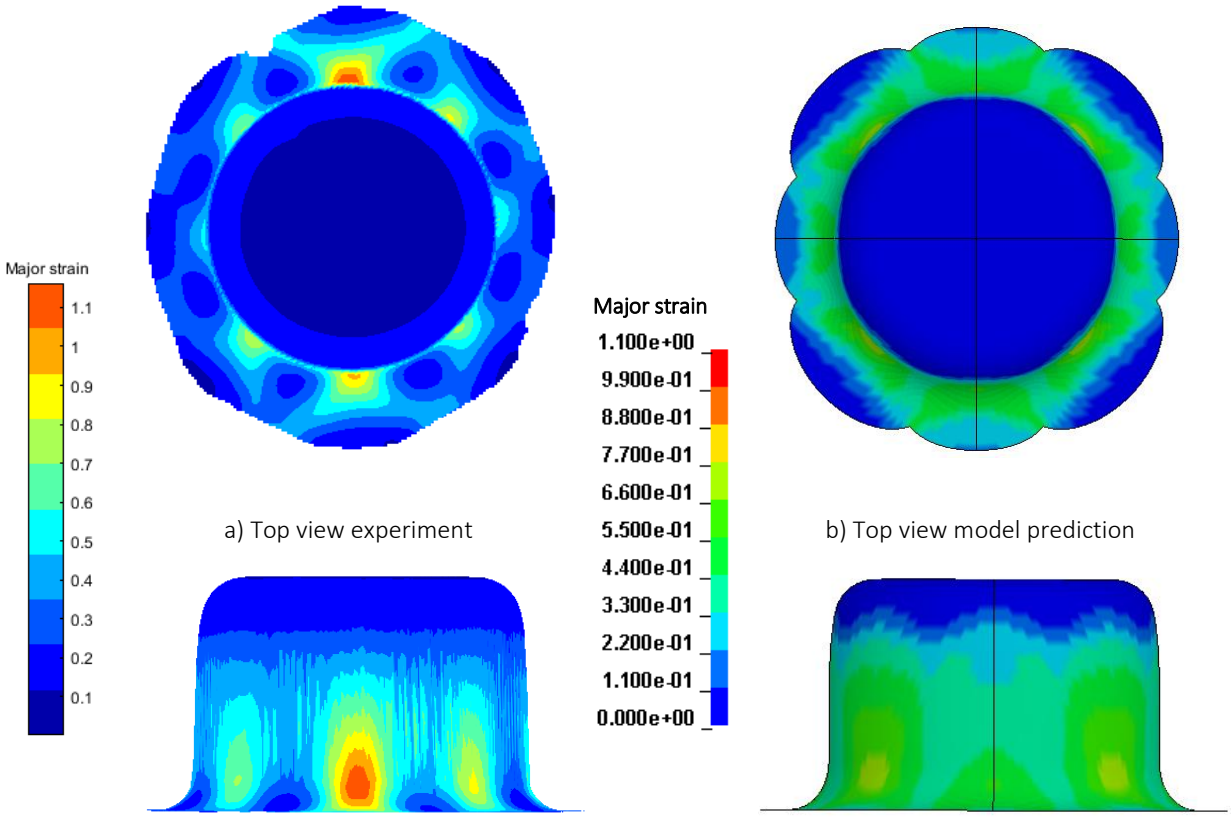

a) Top view experiment

b) Top view model prediction

c) Side view (RD) experiment

d) Side view (RD) model prediction

Figure 113: Major strain distribution in the non-isothermally drawn AA70XX T76 cup; left column represents experimental results from Argus optical strain measurements; right column refers to model predictions by non-associative Hosford-Barlat YLD2000-2d for the yield stress function and the plastic potential and, respectively.

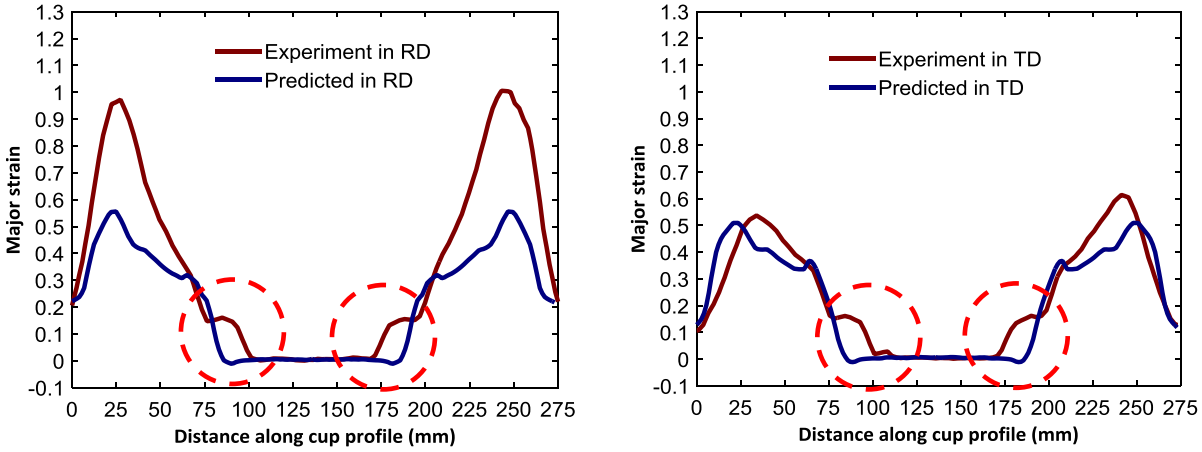

a) In the rolling direction

Figure 114: Comparison between major strain measurements and predictions by non-associative Hosford-Barlat YLD2000-2d for the yield stress function and the plastic potential and, respectively

Interestingly, for the strain distribution in both directions (Figure 114a and Figure 114b), the hat radius region, circled in red, exhibited very low strain whereas the experiment measured a sharp increase since this point represents the contact point with the punch radius and hence cools down fastest and undergoes hardening. The absence of this occurrence in the current predictions emphasizes the need for the thermo-mechanical coupling

5.4 Summary of Model Development

Circular cup drawing, discussed in Chapter 4, was modeled for AA70XX T76 (a 7xxx series aluminum alloy under development) under non-isothermal conditions (die and binder at 200°C and punch at 100°C). The initial 228.6 mm blank diameter was drawn to a target depth of 75 mm. For simplification, a temperature-dependent boundary condition was applied to the blank that allowed a mechanical analysis since no heat transfer was involved.

The developed thermo-viscous constitutive model, discussed in Section 2, was implemented in a umat provided by Prof. Butcher [6]. From a parameter study on various flow rules and yield surfaces, calibrated by Abedini [18], it was found that the associative Barlat YLD2000-2d could predict only four ears, whereas non-associative Barlat YLD2000-2d and non-associative Hosford-Barlat YLD2000-2d resulted in eight ears, as observed in the experiments. Comparison of the normalized draw-in length revealed that the non-associative Hosford-Barlat YLD2000-2d could predict the earing size more

accurately, while the draw-in length in the RD and the TD was slightly overpredicted by the model. The utilized friction coefficient was identified as a powerful impact on the earing height that was confirmed in experiments with the Fuchs and the Teflon film.

Both the punch force and the major strain distribution in the RD, obtained from Argus optical strain measurements, differed somewhat from experiments. It is believed that the adopted simplifications in addition to time-scaling of the punch velocity contributed to the observed deviations. A thermo-mechanical model is in progress.

6 Rail Warm Forming

This chapter represents knowledge transfer from the coupon-level characterization and validation work to a near-commercial structural part, hereinafter referred to as a "rail". In view of the sensitivity of 7xxx series aluminum alloys to thermal processing conditions, the aim of this forming study is to define the process window in terms of final part strength (determined through micro hardness measurements) and lubricant performance that was evaluated based on the surface quality of the as-formed parts. Even though formability is not believed to be an issue, given the simple part geometry, thinning was studied and could serve as future metric for rail forming simulations.

6.1 Forming Routes

Two different forming routes were investigated in the rail forming experiments. The conventional method represents forming under isothermal conditions for that the blank was heated through contact with the tooling. Contact heating allows short heating times and minimum heat exposure due to the absence of a temperature drop during transfer. The second forming route comprises forming in that the blank is heated in a furnace and then formed using room temperature tooling. The latter forming process required a higher initial blank temperature to account for heat loss when the blank was transferred from the furnace to the press. The forming sequence for both process routes were as follows:

Isothermal forming (hereinafter referred to as ISO):

(1) Blank is aligned with pins in tooling.

(2) Binder closes and heats the blank. Heating times are listed in Table 29.

(3) Blank is formed at a peak velocity of 50 mm/s.

(4) Formed blank is held in the closed dies for 3 s at a force of 498.2 kN (50 tons).

(5) Part is extracted from the tooling and cooled in air.

Non-isothermal forming (hereinafter referred to as NON-ISO):

(1) Blank is placed into the preheated forced-convection furnace.

(2) Within approximately 10 s, the blank is manually transferred into the press using pliers and aligned with pins in the tooling.

(3) Blank is formed at a peak velocity of 50 mm/s.

(4) Formed blank is held in the closed dies for 3 s at a force of 498.2 kN (50 tons).

(5) Part is extracted from the tooling and cooled in air (it takes about 21 min for a blank formed at 233°C to reach room temperature)

Test Scope

As can be seen from the test matrix in Table 27, the emphasis of the rail forming study was placed on the conventional isothermal forming route and the Fuchs lubricant since friction characterization results, presented in Chapter 3, demonstrated that among tested lubricants, the Fuchs lubricant could best prevent galling and is in industrial use for high-volume sheet forming. Nevertheless, a few rails were formed with the OKS and PTFE Spray to evaluate the lubricant performance and to allow comparison with the TCT results in Chapter 3 and isothermal deep draw results in Chapter 4. Considering that lubricant breakdown occurred for the PTFE Spray at 170°C and 200°C for the OKS, a rail forming temperature of 204°C was selected for lubricant comparison. It is also important to note that only one rail was formed per lubricant condition since possible lubricant breakdown causes significant tool wear and requires polishing before the next part can be formed. For all other testing conditions, three parts were formed to assess repeatability. To study the non-isothermal forming route, AA6013 T6 was selected as baseline comparison to the performance of the 7xxx series aluminum under development, AA70XX T76, at two forming temperatures.

Table 27: Test matrix for rail forming

		Forming temperature		
Process route	Lubricant	177°C	204°C	233°C
ISO	Fuchs	AA6013 T6	AA7075 T6	AA6013 T6
		AA7075 T6	AA70XX T76	AA7075 T6
		AA70XX T76		AA70XX T76
	OKS	-	AA70XX T76	-
	PTFE Spray	-	AA70XX T76	-
NON-ISO	Fuchs	AA70XX T76	-	AA70XX T76
		AA6013 T6		AA6013 T6

In the scope of this warm forming study, three different forming temperatures were studied. The lowest temperature, 177°C, was selected since it corresponds to the heat treatment during a conventional paint bake cycle in the automobile industry. Forming at 233°C was studied since research for comparable 7xxx series aluminum alloys identified this temperature level as critical for over-aging, that involves significant precipitate coarsening and results in a drop in the final part strength. Finally, 204°C was considered as an intermediate temperature.

Part geometry

Dimensions of the 2 mm thick pre-cut blank and the as-formed rail studied in this thesis are illustrated in Figure 115 and Figure 116 respectively. Note that the function of the tabs in Figure 115 is to align the blank with pins in the tooling. For simplicity, these alignment tabs are omitted in Figure 116.

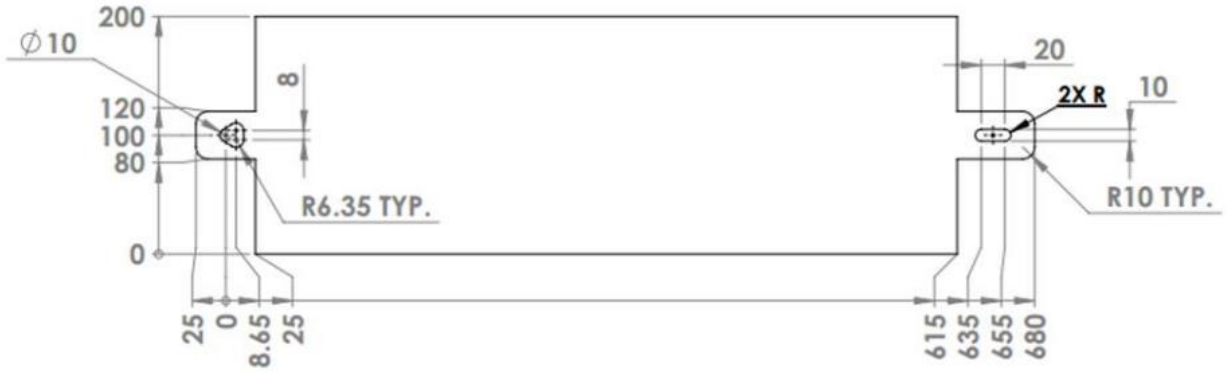

Figure 115: Utilized pre-cut blank geometry for rail forming [125]

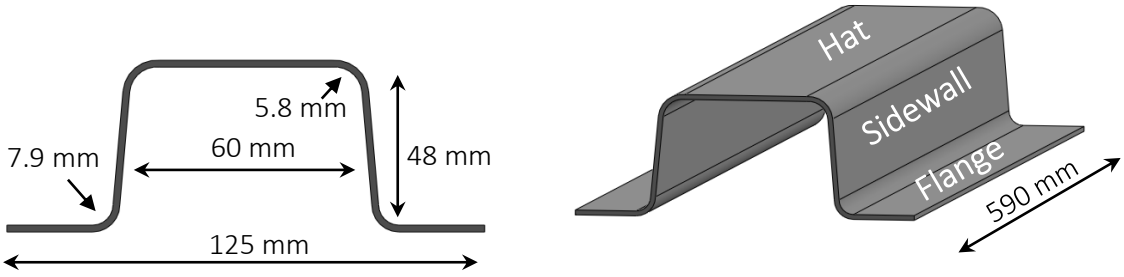

a) Front view b) Sidew view

Figure 116: Geometric dimensions of as-formed rail (alignment tabs are omitted for simplicity)

6.2 Equipment and Tooling

This section describes the tooling and equipment utilized for studying the isothermal and non-isothermal process routes (Table 27) for the structural rails illustrated in Figure 116.

The tooling was designed by DiCecco [2], and comprises a punch, die, and binder, as illustrated in Figure 117. Geometric dimensions can be retrieved from Table 28. The sidewall clearance is approximately 10% of the 2 mm blank thickness.

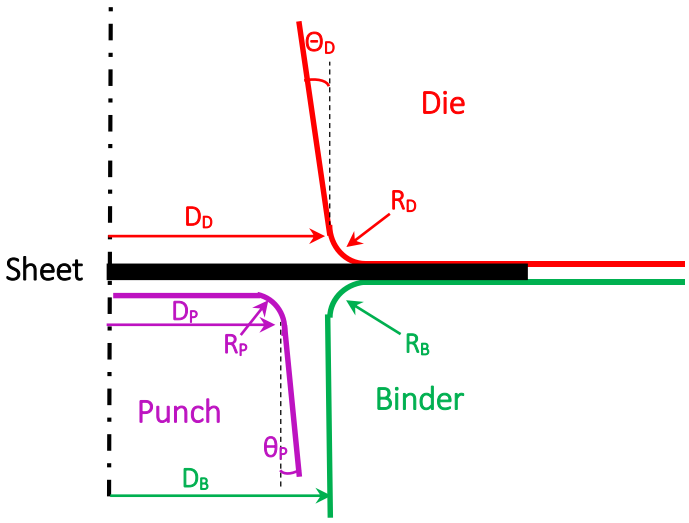

Figure 117: Labels for geometric dimensions of warm forming tooling

Table 28: Geometric dimensions of tooling for rail warm forming

Process	D_P	θ_P	R_P	D_B	R_B	D_D	R_D	Θ_D
Rail forming	63 mm	5°	5.8 mm	70.2 mm	4.8 mm	67.1 mm	7.9 mm	5°

The punch is stationary whereas the die moves downwards with the press slide. The binder load is controlled through four nitrogen springs that are charged to a pressure of 12.4 MPa (124 bar) each, yielding a binder force of 24.4 kN at first contact, increasing to approximately 31.7 kN at 48 mm press stroke [126]. Considering the contact area of the blank with the binder and the blank draw-in during forming, the binder contact pressure ranges from 0.3 MPa (initial contact) to 1 MPa (end of forming). This rather low binder load is sufficient due to the simple part geometry and the large die entry radius (7.9 mm).

The tool set, illustrated in Figure 118, is installed in a Macrodyne 900 ton hydraulic forming press. The press capacity is 900 ton that comprises a main 600 Ton cylindrical actuator and four smaller cylinders (with 300 ton capacity). For the scope of this work, the four smaller cylinders were utilized. Pressure transducers are installed in the cylinders and measure fluid pressure that, based on the cylinder cross-sectional area, allows calculation of tool force. In order to accommodate warm forming, the tooling is equipped with a total of 56 cartridge resistance heaters (550 W each) and thermocouples that are arranged in a total of seven control circuits. Figure 119 gives an overview on the respective control zones. Cooling channels are drilled into the bolster plate on that the binder is installed to isolate the tooling and prevent heating of the nitrogen cylinders or the electrical components. Additionally, to preclude heat loss to the surrounding medium, Zircal insulation plates are mounted on the outer tooling faces.

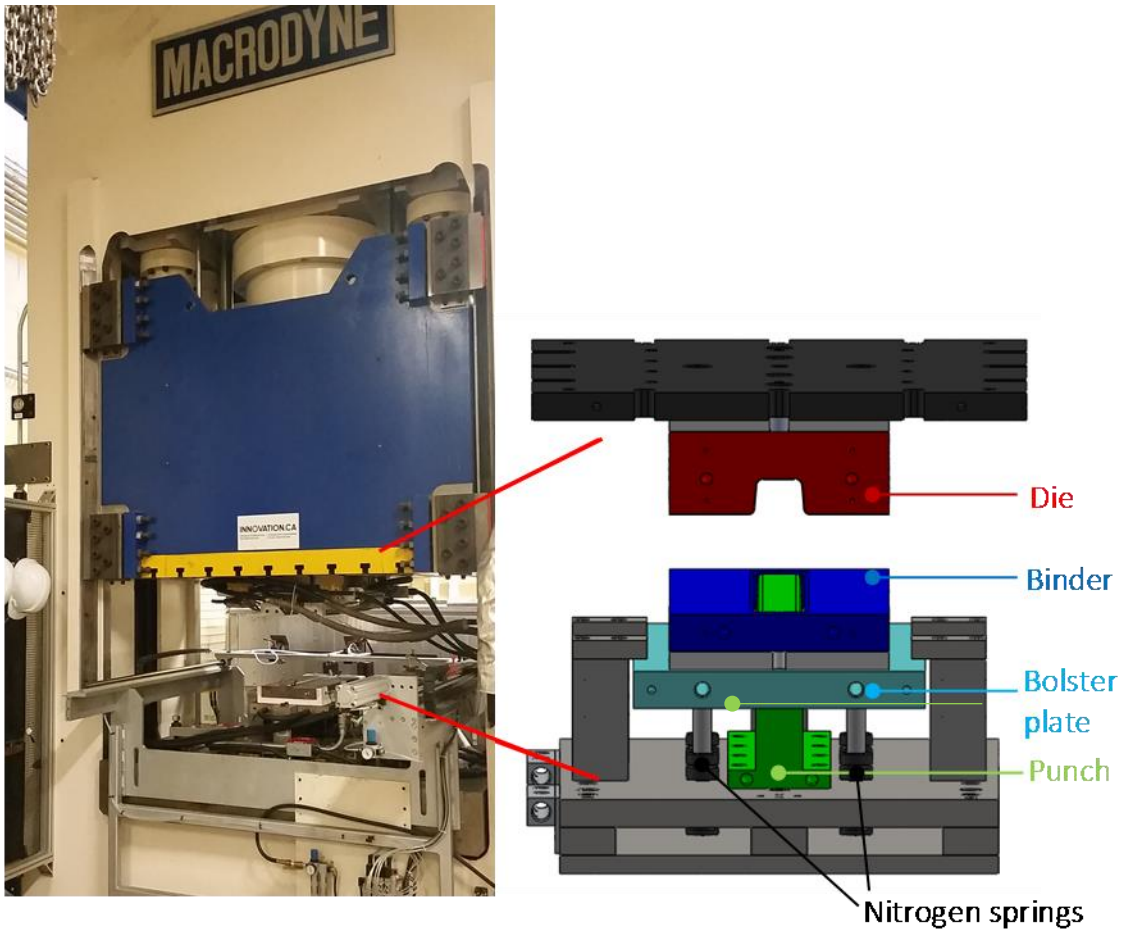

Figure 118: Tool set and equipment used for rail warm forming

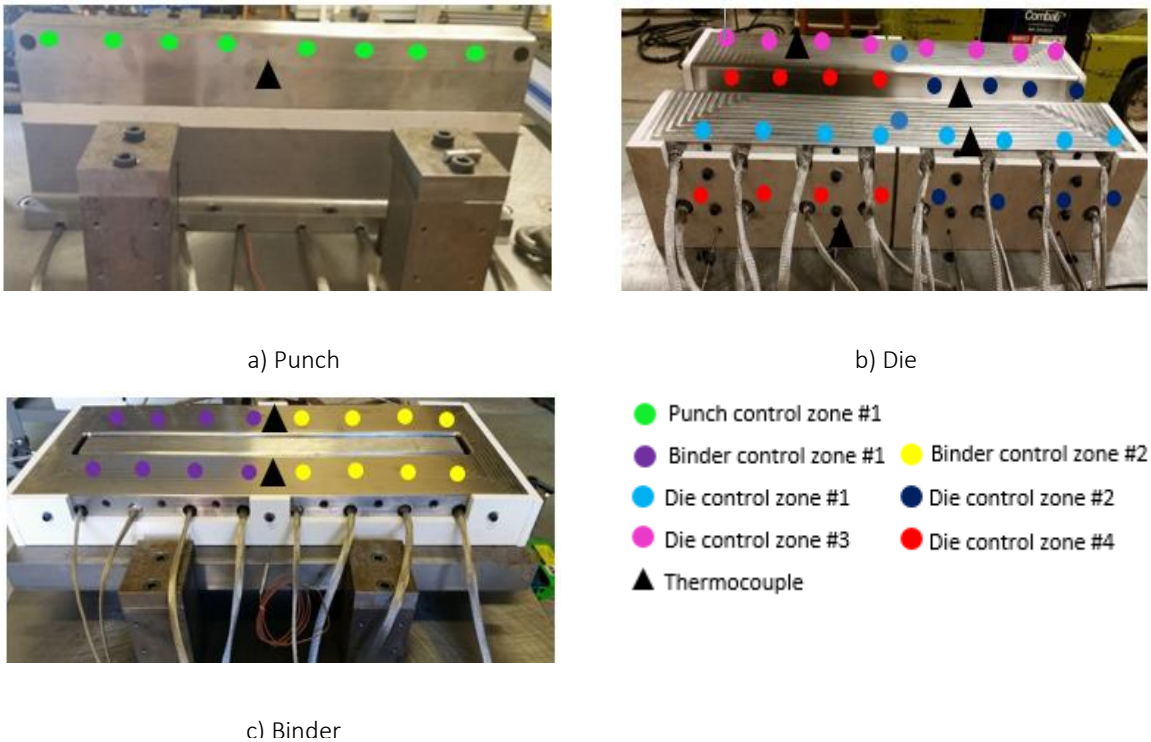

Figure 119: Heating zones of rail forming die set

As outlined in Figure 120, the press is arranged in process flow direction and the conventional forming sequence is as follows: the blank is heated in the furnace (behind the press), then pulled into the press by a pneumatic-powered transfer mechanism, aligned with the help of pins, and promptly formed. With the intention of limiting heat exposure and hence prevent or limit over-aging, a different procedure was adopted for this study. For isothermal forming, the blank was heated through contact with the tooling for that no furnace was required. For the non-isothermal process route, a different, forced convection, furnace was utilized that allowed shorter heating times. As a result, the following forming sequence was employed:

(i) Blank is loaded into the forced convection furnace

(ii) Manual transfer of the blank into the press and alignment with pins

(ii) Prompt forming

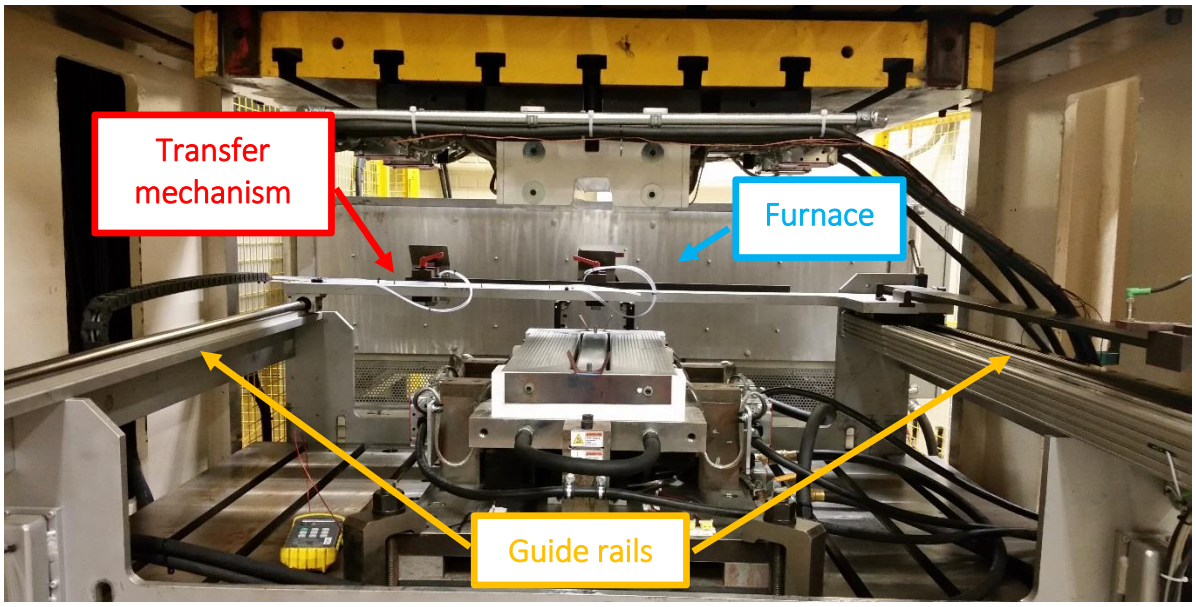

Figure 120: Press arranged in process flow direction for conventional operation; in this thesis, a different furnace was utilized that allowed faster heating times with the intention of limiting heat exposure of 7xxx series aluminum alloys. Hence, blanks were manually transferred into the press.

6.3 Process Parameters

The rail warm forming experiments considered the effect of three different forming temperatures (177°C, 204°C, and 233°C) and two different forming routes (isothermal and non-isothermal) on the as-formed part properties such as micro hardness, thinning, and surface quality. To ensure forming at the target temperature, heating times were determined in pre-tests through attached thermocouples.

As shown in Figure 121, a blank was prepared with a 100 mm long and 1.2 mm deep slot, to that a thermocouple was attached utilizing high-temperature resistance glue and tape. One heating cycle was recorded for each process route and forming temperature, 177°C, 204°C, and 233°C with a lubricated blank.

Before thermocouple is attached

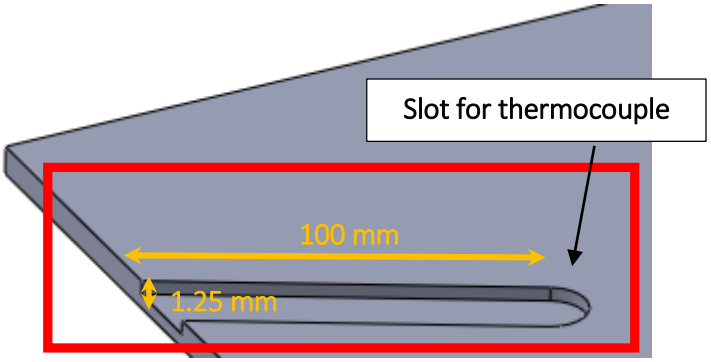

After thermocuple is attached

Figure 121: Blank preparation with a thermocouple to determine heating times

The temperature history was recorded with a DAQ system and a sampling rate of 0.1 s. For the isothermal forming route, the blank was heated through contact with the tooling that allowed fast heating times as demonstrated in Figure 122 and is the reason why heating and forming temperature were identical. Including a safety margin, a heating time of 90 s, 120 s, and 180 s was selected for isothermal forming at 177°C, 204°C, and 233°C, respectively.

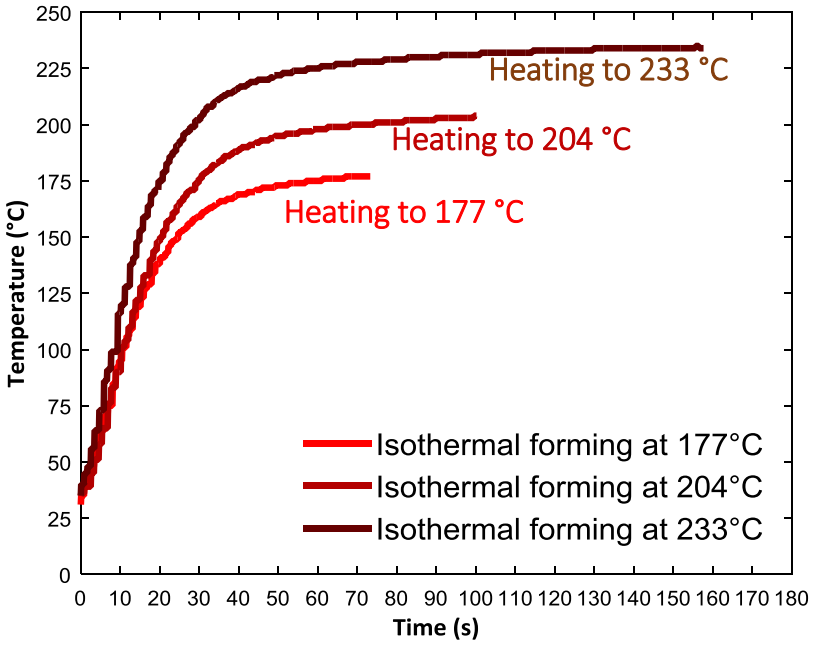

Figure 122: Recorded heating times for the isothermal process route

Table 29 records heating times together with tooling temperature. It is worth noting that for isothermal forming, the punch was set to a higher temperature than the die and binder. The reason for this setting can be seen in Figure 123. When the die closed to heat the blank, blank zone 1 and 3 were heated from both sides whereas only the lower blank surface of zone 2 was in tooling contact (with the punch). To compensate for this one-sided contact in zone 2, the punch temperature was set 10°C higher.

Table 29: Selected heating times and temperatures for rail warm forming

	Isothermal forming			Non-isothermal forming		
Forming temperature	Punch temperature	Die + binder temperature	Heating time	Tooling temperature	Oven temperature	Heating time
177°C	187°C	177°C	90 s	25°C	200°C	300 s
204°C	214°C	204°C	120 s	-	-	-
233°C	243°C	233°C	180 s	25°C	275°C	300 s

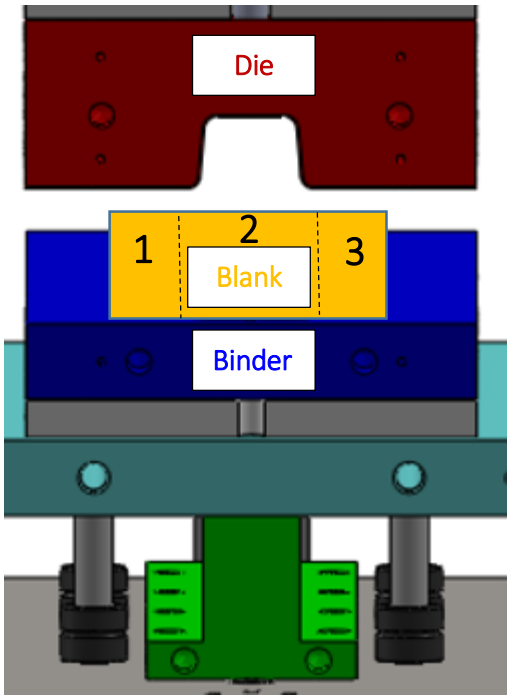

Figure 123: Heating zones in the blank during in-die heating for isothermal warm forming; when the die closed, blank zone 1 and 3 were heated from both sides whereas only the lower blank of zone 2 was in direct tooling contact. Compensating for this observation, the punch was set 10°C higher than the die and binder.

The non-isothermal process route required heating in a furnace and transfer to the press that incurred heat losses; hence, the blank required heating to a higher temperature to compensate for the temperature drop during transfer. Compared to heating the blank through contact with the tooling for isothermal forming, heating in a forced convection furnace was associated with longer heating times that was a concern considering heat-sensitivity of 7xxx aluminum alloys and the risk of over-aging. With the intention to speed up heating times, the furnace temperature was set higher than the target heating temperature as recorded in Table 29. Figure 124 records heating and transfer times for non-isothermal forming at 177°C and 233°C. The reduction in slope in the later stages of heating reduced concerns over potential temperature deviations with slight time variations: within the last 60 s of heating, the temperature changed by approximately 6°C and 3°C for a forming temperature of 233°C and 177°C, respectively. For both forming temperatures, a heating time of 300 s was selected. To account for the temperature drop during transfer from the furnace to the press, within approximately 10 s, the required blank temperature was approximately 253°C and 187°C to meet the target forming temperature of 233°C and 177°C, respectively.

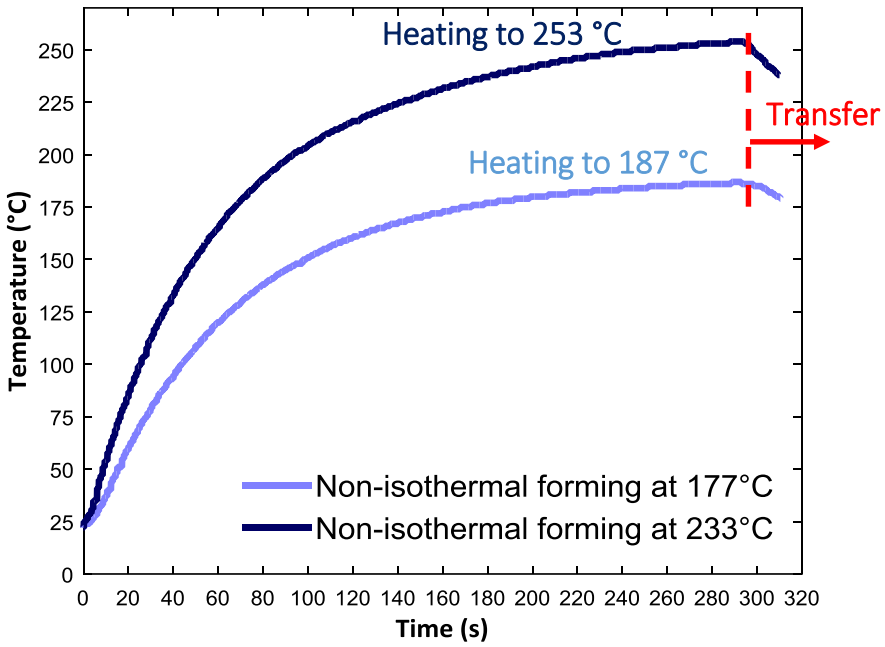

Figure 124: Recorded heating times for the non-isothermal process route

6.4 Blank Preparation for Rail Forming

The material characterization results in Chapter 2, particularly the flow-stress curves [2] in Figure 29, indicate that thermal exposure can result in a drop in material strength; the drop is strongly dependent on the forming temperature and will lead to a reduction in required forming forces. Hence, it is important to know for the non-isothermal process route, how quickly the blank cools down during forming. This information is also valuable for modelling, as demonstrated by Noder *et al.* [127], since heat transfer between the sheet and tools must be accounted for to predict the temperature decrease and associated drop in flow stress during forming.

To measure the temperature change during the non-isothermal process, thermocouples were attached to the blank prior to forming. To recess the thermocouple wires, 100 mm long and 1.25 mm deep slots were milled into the blank (Figure 125) and thermocouples were attached with high-temperature resistance glue and tape at the as-formed hat, sidewall, and flange in a similar fashion as outlined in Section 6.3. This allowed the temperature history of a complete forming cycle, including heating, transfer, forming, and cooling to room temperature, to be recorded by a DAQ system with a sampling rate of 0.1 s.

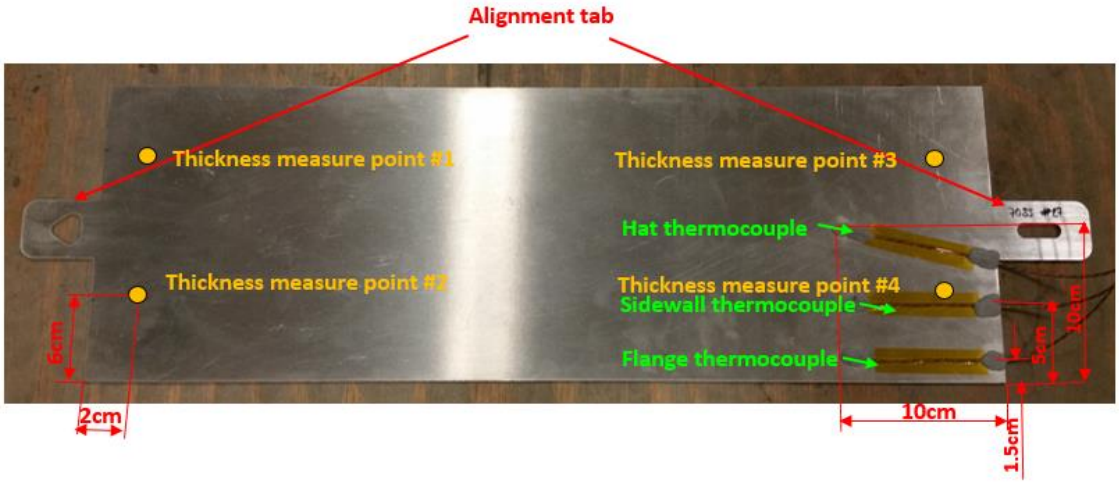

Figure 125: Blank preparation for thickness measurements and recording of the thermal response during forming

Excessive thinning in a forming process will result in fracture. Even though forming problems in terms of formability limits were not expected owing to the simple geometry of the rail, the influence of forming route and forming temperature was studied. The as-formed sidewall was adopted as measurement position since higher strain values were expected due to the plane strain loading condition. After cleaning the blank with Acetone, the thickness was measured with a micrometer, before and after forming on four locations, as illustrated by the orange circles in Figure 125.

6.5 Micro Hardness Measurements

In view of the rapid aging response of 7xxx-series aluminum alloys, excessive exposure to elevated temperatures can result in a considerable drop in part strength. Hence, the effect of heat exposure during warm forming was studied through micro hardness measurements from as-formed parts.

The alignment tab (illustrated in Figure 115) was removed after forming and 30 mm-wide strips, shown in Figure 126a, were extracted from the formed part. A precision saw and a hand shear were utilized to fabricate sample sizes of about 10 mm by 10 mm from the hat, hat radius, sidewall, flange radius, and flange section, as pictured in Figure 126c. Samples were stacked together and a cold mount of epoxy and resin (25 weight parts resin, three weight parts hardener) was prepared (see Figure 126b). Sandpaper of grit sizes 120, 400, 800, 1200, 2400 were utilized to polish pucks. A Wilson 402MVD Vickers hardness tester was utilized to form pyramid indents into the specimen surface at a load of

200 gf and a holding time of 15 s as per ASTM E384 standard. A light microscope with a filar type eyepiece was utilized to measure the diagonals (in µm) of the imprint that allowed calculation of the Vickers hardness number.

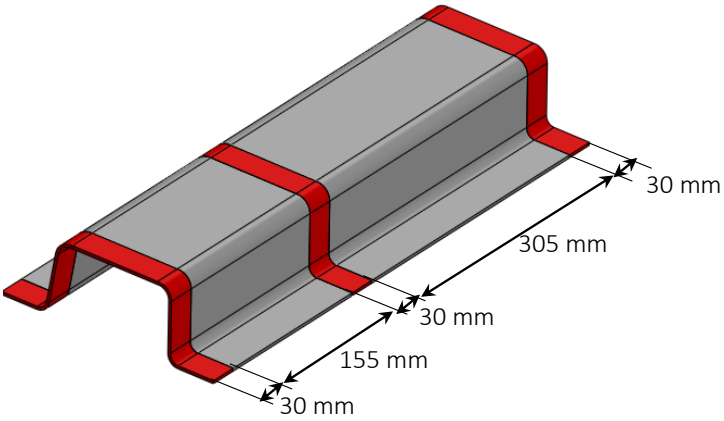

a) Extracted micro hardness samples along the rail length

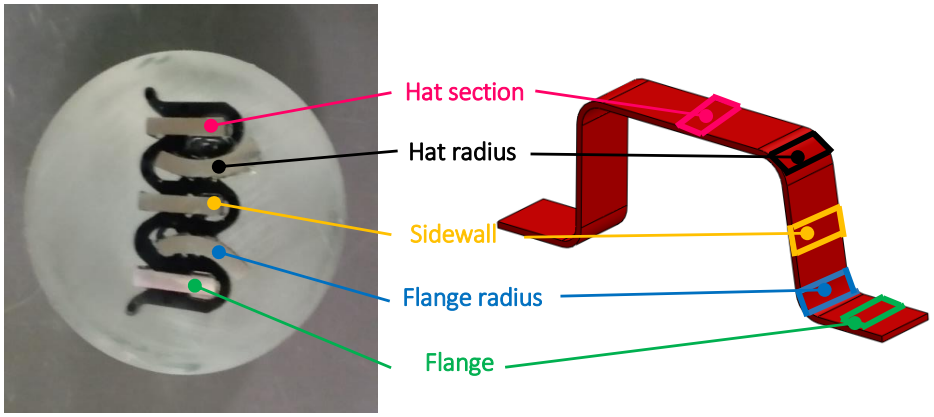

b) Puck with mounted samples

c) Measurement positions along the sample profile

Figure 126: Micro hardness measurement positions on the as-formed rail

6.6 Rail Warm Forming Results

This section discusses the results of the rail warm forming experiments that had the objective to define the process window of a near-commercial structural rail in terms of micro hardness, surface quality and amount of thinning. First, the forming force between different forming conditions is compared, followed by a discussion on thermal history during non-isothermal forming and the level of thinning. The effect of temperature on the lubricant performance is studied through assessment of the surface condition of the as-formed rails. Finally, the chapter terminates with a discussion of micro hardness

measurements of the as-formed rails to assess the effect of heat exposure on the final condition of these high strength, age hardening alloys.

6.6.1 Process Forces in Rail Forming

In the long run, higher forming forces may cause increased wear to the equipment that eventually contributes to higher costs. An increase in forming temperature lowers process forces in view of the thermally-induced drop in the material flow stress. This subsection compares forming forces for isothermal and non-isothermal forming trials on all three alloys.

Figure 127, Figure 128, and Figure 129 provide the force-displacement history during forming of the AA70XX T76, AA7075 T6, and AA6013 T6 rails, respectively, with different blank and tooling temperatures. Before discussing the various test conditions, it is worth noting that excellent repeatability between three formed parts for the same test condition was achieved and that the curves were almost coincident. To facilitate comparison between different alloys, the recorded punch force at 40 mm punch displacement is plotted in Figure 130, where error bars represent highest and lowest force value, respectively. Note that the force increases sharply for all lubricants at the end of the stroke since the punch bottomed out.

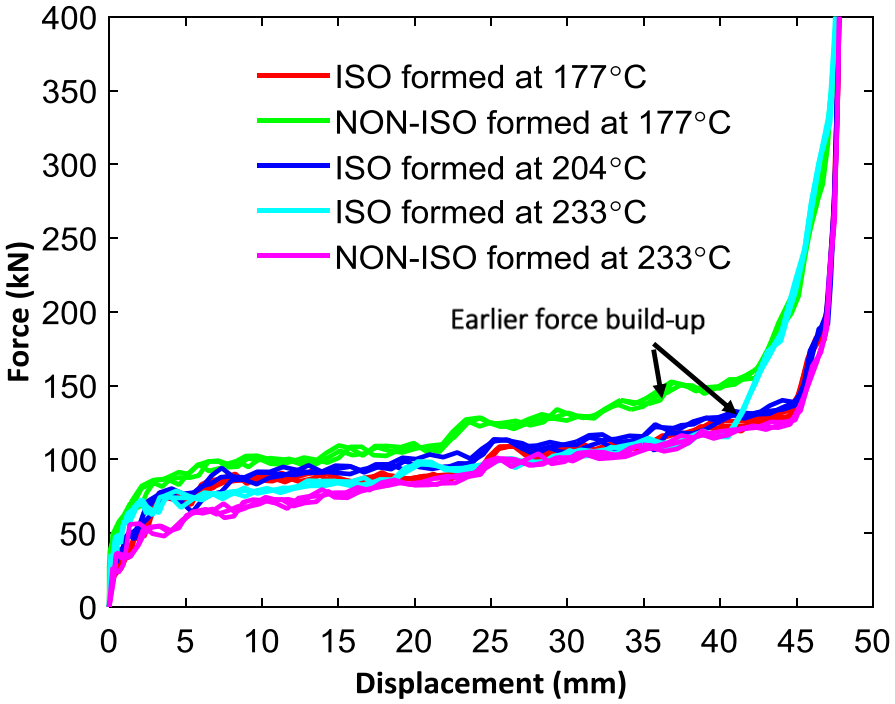

Figure 127: Force-displacement curves for AA70XX T76 at different forming temperatures

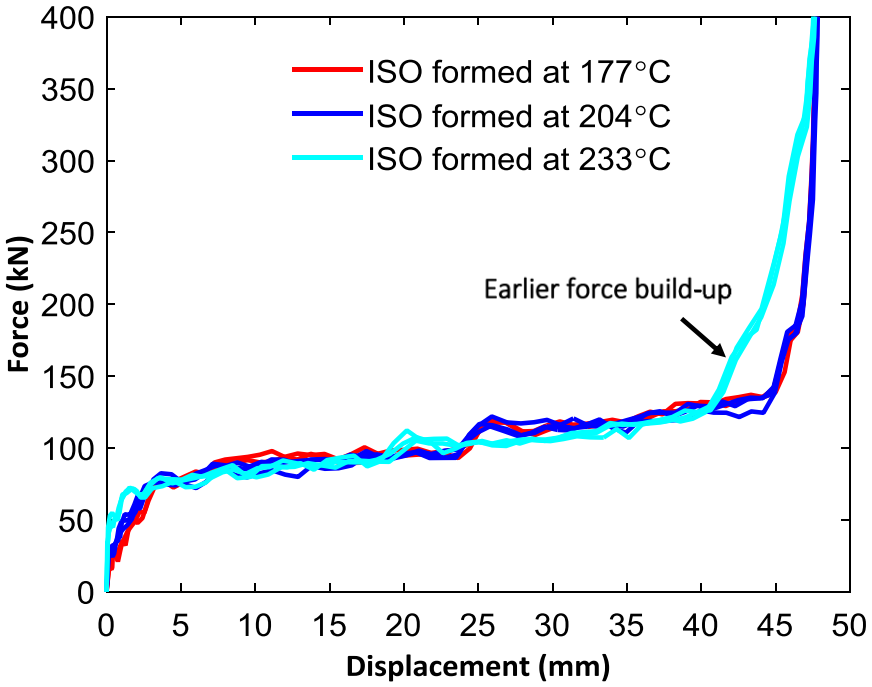

Figure 128: Force-displacement curves for AA7075 T6 at different forming temperatures

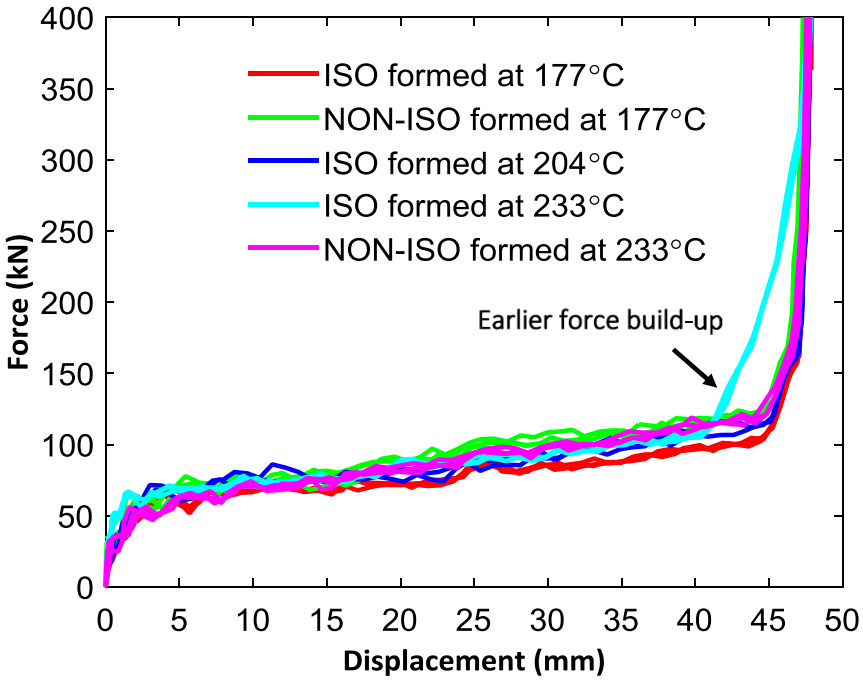

Figure 129: Force-displacement curves for AA6013 T6 at different forming temperatures; note that force curves at 204°C represent only 2 instead of 3 repeats

The forming forces for AA7075 T6 were slightly higher than the required process forces for the over-aged AA70XX T76 for the same forming conditions. As expected, the lower-strength alloy AA6013 T6 consistently recorded lower punch forces to form the rail. Compared to the isothermal route, non-isothermal forming using room temperature tooling required higher forming forces since the blank cooled down during forming that directly influenced the material flow behavior. For AA6013 T6, the force increase was less at 233°C than at 187°C owing to the temperature-induced drop in the flow stress. The same trend of significantly higher process forces (from 123 kN to 150 kN) was observed for isothermal and non-isothermal rail forming of AA70XX T76 at 177°C. A similar behavior would have been expected at 233°C. However, the force increase was within the scatter bands of repeats. Possible over-aging and associated strength loss might serve as plausible explanation and will be discussed in Section 6.6.5. Interestingly, compared to 177°C, a force reduction would have been expected when forming at 204°C, for that minor changes for both AA7075 T6 and AA70XX T76 and even an increase for AA6013 T6 was observed. Since visual inspection invalidated the theory of a change in lubrication condition, process variation might serve as explanation for this occurrence.

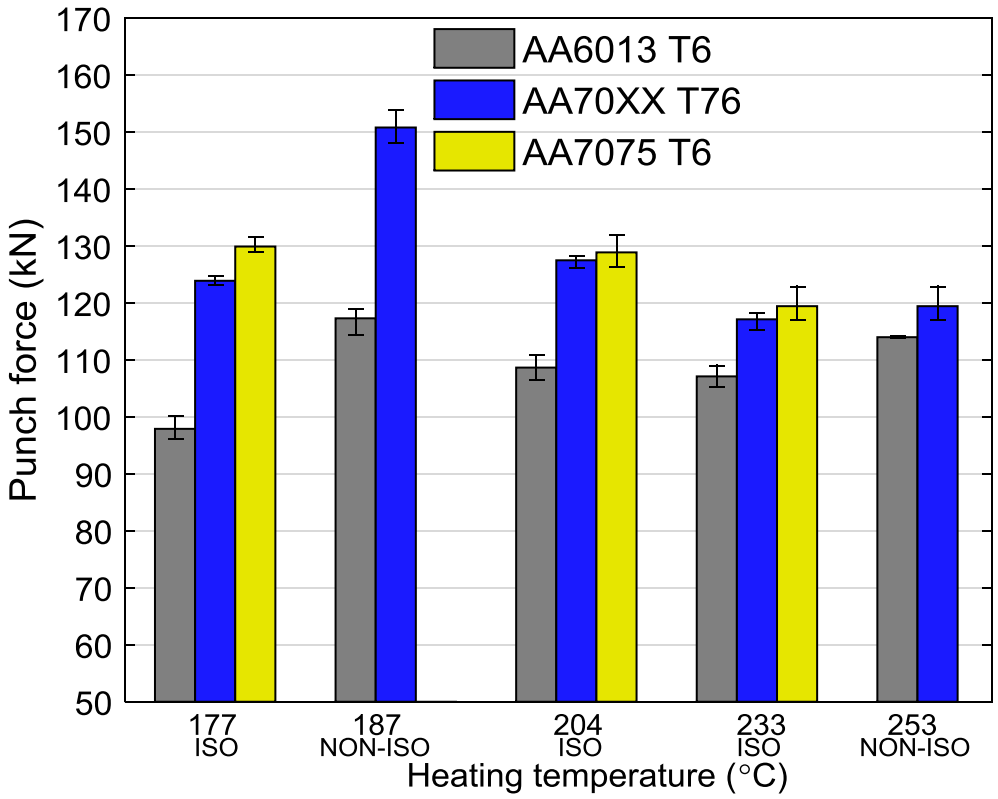

Figure 130: Comparison between forming force at a punch displacement of 40 mm for different alloys; note that error bars represent highest and lowest measured value among repeats and that there are only 2 instead of 3 repeats for AA6013 T6 at 204°C.

It is interesting to note the earlier force build-up (prior to the punch bottoming out) for parts isothermally formed at 233°C for all alloys, and non-isothermally formed at 177°C for AA70XX T76 in Figure 127, Figure 128, and Figure 129. Investigations revealed that this increases in load may be due to a loss in forming clearance in the tooling due to thermal expansion and overly-tight die clearances.

While forming temperature has a key impact on the required process force, the choice of lubricant also plays a major role, as demonstrated in Figure 131, that plots the punch force to form a rail under isothermal conditions at 204°C utilizing Fuchs (blue curve), PTFE Spray (turquois curve), and OKS (pink curve). For the first 10 mm, all three lubricants required similar forces, whereas the OKS and PTFE Spray-lubricated rails required higher forces to complete the rail geometry; at a 40 mm punch displacement, the OKS and PTFE Spray required roughly 28.6% and 21.6% higher process forces, respectively, compared to the Fuchs lubricant.

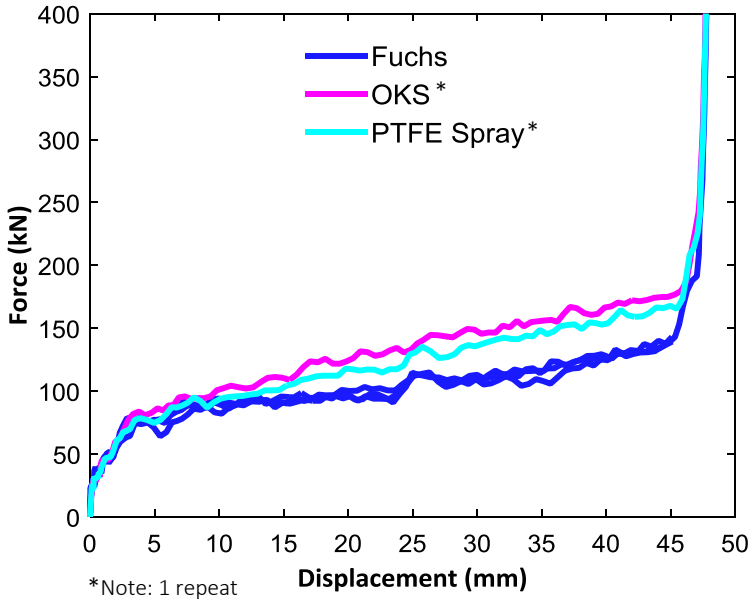

Figure 131: Force for isothermal rail warm forming of AA70XX T76 at 204°C with Fuchs (blue curve), OKS (pink curve), and PTFE Spray (turquois curve)

6.6.2 Thermal History in Non-isothermal Rail Forming

The force-time history of the formed rails under different process conditions revealed an interesting increase in forming force when forming the 177°C hot blank in room temperature tooling compared to heated tooling (177°C). Hence, it is important to know the temperature drop the blank experienced during forming. The findings using thermocouples attached to the blank are presented in this subsection.

As illustrated in Figure 132, the sidewall thermocouple attached during forming came off due to material cracking. However, the hat and flange thermocouple recorded the thermal history for a complete non-isothermal forming cycle at 177°C and 233°C.

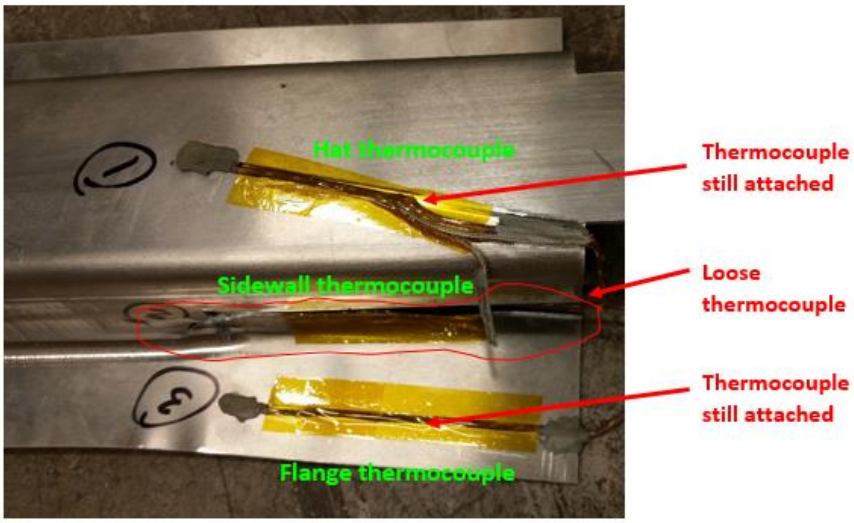

Figure 132: Rail with thermocouples attached during forming with the intention to record the thermal history

Figure 133 plots the temperature-time distribution for both forming temperatures. The green and purple curve correspond to the hat and flange thermocouple data, respectively, for the rail formed at 177°C, whereas hat and flange readings at a forming temperature of 233°C are represented by the orange and blue curve, respectively. Temperature readings after each forming step are recorded in Table 30. Please note that these temperatures represent rough approximations and that a delay in the thermocouple response as well as slight time deviations due to manual transfer of the blank could influence stated temperature values.

The target forming temperature after transfer to the press was reasonably met by both forming conditions (see Table 30). Due to contact with the room temperature tooling during forming, the blank experienced a significant drop in temperature: a blank formed at 233°C (temperature at initial tool contact) cooled down to roughly 153°C and 141°C in the rail hat and flange section, respectively. Cooling to a temperature of 66°C and 96°C in the rail hat and flange section, respectively, was observed for a forming temperature of 253°C. A higher temperature in the flange instead of the hat section contradicted expectations since the rail hat contacted the room temperature tooling only at the end of the forming stage. It is assumed that a delay in the thermocouple response was responsible for this outlier. After the die retracted, a similar blank temperature was observed for both forming temperatures: the flange recorded roughly 55°C and 73°C for a forming temperature of 177°C and 233°C, respectively, whereas the hat thermocouple read approximately 64°C and 80°C, respectively.

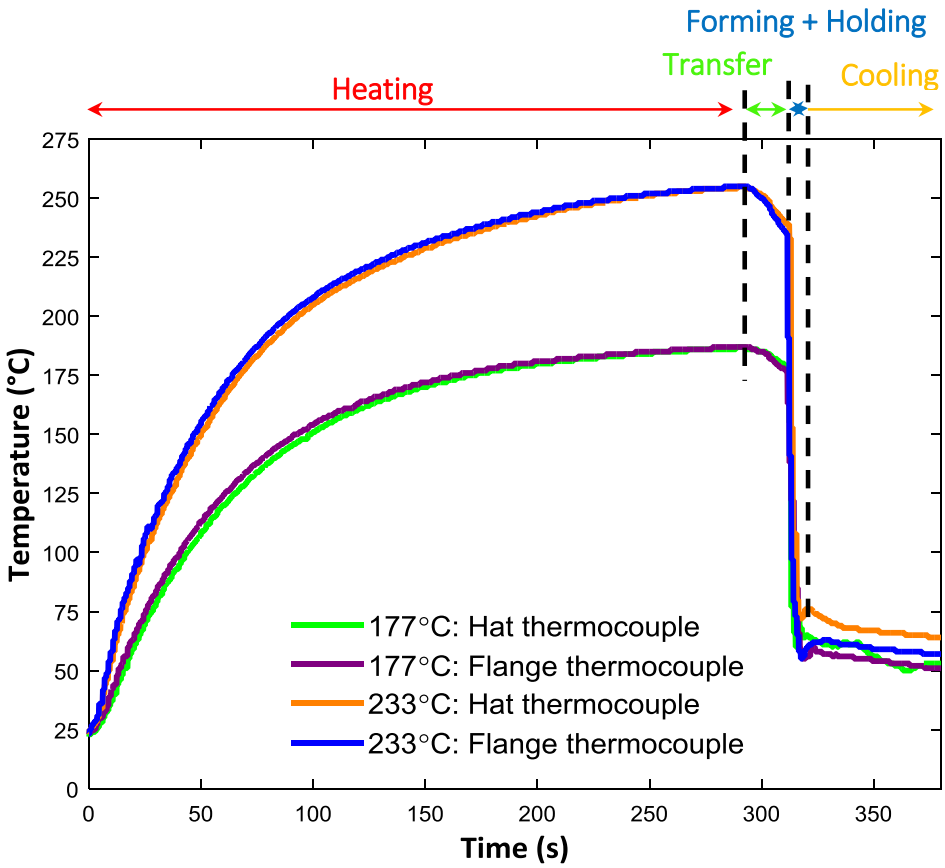

Figure 133: Thermocouple recordings of a complete forming cycle, for the non-isothermal process, at a forming temperature of 177°C (green and purple curves) and at 233°C (orange and blue curves). The sidewall thermocouple is not included in this figure since it came off during forming

Table 30: Recorded thermocouple readings during non-isothermal rail forming

	Forming temperature			
	177°C		233°C	
Forming sequence	Hat section	Flange section	Hat section	Flange section
After holding	186°C	186°C	253°C	253°C
After transfer	178°C	177°C	239°C	235°C
After forming	66°C	96°C	153°C	141°C
After holding	64°C	55°C	80°C	73°C

From material characterization in Chapter 2, between 25°C and 150°C, the flow stress curves by DiCecco [2] demonstrated only a moderate gain in terms of reduced material flow stress, compared to

the range between 190°C and 240°C. This observation in combination with the significant drop in temperature during forming might explain the higher process forces for non-isothermally formed rails at 177°C in Figure 130.

6.6.3 Thinning in Rail Forming

This subsection discusses the influence of the forming temperature and process route (isothermal or non-isothermal) on the percent thickness change on formed rails for AA70XX T76, AA7075 T6, and AA6013 T6. As described in Section 6.4, the rail sidewall was chosen as measurement position to that the initial sheet thickness was compared. The results in Figure 134 demonstrate that, in general, the thickness change was small for all alloys and forming conditions since the deformation comprises primarily a bend-unbend operation as the sheet traverses the die entry radius.

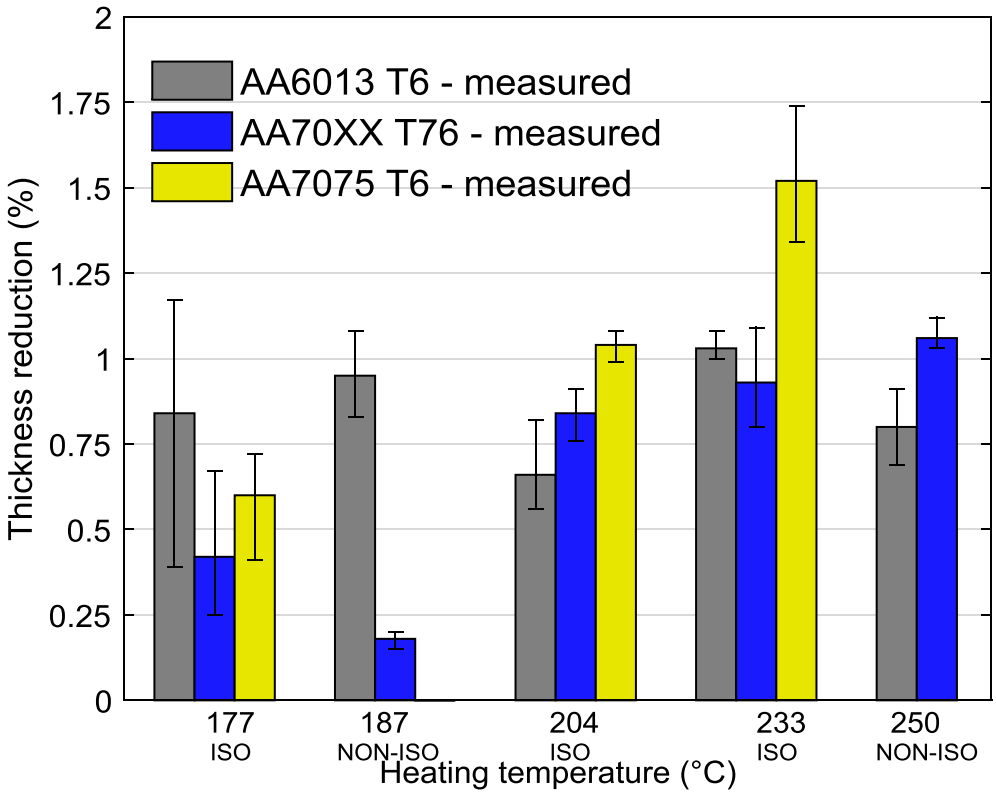

Figure 134: Percent thinning in the formed rail sidewall for different alloys and forming conditions

6.6.4 Surface Condition in Rail Warm Forming

After the forming operation and retraction of the die, the rails formed using the OKS and PTFE Spray lubricants were stuck in the die, whereas the Fuchs-lubricated rails could easily be extracted.

Photographs of the part sidewall for each lubricant, shown in Figure 135, demonstrate the range of lubricant performance. The rails formed with the Fuchs (Figure 135a) exhibited good surface quality. In contrast, galling was observed for parts formed using both the PTFE Spray and OKS lubrication, as shown in Figure 135b and Figure 135c. These trends correlated well with the observed lubricant breakdown behavior in the TCT in that film failure of the OKS and PTFE Spray was observed at 200°C and 170°C, respectively, but not for the Fuchs lubricant. The TCT records did reveal initiation of galling for Fuchs (without die coating) at 230°C, so the rail sidewall was also inspected at this temperature. The rail sidewall formed with Fuchs at 233°C is shown in Figure 135d and did exhibit occasional scratches that was consistent with the TCT trends.

Note that the isothermal deep draw study found a similar performance for the OKS and Fuchs since the forming temperature for circular cup drawing was 170°C in contrast to 204°C for this rail study. For a test temperature of 170°C, the TCT results indeed predicted a similar behavior for OKS and Fuchs (see Figure 46) with a more pronounced increase in the COF for the OKS.

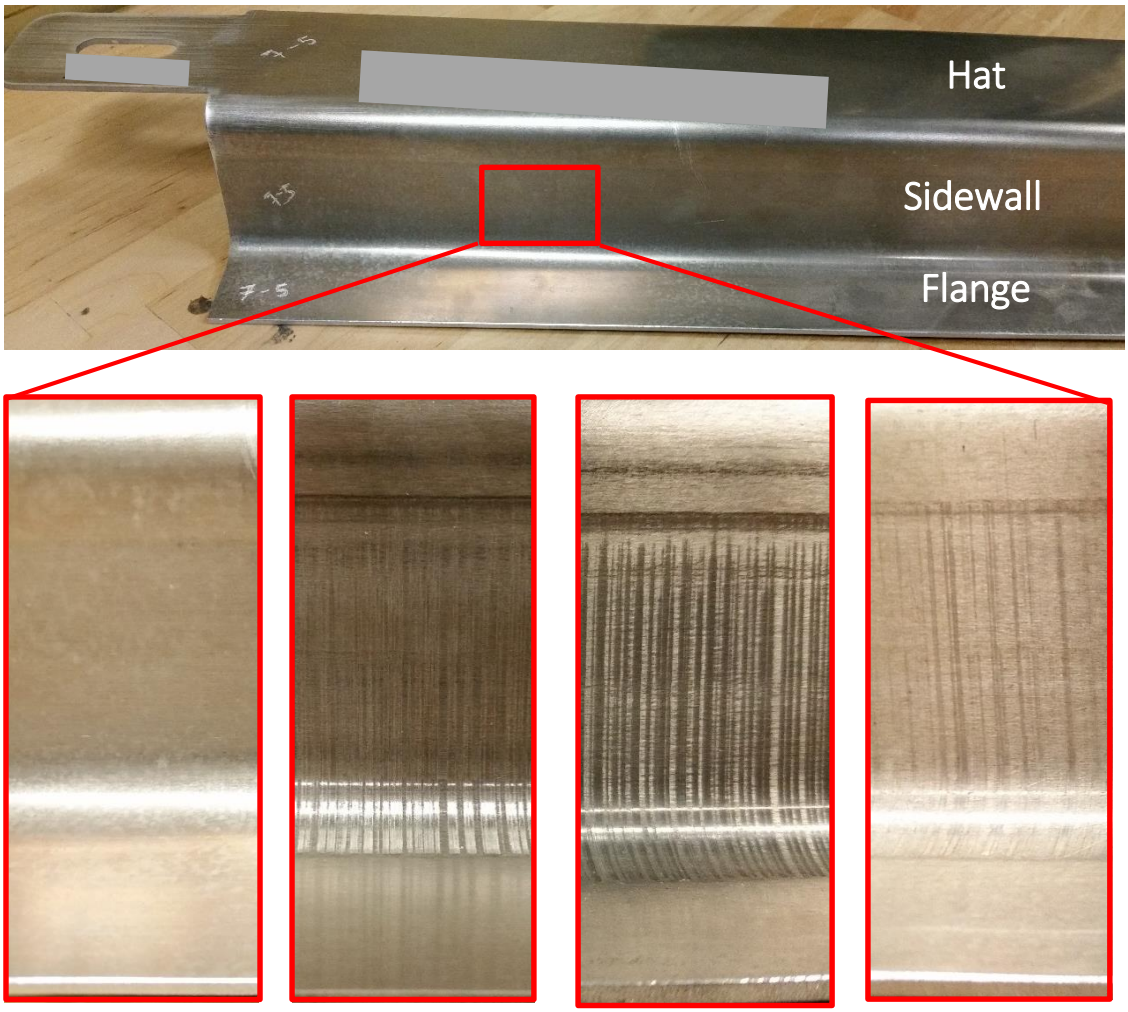

a) Fuchs at 204°C b) PTFE Spray at 204°C c) OKS at 204°C d) Fuchs at 233 °C

Figure 135: Visual inspection of the AA70XX T76 rail sidewall isothermally formed at 204°C (a, b, and c) with different lubricants and at 233°C with Fuchs (d)

6.6.5 Effect of Heat Exposure on Micro Hardness

In view of the temperature-sensitivity of 7xxx series aluminum alloys and the potential to overage these alloys, micro hardness measurements were taken on the rails to investigate the final part strength.

Figure 136 offers a time sequence of when parts were formed, micro hardness measurements taken, and heat treatments (paint bake cycle) performed. After forming, rails were stored at room temperature for about 30 days after that micro hardness measurements were taken within two days. For simulation of the paint bake cycle, selected samples were placed in a 177°C heated sand bath, kept

for 30 min, and water-quenched. Micro hardness measurements were taken on the paint-baked samples. Note that the waiting times in between different steps and treatments were due to equipment availability and sample preparation. However, it is important to note that these waiting times represent time for natural aging that might influence the material micro hardness.

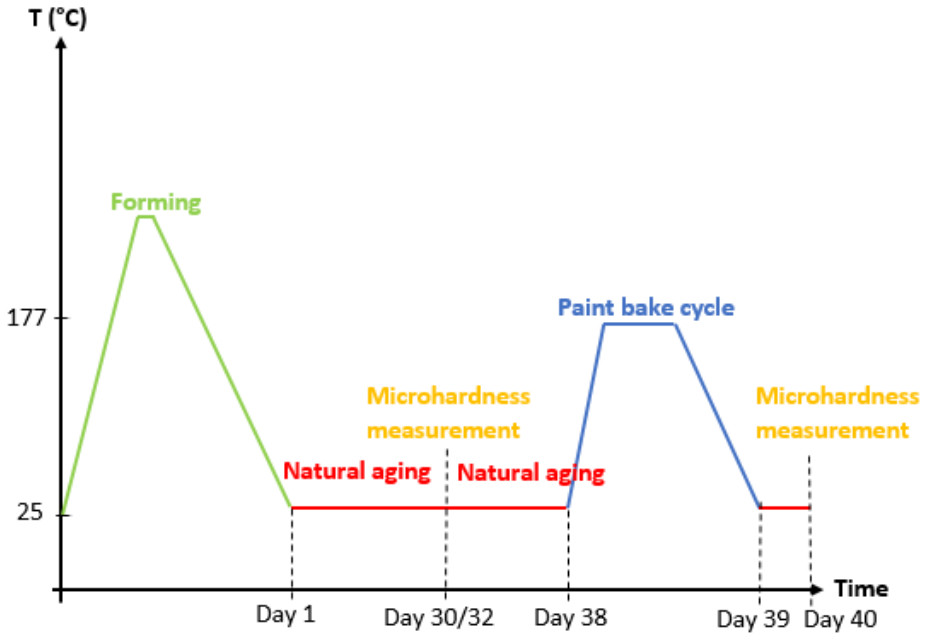

Figure 136: Time sequence for micro hardness measurements on formed rails

Initial experiments and hardness measurements, shown in Figure 137, were performed to verify the uniformity of the material properties along the rail length and cross-section, for AA70XX T76 rails isothermally formed at 177°C. A total of six measurements were taken from each hat, hat radius, sidewall, flange radius, and flange section and an average Vickers hardness was calculated. The plotted error bars display the highest and lowest value among 18 measurements, considering three repeats per forming condition. Considering the relatively small scatter bands, it was found that variation in micro hardness at different positions was negligible. The highest strain was expected in the rail sidewall and profile radii, however, since work hardening plays a minor role at elevated temperature, the small variation in hardness within the formed rails was considered reasonable. Consistent properties along the rail length, in distances outlined in Figure 126, were confirmed by the second group in Figure 137.

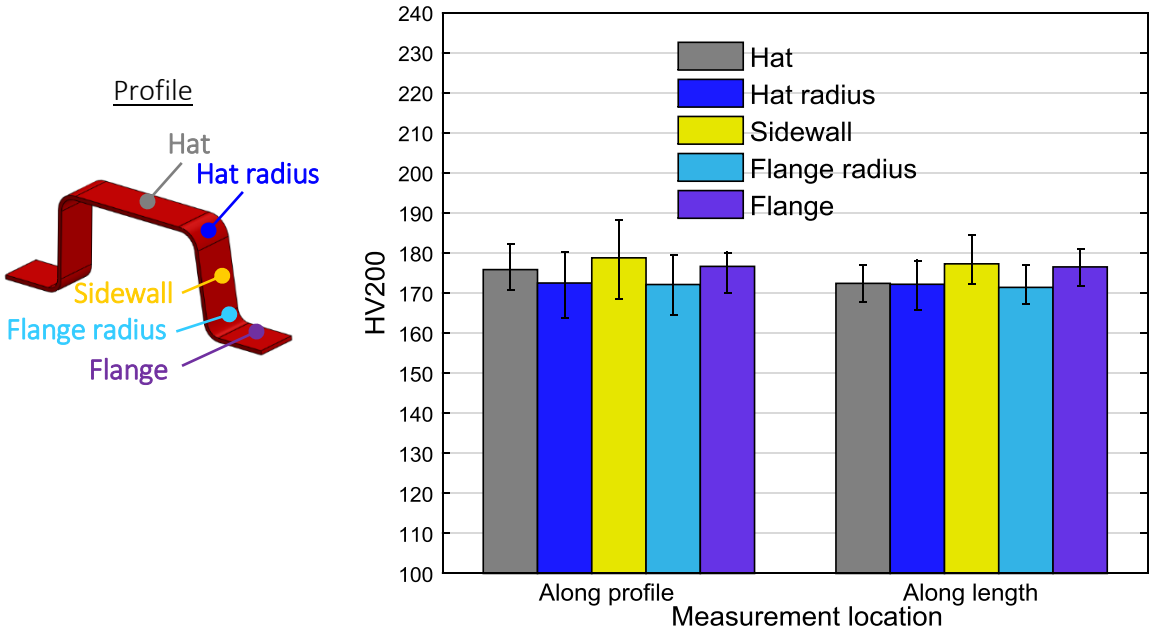

Figure 137: Vickers hardness on different locations of an AA70XX T76 rail exposed to 177°C

Effect of warm forming on as-formed hardness

In Figure 138, the micro hardness of the rail after forming is compared to as-received Vickers hardness values at 25°C. As expected, AA6013 T6 showed far lower strength than AA70XX T76 and AA7075 T6. The latter recorded peak values of approximately 194.4 HV200 whereas AA70XX T76 exhibited roughly 16 hardness units lower. This observation can be explained through the as-received temper since AA7075 was peak-aged whereas AA70XX was over-aged and sacrificed some strength in return for improved corrosion resistance.

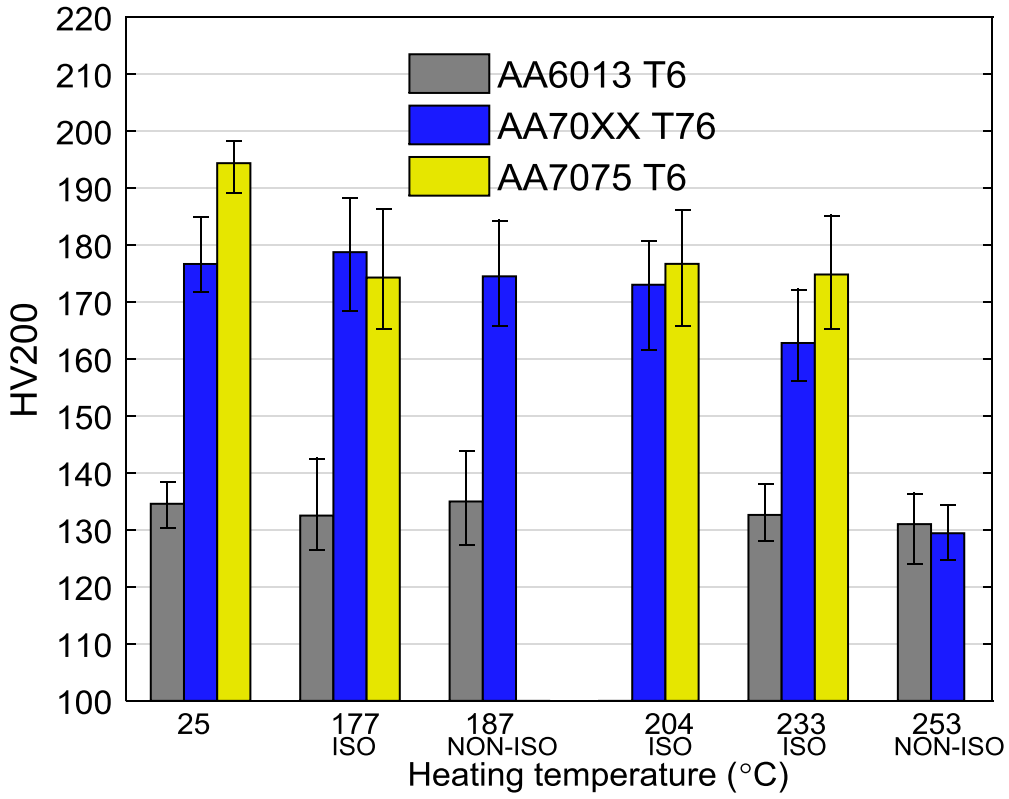

Figure 138: Influence of heat exposure on the micro hardness for different alloys (without paint bake cycle)

When looking at strength levels for AA6013 T6 exposed to different temperatures, negligible hardness losses were recorded. Even at a heating temperature of 253°C, scatter bands were within average strength levels of the as-received material. Considering this observation, no micro hardness measurements were taken for the forming condition at 204°C.

AA7075 T6 suffered an approximate 8.7% loss in hardness when exposed to 177°C for a rather short duration of 90 s, however, exhibited a relatively stable hardness level beyond this point including heating to 233°C.

In contrast to the peak-aged AA7075, the initially over-aged AA70XX T76 exhibited a lower strength in the as-received condition and more or less maintained its strength up to 204°C. A 7.8% hardness loss to approximately 162.8 HV200 was measured when heated to 233°C for 180 s. When exposed to even higher temperatures such as 253°C for 300 s, the strength level dropped by 26.8% and was comparable to the hardness of peak-aged AA6013. The strength drop observed for peak-aged AA7075 at lower temperatures could be explained through its initial temper. T6 is characterized through finely-

dispersed precipitates for that, compared to T76, less energy is required to initiate precipitate coarsening and/ or dissolution [128] that would also serve as plausible explanation why the over-aged AA70XX only experienced a drop when exposed to 233°C. The significant degradation at 253°C for this alloy could be associated with severe precipitate coarsening accompanied by dissolution of some precipitates for that RRA treatment could be attractive to partially recover the as-received strength. Hence, this material sample was selected to undergo a paint bake cycle at 177°C for 30 min.

Effect of paint bake cycle

The paint bake treatment on the AA70XX T76, previously formed after heating to 253°C, in Figure 139a yielded a moderate increase by about six Vickers hardness units that was still far below the as-received part strength. The 30-day waiting time between forming and first micro hardness measurements might contribute to the minor hardness difference between forming and paint bake cycle. If precipitates were dissolved in the retrogression phase, re-precipitation and formation of GP zones might have occurred during the 30 day natural aging period that was associated with a strength increase. This would imply that the micro hardness directly after forming was lower and that the strength gain through the 30 day natural aging period was somehow limiting the strength increase from the paint bake cycle [128]. Another reason for the low part strength might be significant precipitate coarsening and only limited re-precipitation. Microstructural studies would give clarification and should be considered in future work.

The micro hardness of peak-aged AA7075 T6 formed at 177°C and 233°C cycle exhibited moderate and negligible gains in hardness after paint bake, respectively (see Figure 139b). The final part strength still lied below the initial temper.

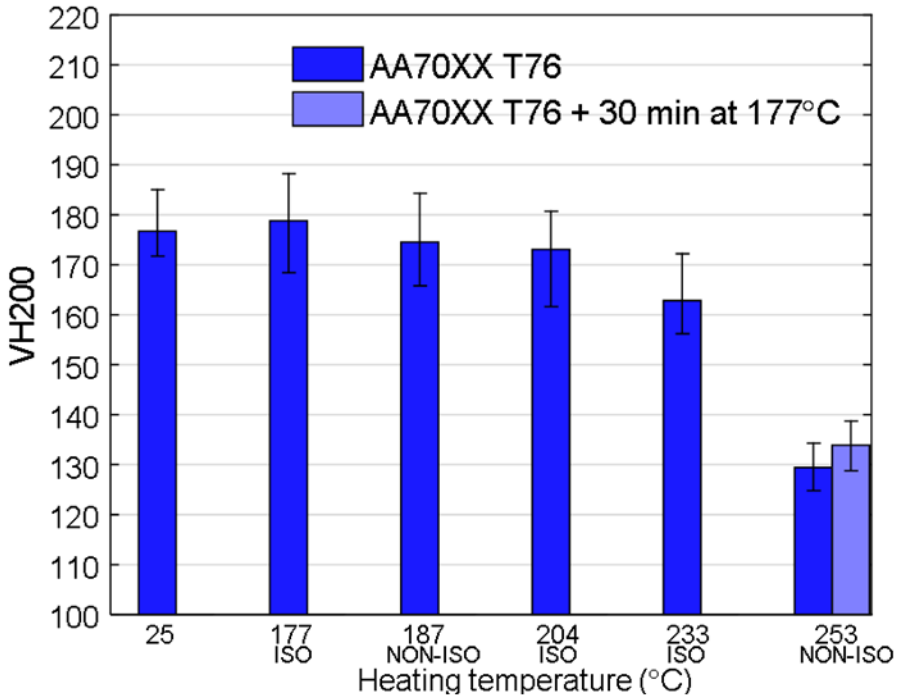

a) AA70XX T76

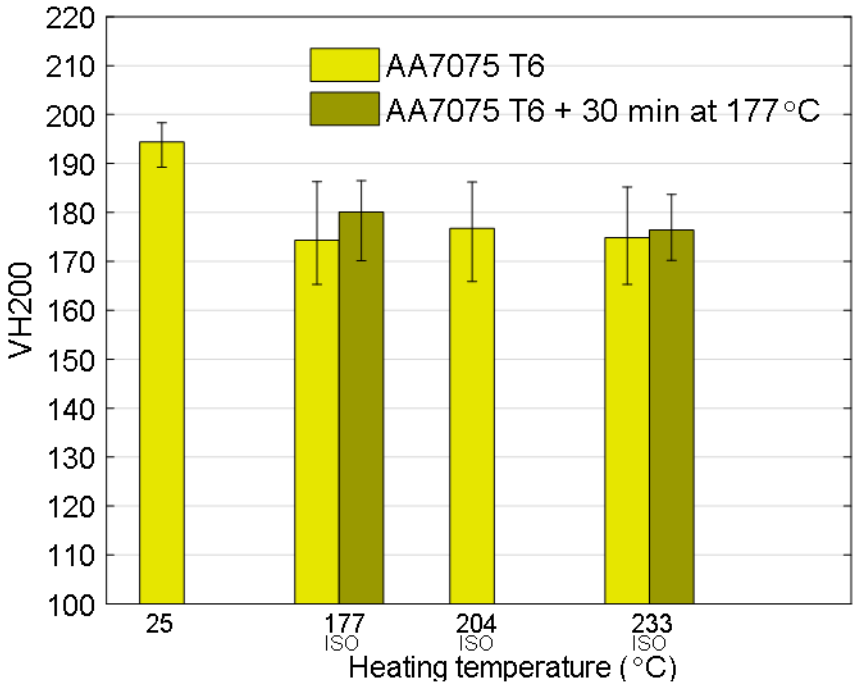

b) AA7075 T6

Figure 139: Effect of paint bake cycle on part strength level for different alloys prior exposed to different thermal conditions

Comparison to literature

Minor changes in micro hardness for AA6013 T6 over the studied temperature range from 177°C to 233°C, compared well with findings by Di Ciano *et al.* [129]. They found that in order to limit the decrease in yield stress and ultimate tensile strength to less than 10% for AA6013 T6, heat exposure between 220°C to 240°C should be limited to 30 min whereas heating times of less than one minute were permitted at temperatures between 260°C and 300°C.

Experimental results for AA7075 T6 with paint bake cycle were somewhat different from what Hui *et al.* [11] found for the same alloy and temper condition. In contrast to the reported partial strength recovery if formed between 200°C-260°C (300 s holding time at the target temperature) [11], a mild increase in micro hardness was observed for a forming temperature of 177°C and negligible gains for a target temperature of 233°C. It was assumed that due to the absence of a holding time at the target temperature, supplied energy levels during heating and warm forming were not sufficient to cause significant dissolution of precipitates that would serve as nucleation sites in the re-aging treatment [128]. It is important to note that while microstructural studies will certainly shed light into the presence of different precipitates, the focus of this mechanical study was to identify the effect of heat exposure on the part strength (hardness). Possible countermeasures could represent limitations of heat exposure to temperatures that yield acceptable final part strength that is about 204°C for AA70XX T6. Alternatively, faster heating methods such as use of an infrared heater [12] could be effective in reducing heat exposure time.

6.7 Summary of Rail Warm Forming

The purpose of this warm forming study was to assess the process window for warm forming of a near-structural part in view of retention of hardness (strength), limit amount of thinning, and the surface quality of the as-formed part. Parts were formed under isothermal and non-isothermal conditions at three different forming temperatures, 177°C, 204°C, and 233°C.

Due to the simple part geometry, thinning in the rail sidewall was found to be negligible for all forming conditions and alloys. In contrast to isothermal forming at 177°C, forming forces were considerably higher if formed at the same target temperature but in room temperature tooling. The thermal history, obtained from attached thermocouples to the blank during forming, confirmed significant blank cooling to 66°C at the stroke end. For a target forming temperature of 233°C, a similar forming force

was observed for the 7xxx series aluminum alloy under development,AA70XX T76, in both process routes (isothermal and non-isothermal), that might be due to the occurrence of over-aging since micro hardness measurements revealed a considerable strength drop from 176.7 to 129.4 Vickers Hardness for this alloy. Micro hardness measurements on AA6013 T6 formed rails demonstrated minor temperature sensitivity, whereas peak-aged AA7075 incurred an approximate 8.7% loss in hardness when exposed to 177°C that was relatively stable up to 233°C. The over-aged AA70XX maintained its strength up to 204°C.

Isothermally formed rails at 204°C, corresponding to the critical breakdown temperature for the OKS lubricant identified by the TCT, confirmed the lubricant ranking observed in the TCT. Compared to the Fuchs, both the OKS and PTFE Spray recorded higher process forces and exhibited scored surfaces in the rail sidewall.

7 Conclusions and Recommendations

7.1 Conclusions

This work has comprised material and warm friction characterization, validation through numerical-experimental circular cup draws, and application of these efforts to a near-commercial structural part for definition of the process window in terms of heat exposure, thinning, and surface quality. While most of the work has been done for all three alloys, AA6013 T6, AA7075 T6, and AA70XX T76 (the 7000 series developmental alloy), in selected cases, the emphasis was placed on the AA70XX T76 alloy in view of its novelty.

The current work has served to identify process windows for warm forming of medium-strength 6xxx and high-strength 7xxx series aluminum alloys within which moderate formability (drawability) can be achieved without significant degradation of strength relative to the as-received T6 or T76 conditions. In addition, lubrication/die coating combinations have been identified that are suitable for drawing of these alloys within these thermal process windows. Thus, warm forming represents a potentially viable option for the fabrication of high strength, light weight automotive components. This outcome is significant since the 7xxx series alloys studied offer a specific strength that is comparable to that of ultra-high strength steels, making them attractive for use within anti-intrusion elements of all-aluminum vehicle structures.

From this research, the following specific conclusions can be drawn:

(1) All three sheet alloys exhibit significant transverse anisotropy as evidenced by R-values that differ considerably from unity. AA70XX T76 exhibits a very mild directionality in yield stress but a strongly pronounced in-plane variation in R-values (in-plane anisotropy) that ranges from 0.677 in the RD to 1.87 in the TD [3]. Compared to this alloy, AA7075 T6 and AA6013 T6 exhibit lower in-plane anisotropy with R-values ranging from 0.67 and 0.8 in the RD to 1.12 and 1.0 in the TD respectively [3]. Circular cup draws were consistent with these trends in anisotropy, with the presence of eight clearly defined ears in the flange profile for AA70XX T76, compared

to only mildly pronounced ears for AA7075 T6, respectively. An ellipsoidal shape was recorded for AA6013 T6.

(2) Constitutive calibrations for warm forming simulations were developed for AA70XX T76. The absence of rate effects at room temperature and the temperature-induced rate sensitivity for AA70XX T76 was modeled through a proposed thermo-viscous constitutive model based on Hockett-Sherby [1]. In comparison to predictions using the Bergström [130] and the extended Nadai model [30], [44], [45], the new model described the observed material behavior more accurately.

(3) Warm friction characterization with the TCT revealed occasional lubricant breakdown for the PTFE Spray at RT and clear film failure at 170°C, whereas the OKS recorded a sharp increase in the COF at a test temperature of 200°C. The Fuchs lubricant was found to perform well up to 200°C, with onset of mild scoring at 230°C that can be prevented in combination with CrWN PVD-coated (Ionbond35) cups. It was found that surface roughness influences the steady-state COF. AA7075 T76 exhibits a smoother surface for which lower COFs were found, whereas AA70XX T76 and AA6013 T6 revealed a similar performance.

(4) Isothermal deep draws under comparable thermal conditions to the TCT experiments confirmed the predicted lubricant performance and identified surface condition (scoring), punch force, flange perimeter and draw-in length as parameters that could be used to distinguish lubricant performances; whereas thickness measurements and major strain in the formed cups did not allow distinction between the studied lubricants.

(5) Among the studied yield functions [18] and flow rules in the non-isothermal deep draw simulation for AA70XX T76, the associative Barlat YLD2000-2d [4] could only predict four ears whereas non-associative Barlat YLD2000-2d [4] and non-associative Hosford [5]-Barlat YLD2000-2d [4] for the yield stress function and the plastic potential, respectively, could predict eight ears. The Hosford-Barlat formulation better predicted the earing profile and was in good agreement with experiments. Some deviations were observed in the force-displacement and predicted surface strains that might be attributed to model simplifications implemented to speed up computation times.

(6) Micro hardness measurements on formed rails indicated that AA6013 T6 is less heat sensitive compared to AA7075 T6 and AA70XX T76. Exposure of AA6013 T6 to 253°C for 300 s resulted in negligible strength losses compared to the as-received material. Peak-aged AA7075 T6

experienced an 8.7% hardness drop when exposed to temperatures of 177°C for 90 s but could maintain this strength level up to 233°C. Over-aged AA70XX T76 is less heat-sensitive at temperatures up to 204°C whereas moderate and severe strength losses (7.8% and 26.8%) were measured at 233°C and 253°C, respectively. At this highest heating temperature, the strength level was comparable to AA6013 T6.

(7) The paint bake cycle for AA7075 T6 formed at 177°C and 233°C recorded little to negligible strength changes. AA70XX T76 exposed to 253°C showed a similar trend. This lack of re-aging response could be due to the 30 day (natural aging) period between warm forming and paint bake.

(8) Due to the simple rail geometry, thinning was not found to be of concern in the studied rail forming process. Visual inspection of the rail sidewall confirmed better performance of the Fuchs lubricant below temperatures of 230°C.

7.2 Recommendations

(1) At the point in time when the friction tests were performed, the equipment design did not allow dry testing at higher temperatures in view of mechanical limitations. Since the equipment has been re-designed, it would be interesting to explore the studied die coating performance of Ionbond35 at higher temperatures without lubricant (dry). Additionally, for better accuracy for low COFs, the use of a lower-capacity torque load cell is recommended.

(2) For better evaluation of the proposed thermo-viscous constitutive model, elevated temperature shear tests at various rates should be performed.

(3) Additional non-isothermal 228.6 mm diameter circular cups with Teflon film, utilized for material model validation, should be tested to assess repeatability of the observed earing profiles.

(4) It is suggested to thermo-mechanically couple the non-isothermal deep drawing simulations to explore observed deviations from the experiment due to adopted simplifications.

(5) Rails should be re-formed with the re-machined tooling incorporating larger clearance to investigate whether force increase prior to reaching full-stroke of the tool has been resolved.

(6) The validated material model from the circular cup draw simulation should be implemented in the rail simulation model in Appendix B, and evaluated in terms of forming force, thermal history, and springback.

(7) Microstructural studies on formed rails are recommended with the intention to gather a better understanding of ongoing precipitation processes in the material.

Bibliography

[1] J. E. Hockett and O. D. Sherby, “Large strain deformation of polycrystalline metals at low homologous temperatures,” *J. Mech. Phys. Solids*, vol. 23, pp. 87–98, 1975.

[2] S. DiCecco, “Personal communication,” Waterloo, 2017.

[3] T. Rahmaan, forthcoming paper, 2017.

[4] F. Barlat, J. C. Brem, J. W. Yoon, K. Chung, R. E. Dick, D. J. Lege, F. Pourboghrat, S. H. Choi, and E. Chu, “Plane stress yield function for aluminum alloy sheets—part 1: theory,” *Int. J. Plast.*, vol. 19, no. 9, pp. 1297–1319, 2003.

[5] W.F. Hosford, “A Generalized Isotropic Yield Criterion,” *J. Appl. Mech.*, vol. 39, pp. 607–609, 1972.

[6] C. Butcher, “Personal communication,” Waterloo, 2017.

[7] S. Toros, F. Ozturk, and I. Kacar, “Review of warm forming of aluminum-magnesium alloys,” *J. Mater. Process. Technol.*, vol. 207, no. 1–3, pp. 1–12, 2008.

[8] K.U. Kainer, “Potential von Magnesium in der Karosserie — Möglichkeiten und Entwicklungsbedarf,” in *Stahl, Aluminium und Magnesium im Wettbewerb, EUROFORUM-Konferenz*, 1998.

[9] C.-P. Koeth, “Audi und die Geisteshaltung Leichtbau,” 2012. [Online]. Available: http://www.automobil-industrie.vogel.de/audi-und-die-geisteshaltung-leichtbau-a-376068/]/. [Accessed: 20-Jul-2017].

[10] C. A. Ungureanu, S. Das, and I. S. Jawahir, “Life-cycle Cost Analysis : Aluminum versus Steel in Passenger Cars,” *Miner. Met. Mater. Soc.*, pp. 11–24, 2007.

[11] W. Hui, L. U. O. Ying-bing, P. Friedman, C. Ming-he, and G. A. O. Lin, “Warm forming behavior of high strength aluminum alloy AA7075,” *Trans. Nonferrous Met. Soc. China*, vol. 22, no. 1, pp. 1–7, 2012.

[12] L. Morris and R. George, “Warm Forming High-Strength Aluminum Automotive Parts,” in *SAE Technical Paper Series 770206*, 1977.

[13] M. Boba, C. Butcher, N. Panahi, M. J. Worswick, R. K. Mishra, and J. T. Carter, “Warm forming limits of rare earth-magnesium alloy ZEK100 sheet.pdf,” *Int. J. Mater. Form.*, vol. 10, pp. 181–191, 2017.

[14] T. Sato and T. Besshi, “Anti-galling evaluation in aluminum sheet forming,” *J. Mater. Process. Technol.*, vol. 83, no. 1–3, pp. 185–191, 1998.

[15] S. Wagner, “Tribology in Drawing Car Body Parts,” in *SAE Technical Paper Series 1999-01-3228*, 1999.

[16] H. Darendeliler, M. Akkoek, and C. A. Yuecesoy, “Effect of variable friction coefficient on sheet metal drawing,” *Tribol. Int.*, vol. 35, no. 2, pp. 97–104, 2002.

[17] M. Meiler and H. Jaschke, “Lubrication of aluminium sheet metal within the automotive industry,” *Adv. Mater. Res.*, vol. 6–8, pp. 551–558, 2005.

[18] A. Abedini, “Personal communication,” Waterloo, 2017.

[19] “ESAB Knowledge center.” [Online]. Available: http://www.esabna.com/us/en/education/blog/understanding-the-aluminum-alloy-designation-system.cfm. [Accessed: 15-Jun-2017].

[20] J. G. Kaufman, “Introduction to Aluminium Alloys and Tempers,” in *ASM International*, ASM International - the Material Information Society, 2000, pp. 14–28.

[21] R. Bagheriasl, “Formability of Aluminum Alloy Sheet at Elevated Temperature,” University of Waterloo, 2012.

[22] R. P. Farouk Ahmed Shehata, M. J. Painter, “Warm forming of aluminum/ magnesium alloy sheet,” *J. Mech. Work. Technol.*, pp. 279–290, 1978.

[23] J. C. Benedyk, “International Temper Designation Systems for Wrought Aluminum Alloys,” *Light Metal Age*, vol. 67, pp. 3–6, 2010.

[24] K. Omer, forthcoming paper, 2017.

[25] R. P. Garrett, J. Lin, and T. A. Dean, “Solution Heat Treatment and Cold Die Quenching in Forming AA 6xxx Sheet Components : Feasibility Study,” in *Advanced Materials Research*, 2005, pp. 673–680.

[26] O. El, L. Wang, D. Balint, J. P. Dear, J. Lin, and T. A. Dean, “Numerical study of the solution heat treatment , forming , and in-die quenching (HFQ) process on AA5754,” *Int. J. Mach. Tools Manuf.*, vol. 87, pp. 39–48, 2014.

[27] D. Finch, S. Wilson, and J. Dorn, “Deep drawing aluminum alloys at elevated temperatures. Part I,” *Trans. ASM*, vol. 36, pp. 254–289, 1946.

[28] J. E. D. D.M. Finch, S.P. Wilson, “Deep drawing aluminum alloys at elevated temperatures. Part II,” *Trans. ASM*, vol. 36, pp. 290–310, 1946.

[29] R. A. Ayres and M. L. Wenner, “Strain and strain-rate hardening effects in punch stretching of 5182-0 aluminum at elevated temperatures,” *Metall. Trans. A*, vol. 10, no. 1, pp. 41–46, 1979.

[30] A.H. van den Boogaard, “Thermally Enhanced Forming of Aluminium Sheet. Modelling and experiments,” University of Twente, 2002.

[31] D. Li and A. K. Ghosh, “Biaxial warm forming behavior of aluminum sheet alloys,” *J. Mater. Process. Technol.*, vol. 145, no. 3, pp. 281–293, 2004.

[32] D. Li and A. Ghosh, “Tensile deformation behavior of aluminum alloys at warm forming temperatures,” *Mater. Sci. Eng. A*, vol. 352, no. 1–2, pp. 279–286, 2003.

[33] P. E. Krajewski, “The Warm Ductility of Commercial Aluminum Sheet Alloys,” *SAE Tech. Pap. Ser. 2005-01-1388*, no. 724, 2005.

[34] E. D. Szakaly and J. G. Lenard, “The effect of process and material parameters on the coefficient of friction in the flat-die test,” *J. Mater. Process. Technol.*, vol. 210, no. 6–7, pp. 868–876, 2010.

[35] T. Naka and F. Yoshida, “Deep drawability of type 5083 aluminium-magnesium alloy sheet under various conditions of temperature and forming speed,” *J. Mater. Process. Technol.*, vol. 89–90, pp. 19–23, 1999.

[36] F. Viana, A. M. P. Pinto, H. M. C. Santos, and A. B. Lopes, “Retrogression and re-ageing of 7075 aluminium alloy : microstructural characterization,” vol. 93, pp. 54–59, 1999.

[37] J. K. Park, “Influence of Retrogression and Reaging Treatments on the Strength and Stress Corrosion Resistance of Aluminium Alloy 7075-T 6,” vol. 103, pp. 223–231, 1988.

[38] X. J. Wu, M. . Raizenne, W. R. Chen, C. Poon, and W. Walllace, “Thirty years of retrogressoin and re-aging,” in *ICAS 2002 Congress*, 2002, pp. 1–11.

[39] F. Barlat, H. Aretz, J. W. Yoon, M. E. Karabin, J. C. Brem, and R. E. Dick, “Linear transfomation-based anisotropic yield functions,” *Int. J. Plast.*, vol. 21, no. 5, pp. 1009–1039, 2005.

[40] G. Quan, K. Liu, Z. Jie, and C. Bin, “Dynamic softening behaviors of 7075 aluminum alloy,” *Trans. Nonferrous Met. Soc. China*, vol. 19, pp. 537–541, 2009.

[41] P. Larour, “Strain rate sensitivity of automotive shee steels: influence of plastic strain, strain rate, temperature, microstructure, bake hardening and pre-strain,” Rheinisch-Wesfaelische Technische Hochschule Aachen, 2010.

[42] E. Voce, “The relationship between stress and strain for homogeneous deformations,” *J. Inst. Met.*, vol. 74, pp. 537–562, 1948.

[43] G. R. Johnson and W. H. Cook, “A constitutive model and data for metals subjected to large strains, high strain rates, and high temperatures,” in *7th International Symposium on Ballistics*, 1983, pp. 541–547.

[44] A. H. Van Den Boogaard and J. Huétink, “Modelling of aluminium sheet forming at elevated temperatures,” in *The 8th International Conference On Numerical Methods In Industrial Forming Processes*, 2004, vol. 712, pp. 893–898.

[45] L. Van Haaren, “Deformation of Aluminium Sheet at Elevated Temperatures,” University of Twente, 2002.

[46] Y. Bergström and H. Hallén, “An Improved Dislocation Model for the Stress-Strain Behaviour of Polycrystalline a-Fe,” *Mater. Sci. Eng.*, vol. 55, pp. 49–61, 1982.

[47] W. Tang, S. Huang, D. Li, and Y. Peng, “Mechanical anisotropy and deep drawing behaviors of AZ31 magnesium alloy sheets by undirectional and cross rolling,” *J. Mater. Process. Technol.*, vol. 215, pp. 320–326, 2015.

[48] D. Banabic, *Sheet Metal Forming Processes*. Springer, 2010.

[49] R. Hill, “A theory of the yielding and plastic flow of anisotropic metals,” *Proc. R. Soc. London A*, vol. 193, pp. 281–297, 1948.

[50] H. J. Bong, F. Barlat, M.-G. Lee, and D. C. Ahn, “The forming limit diagram of ferritic stainless steel sheets: Experiments and modeling,” *Int. J. Mech. Sci.*, vol. 64, pp. 1–10, 2012.

[51] S. Esmaeili, X. Wang, D. J. Lloyd, and W. J. Poole, “On the Precipitation-Hardening Behavior of the Al-Mg-Si-Cu Alloy AA6111,” *Metall. Mater. Trans.*, vol. 34, no. 13, pp. 751–763, 2003.

[52] F. Barlat and K. Lian, “Plastic behavior and stretchability of sheet metals. Part I: A yield function for orthotropic sheets under plane stress conditions,” *Int. J. Plast.*, vol. 5, no. 1, pp. 51–66, 1989.

[53] F. Barlat, D. J. Lege, and J. C. Brem, “A six-component yield function for anisotropic materials,” *Int. J. Plast.*, vol. 7, no. 7, pp. 693–712, 1991.

[54] A. Abedini, C. Butcher, T. Rahmaan, and M. J. Worswick, “Evaluation and Calibration of Anisotropic Yield Criteria in Shear Loading: Constraints to Eliminate Numerical Artefacts,” *Int. J. Solids Struct.*, pp. 1–17, 2017.

[55] J. W. Yoon, F. Barlat, R. E. Dick, K. Chung, and T. J. Kang, “Plane stress yield function for aluminum alloy sheets - Part II: FE formulation and its implementation,” *Int. J. Plast.*, vol. 20, no. 3, pp. 495–522, 2004.

[56] J. W. Yoon, F. Barlat, R. E. Dick, and M. E. Karabin, “Prediction of six or eight ears in a drawn cup based on a new anisotropic yield function,” *Int. J. Plast.*, vol. 22, no. 1, pp. 174–193, 2006.

[57] T. Park and K. Chung, “Non-associated flow rule with symmetric stiffness modulus for isotropic-kinematic hardening and its application for earing in circular cup drawing,” *Int. J. Solids Struct.*, vol. 49, no. 25, pp. 3582–3593, 2012.

[58] J. H. Beynon, “Tribology of hot metal forming,” *Tribol. Int.*, vol. 31, no. 1–3, pp. 73–77, 1998.

[59] W. R. D. Wilson, “Tribology in Cold Metal Forming,” *J. Manuf. Sci. Eng.*, vol. 119, pp. 695–698, 1997.

[60] W. R. D. Wilson, “Friction Models for Metal Forming in the Boundary Lubrication Regime,” *J. Eng. Mater. Technol.*, vol. 113, no. 1, pp. 60–68, 1991.

[61] S. Kalpakjian, “Recent progress in metal forming tribology,” *J. Appl. Metalwork.*, vol. 4, no. 3, pp. 270–280, 1986.

[62] J. A. Schey, *Tribology in Metalworking : Friction, Lubrication and Wear*. Metals Park: American Society for Metals, 1984.

[63] H. Kim, “Prediction and elimination of galling in forming galvanized advanced high strength steels (AHSS),” The Ohio State University, 2008.

[64] M. Osman and R. A. Sauer, “A parametric study of the hydrophobicity of rough surfaces based on finite element computations,” *Clloids Surfaces A Physicochem. Eng. Asp.*, vol. 461, pp. 119–125, 2014.

[65] J. Bech, N. Bay, and M. Eriksen, “Entrapment and escape of liquid lubricant in metal forming,” *Wear*, vol. 232, no. 2, pp. 134–139, 1999.

[66] J. Kosanov, J. G. Lenard, J. Uhrig, and B. Wallfarth, “The effect of lubricant additives on the coefficient of friction in the flat-die test,” *Mater. Sci. Eng. A*, vol. 427, no. 1–2, pp. 274–281, 2006.

[67] F. P. Bowden and D. Tabor, *The Friction and Lubrication of Solids*. Oxford University Press Inc., 1950.

[68] W. R. D. Wilson, *Mechanics of Sheet Metal Forming*. General Motors Reserach Laboratories,

1978.

[69] C. Demare, J. Scheers, K. Mesure, and M. Vermeulen, “Sibetex steel sheet textures: an effective way to improve quality and reduce cost in car manufacturing,” in *International Body Engineering Conference*, 1997.

[70] G. M. Dalton, “A novel method of detecting galling and other forms of catastrophic adhesion in tribotests,” Laurentian University, 2014.

[71] E. Orowan, “The calculation of roll pressure in hot and cold flat rolling,” *Proc. Inst. Mech. Eng.*, vol. 150, no. 1943, pp. 140–167, 1943.

[72] T. Wanheim, N. Bay, and A. S. Petersen, “A theoretically determined model for friction in metal working processes,” *Wear*, vol. 28, no. 2, pp. 251–258, 1974.

[73] H. Gh, *Sheet Metal Forming - Fundamentals*, vol. 25, no. 8. ASM International - the Material Information Society, 1989.

[74] J. Hol, M. V. Cid Alfaro, M. B. de Rooij, and T. Meinders, “Advanced friction modeling for sheet metal forming,” *Wear*, vol. 286–287, pp. 66–78, 2012.

[75] M. Sigvant, J. Pilthammar, J. Hol, J. H. Wiebenga, T. Chezan, B. Carleer, and A. H. van den Boogaard, “Friction and lubrication modelling in sheet metal forming simulations of the Volvo XC90 inner door,” in *Numisheet - Journal of Physics*, 2016, vol. 734, pp. 1–4.

[76] T. Skåre and F. Krantz, “Wear and frictional behaviour of high strength steel in stamping monitored by acoustic emission technique,” *Wear*, vol. 255, no. 7–12, pp. 1471–1479, 2003.

[77] H. Kim, S. Han, Q. Yan, and T. Altan, “Evaluation of tool materials, coatings and lubricants in forming galvanized advanced high strength steels (AHSS),” *CIRP Ann. - Manuf. Technol.*, vol. 57, no. 1, pp. 299–304, 2008.

[78] G. Dalton, “New Friction Model for Sheet Metalforming,” in *SAE Technical Paper Series 2001-01-0081*, 2001, no. 724.

[79] J. L. Andreasen, N. Bay, M. Andersen, E.Christensen, and N.Bjerrum, “Screening the

performance of lubricants for the ironing of stainless steel with a strip reduction test," *Wear*, vol. 207, no. 1–2, pp. 1–5, 1997.

[80] J. L. Andreasen, N. Bay, and L. De Chiffre, "Quantification of galling in sheet metal forming by surface topography characterisation," *Int. J. Mach. Tools Manuf.*, vol. 38, no. 5–6, pp. 503–510, 1998.

[81] H. Kim, T. Altan, and Q. Yan, "Evaluation of stamping lubricants in forming advanced high strength steels (AHSS) using deep drawing and ironing tests," *J. Mater. Process. Technol.*, vol. 209, no. 8, pp. 4122–4133, 2009.

[82] D. D. Olsson, N. Bay, and J. L. Andreasen, "Prediction of limits of lubrication in strip reduction testing," *CIRP Ann. - Manuf. Technol.*, vol. 53, no. 1, pp. 231–234, 2004.

[83] N. Bay, D. D. Olsson, and J. L. Andreasen, "Lubricant test methods for sheet metal forming," *Tribol. Int.*, vol. 41, no. 9–10, pp. 844–853, 2008.

[84] H. Kim, J. H. Sung, R. Sivakumar, and T. Altan, "Evaluation of stamping lubricants using the deep drawing test," *Int. J. Mach. Tools Manuf.*, vol. 47, no. 14, pp. 2120–2132, 2007.

[85] "G 99: Standard Test Method for Wear Testing with a Pin-on-Disk Apparatus," *ASTM International*, pp. 1–5, 2000.

[86] A. Erdemir and G. R. Fenske, "Clean and Cost-effective Dry Boundary Lubricants for Aluminum Forming," in *SAE Technical Paper Series 980453*, 1998, pp. 1–4.

[87] A. Ghiotti, F. Sgarabotto, and S. Bruschi, "A novel approach to wear testing in hot stamping of high strength boron steel sheets," *Wear*, vol. 302, no. 1–2, pp. 1319–1326, 2013.

[88] A. Yanagida, T. Kurihara, and A. Azushima, "Development of tribo-simulator for hot stamping," *J. Mater. Process. Technol.*, vol. 210, no. 3, pp. 456–460, 2010.

[89] A. Yanagida and A. Azushima, "Evaluation of coefficients of friction in hot stamping by hot flat drawing test," *CIRP Ann. - Manuf. Technol.*, vol. 58, no. 1, pp. 247–250, 2009.

[90] K. Xu, "Effects of Contact Pressure on the Coefficient of Friction in Friction Tests," in *SAE*

Technical Paper Series 2003-01-1153, 2003, no. 724.

[91] H. Kim, J. Sung, F. E. Goodwin, and T. Altan, "Investigation of galling in forming galvanized advanced high strength steels (AHSSs) using the twist compression test (TCT)," *J. Mater. Process. Technol.*, vol. 205, no. 1–3, pp. 459–468, 2008.

[92] H. D. Nine, "Drawbead forces in sheet metal forming," in *Mechanics of sheet metal forming - Material Behavior and Deformation Analysis*, New York: Plenum Press, 1978, pp. 179–207.

[93] J. A. Schey and G. M. Dalton, "Lubrication Mechanisms in the forming of galvanized steel sheet," *J. Mater. Process. Technol.*, vol. 24, pp. 365–374, 1990.

[94] K. . Rao and J. . Wei, "Performance of a new dry lubricant in the forming of aluminum alloy sheets," *Wear*, vol. 249, no. 1–2, pp. 85–92, 2001.

[95] M. Geiger, M. Merklein, and J. Lechler, "Determination of tribological conditions within hot stamping," *Prod. Eng.*, vol. 2, no. 3, pp. 269–276, 2008.

[96] N. Bay, A. Azushima, P. Groche, I. Ishibashi, M. Merklein, M. Morishita, T. Nakamura, S. Schmid, and M. Yoshida, "Environmentally benign tribo-systems for metal forming," *CIRP Ann. - Manuf. Technol.*, vol. 59, no. 2, pp. 760–780, 2010.

[97] "Development of Replacements for Phoscoating Used in Forging , Extrusion and Metal Forming Processes," *National Center for Manufacturing Sciences*, Michigan, 2003.

[98] B. Podgornik, J. Vižintin, and V. Leskovšek, "Wear properties of induction hardened, conventional plasma nitrided and pulse plasma nitrided AISI 4140 steel in dry sliding conditions," *Wear*, vol. 232, no. 2, pp. 231–242, 1999.

[99] K. S. Lee, K. H. W. Seah, and C. Y. H. Lim, "The effects of using coated tools in the deep drawing of aluminium," vol. 29, pp. 235–244, 1992.

[100] B. Podgornik and S. Hogmark, "Surface modification to improve friction and galling properties of forming tools," *J. Mater. Process. Technol.*, vol. 174, no. 1–3, pp. 334–341, 2006.

[101] G. Reisel, S. Steinhäuser, and B. Wielage, “The behaviour of DLC under high mechanical and thermal load,” *Diam. Relat. Mater.*, vol. 13, no. 4–8, pp. 1516–1520, 2004.

[102] B. Wielage, A. Wank, C. Rupprecht, G. Schmidt, and S. Stark, “Schichtentwicklung für die Schmiermittelfreie Umformung von Hochfesten Aluminiumwerkstoffen,” *Materwiss. Werksttech.*, vol. 39, no. 12, pp. 871–875, 2008.

[103] B. Podgornik, S. Hogmark, and J. Pezdirnik, “Comparison between different test methods for evaluation of galling properties of surface engineered tool surfaces,” *Wear*, vol. 257, no. 7–8, pp. 843–851, 2004.

[104] T. Horiuchi, S. Yoshihara, and Y. Iriyama, “Dry deep drawability of A5052 aluminum alloy sheet with DLC-coating,” *Wear*, vol. 286–287, pp. 79–83, 2012.

[105] T. Murakawa, M, Koga, N, Kumagai, “Deep-drawing of aluminium sheets without lubricant by use of dimond-like carbon coated dies,” *Surf. Coatings Technol.*, vol. 76–77, no. 1–3, pp. 553–558, 1995.

[106] P. Rambabu, N. E. Prasad, K. V.V., and R. J. H. Wanhill, “Aluminum Alloys for Aerospace Applications,” in *Aerospace Materials and Material Technologies*, Springer Science+Business Media, 2017, pp. 29–52.

[107] “International Alloy Designations and Chemical Compositions Limits for Wrought Aluminum and Wrought Aluminum Alloys,” *The Aluminum Association*, 2015.

[108] T. Rahmaan, A. Abedini, C. Butcher, N. Pathak, and M. J. Worswick, “Investigation into the shear stress, localization and fracture behaviour of DP600 and AA5182-O sheet metal alloys under elevated strain rates,” *Int. J. Impact Eng.*, vol. 108, pp. 303–321, 2017.

[109] D. Steglich, X. Tian, J. Bohlen, and T. Kuwabara, “Mechanical Testing of Thin Sheet Magnesium Alloys in Biaxial Tension and Uniaxial Compression.pdf,” *Exp. Mech.*, vol. 54, no. 7, pp. 1247–1258, 2014.

[110] K. Omer, S. Kim, C. Butcher, and M. Worswick, “Characterizing the Constitutive Properties of AA7075 for Hot Forming,” in *IDDRG (in press)*, 2017.

[111] K. Omer, “Personal communication,” Waterloo, 2017.

[112] J. W. Yoon, R. E. Dick, and F. Barlat, “A new analytical theory for earing generated from anisotropic plasticity,” *Int. J. Plast.*, vol. 27, no. 8, pp. 1165–1184, 2011.

[113] “7075 Aluminum Composition Specification,” *MatWeb Material Property Data*. [Online]. Available: http://asm.matweb.com/search/SpecificMaterial.asp?bassnum=MA7075T6. [Accessed: 03-Aug-2017].

[114] R. George, “Personal communication,” Waterloo, 2017.

[115] “MSDS Lubricant datasheet Forge Ease AL278,” *Fuchs Lubricants Co.*

[116] “Personal communication with product manager of Fuchs Lubricants Co.”

[117] “MSDS Lubricant datasheet OKS 536,” *OKS Spezialschmierstoffe GmbH*.

[118] “MSDS Lubricant datasheet LPS Dry Film PTFE Lubricant,” *ITW Pro Brands*.

[119] “Teflon PTFE Properties Handbook,” *Dupon*, 1996. [Online]. Available: http://www.rjchase.com/ptfe_handbook.pdf.

[120] “Die coating: ionbond35.” [Online]. Available: http://www.ionbond.com/en/coating-services/forming-molding-tools/coating-portfolio/ionbondtm-35-facts/. [Accessed: 05-Aug-2017].

[121] Bohler-Uddelholm, “Dievar Data Sheets,” 2013. [Online]. Available: http://www.uddeholm.com/files/dievar-english.pdf.

[122] “G115-10: Standard guide for Measuring and Reporting Friction Coefficients,” *ASTM International*, pp. 1–13.

[123] J. A. Schey and P. C. Nautiyal, “Effects of surface roughness on friction and metal transfer in lubricated sliding of aluminium alloys against steel surfaces,” *Wear*, vol. 146, no. 1, pp. 37–51, 1991.

[124] F. Ozturk, M. Dilmec, M. Turkoz, R. E. Ece, and H. S. Halkaci, “Grid Marking and Measurement Methods for Sheet Metal Formability,” in *5th International Conference and*

Exhibition on Design and Production of Machines and Dies/Molds, 2009, pp. 1–10.

[125] M. Ortiz and J. C. Simo, "An analysis of a new class of integration algorithms for elastoplastic constitutive relations," *International Journal for Numerical Methods in Engineering*, vol. 23, no. 3. pp. 353–366, 1986.

[126] "Ultra Force Nitrogen Gas Springs," *DADCO*.

[127] J. Noder, S. DiCecco, C. Butcher, and M. Worswick, "Finite Element Simulation of Non-Isothermal Warm Forming of High-Strength Aluminum Alloy Sheet," in *ESAFORM (in press)*, 2017.

[128] M. DiCiano, "Personal communication," Waterloo, 2017.

[129] M. Di Ciano, S. DiCecco, M. Wells, E. Shahrzad, and M. Worswick, "Coarsening of AA6013-T6 Precipitates During Sheet Warm Forming Applications," *Submitt. to J. Mater. Eng. Perform.*, 2017.

[130] Y. Bergström, "A Dislocation Model for the Stress-Strain Behaviour of Polycrystalline alpha-Fe with Special Emphasis on the Variation of the Densities of Mobile and Immobile Dislocations," vol. 5, no. 4, pp. 193–200, 1970.

[131] Z. Wang, Q. Hu, J. Yan, and J. Chen, "Springback prediction and compensation for the third generation of UHSS stamping based on a new kinematic hardening model and inertia relief approach," *Int. J. Adv. Manuf. Technol.*, vol. 90, no. 1–4, pp. 875–885, 2017.

Appendix

Appendix A: Friction Characterization

Table 31: Friction coefficient at elevated temperature for AA70XX T76 with different lubricants (a failure COF of 0.1 was employed)

	Fuchs	Teflon film	OKS	PTFE Spray	Unlubricated
25°C	0.075	0.037	0.072	0.049	0.343
Standard Deviation	0.008	0.007	0.005	0.006	0.009
170°C	0.032	0.007	0.048	0.047	0.351
Standard Deviation	0.006	0.002	0.006	0.005	0.019
200°C	0.044	Not tested	0.079	Not tested	Not tested
Standard Deviation	0.007	-	0.006	-	-
230°C	0.073	Not tested	Not tested	Not tested	Not tested
Standard Deviation	0.007	-	-	-	-

Appendix B: Rail Forming Simulation

This section discusses the model set-up for rail forming discussed in Chapter 6. This model was utilized to compute the average forming pressure for the TCT study (see Section 3.2). The thermal history, force-displacement and thinning were evaluated with a von-Mises material model and are documented in [127]. The validated anisotropic material model, discussed in Chapter 5, can readily be implemented into this model.

Since the non-isothermal simulation model is more complex in nature, its set-up is discussed first and simplifications for the isothermal model are pointed out afterwards. For the main simulation model,

heating of the process is simulated since in view of the rail dimension, thermal expansion is felt to be important.

Non-isothermal Rail Forming FE Model

The thermo-mechanical simulation model is structured into five stages to allow a more efficient computation of the forming operation as the type of mechanical solver (explicit or implicit) can be switched after one simulation stage. The strain, stress, and temperature output at the end of one simulation are imported into the next model. An overview of the model structure and time sequence is given in Figure 140 in that one box corresponds to one simulation stage while the color represents the utilized mechanical solver.

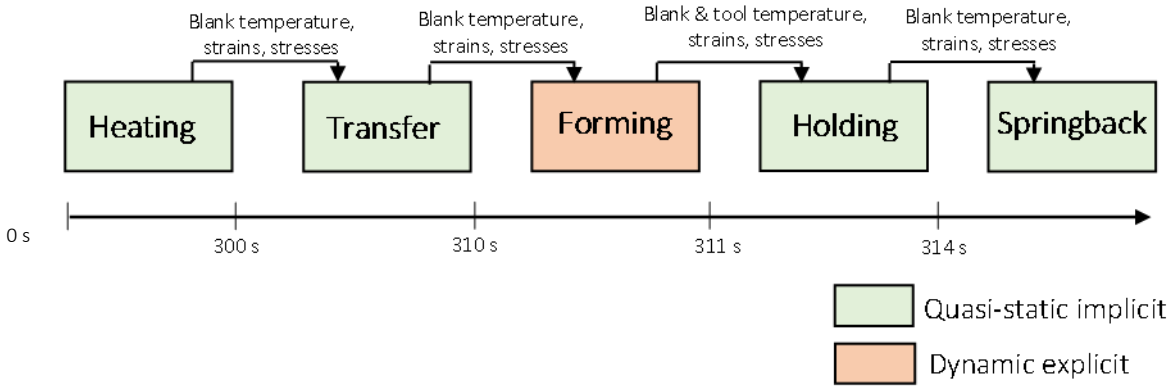

Figure 140: Structure of simulation model for warm forming of rails

As non-isothermal forming required heating in a furnace and transfer to the press, that was associated with a temperature drop, heating process, that includes thermal expansion, and the transfer to the press, that accounts for temperature drop, was simulated in two separate stages. Whereas a mechanical quasi-static implicit solver was used for the first two simulations, a dynamic explicit solver was required for the main simulation (forming of the geometry) to account for constitutive, geometric and contact nonlinearities. Holding the blank in closed dies for 3 s to fix the geometry was simulated with a quasi-static implicit solver. Finally, the last stage simulated cooling of the rail to room temperature and captured spring back phenomenon.

The simulation model comprises a blank, die, binder and punch. The geometry and mesh structure of the simulation model is illustrated in Figure 141. Note that due to symmetry, the simulation model was

reduced to one quarter and respective symmetry constraints were enforced to account for this simplification.

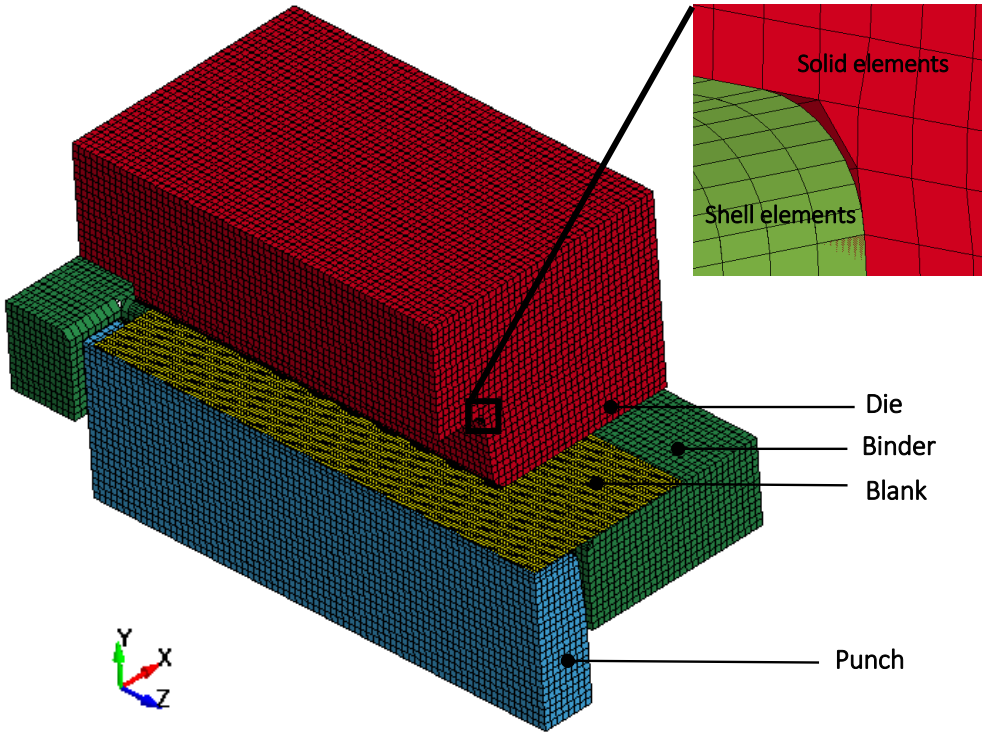

Note: for visualization purpose, a few element rows of the die are blanked

Figure 141: Geometry and mesh structure of the non-isothermal rail forming model

In order to model the cooling of the blank when contacting the tooling, mostly hexahedral and a few pentahedron volume elements were required for the tooling. At the same time, however, a very fine mesh along the tooling radius was needed to accurately capture the geometry and to ensure proper contact detection. Hence a finely meshed rigid shell layer, illustrated in Figure 141, was constrained on top of the tooling surface and used for mechanical and thermal contact definition. The blank was discretized with fully-integrated thick thermal shells. In view of a minimum number of three elements along the bending radius and a reasonable element size to yield acceptable computational costs, 2 mm quadrilateral elements were utilized.

Within 300 s, the initially room temperature blank was heated to 187°C and 253°C respectively through a temperature boundary condition. The temperature drop when, within approximately 10 s, the blank

was transferred from the oven to the press was simulated through a convection boundary condition, with a coefficient of 20.5 Wm^2/K, applied to the upper and lower blank surface.

The third stage simulated the shaping of the rail geometry. The die moved at a peak velocity of 50 mm/s that was prescribed using a ramp function to prevent inertial effects. The binder load was realized through a spring force with an on-contact force of 6.1 kN and a peak load of 7.9 kN after 48 mm travel distance. Note that these force magnitudes correspond to one quarter of the total load exerted by the nitrogen springs in the physical forming process. At the same time, the velocity of the binder was limited to the peak velocity of the die (50 mm/s) to control the die-binder gap. To capture the thermal interaction, the initially room-temperature tooling was assigned a thermal two way penalty-based contact with contact pressure-dependent heat transfer coefficients listed in Table 26. Distance values for that thermal contact is detected were adopted from the deep drawing simulation. For heat transfer from the constrained shell layer to the volume elements, a thermal tied contact with a high heat transfer value of 5000 Wm^2/K was utilized. A convection boundary condition was applied to the blank upper surface that was automatically switched off once contact with the die was detected. Temperature-dependent COFs for Fuchs, recorded in Table 31, were implemented and the frictional shear stress was restricted to the factor of 0.58 of the material yield strength.

After the rail was formed, the blank was held in closed dies and a load of 124.6 kN, that corresponds to one quarter, was applied for another 3 s to fix geometry.

Finally, similarly to the second simulation stage, cooling of the formed rail was realized through a convection boundary condition on the upper and lower blank surface. Additionally, the inertia relief method was utilized to calculate inertia relief forces from rigid body modes to constrain the part and prevent movement [131]. The solver settings utilized and discussed in Chapter 5 were adopted for this simulation

Isothermal Rail Warm-forming

Modeling the isothermal rail forming process did not involve heat transfer between the blank and tooling. Hence, the tooling discretization was simplified to shell elements and a mechanical contact.

The five-stage non-isothermal model was reduced to three stages, heating, forming, and cooling. Note that holding was not simulated since the absence of thermal interaction for this forming route made

this simulation stage indifferent for the blank deformation behavior. Remaining boundary conditions and constraints were identical to the discussed set-up for the non-isothermal rail model.